The University of Nottingham
UNITED KINGDOM · CHINA · MALAYSIA

Nottingham Geospatial Institute

LONG-TERM PEATLAND CONDITION ASSESSMENT VIA SURFACE MOTION MONITORING USING THE ISBAS DINSAR TECHNIQUE

By

LUBNA SALIH ALSHAMMARI

Thesis submitted to the University of Nottingham
For the degree of Doctor of Philosophy
December. 2018

ABSTRACT

Satellite Earth Observation (EO) is often used as a cost-effective method to report on the condition of remote and inaccessible peatland areas. Current EO techniques are primarily limited to reporting on the vegetation classes and properties of the immediate peat surface using optical data, which can be used to infer peatland condition. Another useful indicator of peatland condition is that of surface motion, which has the potential to report on mass accumulation and loss of peat. InSAR techniques can provide this using data from space. However, the most common InSAR techniques for information extraction, such as persistent scatterers interferometry (PSI), have seen limited application over peat as they are primarily tuned to work in areas of high coherence (i.e., on hard, non-vegetated surfaces only). A new InSAR technique, called the Intermittent Small Baseline Subset (ISBAS) method, has been recently developed to provide measurements over vegetated areas from SAR data acquired by satellite sensors, providing the opportunity to apply InSAR data to peatland studies effectively for the first time.

This research examines the feasibility of the ISBAS technique applied to only C-band SAR data for monitoring long-term surface motion over two peatland areas with different environments. The first peatland area is the Flow Country in the North east of Scotland which is the largest expanse of blanket bog in Europe (open peatland area) and the second peatland area is known as Zennare Basin in the south of the Venice Lagoon, Italy, which is characterized by the presence of the marsh zone covered with peat (farmed peatland area). The assessment of long-term deformation in the Flow Country is made by analysing two sets of SAR data (ERS covering the period 1992-2000 and Sentinel-1 for the period 2015-2016). For Zennare Basin three sets of SAR data have been used in the analysis (ERS SAR data 1992-2001, ENVISAT 2003-2008, and Sentinel-1 2015-2018). The results revealed that the ISBAS DInSAR technique over open peatland areas could offer extensive support for peatland surveying which would reduce the long-term monitoring cost by assessing the relative magnitude and spatial pattern of the deformed areas that are caused by, for example, drainage, afforestation or erosion which in turn provides a key information for guiding the future management. Over farm peatland areas where the coherence is highly variable, the results also revealed a real potential of using the ISBAS technique to provide a surface motion for Venice Lagoon, where the agricultural land class (unfavourable for InSAR) is the dominant class in this area. However, the limited of both ISBAS coverage and ground data on the extent of the Zennare Basin hindered the true assessment of ISBAS accuracy. In addition to the assessment of long-term

deformation using the ISBAS technique, a novel analysis of the ISBAS DInSAR time-series was found linking between the characteristics of surface motion derived by InSAR and peat condition using Sentinel-1 ISBAS time-series over the Flow Country through the application of Singular Spectrum Analysis (SSA) and Multi-channel Singular Spectrum Analysis (MSSA).

This research suggests that the ISBAS DInSAR technique is feasible for long-term peatland monitoring, particularly over open peatland areas, can provide new insight into peatland surface dynamic changes and helps to understand the seasonal kinematic behaviour of peatland from local to regional scales.

ACKNOWLEDGEMENTS

This PhD scholarship is funded by the Ministry of Higher Education and Scientific Research in Iraq and the research has been undertaken at Nottingham University, Engineering Surveying and Space Geodesy Institute.

I would like to express my sincere gratitude to my principal supervisor Professor Stuart Marsh for his encouragement, advice and guidance throughout the study period. I would also like to express my deepest appreciation and gratitude to my second supervisor, Associate Professor Doreen Boyd for her constant support, patience, motivation and trust during the past four years of my PhD study. I am grateful for their invaluable time during thesis writing up. This appreciation and gratitude extend to my former principal supervisor Dr. Andrew Sowter who introduced me to InSAR and inspired me to apply this technique over peatland. I am gratitude for his continued support and guidance throughout the research.

Very special gratitude goes to Dr. David Large, head of the department of Chemical & Environmental Engineering in Nottingham University for his creative ideas that have been tested in this thesis, continued support as a supervisor, constructive comments and advice during the study period. I would also like to thank all of the peat research group, in particular, Russell Anderson and Roxane Andersen for supporting my work and providing access to the archived field data which have profoundly supported the validation of the work.

Similar, profound gratitude goes to all members of Nottingham Geospatial institute, particularly for the former PhD student Dr. Jareer Mohammed, who has provided help and assistance in many levels and for the InSAR group in Geomatic Ventures Limited for their help, useful discussion and thoughts. Special thanks also go to Dr. Alessandro Novellino, Remote Sensing Geoscientist in British Geological Survey (BGS) for his support and help during the first half of the research.

To my mother Intisar Abdualhadi and the late father Salih Alshammari, thanks for your love, support, prayers and for all sacrifices you made to raise me this far.

Utmost appreciation and gratitude go to my beloved husband Eng. Omar Mohammed, who has supported me and always lifted my spirits up in moments of doubts. To my two wonderful children, Dimah and Mustafa who provide me unending inspiration.

Finally, very special thanks to my brother, sisters and friends for their endless support.

DECLARATION

This is to declare that the contents of this thesis are my own work and were performed at the University of Nottingham, Engineering Surveying and Space Geodesy Institute from 2014 to 2018. This thesis has not been submitted to any other institution for another degree.

Lubna Al-shammari

Faculty of Engineering, University of Nottingham

December 2018

Email: Lubna.Alshammari@nottingham.ac.uk, lubna_alshammari@yahoo.com

DECLARATION

We declare that the contents and the work described in this thesis were performed at the University of Nottingham, Engineering Surveying and Space Geodesy Institute from October 2014 to December 2018 under our supervision.

Stuart Marsh

Professor

Faculty of Engineering, University of Nottingham

Email: Stuart.Marsh@nottingham.ac.uk

December 2018

Doreen Boyd

Associate Professor

Faculty of Social Sciences, University of Nottingham

Email: Doreen.Boyd@nottingham.ac.uk

December 2018

TABLE OF CONTENT

ABSTRACT I

ACKNOWLEDGEMENTS III

TABLE OF CONTENT VI

LIST OF FIGURES XII

LIST OF TABLES XVI

LIST OF ABBREVIATIONS XVII

CHAPTER 1: INTRODUCTION 1

1.1 Preface 1

1.2 Aims and Objectives 4

1.3 Research Methodology 4

1.4 Thesis Overview 5

1.5 Summary 6

CHAPTER 2: PRINCIPLES OF SAR, INSAR, ISBAS, SSA AND MSSA 7

2.1 Overview 7

2.2 Radar background 7

2.2.1 Synthetic Aperture Radar (SAR) basics and geometry 7

2.2.1.1 Spatial resolution of SAR systems 9

2.2.1.2 Geometrical distortion of SAR system 10

2.2.1.3 Backscatter mechanisms 12

2.2.2 Interferometric SAR 13

2.2.3 InSAR errors and limitations 15

2.2.3.1 Ground-related errors 15

2.2.3.2 Satellite-related errors 16

2.2.3.3 Atmospheric-related errors 16

2.3 Punnet software 16
2.3.1 ISBAS linear processing chain 17
2.3.1.1 Debursting and merging for Sentinel 1 IW SLC product 17
2.3.1.2 Coregistration and resampling for Sentinel 1 and standard SLC products 19
2.3.1.3 Generation of the differential interferogram 22
2.3.1.4 Estimation of coherence maps 24
2.3.1.5 Selection of the reference point 26
2.3.1.6 Phase unwrapping 27
2.3.1.7 Stacking 28
2.3.1.8 Estimation of the linear deformation 29
2.3.2 ISBAS non-linear processing chain 30
2.4 Singular Spectrum Analysis (SSA) overview 31
2.4.1 Univariate SSA 32
2.4.2 Multivariate SSA (MSSA) 34
2.4.3 Monte Carlo SSA (MC-SSA) 36
2.4.4 Iterative gap filling using SSA 37
2.5 Summary 38
CHAPTER 3: LITERATURE REVIEW 39
3.1 Introduction 39
3.2 Peatland characteristics and ecosystem services 39
3.3 Peatland distribution and types 41
3.4 Climate control on peatland characteristics and ecosystem services 43
3.5 Peatland degradation 43
3.6 Causes of peatland degradation 44
3.7 Peatland degradation and the environmental hazard 45
3.8 Techniques for monitoring change in peat surface (degradation and accumulation) 45

3.9 Difficulty in monitoring peatland areas 48
3.10 The use of InSAR for deformation monitoring 50
3.11 Limitations summary 54
3.12 Summary 55
CHAPTER 4: THE STUDY SITES 56
4.1 Introduction 56
4.2 Flow Country 56
4.2.1 Topography and geology 57
4.2.2 Climate 60
4.2.3 Hydrology and ecology 60
4.2.4 Deformation in Flow Country 61
4.2.5 List of data sources 62
4.2.5.1 SAR dataset 63
4.2.5.2 Field data measurements 68
4.3 Zennare Basin 68
4.3.1 Land subsidence due to peat oxidation 71
4.3.2 List of SAR datasets 72
4.3.2.1 ERS 1/2 dataset 72
4.3.2.2 ENVISAT ASAR dataset 73
4.3.2.3 Sentinel-1 dataset 75
4.4 Summary 76
CHAPTER 5: LONG-TERM PEATLAND CONDITION ASSESSMENT USING INSAR TECHNIQUE 77
5.1 Introduction 77
5.2 SAR data processing over Flow Country (Scotland) 77
5.2.1 Site overview 77

5.2.2 Data 79
5.2.3 SAR data processing using ISBAS technique 81
5.2.3.1 ERS ISBAS processing 84
5.2.3.2 Sentinel-1 ISBAS processing 84
5.2.4 Data analysis 85
5.2.5 Results 87
5.2.5.1 Qualitative analysis 92
5.2.5.2 Quantitative analyses 94
5.2.6 Discussion 99
5.2.6.1 Qualitative discussion 99
5.2.6.2 Quantitative discussion 100
5.3 SAR data processing over Zennare Basin (Venice Lagoon, Italy) 102
5.3.1 Site overview 102
5.3.2 Data 102
5.3.3 SAR data processing using ISBAS technique 104
5.3.3.1 ERS ISBAS processing 105
5.3.3.2 ENVISAT ISBAS processing 105
5.3.3.3 Sentinel-1 ISBAS processing 107
5.3.4 Data analysis 107
5.3.5 Results 107
5.3.5.1 Qualitative analysis 108
5.3.6 Discussion 114
5.4 Summary of the limitation of using ISBAS technique over peatland 115
5.5 Summary 116
CHAPTER 6: QUENTIFYING PEATLAND CONDITION FROM INSAR TIME-SERIES 117

6.1 Introduction 117

6.2 Peatland surface motion 117

6.3 Application of univariate SSA to analyse peatland surface motion from ISBAS DInSAR time-series over the Flow Country, Scotland 118

6.3.1 Sampling strategies of InSAR 119

6.3.1.1 Location and site selection 119

6.3.1.2 Stacking of time-series 123

6.3.1.3 ISBAS DInSAR time-series gap filling 123

6.3.1.4 Trend identification using SSA 125

6.3.1.5 Normalising the time-series 127

6.3.2 Field data 128

6.3.2.1 Land cover classification 128

6.3.2.2 Water table depth 129

6.3.3 Results 130

6.3.3.1 ISBAS DInSAR linear trend and peat condition 130

6.3.3.2 ISBAS DInSAR time-series and peat condition 131

6.3.3.3 Interpretation of the results 141

6.4 Application of multivariate SSA (MSSA) to analyse seasonal variation from ISBAS DInSAR time-series 143

6.4.1 Methodology 143

6.4.1.1 ISBAS DInSAR time-series gap filling using MSSA 143

6.4.1.2 Seasonal trend identification using MSSA 144

6.4.2 Results 146

6.4.2.1 Comparison with univariate SSA 146

6.4.2.2 Comparison of MSSA trends with peat condition 150

6.4.2.3 Spatial variation of peat condition 154

6.4.3 Discussion 162
6.5 Limitations of using ISBAS time-series to quantify peat condition 166
6.6 Summary 167
CHAPTER 7: CONCLUSIONS AND RECOMMENDATIONS 168
7.1 Review the aims and objectives 168
7.2 Research gaps 168
7.3 Using ISBAS DInSAR technique for long-term peatland monitoring 169
7.4 Using ISBAS time-series to quantify peat condition 170
7.5 ISBAS accuracy 171
7.6 Limitations of the methodologies 171
7.7 Suggestions and recommendations for future work 173
REFERENCES 174
APPENDIX A A-1
APPENDIX B A-2
APPENDIX C A-3

LIST OF FIGURES

Figure 2.1: Imaging radar geometry.. 9

Figure 2.2: Geometrical distortion of SAR system.....11

Figure 2.3: Different cases of surface roughness and impact on the backscattered signal.. ...12

Figure 2.4: Processing scheme of Punnet software.. 18

Figure 2.5: Debursting and merging processes for Sentinel 1 IW product.....19

Figure 2.6: Geometry differences between 'master' and 'slave' image.. 20

Figure 2.7: Average amplitude maps of North East of Scotland (Flow Country).. 22

Figure 2.8: The average coherence map from the ENVISAT dataset with the statistical information of SBAS points for reference point selection.....26

Figure 2.9: The ambiguity of the phase. 27

Figure 2.10: The diagram of the non-linear processing chain. Figure.....31

Figure 3.1: Ecosystem interrelations and ecosystem services of mires and peatlands. 41

Figure 3.2: Peatland cover per country.. 42

Figure 3.3: Design of the of the anchor posts used to measure the rise and fall of bog. 47

Figure 3.4: The variation in peatland surface features.....50

Figure 4.1: The distribution of blanket peat in the Flow Country 57

Figure 4.2: Digital Elevation Model from SRTM at 30 m resolution over Flow Country. 58

Figure 4.3: The geological map of the Flow Country (Caithness and Sutherland). 59

Figure 4.4: Cross section of degraded blanket bog.....62

Figure 4.5: Interface of Sentinel-1 Scientific Hub.....67

Figure 4.6: Location of Zennare Basin in the South of Venice Lagoon.. 69

Figure 4.7: Digital Elevation Model from SRTM at 30 m resolution of the Zennare Basin ..70

Figure 4.8: Geomorphological map of Zennare Basin extracted from remote sensing data.. 72

Figure 5.1: The distribution of blanket peat of the United Kingdom and Ireland,. 78

Figure 5.2: A very high resolution RGB image of the UK Forestry Commission's Bad a' Cheo Forest Research Reserve. 81

Figure 5.3: Relative location of ISBAS reference point used and the nearby THUS GNSS station over Flow Country. 83

Figure 5.4: ISBAS interferograms networks over Flow Country. 86

Figure 5.5: ERS ISBAS vertical velocity map over Flow Country. 89

Figure 5.6: Sentinel-1 ISBAS (6 months temporal baseline) vertical velocity map over Flow Country. 90

Figure 5.7: Sentinel-1 ISBAS (2 years temporal baseline) vertical velocity map over Flow Country. 91

Figure 5.8: Sentinel-1 ISBAS vertical velocity maps along with their outputs having undergone unsupervised segmentation for four different locations over Flow Country. 93

Figure 5.9: Comparison the rate of the deformation between ERS ISBAS points and levelling transect block means over Bad a Cheo forest Reserve. 95

Figure 5.10 The 4 levelling transect mean heights. over Bad a Cheo forest Reserve.....97

Figure 5.11: ISBAS vertical velocities maps with levelling benchmarks overlaid 98

Figure 5.12: A land cover classification map of the Venice Lagoon, Italy 103

Figure 5.13: Footprints of the ERS, ENVISAT and Sentinel-1 SAR image frames 104

Figure 5.14: ISBAS interferograms networks over Venice Lagoon, Italy. 106

Figure 5.15: ERS ISBAS and SBAS LOS velocity maps over Venice Lagoon, Italy.....110

Figure 5.16: ENVISAT ISBAS and SBAS LOS velocity maps over Venice Lagoon, Italy. 111

Figure 5.17: Sentinel-1 ISBAS and SBAS LOS velocity maps over Venice Lagoon, Italy 112

Figure 5.18: ISBAS LOS velocity maps over farmed peatland area (Zennare Basin). 113

Figure 6.1: Locations of the selected sites for quantifying peat condition from InSAR time-series. 119

Figure 6.2: Shows the deformation pattern from Sentinel-1 ISBAS DInSAR technique for each selected site 122

Figure 6.3: The flow chart of the proposed methodology for the analysis of ISBAS DInSAR time-series using SSA. 124

Figure 6.4: Example of SSA spectrum of filled ISBAS time-series over Flow Country 125

Figure 6.5: Comparison between the non-linear trend (seasonal trend) extracted using (a) linear interpolation to fill the gaps and (b) using SSA method. 125

Figure 6.6: Monte Carlo singular spectrum of the ISBAS DInSAR time-series over site1..127

Figure 6.7: The first two leading Empirical Orthogonal Functions (EOFs) of ISBAS DInSAR time-series over site 1. 127

Figure 6.8: WTD time-series along with seasonal fluctuations extracted using SSA over site 12, 13, 14, and 15. 130

Figure 6.9: Comparison of the linear trend of 103 ISBAS points distributed in 22 sites with the peat condition for each point. 131

Figure 6.10: The non-linear trend derived from ISBAS DInSAR time-series using SSA. ..135

Figure 6.11: Peat condition over each 22 sites 135

Figure 6.12: Comparison of WT level and rainfall with ISBAS DInSAR time-series.....140

Figure 6.13: MSSA estimate of filled in ISBAS data over Flow Country. 144

Figure 6.14: Variance of data explained by certain modes of MSSA for thousands of channels using two different window sizes with reduce covariance matrix. 145

Figure 6.15: Comparison of the non-linear trend (seasonal trend) extracted from SSA and MSSA for each category over each site. 150

Figure 6.16: Comparison between the non-linear trend extracted using MSSA for 97 ISBAS points distributed over 20 sites with the peat condition for each point 151

Figure 6.17: Comparison between the non-linear trend extracted using MSSA for each ISBAS point over 20 sites with the peat condition. It shows only the correlated trend with the peat condition (**Figure 6.16**).. 153

Figure 6.18: Example of seasonal trend extracted for each ISBAS DInSAR time series using MSSA before and after removing the linear trend. 154

Figure 6.19: Average non-linear trend for correlated ISBAS points under each condition to aid interpretation of seasonal changes (peak subsidence and peak uplift) in regional scale. 155

Figure 6.20: Regional seasonal trend maps over peatland Scotland..... 157

Figure 6.21: Local scale ISBAS DInSAR trend maps obtained from the reconstruction of PCs 1, 2, 3 and 4 using W=27 which is approximately 11 months for each ISBAS point over peatland Scotland for the period (12/03/2015 to 7/12/2016). 160

Figure 6.22: ISBAS DInSAR LOS velocity map along with the trend maps over site 1 and the surrounding area..... 162

LIST OF TABLES

Table 2.1: Different frequencies used by satellite radar sensors. 8

Table 2.2: Properties of three radar sensors used in this research 18

Table 4.1: List of the proposal submitted to ESA for ERS 1/2 data acquisition over Flow Country. 64

Table 4.2: Sentinel satellites with a brief description of their mission objectives. 65

Table 4.3: The basic specification of Sentinel -1 interferometric wide (IW)single look complex product (SLC) 66

Table 4.4: List of Sentinel-1 images used in this study. 67

Table 4.5: List of submitted proposal to ESA to request ERS1/2 images in Venice Lagoon (Italy)..... 73

Table 4.6: List of the proposal submitted to ESA for ENVISAT ASAR data acquisition over Vennice Lagoon (Italy). 75

Table 4.7: List of Sentinel-1 images used in the processing over Venice Lagoon (Italy). 76

LIST OF ABBREVIATIONS

ALOS	Advanced Land Observation Satellite
AOI	Area Of Interest
AR	Autoregressive process
ASAR	Advanced Syenthetic Aperture Radar
CORINE	Co-ordinated Information on the Environment
DEM	Digital Elevation Model
DGPS	Differential Global Positioning system
DOC	Dissolved Organic Carbon
EC	European Commission
ENVISAT	Environmental Satellite
EO	Earth Observation
EOFs	Empirical Orthogonal Functions
ERS	European Remote-sensing Satellite
ESA	European Space Agency
FM	Frequency Modulator
GHGs	Greenhouse Gases
GNSS	Global Navigation Satellite System
GPS	Global Positioning System
InSAR	Interferometric Synthetic Aperture Radar
IPTA	Interferometric Point Target
ISBAS	Intermittent Small Baseline Subset
ITRF	International Terrestrial Reference Frame
IW	Interferometric Wide
LOS	Line of Sight
MC-SSA	Monte Carlo SSA
MSI	Multi Spectral Instrument
MSSA	Multi-channel Singular Spectrum Analysis
MTG-S	Meteosat Third Generation-Sounder
PAR	Photosynthetic Active Radiation

PCA	Principle Component Analysis
PCS	Principle Components
PSI	Persistent Scatterers Interferometry
PSP	Persistence Scatterer pairs
RCS	Reconstructed Components
SAR	Synthetic Aperture Radar
SBAS	Small Baseline Subset
SE	Standard Error
SLAR	Side Looking Airborne Radar
SLC	Ingle look Complex
SNAPHU	Statistical-cost Network-flow Algorithm for Phase Unwrapping
SNR	Signal-to-noise Ratio
SRTM	Shuttle Radar Topography Mission
SSA	Singular Spectrum Analysis
STaMPS	Standford Method for Persistant Scatterers
SVD	Singular Value Decomposition
THUS	Thurso Global Navigation Satellite System (GNSS) station
TOPS	Terrain Observation with Progressive Scans
UTM	Universal Transverse Mercator
VHR	Very high Resolution
WGS	World Geodetic System
WT	Water Table
WTD	Water Table Depth

CHAPTER 1

INTRODUCTION

1.1 Preface

Peatlands are fragile ecosystems, characterised by permanent water logging (Zanello et al., 2011), with their condition an important determinant of their ecosystem services (Hooijer et al., 2012). Globally, peatlands store approximately one third of global soil carbon, while covering only approximately 3% of the land and freshwater surface (Holden, 2005). They contribute to the global atmospheric balance of greenhouse gases (GHGs) (Yu et al., 2010): intact peatlands are typically net sinks for carbon (Freeman et al., 1993; Nykanen et al., 1995; Smith et al., 2004; Kirschke et al., 2013), whereas degraded or disturbed peatlands are known to be carbon sources (Crichton et al., 2015). They also provide maintenance of biodiversity and protection of water resources (Lindsay et al., 1988; Drew et al., 2013).

Historically, peatland areas were deemed to be of low economic value (Shotbolt et al., 1998; Zanello et al., 2011) and thus large areas were drained and used for agriculture and other activity (Holden et al., 2007), including plantation forestry (Cannell et al., 1993; Anderson et al., 2000). Over time it has become apparent that such practices cause largely irreversible subsidence of the land as a consequence of the consolidation, compression, biological oxidation and shrinkage of the peat in the upper aerated zone. This process can result in the emission of carbon dioxide (CO_2) into the atmosphere (Gambolati et al., 2005; Zanello et al., 2011; Hooijer et al., 2012), as well as loss of habitats that are of high value for nature conservation (Ramchunder et al., 2009).

Across the globe, humans are interacting with peatlands in some different ways, determined by peatland type, local governance, and climate. For example, in the UK much of the peatland is blanket mire (covering 2.1 million ha, 17% of the landscape (Baird et al., 2009)), a type of bog (rainwater-fed peatland) which can occur on flat or sloping terrain if there is sufficient rainfall and impeded subsurface drainage. These peatlands are considered to be of national and international importance (Lindsay et al., 1988; Bain et al., 2011). This has not always been the case, however, since 1945 large areas of blanket bog over 50cm in depth were afforested (Cannell et al., 1993; Anderson et al., 2000) by planting areas that were considered to be unsuitable for the environment (Shotbolt et al., 1998). This has been particularly the case in the Flow Country of Caithness and Sutherland (Scotland) which has the largest extent of

blanket bogs in Europe (.Lindsay, 1987; Shotbolt et al., 1998). Although there has been a recent activity to restore the peatlands (Parry et al., 2014), there now exists a spatially and temporally dynamic system of subsidence (and accumulation) which requires monitoring. This surface motion of the peat is a responsive indicator of the changing condition of peatland. Sustained subsidence on account of compaction, loss of water, carbon or gas is generally indicative of poor condition and slow growth, while sustained stability or even growth is an indicator of good condition. A reliable monitoring system of surface motion would thus inform future management and conservation decisions pertaining to this valuable landscape. Monitoring land-subsidence in drained cultivated peatland is also important because the systematic drainage is responsible for a number of serious environmental hazards and economic issues through local to global scale (Zanello et al., 2011). For example, a coastland area (Zennare Basin) in the south of Venice Lagoon, is characterised by the presence of soil with high organic matter content (peat). This area was progressively reclaimed from the middle of 19th century to the late 1930s and at present, lies entirely below mean sea level (Teatini et al., 2007; Zanello et al., 2011). The systematic drainage of the outcropping peat soil along with ploughing and harvesting for agriculture purposes resulted in land subsidence of about 0.02 m/year (Gambolati et al., 2006) which represents a major environmental hazard because it enhances the risk of flooding and thus increases the cost of land drainage and or maintenance of the system to keep the agriculture area dry.

Given the vast extent of these peatlands and their dynamic nature, any monitoring system should be continuous over space and time (Lees et al., 2018). Various methods of surveying peatland surface motion, such as site surveys (PVC tubes, Levelling and Differential Global Positioning system (DGPS), terrestrial LiDAR) and remote sensing via airborne platforms, are limited (Crichton et al., 2015). Indeed, systematic field measurement of surface motion over large areas is difficult and prohibitively expensive, so few field studies have gathered surface motion data. Furthermore, the effective field-based monitoring of surface motion over global peatlands is impossible on account of their extent and inaccessibility. Satellite remote sensing, specifically Synthetic Aperture Radar (SAR), on the other hand, improves spatial and temporal coverage, and the data is relatively inexpensive (often free) (Tofani et al., 2014; Novellino et al., 2017) and overcomes the frequent cloud cover of these peatland areas (e.g., Rosen et al., 2000). Advanced Differential Interferometry Synthetic Aperture Radar (DInSAR) techniques can monitor the motion of the Earth's surface along the sensor Line-of-Sight (LOS) and measure its change (Massonnet and Feigl, 1998), based on the

signal phase difference observed in an interferogram formed between two co-registered SAR scenes acquired at different times over the same area of interest (AOI) (Rosen et al., 2000). There is now theoretically (subject to data availability) a temporal dataset for the past 25-years of C-band SAR data from the ERS1/2 and ENIVISAT missions and most recently the Sentinel-1 A and B satellites (which assures data for the foreseeable future). This affords a dataset with which surface motion of the peatlands can be explored. Indeed, as Kim et al. (2017) note, advancements in the capabilities and data products provided by SAR sensors should be used to understand and thus preserve our peatlands.

Previously, DInSAR has shown a clear capability to map and analyse the dynamics of surface motion associated with tectonic processes (Colesanti et al., 2003; Burgmann et al., 2006), land subsidence (Canuti et al., 2005; Stramondo et al., 2008; Osmanoglu et al., 2011), slow landslides (Hilley et al., 2004; Cigna et al., 2010; Cigna et al., 2011; Novellino et al., 2017) and volcanic activity (Salvi et al., 2004; Tizzani et al., 2007). Other studies have used DInSAR techniques to construct subsidence maps over peatland areas (Teatini et al., 2007; Zhou et al., 2009). However, these have been limited to urban and bare/rocky land cover types due to the fact that the most common DInSAR techniques require pixels to display high coherence consistently over a long period. Consequently, this almost completely precludes the detection and interpretation of subsidence (and indeed surface uplift) over rural and vegetated areas, as vegetation cover, almost by definition, exhibits highly variable coherence due to changes over seasonal cycles and the often diffuse scattering of the radar signal. Furthermore, this issue is particularly challenging when using C-band SAR data.

The novel Intermittent Small Baseline Subset (ISBAS) method (Sowter et al., 2013), which is related to the SBAS technique described by (Berardino et al., 2002), permits pixels of variable coherence to be considered alongside those with consistently high coherence (Cigna et al., 2014; Bateson et al., 2015; Sowter et al., 2016). Over a range of land covers it has been demonstrated that the ISBAS method provides up to 26 times more coverage than SBAS (Cigna and Sowter, 2017). Thus, it is well worth exploring the potential to use the ISBAS method with SAR data for surface motion measurement over peatland areas within different environments. In addition, the ISBAS technique could be used to generate the time-series of surface motion that may capture the annual and seasonal motion of the peat surface. The characteristics of time-series of surface motion are potentially diagnostic of peatland condition (Howie and Hebda, 2018). This is the focus of this thesis.

To optimally investigate the use of the ISBAS technique for peatland surface motion measurement, the outputs need to be validated. However, thus so far very few studies have provided the detailed information on peatland surface motion that would be required. Further, these have been confined to small geographic areas because of the logistical and financial challenges imposed by large-scale field surveys (Kennedy and Price, 2005; Fritz et al., 2008; Reeve et al., 2013). Moreover, there may be mismatches in time between the ground data on peatland surface motion and the satellite-derived data. This presents a major barrier in applying the InSAR technique and it is something that this thesis has to address.

1.2 Aims and Objectives

The overarching goal of this thesis is the quantification at complete spatial extents of the surface motion of peatlands in different environments through the application of the ISBAS technique to SAR data. Regarding this, three research aims are as follows:

- Conduct background research regarding the application of InSAR over peatland areas.
- Analyse what value the ISBAS technique, in particular, might bring in peatland monitoring.
- Consider how the ISBAS technique might be used to infer the peat condition.

These research aims can be further broken down into a set of study objectives:

- Identify gaps in the use of InSAR for peatland deformation monitoring.
- Investigate the potential of using the ISBAS DInSAR technique for long-term peatland monitoring.
- Investigate the potential of using the ISBAS DInSAR time-series to quantify peat condition.
- Determine how other sources of data might be used to validate the ISBAS results.

1.3 Research Methodology

Having clearly stated what the objectives of the research are, the research methodology of how these objectives can be achieved is as follows:

- Conduct a literature review relevant to the topics of this research by referencing the definitive sources.
- Select suitable test sites for this research in conjunction with the collection of a large enough set of SAR images from different satellites to investigate the application of the ISBAS technique over peatland areas.

- Use the application of SSA and MSSA to analyse the time-series of surface motion from the ISBAS DInSAR technique.
- Analyse and assess the long-term deformation maps and time-series of surface motion from the ISBAS DInSAR technique to quantify peat condition.

1.4 Thesis Overview

This thesis is organised into seven chapters. Following this chapter, the structure is as follows:

- **Chapter Two:** presents the fundamental principles and techniques relevant to the topics of this research. This includes SAR, InSAR, ISBAS, SSA, and MSSA.
- **Chapter Three:** presents the literature review involving the importance of peatland in ecosystem services, highlighting the causes and consequences of peatland degradation and the main difficulties in monitoring these areas. Also, the techniques used for monitoring peatland surface motion and the use of InSAR for surface motion monitoring are reviewed. The chapter is ended by identifying the research gaps in this field.
- **Chapter Four:** discusses the selection of the Flow Country in Scotland and Zennare basin in the south of Venice Lagoon, Italy as the test sites for this research. This includes general descriptions of the geology, hydrology and the availability of SAR data and ground data measurements in these areas.
- **Chapter Five:** presents the methodology used to process SAR data using the Linear part of the Punnet software over the sites selected in **Chapter 4**. Results are then presented, and an analysis of their respective quality is discussed which leads into the next chapter. The SAR datasets are also compared with ground data measurements wherever possible.
- **Chapter Six:** uses the non-linear part (time-series) of the Sentinel-1 results processed in the previous chapter to quantify peat condition over the Flow Country. It presents the methodology used to analyse InSAR time-series using both SSA and MSSA. The results are also presented and compared with ground data measurements. The interpretation of the results and the discussion are then presented and supported by previous studies.
- **Chapter Seven:** presents the conclusions on the various aspects of the research by restating the aims and objectives and summarising how each was achieved, which leads to a list of suggestions and recommendations for future work.

1.5 Summary

This chapter of the thesis has provided a background to the impotence of peatland in ecosystem services and the current techniques used in monitoring and evaluating the deformation in these areas, pointing out to their limitations that might be overcome through using the ISBAS DInSAR technique. Following the research methodology, the aims and objectives were then presented. Finally, the thesis overview provided a brief description for each chapter in turn.

CHAPTER 2

PRINCIPLES OF SAR, InSAR, SSA AND MSSA

2.1 Overview

This chapter starts with a brief introduction to the interferometric SAR (InSAR) as an important tool for detecting and monitoring the deformation on the earth surface.It explains the sources of errors in InSAR measurements for better interpretation of the results; and gives an introduction to the Punnet software that has been used to obtain the fully formed ISBAS results from Single Look Complex (SLC) format data. Following that, it provides a brief introduction to the Singular Spectral Analysis method (SSA) used to analyse the peat surface dynamics from InSAR time series.

2.2 Radar background

2.2.1 Synthetic Aperture Radar (SAR) basics and geometry

Synthetic Aperture Radar (SAR) is an active microwave imaging system that has capabilities to operate day and night and penetrate clouds, making it a unique tool for monitoring earth's surface. Many radar sensors are operating at different frequencies with a wavelength of a few centimetres (**Table 2.1**), 100,000 times longer than the wavelengths of the visible spectrum. This longer wavelength increases the capability of the active sensor to penetrate dielectric materials. As an active system, all SAR images are created through illuminating the area of interest with electromagnetic pulses, independent of sun illumination, and the radar antenna records the backscattered echoes from natural and human-made objects (Ferretti, 2014).

Radar sensors are coherent sensors (Skolnik., 2002) that can record both amplitude and phase for each target on the ground. The main advantage of a coherent sensor is its ability to preserve the phase information of the received signal for later processing, in contrast to the optical sensors which are non-coherent and hence non-phase preserving sensors. Therefore, SAR images provide an exceptional opportunity to exploit the data in ways that are not available with the optical imagery.

Table 2.1: Different frequencies used by satellite radar sensors.

Band	Frequencies	Wavelengths	Sensors
L	1 – 2 GHz	30 – 15 cm	SEASAT, JERS-1, ALOS-PALSAR
S	2 – 4 GHz	15 – 7.5 cm	HJ-1, NovaSAR-S
C	4 – 8 GHz	7.5 – 3.75 cm	ERS-1, ERS-2, RADARSAT-1, ENVISAT, Sentinel-1
X	8 – 12 GHz	3.75 – 2.5 cm	COSMO-SkyMed, TerraSAR-X, Tandem-X

The basic geometry of a SAR system is illustrated in **Figure 2.1**. The side looking configuration of SAR is necessary to eliminate the ambiguity of superimposed return echoes from either side of the satellite track, based on the concept that the echoes from the far range will take a longer time to return than those in the near range (Woodhouse, 2006).

The satellite flight path is known as the velocity vector. The microwave beam on the satellite illuminates an area on the ground known as a footprint or swath; the width of the swath relies on the elevation beamwidth, which is proportional to the wavelength and length of the antenna. The part of the swath nearest to the satellite's nadir is called the near range, while the part furthest from the satellite's nadir is the far range. The incidence angle (θ) of the satellite represents the angle between the transmitted microwave beam and the nadir of the satellite and this angle increases when the microwave beam moves from the near range to the far range. The range from SAR satellite to a specific target is called the slant range (ρ) which is a function of incidence angle and other factors such as topography. The antenna of the satellite is pointed perpendicular to the velocity vector, which is also called the look direction.

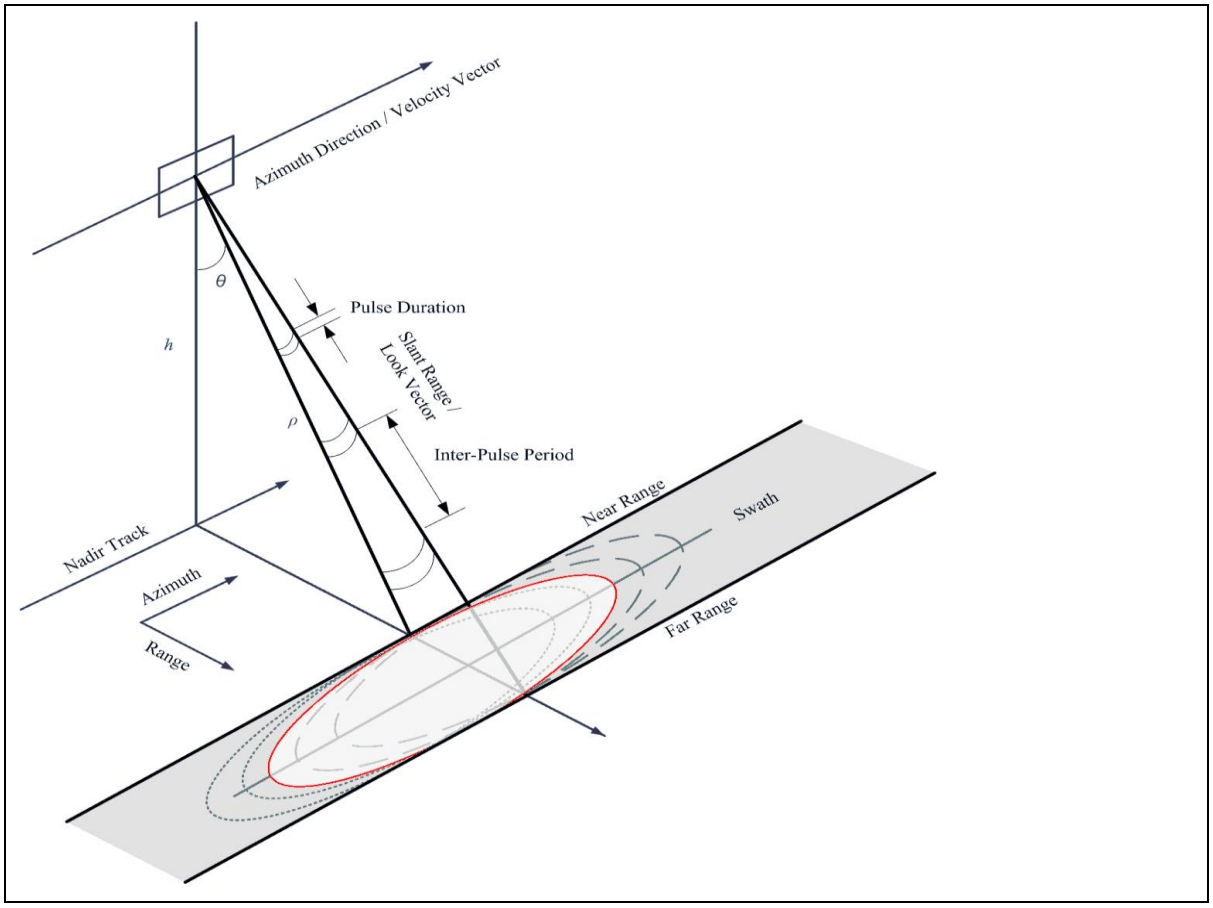


Figure 2.1: Imaging radar geometry. Pulses are emitted at high frequency as the platform moves along the velocity vector (Skolnik, 1990). The footprint of each pulse is indicated by successive ellipse in the swath. The entire image is limited in range by the near and far range limits, and in azimuth by the early and late azimuth times.

2.2.1.1 Spatial resolution of SAR systems

Spatial resolution in both range and azimuth direction represents the shortest distance between two targets which can be distinguished as separate objects in the image (Curlander and McDonough, 1991).

For range resolution, the two targets must be separated by a distance in slant range greater than half the length of the pulse. Before transmission, the electromagnetic pulse is Frequency Modulated (FM), which is called chirping. The electromagnetic pulse is then transmitted and reflected from the targets on the earth's surface; the reflected energy depends on the geometric and dielectric properties of the imaged surface, such as roughness, plant geometry and soil moisture (Ribbes et al., 1997). The SAR sensor then receives the echoes from the electromagnetic pulse at different times, which are directly proportional to their ranges (Skolnik, 1990). Chirping means that the received signal is filtered using a matched filter; in

this case, the different frequency components of the signal are delayed separately so that they all arrive at the same time. This is analogous to transmitting a short, high-powered pulse with less energy. This is important because the shorter the pulse, the closer two targets can be and still be resolved before their echoes begin to overlap (Woodhouse, 2006).

The azimuth resolution, on the other hand, describes the spatial resolution in the azimuth direction. For two targets at the same range value to be distinguished in the azimuth direction, they need to be separated by a distance greater than the azimuth beamwidth on the ground. The resolution in the azimuth direction is dependent on the synthetic aperture of the radar system. Due to the motion of the platform, the Doppler Effect causes a shift in the frequency of the received signal. From the first moment of the beam striking the target, multiple backscattered echoes from electromagnetic pulses are recorded until the time that the beam leaves the target. In real aperture radar, the footprint of the beam on the ground is a few kilometers in the azimuth direction. The synthetic aperture, on the other hand, involves resolving the multiple returns from a single target into a single response which helps to reduce the resolution in the azimuth direction to meters (Hanssen, 2001). This process of synthesizing the returns is known as azimuth compression and is analogous to the matched filter (also called range compression) that is utilized to enhance the range resolution. For more details, refer to (Ulaby et al., 1982).

2.2.1.2 Geometrical distortion of SAR system

One result of the side looking nature of the SAR system (SLAR) is the geometrical distortion that exhibits itself in three distinct ways; these are foreshortening, layover, and shadow, which are all related to topographic relief features and linked directly to the operational parameters of the SAR system, such as incidence angle and the antenna design (Woodhouse, 2006).

Foreshortening phenomenon occurs when the sides of the features such as hills face the look direction which is illustrated in **Figure 2.2 a**. The return pulses from both the base of the slope of point (A) and the summit of point (B) will arrive back to the sensor at the same times because of the near equivalent slant range, regardless of the actual ground range distance between them.

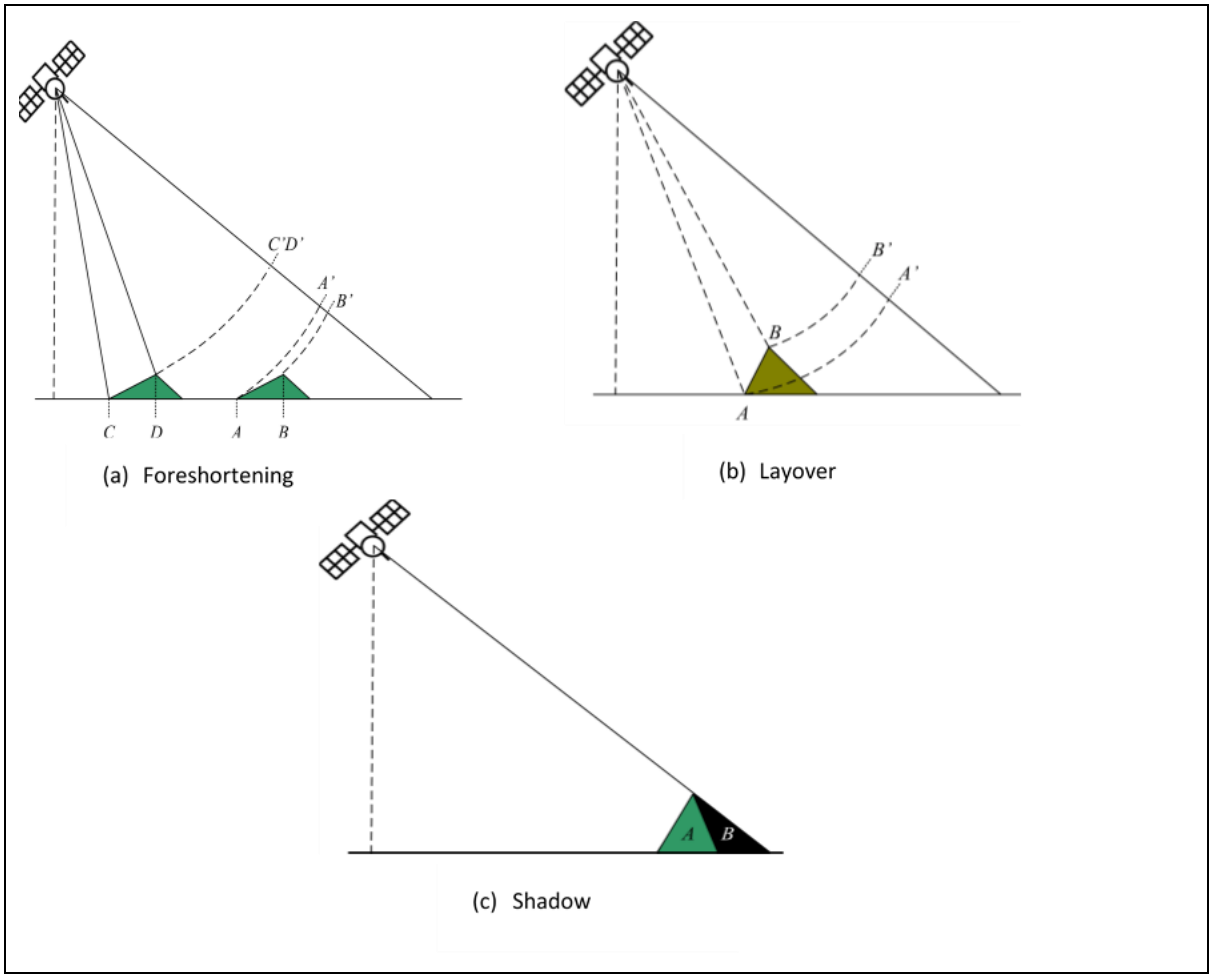


Figure 2.2: (a) two different cases of foreshortening phenomenon. In case 1, Points A and B appear much closer in SAR image than in reality, where the SAR sensor will receive echoes from the points at similar times due to the similarity of the path lengths. In case 2, points C and D cannot be distinguished in SAR image because they have the same path lengths which make their echoes arrive at the same time. (b) SAR antenna will receive the echo from point B before point A even though point B is further in ground range than point A. (c) terrain deep slope blocks radar signal on side B.

Layover represents an extreme version of foreshortening which is illustrated in **Figure 2.2.b**. This phenomenon occurs when the slant range of the point (B) is smaller than the slant range of point (A). Accordingly, the SAR antenna will receive the return signal from point (B) before the return from point (A), and this will cause a wrong record in the range bin.

The last phenomenon which is called shadow is shown in **Figure 2.2.c.** This occurs when the radar signal is unable to illuminate one side of the feature, and so occurs on very steep back slope, resulting in a dark area in the radar image.

2.2.1.3 Backscatter mechanisms

There are several factors that influence the signal being backscattered, such as the radar system parameters (polarization, the wavelength of the transmitted pulse, incidence angle), soil moisture and surface roughness (Ulaby et al., 1986). The latter represents the main factor affecting the amount of the backscattered signal that is returned to the radar antenna. **Figure 2.3** illustrates the effect of surface roughness on the response of the radar signal.

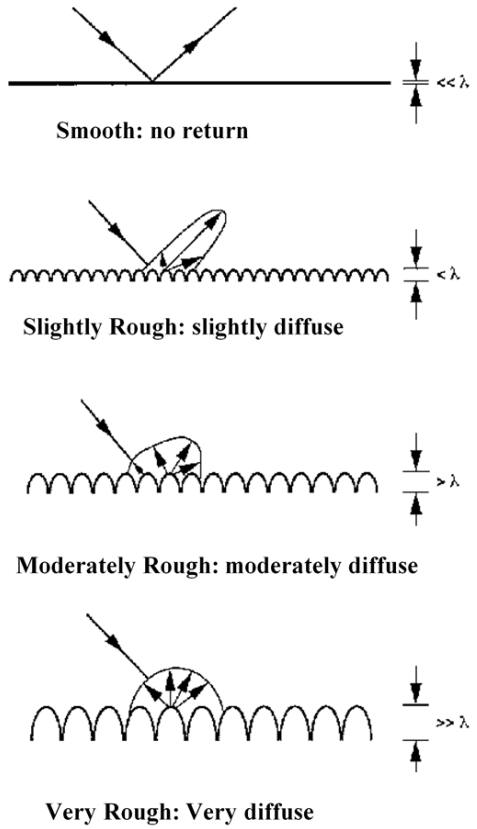


Figure 2.3: Different cases of surface roughness and impact on the backscattered signal. Adapted from Farr (1993).

The roughness of the surface determines the reflection of the emitted radar signal which can be either specular or diffuse. Specular reflection occurs when the emitted radar signal reflects from smooth, mirror-like surfaces such as glass, water and metallic surfaces (Lillesand et al., 2004), where the angle that the reflected signal creates with the normal is equal to the angle that the incidence signal creates with the same normal. In this case, very little backscattered signal returns to the antenna, resulting in low amplitude radar signal and black

appearance on the radar image. Increasing surface roughness will increase the returned signal to the antenna due to diffuse scattering.

Generally, the pixels that have a high amplitude on the radar image (bright appearance) correspond to strong backscattered signal, mostly from urban areas (such as buildings, bridges) and rocky terrains which act as natural reflectors (most of the emitted signal returned to the antenna). The corner reflectors-like structures provide a stronger returned signal as the double-bounced echoes arrive at the antenna with less degradation in the emitted signal, thus resulting in bright pixels in the image. The low amplitude pixels (dark appearance), on the other hand, correspond to low backscatterd signal, mostly from rural and vegetated areas, where most of the transmitted radar signal is reflected away from the antenna.

2.2.2 Interferometric SAR

Radar images used in interferometry are single look complex images (SLC) with complex arrays of pixels. Each pixel contains both amplitude and phase for each ground target. The amplitude of the radar sensor is related to the brightness of the radar backscattered signal, where the pixel with a strong backscatter signal is brighter than the pixel with the low backscattered signal. The phase represents the sensor-to-target distance as well as the interaction mechanism of the electromagnetic signal with radar targets. The sensor-to-target distance can always be expressed as an integer number of cycles (wavelengths) plus a segment that is equal to a fraction of a cycle (wavelength). The phase related to a sample of the radar signal presents just this fraction of the cycle, which is typically known as modulo-2π with a value ranging from 0-2π. Since the radar pulse has a two-way travel path, the effective range sensitivity of the system is equal to the half wavelength (effective wavelength) (Ferretti, 2014). Therefore, it is essential to select an appropriate SAR system for specific application in relation to its wavelength because the selected system will be less effective in measuring the phase changes exceeding the effective wavelength.

A phase value of a single SAR image can be modelled as the sum of different components:

- Phase contribution due to the range;
- Phase contribution due to scattering; and
- Phase contribution due to noise.

The scattering component of the SAR image is a deterministic quantity, so it is unpredictable. However, if two SAR acquisitions occurred under identical circumstances, then their scattering components would be identical. In reality, the scattering components in SAR images are often similar; under these conditions, the image can be considered as coherent (Hanssen, 2001). The correlation level between two SAR acquisitions depends on the temporal decorrelation, geometrical decorrelation (baseline geometry) and the determination of the Doppler-centroid frequency. Also, the noise component is modeled as a Gaussian signal, and most of it can be filtered effectively. Therefore, the phase difference between two SAR acquisitions is mainly reliant on the difference in range (Zebker et al., 1994) without taking into account the variations of atmospheric conditions and their impact on the phase.

Due to the differencing of the scattering component, the phase map of an individual SAR image is not useful. However, valuable information could be extracted from successful formation of an interferogram; the phase difference between two SAR images acquired at different times (also known as repeat-pass InSAR). More precisely, the interferogram is computed from multiplying the complex values of the first image (known as a master image) by the complex conjugate of the second image of the time-series (known as a slave image) (Ferretti, 2014). The phase difference Φ between two SAR acquisitions can be considered of as the sum of a number of contributions:

$$\Phi = \phi_{Deformation} + \phi_{Topography} + \phi_{Atmosphere} + \phi_{Orbit} + \phi_{Noise} \quad \textbf{Eq. 2.1}$$

Where:

$\phi_{Deformation}$ is the phase contribution related to the motion that occurred between two SAR acquisitions dates;

$\phi_{Topography}$ is the phase contribution related to the topographic features such as hills and valleys;

$\phi_{Atmosphere}$ is Phase contribution related to the different of atmospheric effect between the two SAR acquisitions;

ϕ_{Orbit} is the phase contribution related to the orbital error of the satellite; and

ϕ_{Noise} is the phase contribution related to noise.

It is evident from the equation above (**Eq. 2.1**) that valuable information can be extracted from the phase difference of two SAR images. Separating the individual components from the others represents the primary task of InSAR processing (Hanssen, 2001), and this method has been extremely evolved since its first initiation. This research is focused on

extracting the deformation component after eliminating all other contributions, using Punnet software.

2.2.3 InSAR errors and limitations

Although repeat-pass InSAR has been widely used to estimate the deformation of the earth's surface, the quality of estimation of the deformation can be reduced by several factors. These factors can be categorized into three groups depending on the source of errors in InSAR; for completeness, these are briefly described in this section. For more in-depth review, interested readers can refer to, for example, Rodriguez and Martin (1992), Hanssen (2001), or Ferretti (2014).

2.2.3.1 Ground-related errors

As discussed in the previous section, the scattering components within the resolution cell are identical between two SAR acquisitions. Following this assumption, the reflectivity phase related to the deformation that occurred between two SAR acquisitions is expected to cancel out during the formation of the interferogram. However, this is not the case in real interferograms, particularly in rural and vegetated areas where the scatterers are subject to many changes over time such as, seasonal changes of the tree canopy, seasonal growth of ground-level vegetation cover, etc, which cause decorrelation of the radar signal. The amount of decorrelation varies between the objects, but usually, the maximum decorrelation occurs over natural features such as trees and grasses, and it is a minimum over human-made features such as buildings and roads. Since the decorrelation of the radar signal is related to the temporal separation between two SAR acquisitions, some InSAR techniques such as Small Baseline Subset (SBAS) (Berardino et al., 2002) and Intermittent Small Baseline Subset (ISBAS) (Sowter et al., 2013) take advantage of using maximum temporal threshold during the formation of interferograms to decrease the temporal decorrelation effect.

Furthermore, the change of the satellite position in each acquisition will affect the phase difference due to the topographical features of the area, which will enhance the decorrelation of interferograms. This can be eliminated by subtracting the simulated phase created using a DEM and satellite orbit geometry from the original interferograms, which produces differential interferograms. This process represents an essential step to correct the interferogram for topography or baseline-related components. However, any inaccuracies in the DEM will be propagated to the results. Therefore, to minimize the errors due to topography, SBAS and ISBAS techniques form interferograms only for the pairs with small orbital baselines.

Due to the side looking nature of the radar system, the returned signals from mountains or urban areas with tall buildings are subjected to geometrical distortion as explained in **Section 2.2.1.2.** In InSAR, the areas having geometrical distortion can be identified using a DEM and satellite orbital geometry and then can be masked out in the final deformation map.

2.2.3.2 Satellite-related errors

Another source of error described in **Eq. 2.1** is due to different positions of the satellite in the time of SAR acquisitions, which is termed as a geometrical baseline. In the presence of the geometrical baseline, linear phase components are shown in the interferogram, particularly in the range direction. These effects are proportional to the normal baseline and appear even on flat terrain with no surface deformation. The large baseline also creates a geometrical decorrelation; therefore, it should be avoided to get a reliable estimation of the deformation.

2.2.3.3 Atmospheric-related errors

According to different studies (Zebker et al., 1997; Hanssen, 1998; Massonnet and Feigl, 1998), InSAR images exhibit irregular artefacts due to the spatial and temporal atmospheric inhomogeneity across the scene. The contributions of the atmosphere to phase represent the dominant sources of errors in InSAR phases. These artefacts cause a signal delay as radar waves travel through areas of atmospheric water vapour (Onn and Zebker, 2006). The atmospheric phase signal is believed to vary gradually over space and is assumed to be uncorrelated among the time-series of SAR images (Lyons and Sandwell, 2003). Therefore, the atmospheric anomalies are expected to be correlated in space but randomly through the time-series (Kampes, 2006).

In general, the phases contributions due to atmospheric effects are mostly due to the water vapor in the tropospheric layer and can be categorized into two types (Hanssen, 2001). The first type of atmospheric error is due to turbulent mixing in the atmosphere, which is uncorrelated spatially. This effect results from the behavior of water vapour in the troposphere, and the resulting phase delay is independent of the frequency of the SAR system. The vertical changes in the stratification of the troposphere layer represent the second type of atmospheric error and are believed to be highly correlated with topography.

2.3 Punnet software

In this research, the InSAR processing has been carried out using the Punnet software. This in-house software has been developed using the Matlab program by Nottingham Geospatial

institute, University of Nottingham. Punnet software utilizes the Intermittent Small Baseline Subset (ISBAS) algorithm (Sowter et al., 2013; Bateson et al., 2015) which is suitable to monitor the deformation for low coherence, wide area coverage with a range of different land cover classes such as grassland, forest and agriculture cover (Cigna et al., 2014; Sowter et al., 2016; Cigna and Sowter, 2017). In general, the processing chain of the ISBAS algorithm is similar in structure to the Small Baseline Subset algorithm (Berardino et al., 2002) but it has a slightly different approach to identifying the pixels for the final velocity map, the main difference being to relax the threshold value by permitting the intermittent coherence pixels over all interferograms. Punnet software can use single look complex (SLC) data format from most of the radar sensors illustrated in **Table 2.1**.

Depending on the acquisition modes of SAR sensors, the standard processing of the Punnet software can be categorized into two subsets; first, the ISBAS processing chain for Sentinel-1 dataset and second, the processing chain for the standard SLC datasets. **Figure 2.4** illustrates the processing scheme of Punnet software and the differences between the two subsets, where Sentinel-1 data need additional processing such as the debursting and merging step, which is done prior to the image coregistration and resampling, then the use of a known de-ramping function for coregistration and resampling (Sowter et al., 2016).

2.3.1 ISBAS linear processing chain

2.3.1.1 Debursting and merging for Sentinel 1 IW SLC product

Sentinel-1 represents the first of a family of satellites developed by the European Space Agency (ESA) and the European Commission (EC) for the operational demands of the Copernicus programme, designed to provide information to improve the environmental legislation and policies and to monitor the impact of climate change on the earth surface (http://www.copernicus.eu/). The Sentinel-1 mission includes two satellites: Sentinel 1A which launched in April 2014; and Sentinel 1B which launched in early 2016. Both satellites are equipped with C-band instruments operating at 5.405GHz and are placed in a near-polar, sun synchronous orbit at an altitude of about 693km. The repeat cycle for a single satellite is 12 days. However, it was decreased to 6 days when the second satellite launched into orbit.

In this research, Sentinel 1 IW SLC product is used in addition to ERS and ENVISAT products, where the basic specifications of the satellite are shown in **Table 2.2**.

Table 2.2: Properties of three radar sensors used in this research

Dataset	Frequency	Incidence angle	Polarisations	Swath width
ERS1/2	C-Band (5.6 cm wavelength)	20.1°-25.9°	VV	100 km
ENVISAT	C-Band (5.6 cm wavelength)	15°-45°	VV+HH+HV+VH	100 km
Sentinel 1	C-Band (5.6 cm wavelength)	29°-46°	VV+HH+HV+VH	250 km

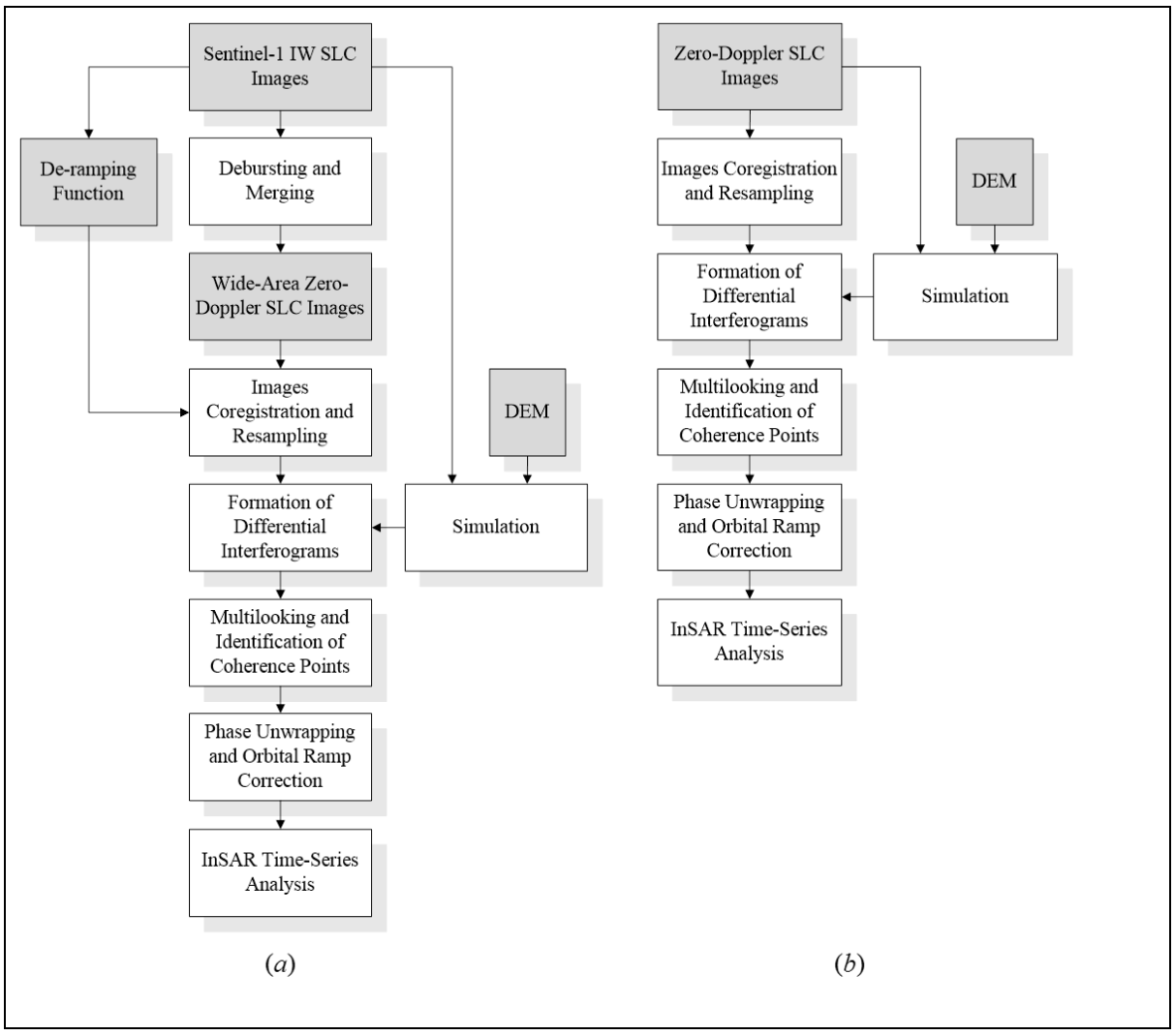


Figure 2.4: Processing scheme of Punnet software. (a) ISBAS processing chain for Sentinel 1 product. (b) ISBAS processing chain for the standard SLC products. Note that Sentinel 1 product needs additional processing, such as debursting and merging before the coregistration process and using the known de-ramping function for resampling process. Other processing steps are the same for all products. This Figure is adapted from Sowter et al. (2016).

Sentinel-1 level-1 IW SLC product is provided with three individual sub-swaths, each one contains a series of bursts and each burst is processed as a single SLC image and included into the sub-swath, in Azimuth time order, with black fill demarcation in between (**Figure 2.5**).

To generate a wide-area product from the three separated sub-swaths of IW SLC product, two processes should be applied in order (ESA, 2013):

- Debursting: This process concatenates the separate bursts from one sub-swath into a single deburst sub-swath where the spacing in the azimuth line is constant from the start to the end and the black-line demarcation between subsequent bursts is non-existent.
- Merging: After applying the debursting process to each of the three sub-swaths (IW1, IW2 and IW3), the mosaic process should be applied for the sub-swaths to generate a single wide-swath product where the range column spacing is constant from near to the far end, and the sub-swaths are aligned in azimuth.

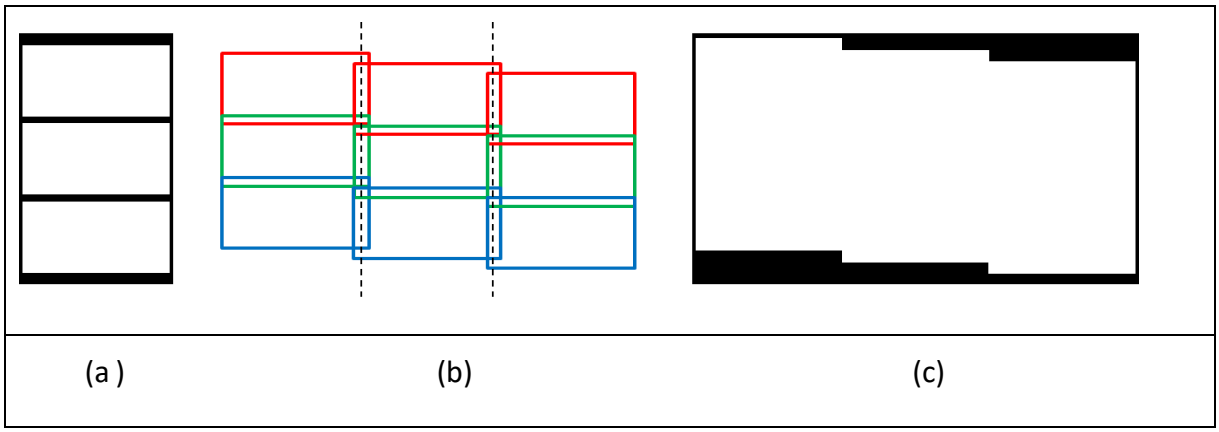


Figure 2.5: Debursting and merging processes for Sentinel 1 IW product. (a) represents the bursts arrangement in the sub-swath of IW product. (b) Shows the structure of the bursts and the overlaps between the bursts and sub-swaths. And (c) illustrates the mosaic process for the three sub-swaths with three bursts in each. Adapted from Sowter et al. (2016).

2.3.1.2 Coregistration and resampling for Sentinel 1 and standard SLC products

The coregistration process is the first step in the processing of InSAR data sets. As the two images in a single data set, 'master' and 'slave,' have been acquired from slightly different orbits, the scattering features of the images might be of a different area on the ground. Therefore, this process aims to transform all SAR images in the data set (slave images) to a common slant-range coordinate system (master image) so that all images have the same coordinate system which is the master coordinate system. **Figure 2.6** shows the differences in

the geometry between master and slave images that should be accounted for in the coregistration process between the two images.

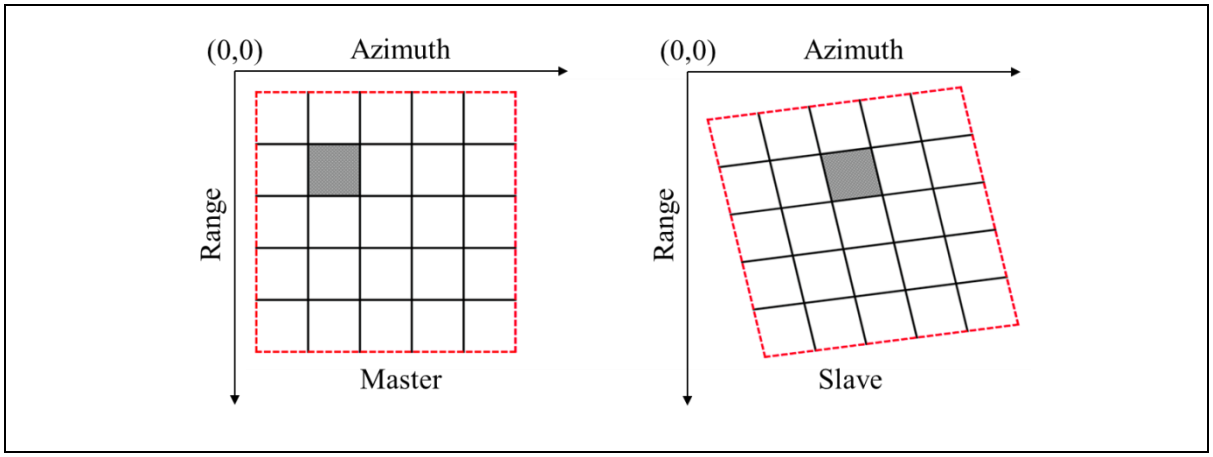


Figure 2.6: Geometry differences between 'master' and 'slave' image. Where these images have acquired from slightly different orbits and any small differences between them may be present. The most common differences are orbit skewing and a shift in both azimuth and range direction. Adapted from Ferretti et al. (2007).

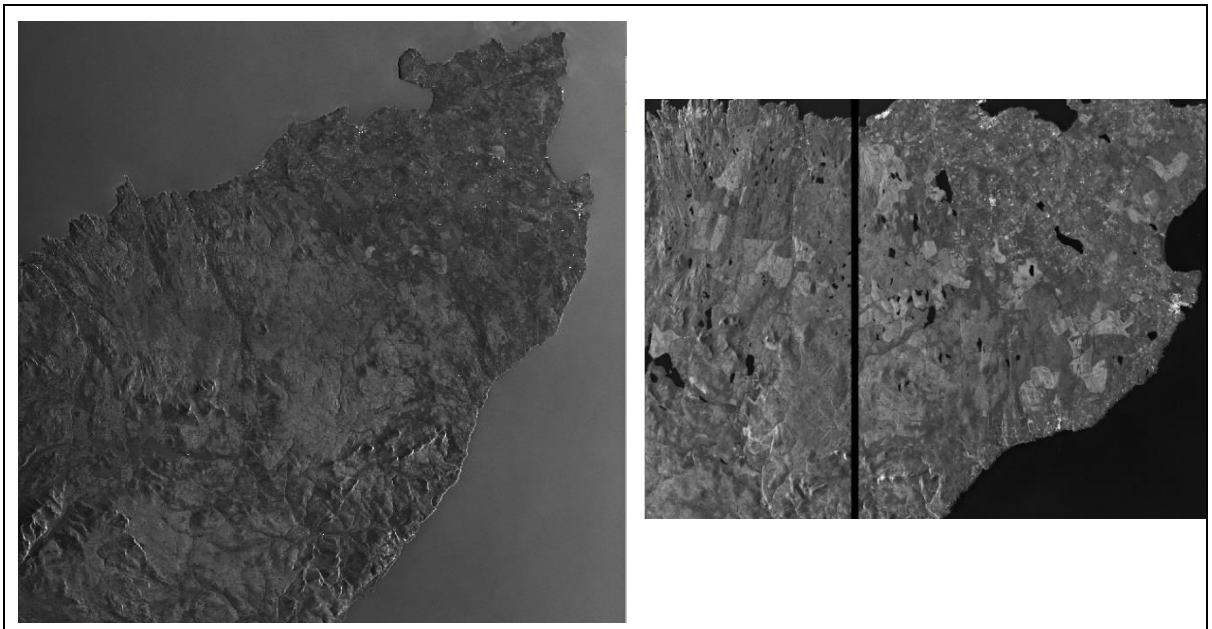
For interferometry, the coregistration and resampling process should be performed with an accuracy on the order of one tenth of a pixel or better (Just and Bamler, 1994). For Sentinel-1 IW SLC data, any imprecision of fewer than one thousands of a pixel in the coregistration process may cause obvious phase ramps on separated bursts (De Zan et al., 2014). This is difficult to obtain through typical convolution methods, however, with the spectral diversity technique (Scheiber and Moreira, 2000), higher levels of accuracy might be obtained as performed in some studies (such as Lanari et al., 2015; Wegnüller et al., 2016). Nevertheless, the spectral diversity technique is not implemented in ISBAS processing due to the more intensive computational requirements than imposed by the simple correlation methods that are used for stripmap products (Sowter et al., 2016). The coregistration and resampling method should be done based on a pixel by pixel approach and, in this research, the process can be summarized as follows:

- **Coarse coregistration:** This process coregisters both master and slave images based on their known acquisition geometry. This process starts with identifying a list of testing candidate points at a regular 50X50 grid in the master image, then any points without elevation information such as water bodies are rejected. In the corresponding slave image, the location of those points can be identified depending on the known

acquisition geometry such as DEM and precise orbits. Then polynomial coefficients are determined from the offset of those points between two images.

- **Fine coregistration:** With the fine co-registration, both images (master and slave) should aligne to sub-pixel accuracy. This can be implemented using either amplitude cross-correlation method, which used in this software, or fringe contrast method. For the amplitude cross-correlation method, the amplitude data are extracted for a small region surrounding the candidate points for both master and slave images. The initial locations of those points in the slave image is determined from coarse coregistration. Then sub-pixel image co-registration is applied using a cross-correlation technique (Guizar-Sicairos et al., 2008). It should be noted that this method can easily apply to wide baselines with less computational cost than the fringe contrast method; however, it has a coarser accuracy (Ferretti et al., 2007).
- **Resampling:** The final step is to resample the slave image data onto the master coordinate system using the calculated co-registration parameters. This process can be approximated by two one-dimensional steps, i.e., along the range and then along the azimuth. This process is usually done using bilinear or bicubic methods. The latter method is adopted by the Punnet software. For Sentinel-1 IW SLC products, a rapid change of the phase in azimuth direction may cause some difficulties in the resampling process due to the ambiguity of the phase difference between adjacent pixels. This effect is well-known, and it can be resolved by first subtracting a simulation of the rapidly-varying phase in the azimuth direction (deramping), which is a known function for Sentinel-1 data (Miranda, 2015), then resampling the remainder phase and finally applying a re-ramping process which is adding back the simulated phase.

After completion of the coregistration and resampling process for the InSAR data set, the average amplitude map is then created from all separated amplitude data in the stack. **Figure 2.7** illustrates an example of average amplitude maps over the Flow Country in Scotland using two different InSAR products (ERS and Sentinel-1). Brighter pixels correspond to urban areas with the high signal return, and darker pixels correspond to rural and vegetated areas with the low signal return due to the low coherence over these areas.



(a) (b)

Figure 2.7: Average amplitude maps of North East of Scotland (Flow Country). Bright pixels correspond to urban areas (high radar return), and dark pixel correspond rural and vegetated areas (low radar return) due to the low coherence. (a) the output map from ERS 1/2 data set. (b) the output from the Sentinel-1 dataset.

2.3.1.3 Generation of the differential interferogram

The complex value of a SAR image used in interferometry (z) can be represented by a real in-phase component and an imaginary quadrature, which are related to the amplitude (A) and (∅) information (Hanssen, 2001). Where both Z_m and Z_S represent the complex value for master and slave image such as follows:

$$Z_m = A_m \,.\, e^{j\,\emptyset_m}$$

$$Z_S = A_S \,.\, e^{j\,\emptyset_S} \qquad \textbf{Eq. 2.2}$$

An interferogram (I) is then formed between master and slave images by multiplying the complex value from the master with complex conjugate from the slave. This process results in multiplying the amplitude values and differencing the phases.

$$I = Z_m Z_S^* = A_m A_S e^{j(\emptyset_m - \emptyset_S)} \qquad \textbf{Eq. 2.3}$$

A differential interferogram is then generated by subtracting the simulated phase, which is synthesized from the precise orbit of the satellite and a digital elevation model (DEM), from the interferogram. This process is also known as interferogram flattening.

Both Persistent Scatterer Interferometry (PSI) and Small Baseline Subset (SBAS) have the same principles in the generation of differential interferograms; however, the selection of the image pairs between those two techniques is different. With the PSI technique, the pairs of differential interferograms are only formed depending on a single master image (Ferretti et al., 2001), to distribute the errors associated with the master equally over all interferograms, where the number of the generated interferograms is equal to the number of images-1. This feature of PSI could help to provide a high accuracy map for full scene processing; however, it needs a big stack of images to provide reliable results (Ferretti et al., 2007). On the other hand, the SBAS technique outlined by Berardino et al. (2002) is a multiple master technique, which generates interferograms from all possible combinations between SAR images that meet specific criteria (threshold values). In contrast to PSI, this technique models the errors by utilizing the phase information from many interferograms.

The ISBAS algorithm is modified based on the SBAS technique (multiple master technique), which forms maximum possible combinations of differential interferograms depending on two parameters: (1) orbital baseline (perpendicular baseline) and (2) temporal baseline between the image pairs. Increasing the threshold values for both perpendicular and temporal baselines will increase the number of the possible pair combinations (interferograms). However, this will affect the quality of the formed interferograms. Therefore, careful thought should be given to the selection of the threshold values. For orbital baseline threshold, decreasing the threshold value will minimize the phase error due to topography but will decrease the number of the produced interferograms. According to Hanssen (2001), the altitude of ambiguity $h_{2\pi}$ represents the phase sensitivity due to local topography, which identifies the change in height needed to increase the phase by 2π in the multi-pass interferogram.

$$h_{2\pi} = \frac{\lambda}{2}.\frac{r_{m\,0}\sin\theta}{B_n} \qquad \textbf{Eq. 2.4}$$

Eq. 2.4 explains the relationship between the altitude of ambiguity and the orbital baseline, B_n, i.e., increasing normal baseline B_n will decrease the altitude of ambiguity $h_{2\pi}$ where the phase will be more sensitive to the height change. Similarly, increasing the wavelength of the radar, λ, incidence angle θ and the distance between the satellite and the target r_{m0} will increase the altitude of ambiguity, which will decrease the sensitivity to the height change. In the case of ERS, the optimum orbital baseline with high signal to noise ratio is about 300-400 m suggested by Ferretti et al. (2007). In this study, the orbital baseline

threshold for processing ERS and ENVISAT data sets is set to be 250 m, and for Sentinel 1 data set is 200 m.

For the temporal baseline threshold, the selection of an appropriate threshold value depends on the rate of deformation and the scatterer's characteristics over the study area. A short temporal baseline threshold should be used if the area is facing rapid deformation to avoid the ambiguity in the phase and fast scatterers changed to eliminate the decorrelation between the InSAR images, which affects the quality of the generated differential interferograms. Although the rate of deformation over peatland areas is expected to be high, the maximum temporal baseline for both ERS and ENVISAT data sets is configured to be four years due to the gaps in the archived data and long revisit cycle of 35 days. In contrast, for Sentinel-1 data sets, different temporal baselines have been examined, owing to the regular observations and short revisit cycle.

The final stage in the generation of differential interferograms is the multi-looking process. This process is used to decrease the noise in the resulting interferograms. For ERS and ENVISAT data, the interferograms were multi-looked using a window size of 4X20 (range X azimuth) to provide final pixel dimension of approximately 100X100m in ground range resolution, and for Sentinel-1, the multi-look window is set to 22X5 pixels, resulting to about 80X70m in ground range.

The final interferogram is a two-dimensional array, where each pixel contains the phase difference in the complex domain. It is presented as an image with a series of fringes, and each fringe corresponds to half a radar wavelength λ (2.8 cm for ERS, ENVISAT and Sentinel-1).

2.3.1.4 Estimation of coherence maps

Coherence maps are used to assess the reliability of the phase (Zebker and Villasenor, 1992). These maps are very useful by products of InSAR and provide valuable information about the quality of the formed interferograms by measuring the phase correlation between the images. According to Ferretti et al. (2007), the noise level in each interferogram depends on the signal-to-noise ratio (SNR); the latter is usually expressed in terms of similarity between the master and slave images (i.e., the higher the SNR, the more similarity in the reflectivity values between the images). In this study, the degree of similarity (coherence) is calculated using the normalized cross-correlation coefficient.

$$\gamma_c = \frac{E[Z_m Z_s^*]}{\sqrt{E(|Z_m|^2).E(|Z_s|^2)}} = \gamma . e^{j\phi f} \qquad \textbf{Eq. 2.5}$$

where γ_c is the coherence between master (Z_m) and slave (Z_s) images and it ranges from 0 to 1; 0 means very poor or lack correlation between the images and 1 means a perfect correlation. $E[.]$ is the expectation operator which represents averaging over the multi-looking window. The size of the multi-looking window is the same for those used to generate differential interferograms (i.e. 4X20 pixels (range X azimuth) for ERS and ENVISAT datasets, and 22X5 pixels for Sentinel-1 dataset). After estimating the coherence map for each differential interferogram, the average coherence map is formed from all image pairs in the data set. **Figure 2.8** shows examples of average coherence map over Venice Lagoon (Italy) using ENVISAT dataset. As expected, urban structures exhibit higher coherence than rural and vegetated areas.

After estimation of the average coherence map, the selection of ISBAS points to generate the final deformation map is made depending on the number of layers used to get an average coherence value of more than 0.25. Urban areas generally have high coherence in all layers and the coherence decreases in rural and vegetated areas. The points that have fewer layers than the threshold value (usually in rural and vegetated areas) will be rejected.

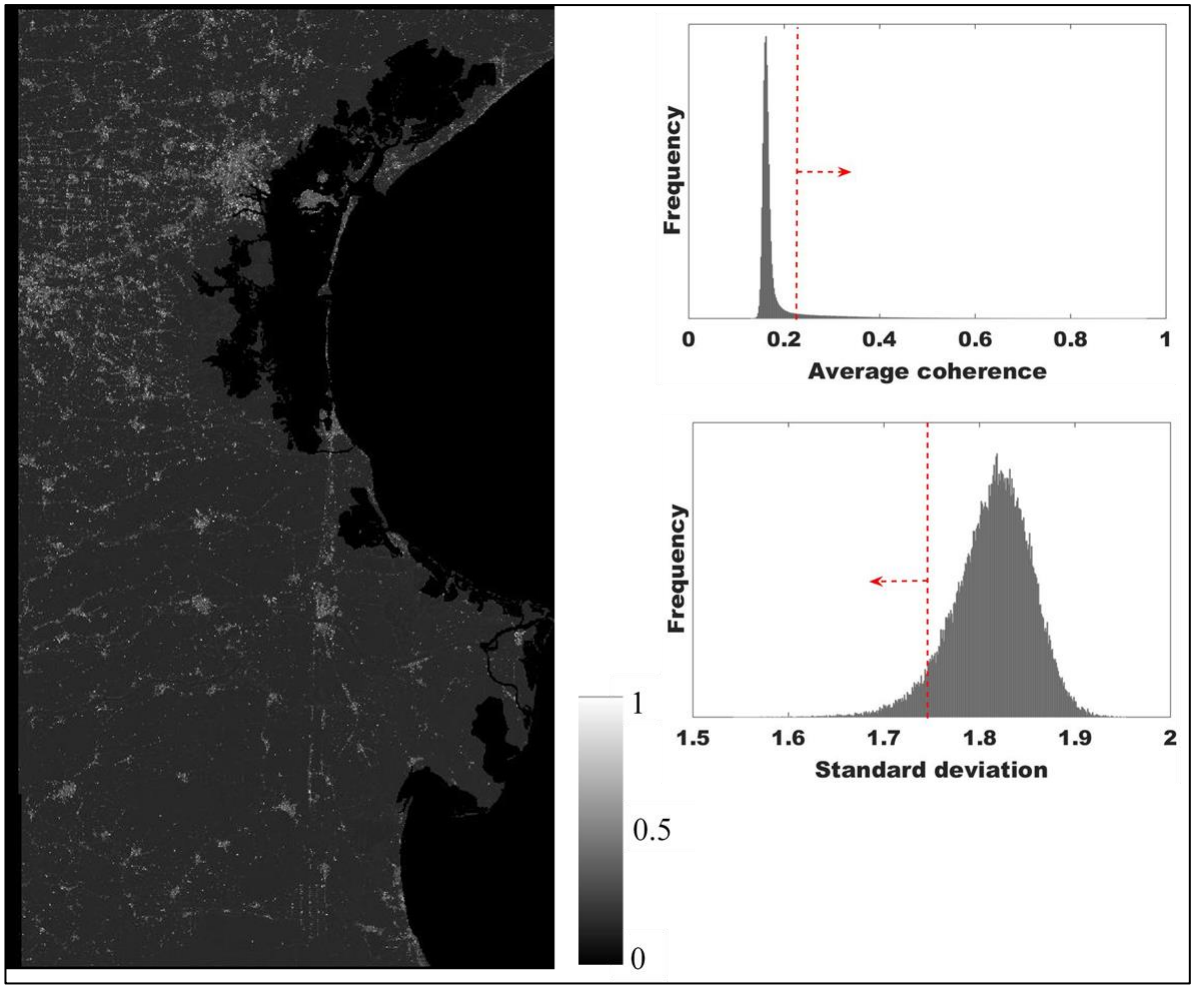


Figure 2.8: The average coherence map from the ENVISAT dataset with the statistical information of SBAS points for reference point selection. Here, the selection of the reference point for phase unwrapping is based on narrowing down the SBAS points using the red dashed arrows (the point that has average coherence more than 0.25 and standard deviation for all interferograms less than 1.75.

2.3.1.5 Selection of the reference point

The selection of the reference point for the phase unwrapping process is extremely important because the wrong selection will not only cause an offset in the estimation of the deformation but will also contribute to the phase unwrapping error. For most InSAR studies, this point is usually selected in a stable area with prior knowledge about the geological setting in that area.

In the case of no knowledge about the subsidence history for the processed scene, the selection of this point will be problematic. Therefore, in this study the reference point is selected based on two criteria:

- The subsidence history over the area of interest (if it is available).

- The reference point should have high coherence in all layers (SBAS point) and exhibit stable phase behavior across the differential interferograms.

Therefore, from the statistical information of the SBAS points (**Figure 2.8**), the SBAS point candidates for the reference point can be narrowed down by selecting points that only have a standard deviation in all differential interferograms of less than 1.75. The reference point is then selected manually from those SBAS point candidates considering the location of the points, (i.e., the stability of the area, if it is available) and their statistical results.

2.3.1.6 Phase unwrapping

As explained in **Section 2.2.2**, the interferometric phase is known as modulo- 2π. This means that only part of the phase is recorded which is the fractional part of the cycle (wavelength) without any information on the number of the entire cycles (wavelengths) that precede it. **Figure 2.9** illustrates this idea, where the recorded phase represents the red color, however, no information is recorded regarding the whole number of the cycles N that comes before it, which is known as the phase ambiguity. To make the interferometric phase more useful in different applications such as topographic mapping and positioning, it is important to relate the phase of the pixel in one differential interferogram to another. This requires reconstruction of the phase such that it is all relative to a reference point in a particular interferogram. This process is called phase unwrapping and the selected reference point, as explained in the previous section, will be common across all interferograms.

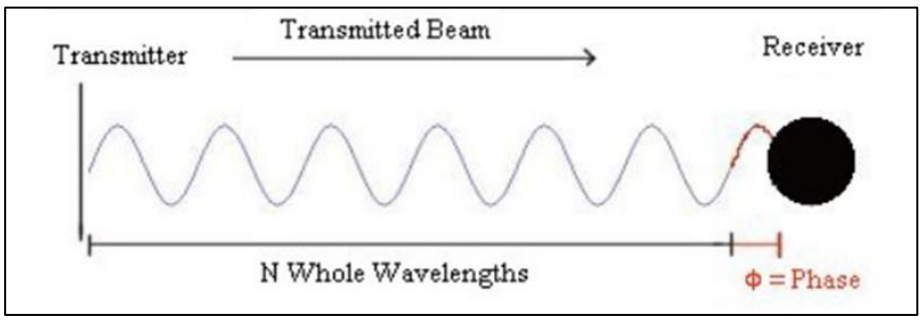


Figure 2.9: The ambiguity of the phase, where the red color represents the recorded phase ∅, without any information on the number of the whole cycles (wavelengths N.) Adapted from Warren (2007).

Generally, the phase unwrapping process is based on the hypothesis that the phase gradient between neighboring pixels varies smoothly within 2π intervals. More accurately, the phase values of the adjacent pixels are expected to be varied within a one-half cycle (π) of one

another (Ferretti, 2014). This assumption is valid for the noiseless phase which is sampled sufficiently (i.e., adjacent pixels are less than (π)). However, the presence of the discontinuity in the phase due to noise and/or fast phase variations caused by rapid deformation (Hanssen, 2001) prevents using the straightforward procedure, which is the phase differences starting from a reference point.

Since InSAR became an active field of research, different algorithms for the phase unwrapping process have been developed such as least square algorithm (Ghiglia and Romero, 1994; Fornaro et al., 1996a; Fornaro et al., 1996b; Ghiglia and Romero, 1996), minimal cost flow algorithm (Costantini, 1998; Chen and Zebker, 2000; Chen and Zebker, 2001) and residue-cut algorithm (Goldstein et al., 1988; Ching et al., 1992). For more in-depth review, interested readers can review the references provided above.

In this research, the Punnet software used the Statistical-cost Network-flow Algorithm for Phase Unwrapping (SNAPHU) program outlined by Chen and Zebker (2002) to individually unwrap the coherent pixels within each differential interferogram. For the phase unwrapping process, the differential interferograms and their respective coherence maps have been used as input files. The latter is used as a weight to specify the areas with a high noise level that will discredit the underlying assumption of smooth variation for the phase gradient. For the same reason, prior to the process, the nearest neighbor interpolation has been applied to all coherence points in the differential interferograms. It is difficult to assess the reliability of the unwrapped phase, but a strong assumption can be made about it depending on the data behavior. The phase unwrapping for longer radar wavelengths such as L band is expected to be more reliable and robust due to the higher signal to noise ratio (SNR) and smoother variation of the phase values (Hanssen, 2001).

Although the unwrapped phase value contains the linear phase component due to different satellite geometry during each acquisition, this effect is easy to model and mitigate as it is proportional to the perpendicular baseline (normal baseline). Punnet software uses a bilinear least square method based on the phase of the coherence points to estimate and remove the baseline error. Then the corrected unwrapped phase for each coherent point is stored for latter processing.

2.3.1.7 Stacking

After the unwrapping process, the phase of the coherent points in each differential interferogram represents the deformation relative to the selected reference point. Several

factors affect the phase and cause changes in the position such as atmospheric delay, DEM errors, geometrical and temporal decorrelation between the satellite passes. Therefore, several stacking techniques have been developed to overcome these limitations and to produce the deformation map from multiple differential interferograms, such as Persistent Scatterer Interferometry (PSI) (Kampes, 2005; Kampes, 2006), Permanent Scatterer InSAR (PSInSAR) (Ferretti et al., 2001), Interferometric Point Target (IPTA) (Werner et al., 2003), Persistence Scatterer pairs (PSP) (Costantini et al., 2008), SqueeSAR (Ferretti et al., 2011), and Stanford Method for Persistant Scatterers (StaMPS) (Hooper et al., 2004; Hooper, 2008). For a more in-depth review, interested readers can refer to Osmanoğlu et al. (2016).

In this study, the ISBAS algorithm (Sowter et al., 2013) has been used to produce the deformation map from multiple-differential interferograms. This algorithm appears to be well suited for low resolution and wide area deformation monitoring over different land cover classes such as grassland, forest and agriculture areas (Cigna et al., 2014; Sowter et al., 2016; Cigna and Sowter, 2017). It represents a modified version of the SBAS technique (Berardino et al., 2002) with a slightly different approach to identifying the intermittent coherent points in InSAR time-series.

2.3.1.8 Estimation of the linear deformation

The ISBAS DInSAR time-series analysis is started with the estimation of the linear velocity and DEM error for each coherent point. These two components are calculated using the least-square regression analysis of N unwrapped phases. The unwrapped phase of each coherent point contains the contribution from the deformation, which is linear with time, and DEM error, which is proportional to the perpendicular baseline. In this stage, the atmospheric effect is considered to be zero due to the assumption that this layer is propagated randomly across the whole unwrapped differential interferograms. **Eq. 2.6** illustrates the possibility of estimation of the linear deformation and DEM error for each ISBAS coherent point using the least-square method.

$$\Delta\emptyset_{m,s} = \frac{4\pi}{\lambda} \cdot (t_m - t_s) \cdot V + \frac{4\pi}{\lambda} \cdot \frac{B_{perp}^{m,s}}{R \cdot \sin\theta} \cdot \delta h + \varepsilon \qquad \textbf{Eq. 2.6}$$

Where,

- $\Delta\emptyset_{m,s}$ represents the unwrapped phase for each coherent point.
- $\frac{4\pi}{\lambda}$ is a unit transformation from cycle to meter considering two-way travel path.
- $(t_m - t_s)$ is the temporal separation between master and slave images.

- $(\frac{B_{perp}^{m,s}}{R \cdot \sin\theta} \cdot \delta h)$ represents the relationship between the DEM error δh, perpendicular baseline $B_{perp}^{i,j}$, sensor to target distance R, and incidence angle θ.
- ε is the noise.

2.3.2 ISBAS non-linear processing chain

The estimation of the linear velocity from DInSAR as discussed in the previous sections provides important information about the deformation of the earth's surface on a dense grid. However, the field of interest for the scientific community is now gradually moving toward the study of the temporal behavior of the detected deformations, which can be done by the generation of a time-series that allows the evolution of the detected phenomena to be followed. The non-linear processing chain of Punnet software is utilized in this study to retrieve such information by using Singular value decomposition (SVD) to link independent SAR acquisitions separated by large baselines. This algorithm is similar to the one outlined by Berardino et al. (2002). **Figure 2.10** illustrates the scheme of the non-linear processing chain.

The non-linear processing is continued from the linear processing. To estimate the non-linear deformation, first, the linear phase model which considers the deformation and the DEM error has to be calculated. Then these two components (linear deformation and DEM error) have to be subtracted from the differential phases over the set of coherent points to obtain the phase residuals. These residuals are considered to contain the phase components due to the non-linear motion, atmosphere and noise.

At this stage, the phase unwrapping of N differential interferograms on the residuals is performed and the deformation components added back. For each coherent point, a system of N equations of known unwrapped differential phases in time, unknown phase values associated with the deformation of the considered point at each acquisition time. Therefore, to reduce the presence of large discontinuities in the results obtained, the phase velocity between time-adjacent images can be used and inverted via SVD to retrieve a minimum-norm least square solution. Then the phase of each coherent point at each acquisition time is derived. A cascade of a high pass filter in the time domain and a low pass filter in the spatial domain is used to retrieve and remove the atmospheric phase components. Finally, the estimated phase at each satellite acquisition for each coherent point is transformed to deformation by multiplying by $\lambda/4\pi$ and then the coherent points are geocoded to map geometry.

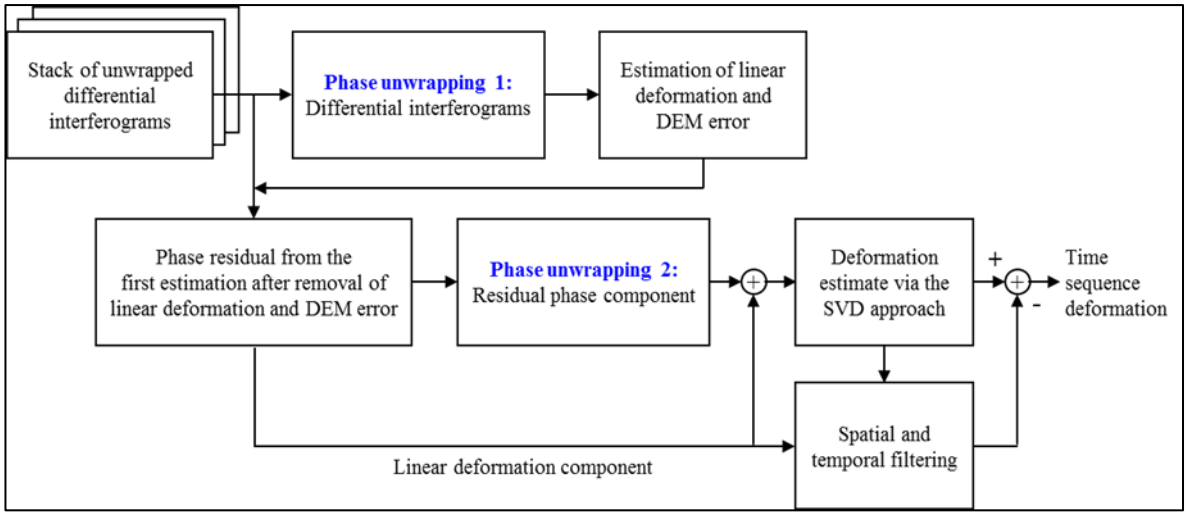


Figure 2.10: The diagram of the non-linear processing chain. Figure adapted from Berardino et al. (2002)

2.4 Singular Spectrum Analysis (SSA) overview

SSA is a novel and robust method designed to extract the useful information from short and noisy time-series, which helps to analyze the unknown or partially known system dynamics that generated the time-series (Broomhead and King, 1986; Vautard and Ghil, 1989; Ghil et al., 2002). SSA has been successfully applied to a number of different fields such as economics, biomedical signal processing, earth science observations and image processing, for example (Golyandina et al., 2001; Ghodsi et al., 2010) and the references therein. This method is very useful to solve many problems – for example, finding the trends of the series, extracting complex seasonal patterns, extracting periodicities with varying amplitude and finding the structure of short time-series. SSA is a non-parametric method and the main advantage of this method is that it can be applied without making any assumptions such as normality of the data (Golyandina et al., 2001). It permits one to make the decomposition of the time-series into their constituent of independent and interpretable components: trend, oscillatory components and noise. Then, it reconstructs the time-series using the computed trend and oscillatory components.

SSA method can be used for a single time-series or jointly to multiple series, where the latter is referred to as Multivariate SSA (MSSA). In the same way as a parametric method, two or more time-series may be related; in MSSA, this relation is represented by matching components of multiple time-series. MSSA has been successfully applied to many studies and the interested reader is referred to Hassani et al. (2013) and the references therein.

The commencement of SSA is usually associated with the publications of papers such as those by Broomhead and King (1986), Vautard and Ghil (1989), Vautard et al. (1992) and Allen and Smith (1996). A detailed description of the theoretical and practical foundation of this technique can be found in Golyandina et al. (2001).

The concept of the SSA method is first to embed the sampled time-series into a sufficiently high dimensional time delayed space and then to find a new orthonormal system which detects the most variance of the time-series using a few components only. This new linear system is specified by principle component analysis. This means that this method linearly decomposes the time-series into a new orthogonal system, which is given as the principle components in a time delayed embedding of the time-series. In relation to a classical Fourier decomposition, the new system is not bounded any more to sine and cosine functions, but it contains data-adaptive functions (Allen and Smith, 1996). As a result, the oscillations detected by SSA method may show the amplitude and /or phase modulation. Such flexibility acts as a remarkable feature when dealing with the complex dynamical system.

One of the aims of this research is to investigate the feasibility of SSA techniques such as univariate and multivariate SSA to determine the variations of surface motion over the complex dynamical system represented by peatlands within differential interferometric SAR (DInSAR) time-series. Therefore, in the sections below, a short introduction to the methodology of SSA is presented with a brief description of using SSA-based methods to fill the gaps in the recorded time-series.

2.4.1 Univariate SSA

The univariate SSA processing can be described in three main steps:

- Embedding of the sampled time-series

The first step of SSA is to embed the sampled time-series (Vautard and Ghil, 1989) to a vector space of dimension M (M represents an integer value and it ranges $1 < M < N$) to transfer the one-dimensional time-series into a multidimensional matrix X (trajectory matrix):

$$X = \begin{pmatrix} x(1) & x(2) & \cdots & x(M) \\ x(2) & x(3) & \cdots & x(M+1) \\ \vdots & \vdots & \ddots & \vdots \\ x(N-M+1) & x(N-M+2) & \cdots & x(N) \end{pmatrix} \qquad \textbf{Eq. 2.7}$$

- Computation of the lag-covariance matrix C

The M x M lag-covariance matrix C_X can be estimated from the trajectory matrix X (Vautard and Ghil, 1989) as a Toeplitz matrix with constant diagonals, where the entries of this matrix (C_{ij}) are dependent only on the lag $|i-j|$:

$$C_{ij} = \frac{1}{N-|i-j|} \sum_{t=1}^{N-|i-j|} x(t)x(t+|i-j|) \qquad \textbf{Eq. 2.8}$$

The eigenelements (eigenvalues λ_k and eigenvectors ρ_k: k=1,……,M) of the covariance matrix C_X are then obtained by solving

$$C_X \rho_k = \lambda_k \rho_k \qquad \textbf{Eq. 2.9}$$

Each eigenvalue λ_k provides the partial variance in the direction of ρ_k of the original time-series x (t):

$$PV(k) = \frac{\lambda_k}{\sum_{k=1}^{M} \lambda_k} \qquad \textbf{Eq. 2.10}$$

The M eigenvalues λ_k of the covariance matrix C_X are determined and arranged in descending order. By plotting them, one can often recognize an initial plateau that consists of most of the true signal separated by a steep slope from the noise, which is characterized by low values that shape a flat floor (Vautard and Ghil, 1989; Ghil et al., 2002).

As the lag covariance matrix C_X is symmetric, the spectral decomposition will be performed efficiently if the window width M is not too large. The selection of M represents a trade-off between the quantity of the extracted information versus the degree of statistical confidence in that information. Where the former needs as large a window width as possible (large M), the latter needs more repetitions of the features of interest, i.e., as large a ratio of N/M as possible (Ghil et al., 2002).

- Reconstruction of the original time series

The final step is the projecting of the time-series onto each eigenvector ρ_k which provides the corresponding principal components (PCS), A_k:

$$A_k(t) = \sum_{j=1}^{M} X(t+j-1)\,\rho_k(j) \qquad \textbf{Eq. 2.11}$$

The power spectrum of the time-series $x(t)$ is equal to the sum of the power spectrum of all the PCS, which makes it possible to study the spectral contribution from the different components. Then, part of the time-series can be reconstructed by using a single PC or by combining several PCS

$$R_{\mathcal{K}}(t) = \begin{cases} \frac{1}{t}\sum_{k\in\mathcal{K}}\sum_{j=1}^{t} A_k(t-j+1)\rho_k(j), & 1 \le t \le M-1 \\ \frac{1}{M}\sum_{k\in\mathcal{K}}\sum_{j=1}^{M} A_k(t-j+1)\rho_k(j), & M \le t \le N' \\ \frac{1}{N-t+1}\sum_{k\in\mathcal{K}}\sum_{j=t-N+M}^{M} A_k(t-j+1)\rho_k(j), & N'+1 \le t \le N \end{cases} \quad \textbf{Eq. 2.12}$$

where $R_{\mathcal{K}}$(t) series of the length N represents the reconstructed components (RCS). It should be noted that during the reconstruction process, there is no loosing of the signal information because the sum of all RCS returns back to the original time series.

2.4.2 Multivariate SSA (MSSA)

MSSA represents an extension of univariate SSA (Broomhead and King, 1986; Broomhead and King, 1986b; Ghil et al., 2002) which was firstly proposed in the context of non-linear dynamics by Broomhead and King (1986b). This approach analyses a set of multi-channels of time-series with the goal of specifying and extracting the dominant spatiotemporal structures of the underlying stochastic process. MSSA in particular extracts the oscillatory patterns common to most time-series in the data set, i.e., the real periodicities to the most channels.

As the MSSA method is a natural extension of SSA, it includes two processing steps: decomposition and reconstruction. The first step of MSSA is the embedding process. For L-channel time-series with N data points given at equally spaced intervals, the window of size M can move through every single observation for each time-series:

$$\{X_l(t): l = 1, \ldots\ldots, L,\ t = 1, \ldots\ldots, N\} \quad \textbf{Eq. 2.13}$$

In this process, the trajectory matrix for each time-series has determined (Broomhead and King, 1986; Broomhead and King, 1986b; Allen and Smith, 1996; Ghil et al., 2002).

$$\widetilde{X_l} = \begin{pmatrix} X_l(1) & X_l(2) & \ldots & X_l(M) \\ X_l(2) & X_l(3) & \ldots & X_l(M+1) \\ \vdots & \vdots & \ldots & \vdots \\ X_l(N'-1) & \vdots & \ldots & X_l(N-1) \\ X_l(N') & X_l(N'+1) & \ldots & X_l(N) \end{pmatrix} \quad \textbf{Eq. 2.14}$$

For individual time-series, the dimension of the trajectory matrix is N′ X M, where (N′=N-M+1). The trajectory matrix $\widetilde{D}$ of multi-channel time-series can be defined as follows:

$$\widetilde{D} = (\tilde{X}_1, \tilde{X}_2, \tilde{X}_3, \ldots\ldots, \tilde{X}_L) \quad \textbf{Eq. 2.15}$$

The full trajectory matrix has L.M columns of length N-M+1. From this matrix, the grand lag covariance matrix can be calculated:

$$\tilde{C}_D = \frac{1}{N'}\tilde{D}^t\tilde{D}\begin{pmatrix} C_{1,1} & C_{1,2} & \dots & . & C_{1,L} \\ . & C_{2,2} & \dots & . & . \\ . & \vdots & \dots & C_{l,l'} & . \\ . & \vdots & \dots & . & . \\ C_{L,1} & C_{L,2} & \dots & . & C_{L,L} \end{pmatrix} \quad \textbf{Eq. 2.16}$$

Then the LMXLM grand covariance matrix of the L-channel time-series $\tilde{C}$ contains all auto-covariances $C_{l,l}$ and cross-covariances$C_{l,l'}$:

$$C_{l,l'} = \frac{1}{N'}\tilde{X}_l^t\tilde{X}_{l'} \quad \textbf{Eq. 2.17}$$

The second step is to diagonalize the grand lag-covariance matrix to obtain the eigenvectors E^k which is also called Empirical Orthogonal function (EOFs) and eigenvalues λ_k by formula:

$$\Lambda = E^t C\, E \quad \textbf{Eq. 2.18}$$

where Λ is the matrix contain eigenvalues λ_k, and E is the eigenvectors matrix E^k.

The eigenpairs (λ_k, E^k) then should be stored in descending order of the eigenvalues. Using the obtained eigenvectors, the k-th principal components (PCs) which represent a single channel time-series are then calculated (Ghil et al., 2002):

$$A^k(t) = \sum_{j=1}^{M}\sum_{l=1}^{L} X_l\,(t+j-1)E_l^k(j) \qquad 1 < k < M \quad \textbf{Eq. 2.19}$$

where t varies from 1 to $N' = N - M + 1$.

The principal components (PCs) are the projection of the original time-series into eigenvectors.

The MSSA method is an extension of classical of principal components analysis (PCA); however, both of them are different. For PCA, the window size M=1 and the covariance matrix is simply a spatial function of data. In MSSA on the other hand, the covariance matrix is enhanced by the time-lagged (Kim and Wu, 1999). The main features of MSSA method over PCA is that the capability to specify the time oscillatory behavior due to the oscillatory pairs.

As in the case of univariate SSA, there is a possibility to reconstruct the detected mode for each channel in MSSA from previously calculated PCs and EOFs, but the reconstruction components RCs may differ from one channel to another:

$$R_k^l(t) = \frac{1}{M_t}\sum_{j=L_t}^{U_t} A_k\,(t-j+1)E_k^l(j) \qquad 1 < k < M, 1 < t < L \quad \textbf{Eq. 2.20}$$

Thus, we can investigate how that particular MSSA-mode affects each time-series. Furthermore, a single oscillation can be significant for all channels time-series even if the

fraction of the variance is not the same in all channels, which means that this oscillation is more energetic rather than the others. Therefore, the MSSA method helps to investigate the spatiotemporal behavior of each channel concerning the others, rather than the evolution of the global process only.

For a dataset with many spatial channels L and large temporal window M as in this research, it is better to select a reduced covariance matrix $C^{(R)}$ with $M = N' = N/2$ to maximize the spectral resolution. So whenever$N' < LM$, consequently $C^{(R)}$ is smaller than $\tilde{C}$ and the latter has a null space of dimension $LM - N'$. The eigenvectors of $\tilde{C}$ that lie outside this null space are identical to eigenvectors of $C^{(R)}$. Therefore, in this case, it is more efficient in MSSA to use the reduced covariance matrix $N'X\ N'$, rather than the $LM\ X\ LM$ covariance matrix.

$$C^R = \frac{1}{LM}\tilde{X}\tilde{X}^t \qquad \textbf{Eq. 2.21}$$

2.4.3 Monte Carlo SSA (MC-SSA)

The important step in SSA is the discrimination of the significant signal from the noise (Ghil et al., 2002). In the case that the signal to noise ratio is low or the noise in the data is not merely white, the traditional method to extract the signal from noisy time-series that is based on specifying the gap in the spectrum between the eigenvalues becomes problematic. Therefore, an alternative approach based on the Monte-Carlo technique has been proposed (Vautard et al., 1992).

The MC-SSA method outlined by Allen and Smith (1996) provides the statistical significance for the extracted spectral components through testing the original data against red noise (the autoregressive process of order 1 (AR(1)) as a null-hypothesis as follows:

$$X(t) = a_1\left[X(t-1) - X_0\right] + \sigma\xi(t) + X_0 \qquad \textbf{Eq. 2.22}$$

X_0 represents the mean process, both a_1, and σ are the constant coefficient and ξ is a white noise Gaussian-distribution with zero mean and unit variance.

To distinguish the signal from the noise using MC-SSA first is to estimate the red noise coefficients a_1, and σ by using maximum-likelihood criterion. Then, an ensemble of simulated red noise data is generated and, for each realization, a covariance matrix C_R is calculated and projected onto eigenvectors E_x such as follow:

$$\Lambda_R = E_x^t C_R E_x \quad \textbf{Eq. 2.23}$$

The matrix $\Lambda_R$is not necessarily diagonal. Instead, it measures the resemblance of the generated surrogate set with the original data by calculating the statistical distribution of its diagonal elements. From these distributions, the confidence intervals outside which the time-series can be considered significantly different from red noise can be obtained.

Care needs to be taken when considering the interpretation of MC-SSA error bars, since the estimate of the dominant frequency may be ambiguous or uncertain due to the possible deviation of the EOFs from being a harmonic oscillator (anharmonicity), particularly for low frequencies.

2.4.4 Iterative gap filling using SSA

Time-series input data for SSA must be equally spaced in the time domain. However, despite the regular revisit cycle for SAR satellites, for example (35 days for ERS1/2 and ENVISAT, 12 days for Sentinel 1, and 11 days for TerraSAR-X), some SAR images are missing or excluded during the processing due to different reasons such as technical problems on the SAR satellite or on its communication system, and/or large baselines of the generated interferograms. As a result, the time-series data obtained from InSAR processing are rarely equally distributed in time. To solve this issue, a gap filling procedure based on SSA for both univariate and multivariate time-series outlined by Kondrashov and Ghil (2006) has been used in this study.

For univariate time-series, the gap filling method based on SSA uses the temporal correlations in the data set to fill the gaps of the missing points. For multivariate time-series, the MSSA gap filling takes advantage of the temporal as well as the spatial correlations. In both cases, gap filling based on the SSA method iteratively obtains estimates of the missing measurements using leading subset of RCs, which are then used to calculate a self-consistent lag covariance matrix C_X, EOF_s and PC_s. The next step is to use cross validation to optimize the window width M and number of dominant SSA modes to fill the gap of the missing data.

For many applications, a few leading EOF_s correspond to the dominant oscillatory and or trend modes, and the rest represents noise (Ghil et al., 2002). From this idea, the original time-series is centered by calculating the unbiased value of the mean and zero values are set for the missing data. The inner-loop iteration is then started working by computing the leading $EOF\ E_1$ of the centered, zero-padded records. Next, the corresponding $RC\ R_1$ is utilized to compute the non-zero values to use in the place of the missing points and the records mean,

covariance matrix and EOF_s are corrected. The reconstruction process is repeated by using a new estimate of R_1 and tested with the previous reconstruction until a satisfied convergence test is obtained; in this study, the convergence test has been set to 0.005 of normalized root-mean-square error (rms) as a criterion. The outer-loop iteration is then performed by adding the EOF_2 to the reconstruction process, starting from the data filled by R_1, and repeating the inner iteration with two EOF_s until it converges. The outer-loop iteration stops once the dominant SSA modes that are attributed to the signal have been processed and the higher ranked modes are assumed to be noise. For a more in depth review, interested readers are referred to Kondrashov and Ghil (2006) and Kondrashov et al. (2010).

2.5 Summary

In this chapter, several techniques relevant to this thesis have been reviewed. The basics and geometry of SAR and InSAR are followed by an examination of the linear and non-linear processing of the ISBAS technique using Punnet software. The SSA method for both univariate and multivariate time-series was then examined as a way to analyze the peatland surface motion and to extract the seasonal trends and amplitude from differential interferometric SAR (DInSAR) time-series. These techniques have been applied over selected sites covered with peat. The results and the discussion are presented in the next chapters.

CHAPTER 3

LITERATURE REVIEWS ON THE TECHNIQUES USE FOR PEATLAND DEFORMATION MONITORING AND ON THE USE OF INSAR FOR SURFACE MOTION MONITORING

3.1 Introduction

Peatlands are wetlands with highly organic soil produced by the accumulation of plant material. Around the globe, there are more than 4 million km^2 of peatlands and they are still in a mostly natural condition; however, there is much pressure on peatlands mainly due to population pressures. These pressures are important to acknowledge since peatlands provide many ecosystem services: for instance, 0.3% of the global degraded peatlands are responsible for the emission of about 5% of the global anthropogenic CO_2 into the atmosphere in any one year (Joosten et al., 2016a). This substantial emission from such a small area of the globe suggests that these areas have remarkable qualities. Thus, we must monitor these important ecosystems to ensure we measure anthropogenic impacts (including climate change) on them and to manage and mitigate these. To understand the operating parameters for such a monitoring system, our current understanding of peatland ecosystems requires review. This chapter, therefore, describes the main characteristics of peatland; provides an overview of peatland distribution, functions and its relationship with the climate; describes the causes and consequences of peatland degradation; and is followed by an overview of various monitoring techniques available to date.

3.2 Peatland characteristics and ecosystem services

The production of plant material in most natural ecosystems is counterbalanced by its decomposition through bacterial and fungal processes. In wetland areas, however, having a stable water table near the surface means that part of the dead plant decays and another part accumulates as peat. These wetlands are called mires, and the areas covered with peat are called peatlands (Joosten and Clarke 2002). In mires, peat accumulates slowly at a rate of about 0.5-1 mm/year and with locally strong variation. If the accumulation is continued for thousands of years, the land may be thickly covered with many layers of peat (Charman 2002).

The main characteristics of natural peatlands are permanent water logging, the formation and long-term storage of peat, and the continuous growth of the peat on the surface.

These characteristics specify the importance, services and functions associated with these areas, which includes long-term storage of carbon and supply of water (Charman et al., 2008; Joosten et al., 2016a; Joosten et al., 2016b). The water logging and continuous upward growth of the surface further determine and provide the special and particular site conditions for peatland organisms. The aforementioned peat growth (i.e., accumulation) occurs when the rate of plant production exceeds the rate of the plant decomposition. This tends to happen in the areas that are saturated with water where the latter restricts decay of organic material due to anaerobic and cold temperature conditions (Charman et al., 2008; Joosten et al., 2016a). Therefore, the accumulation of peat only takes place when the water table in the long-term is near or just above the ground surface. When the water table is below the peat surface, the plants decompose rapidly due to the abundance of oxygen, while when it is too high, the plant production is inhibited by an insufficient amount of oxygen and carbon dioxide provided to the submerged parts (Alexandrov 1988; Joosten et al., 2016a). With fluctuating water tables, a larger part of the organic material decomposes which leads to less peat accumulation and more humified peat.

In cold and wet regions, it is the mosses that predominantly determine peat growth since they have a lack of roots and organs to conduct water, they can only produce considerable biomass when the water table depth at the time of the growing seasons remains very close to their growing surface and the evapotranspiration process is restricted. Moreover, the cold and wet conditions in these regions limit the availability of mineralization and nutrient, which leads to the suppression of the growth of taller and deep-rooted vascular plants. In continental-temperate and subtropical regions of the world, the above-ground plant decomposes quickly at warm and well-aerated mire surfaces and in the drier climate, this therefore limits the peat to be formed under the surface. In these regions, the peat accumulates below the plant surface through rhizomes and rootlets of grasses, sedges and other plants. In tropical areas, the peat forms even deeper underground - under the tall-forest trees by their deep-rooting.

In peatland areas, the plants, water and peat are very closely connected with each other and are mutually interdependent (**Figure 3.1**). The interdependencies make the peatland areas vulnerable to a broad range of human impacts. The plants control the type of peat that will form and its hydraulic properties. The water (hydrology) specifies which type of plants will grow and how much biomass these plants will produce. And the structure of the peat determines how the water will fluctuate and flow. These strong interrelations mean that if any one of these components changes, the others will change too (Charman et al., 2008). These changes may

not necessarily occur at the same time, but in the long-term, they inevitably occur. As the changes have taken place in different components, the ecosystem services of the mire such as carbon storage, water flow regulation and water quality may also change (**Figure 3.1**).

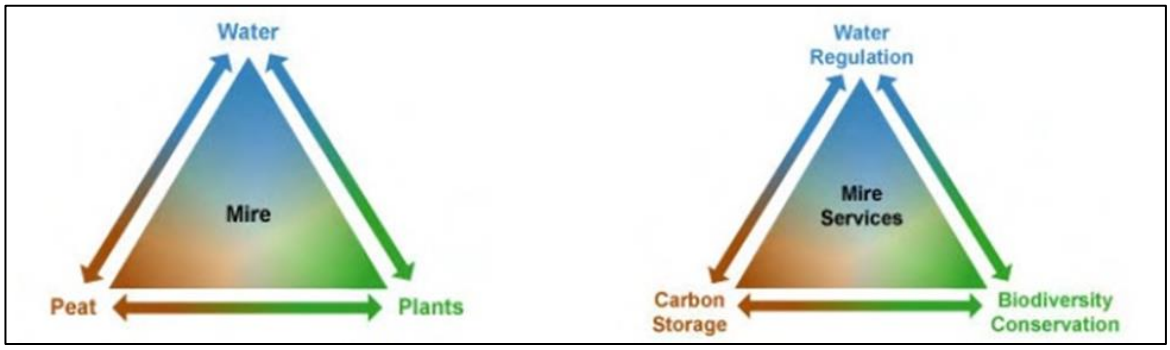


Figure 3.1: Important ecosystem interrelations and ecosystem services of mires and peatlands.

3.3 Peatland distribution and types

The distribution and extent of peatlands are primarily determined by climate: net precipitation specifies the availability of water in the landscape, whereas the temperature controls both the production and the decomposition processes of the organic matter. Therefore, peatlands are abundant, especially in cold regions where evapotranspiration is low, and in the wet regions, i.e., where the precipitation is very high (Charman 2002; Charman et al., 2008; Joosten et al., 2016a). When there is an imbalance between evaporation and precipitation, the peatland areas are found only in landscape features to enable the water to collect, such as bedrock, relief and catchment areas. Generally, peatlands dominate on flat surfaces as the water logging requires a flat surface. Thus large numbers of them prevail on extensively flat landscapes, such as western Siberia, the Hudson Bay Lowlands (Canada), the southeast Asian coastal plains and Congo and Amazon basins (Charman et al., 2008). In some parts of the world with abundant water supply and restricted atmospheric water losses, the peat can be formed on the slopes, forming hillslope peatlands and blanket bogs. The general inventory status of peatland can be seen in **Figure 3.2** (Joosten 2009; Kaat and Joosten, 2009), and the status of the carbon stock of each country can be found in Kaat and Joosten (2009).



Figure 3.2: Peatland cover per country. Adapted from Joosten (2009).

Globally, peatlands are highly diverse, particularly concerning plant species and community compositions. However, they do share echo-hydrological functioning. Peat can be defined by the presence of a large amount of organic matter (more than 30%) (Joosten and Clarke 2002) based on plant origin under a variety of climate conditions, peat can be classified into the four groups as follows (Allison, 1973):

- Highmoor or upland peat: This kind of moss peat forms in cold and wet regions with high rainfall, particularly in Canada and northern Europe and it forms primarily from sphagnum mosses. This peat is a loose, spongy and usually very acidic material that is not easily decomposable.
- Lowmoor or lowland peat: this peat is composed of the remnants of various kinds of plants such as sedges, reeds, shrubs and other plants that grow in marshes with shallow water. This kind of peat is less acidic than moss peat and can provide good agriculture soils if drained.
- Forest peat: which is called woody peat. It is formed from the remains of trees and shrubs that grow in the forest or swamp. This kind of peat has smaller water retention capacity than lowland peat.
- Aquatic peat: this peat is called sedimentary peat and it is obtained from submerged succulent open water plants. This kind of peat seldom provides good agriculture soils if drained.

3.4 Climate control on peatland characteristics and ecosystem services

In high-latitude peatland regions that experience cold winters, warmer temperatures prolong the growing season, which in turn increases plant production. However, these high temperatures increase the rates of decomposition in peat soils (Dorrepaal et al., 2009). Although, the effect of warmer, drier climate conditions in certain nutrient-rich peatlands seems to increase both production and decomposition processes similarly (Flanagan and Syed, 2011), the accumulation of carbon has been shown to be correlated positively with the amount of photosynthetic active radiation (PAR) at the time of the growing season (Charman et al., 2013). Therefore, the period of the growing season represents an important climatic factor controlling the accumulation of carbon. But so is cloudiness, where the cloudiness promotes peatland occurrence due to low potential evaporation while keeping the rates of carbon accumulation low because of low PAR (Gallego-Sala et al., 2016). Consequently, intact peatlands act as an important climate-regulation service by carbon accumulation and more importantly through long-term carbon storage.

3.5 Peatland degradation

According to the available data, 85% of peatland areas around the globe are still in a largely natural condition, particularly the areas in remote parts of Canada, Siberia and Alaska. However, about 500 000 km^2 worldwide is degraded to the extent that there is no longer peat formation and the accumulation has partly or entirely disappeared (Joosten et al., 2016a). Pristine peatlands are dominant in sub-arctic and boreal regions (Wieder and Vitt 2006), while modified peatlands are concentrated in the temperate and sub-tropic regions (Joosten and Clarke 2002). Currently, an additional 5000 km^2 of peatlands are destroyed annually, mainly as a result of human activities (Joosten and Clarke 2002; Joosten et al., 2016a). There are many factors that cause degradation and subsidence in the peatland areas which in turn cause carbon losses in these areas. These factors can be intentional, such as drainage for land use and forestry, peat extraction, development of infrastructure and urbanization, and unintentional that arises for example from climate change, atmospheric pollution, grazing and burning. However, systematic drainage of peatland represents the most significant factor which is responsible for subsiding and lowering the surface elevation by an amount that can reach several meters (Stephens et al., 1984; Wosten et al., 1997). The overall subsidence of the peatland surface is the sum of several components (Wosten et al., 1997; Deverel and Leighton, 2010): consolidation due to the effective stress that increases after lowering the water table (WT);

reduction in the volume of the peat due to the oxidation of the organic matter; shrinking/ swelling of the unsaturated shallow peat layer due to the seasonal wetting/drying cycles; wind erosion and burning. Consolidation and oxidation are considered the dominant forces for irreversible long-term subsidence in drained peatland. It is characterized by an initial rapid consolidation followed by slow oxidation; the latter is being recognized as the main contributor to the overall subsidence (Stephens et al., 1984; Armentano and Menges, 1986). In natural situations, subsidence of the peat occurs but is balanced by the growth of the peat. In drained peatland, however, this balance is lost; the subsidence processes of the peat are higher in magnitude, which results in a rapid decline in both the peat surface and carbon storage.

3.6 Causes of peatland degradation

Peatland systems can be easily destabilized by a change in hydrological and ecological conditions which leads to physical degradation if sustained. Changes in peatland stability can be intentional or unintentional (Parry et al., 2014; Price et al., 2016) as explained in the previous section.

Unintentional disturbance of peatland areas can take place at regional or global scales. Climate change, in particular, is of great concern since many peatlands around the globe will experience a reduction in water during summer, which could lower the water table by about 14 to 22 cm (Roulet et al., 1992). The lower water table will cause a change in vegetation composition (Strack et al., 2006b), enhance carbon loss (Strack and Waddington, 2007) and decrease the rates of peat formation. Broad scale effects on the hydrology of peatlands can also result from the deposition of sulfates and nitrates from the atmosphere, which changes the vegetation composition and increases carbon loss (Vitt et al., 2003). Multiple unintentional changes can cause severe degradation on peatland systems such as the degradation of blanket peatlands of the UK and Ireland. Here a combination of atmospheric pollution along with wildfire, overgrazing and changing climate conditions led to extensive and severe gully erosion and large areas of exposed bare peat (Evans and Warburton 2007).

Intentional changes to peatland areas typically include some form of drainage or de-watering of the peat to facilitate agriculture, forest growth, and peat extraction. The hydrological system of these areas will inevitably be affected by lowering the water table of the peat and increasing runoff (Holden et al., 2006). The drainage process for forestry purposes is to provide aeration for tree roots, which helps to accelerate forest productivity. Here the top layer of the peat is largely maintained, at least initially, due to the minimal peat disturbance

beyond the ditch zone, although the subsidence of the soil affects the hydrology of the peat indirectly (Price et al., 2016). On the other hand, for peat extraction process, the drainage is required to increase the bearing capacity of the surface for heavy machinery and to lower the water content of the peatland for production after removing the top surface layer of the peat. Therefore, although both forestry and peat extraction processes need drainage as an initial step, their hydrological consequences differ considerably.

The drainage of peatland areas causes subsidence and changes to the water balance of the system. The subsidence occurs mainly by decreasing the volume due to the oxidation and shrinkage processes above the water table (WT) and the compression below (Schothorst, 1977). As a result, the hydraulic conductivity and water retention of the peat are affected. The potential negative impact of drainage for a long period (several years) can be buffered by subsidence (Rothwell et al., 1996). The surface elevation of pristine fen lawns and the mat is oscillated with a water table, thus keeping wet under both wet and dry conditions, but this ability is lost when the artificial drainage is installed (Whittington and Price, 2006).

3.7 Peatland degradation and the environmental hazard

A major environmental hazard related to peatland degradation is land subsidence (Zanello et al., 2011). In drained peatland, systematic drainage of these areas causes severe subsidence which enhances the risk of flooding (Mount and Twiss, 2005) and increases the cost of land drainage. Also, degraded peatlands impact on a broad range of ecosystem services. For example, severe erosion can lead to destabilizing the infrastructure such as tracks, resulting in a loss of access to the provisioning services (Parry et al., 2014). Poor water quality can also occur in degraded peatlands, which impact water supplies; increases in the concentrations of dissolved organic carbon (DOC) causes brown coloration of water, which adds significantly to treatment costs if they are used in raw drinking water supplies, and also contributes to release of CO_2 into the atmosphere, which provides an indirect pathway of Greenhouse gases (GHG) emission (Billett et al., 2004).

3.8 Techniques for monitoring change in peat surface (degradation and accumulation)

Different techniques have been used to infer the condition of the peat mass and of the peat itself. These measurement techniques are generally categorized into field and remote methods (Gallant, 2015).

Field measurements are considered the most effective methods as they provide high quality information about changes in peatland functioning and the related environmental

drivers and consequences of these changes (Gallant, 2015). Evans et al. (2006) used 3mm diameter, 60cm long stainless steel pins to measure erosion rates in the blanket bogs in a Pennine site. These pins were inserted into the peat surface in groups of 11 to 14 in a cross formation and measured monthly to account for the vertical and lateral variation in erosion rates over the gully walls. The peat surface levels can change between winter and summer, which is called 'bog-breathing.' Stoneman and Brooks (1997) assessed this phenomenon in situ using a method that measures the movement of a metal plate buried just beneath the peat surface relative to a fixed datum in the underlying mineral substrate (**Figure 3.3**). The top of the fixed datum is not moving, whereas the buried metal plate in the peat surface is expected to move up as the peat swells due to re-wetting. The difference in the height between the fixed datum and the buried metal plate on the peat surface should be reduced when the peat surface swells (Stoneman and Brooks, 1997). Schlotzhauer and Price (1999) monitored changes in the elevation of the peat surface in cutover Quebec peatland using graduated metal rods inserted at different depths in the peat and they found that the changes in the peat elevation exceeded 10 cm and seemed to be directly related to the fluctuation of the water table. Hemond et al. (1984) observed subsurface piezometric head to report the tidal flooding in a Massachusetts salt marsh that caused surface changes of about 1 cm over a tidal cycle. These changes were attributed to peat dilation due to the influx of water driven by vertical hydraulic gradients into a saturated column of peat. Rapid changes in surface elevation over Glacial Lake Agassiz peatlands of northern Minnesota were measured by mounting GPS antennas to the stumps of trees. Motions more than 10 and 20 cm within 12 hours were observed at bog crest and fen (tree island), respectively, that occurred in the time with steep depression cycles within the profile of the peat (Glaser et al., 2004). The rapid decrease and increase of the peat surface in that study area were ascribed to large scale biogenic gas release from the peat surface. Shotbolt et al. (1998) investigated the impact of 28-year-old South Coastal Lodgepole pine forest on blanket bog using levelling measurements. They found that the forest had subsided by about 40-80 cm since planting and the subsidence rates were dependent on the cultivation and drainage treatment used.

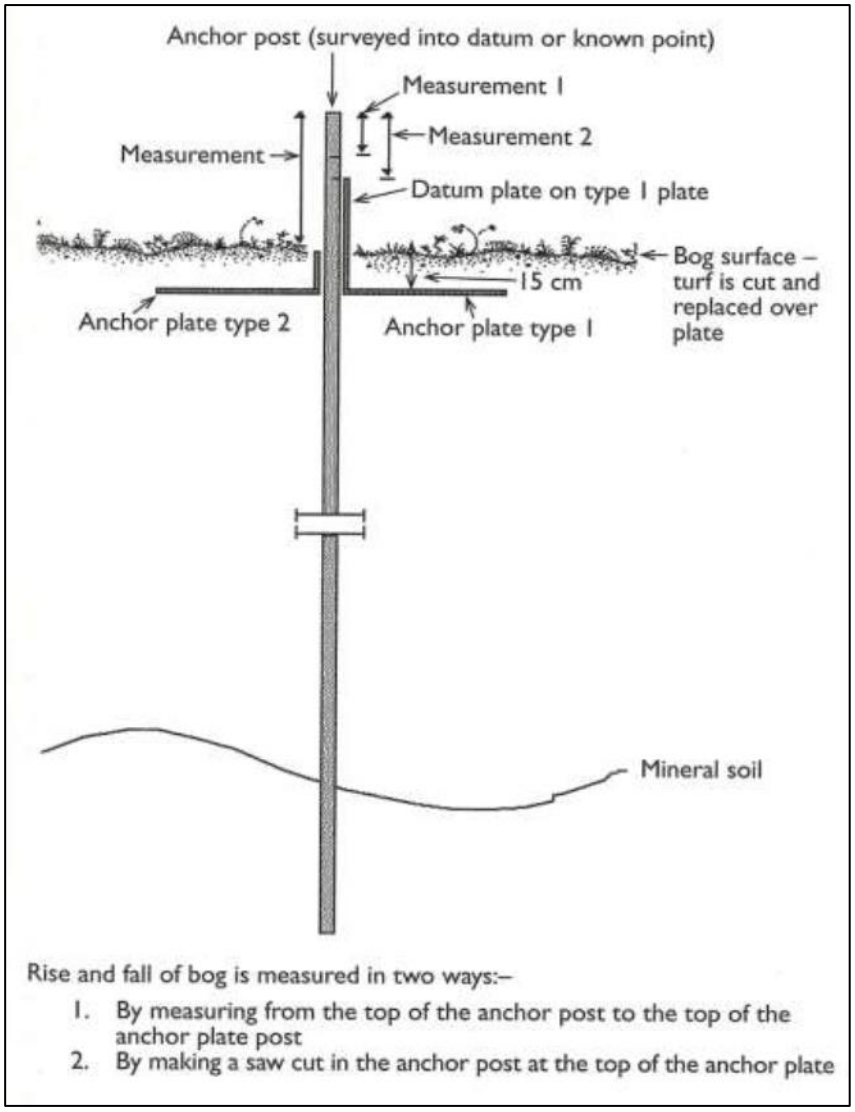


Figure 3.3: Detailed design of the of the anchor posts used to measure the rise and fall of bog adapted from Bonnett et al. (2009).

Such methods are expensive, and many wetland areas are situated in remote locations. Therefore, it is practical to use field measurements to monitor only a small subset of the world's peatland, however, this may affect the peat during the installation of the instruments.

To complement what can be learned from field measurements, broader scale information is needed to assess regional, national and global context. In this regard, remote monitoring of peatlands represents an attractive method because it is comparatively economical and can provide information over a large range of scales (Kuenzer et al., 2011; Euliss et al., 2014).

For assessing peatland habitats, Lidar remote sensing (Light Detection and Ranging) is becoming increasingly used for describing peatlands, identifying suitable areas for restoration and subsequent monitoring (Bonnett et al., 2009). Although this technique is relatively expensive and needs some technical input and data processing, it has several advantages, such as that it can generate a detailed elevation map for the peat surface that coveres large areas at a high spatial resolution and, with an accurate interpretation, huge information can be derived to assist both restoration and monitoring strategies. Milton et al. (2005) suggested that Lidar remote sensing technique can be a highly effective method in surveying the surface of degraded peatland, due to its sufficient vertical resolution that can detect a very subtle change in relief. The disturbance over peatland areas can also be detected from other remote sensing techniques such as aerial photography and satellite imagery (Bonnett et al., 2009). It would be possible to map the extent of the peat surface using satellite data such as IKONOS, Landsat ETM+, SPOT and from another system (Milton et al., 2005). However, more focus has been invested in remote sensing research of coastal wetlands than inland wetlands (Ozesmi and Bauer, 2002; Yang, 2005; Klemas, 2011; Klemas, 2013a; Klemas, 2013b).

Synthetic Aperture radar has also been used to monitor and map wetlands in general (Romshoo, 2004; Englhart et al., 2011). SAR microwave energy is very sensitive to soil moisture variations and is partially attenuated by vegetation, particularly in lower biomass areas (Kasischke and BourgeauChavez, 1997; Baghdadi, 2001; Lang and Kasischke, 2008). These capabilities of SAR make it ideal for detection and identification of hydrological features below vegetation canopies (Kasischke and BourgeauChavez, 1997; Wilson and Rashid, 2005).

Although, remote sensing techniques offer cost effective methods for mapping and monitoring large areas with a myriad of land cover classes and peat depths, it remains difficult to map these areas remotely with sufficient levels of accuracy and consistency for monitoring change (e.g., Rover et al., 2010; Wickham et al., 2010; Brisco et al., 2013; Wickham et al., 2013; Brisco et al., 2014).

3.9 Difficulty in monitoring peatland areas

There are several factors that make it hard to map and monitor peatlands remotely. The first and the primary factor is that peatlands are not unified to a common land cover type (**Figure 3.4**). Moreover, all peatland areas are wetlands and share the characteristic of water presence, which can be at the Earth's surface or below the plants in the rooting zone. This water may be present at all times of the year or seasonally, but is present enough of the time to influence the

development of soil and assist vegetation composition and adapt to the wet conditions (Mitsch and Gosselink, 1993).

The second factor that makes the monitoring of peatlands using remote sensing techniques so challenging is that peatlands are highly dynamic in ways that alter entirely their reflectance and backscatter properties (Kasischke et al., 2003; Kaasalainen et al., 2010; Ollinger, 2011; Gallant et al., 2014) and sometimes this happens within hours or days (Refice et al., 2014; Ticehurst et al., 2014). Individual species at their various developmental stages in the growing season can exhibit significant variation in energy response (Adam et al., 2010; Gallant et al., 2014). Also, the density of vegetation coverage alters the backscatter energy response that is received by satellite sensors (Refice et al., 2014). Water table depth has a strong control on peatland areas and any change in water table affects the abundance of species and the vegetation composition (Valk, 2005; Fritz et al., 2008; Holden et al., 2011). The depths of the water table can be rapidly changed from storm surges, precipitation events and snowmelt. The depth of the water table influences the establishment of different plant species, based on their respective tolerance to flooding and altered water chemistry (Euliss et al., 2014). Climatic change in some regions can be relatively frequent which causes fluctuations in the water table (e.g., Valk, 2005) and assists the establishment of different species in different years, as fed by the local seed bank stored from the past climatic cycles (Euliss et al., 2004). Land use and land management in the contributing watershed have an impact on the amount and the quality of peatland water and the type of aquatic vegetation (Gleason et al., 2003; Hidding et al., 2014; Price et al., 2016). Runoff from surrounding uplands can change the color of the water through transport of sediment or nutrient and chemicals that affect the growth of peatland habitats (e.g., Trebitz et al., 2011). Conversely, water stress that causes by drying of peatland can change the optical properties of the leaf (Adam et al., 2010) and, at some point, the structural properties that in turn affect the backscattered energy.

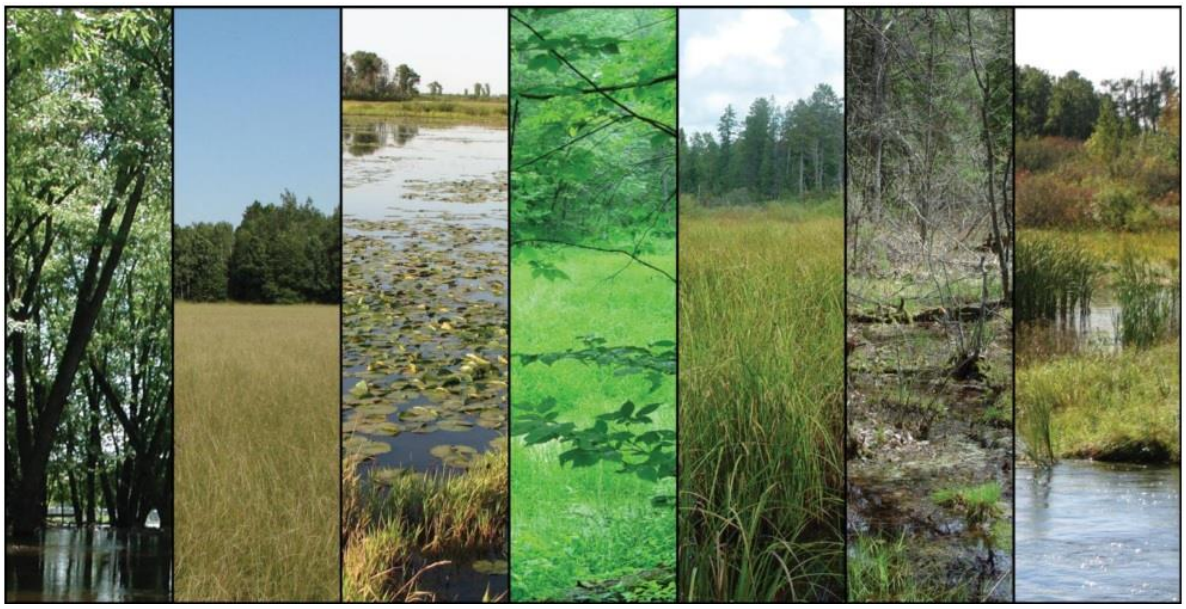


Figure 3.4: The variation in peatland surface features, coupled with dynamic conditions in water availability and vegetation development, make peatland, particularly difficult to monitor and map remotely with the required accuracy and consistency. Adapted from Gallant (2015).

The third factor is that peatland areas have steep environmental gradients which produce narrow ecotones (Adam et al., 2010) that are often smaller than the spatial resolving capacity of remote sensors. Sharp contrast in the characteristics of backscattered energy from both water and land areas can be exploited to assist mapping in some peatland settings (e.g., Wright and Gallant, 2007; White et al., 2014), however, the boundaries between vegetation types may be too tight to be distinguished using satellite remote sensors (Adam et al., 2010).

Peatlands, therefore, are a 'moving target, 'from the remote sensing perspective representing a moisture regime more than a land cover type (Gallant, 2015). Interrelation among peatland dynamics and land cover types and conditions results in a large variation of energy responses that make it highly challenging to map using specific remote sensing techniques with the levels of accuracy and consistency adequate for monitoring.

3.10 The use of InSAR for deformation monitoring

Interferometric Synthetic Aperture Radar remote sensing, on the other hand, represents an interferometric technique linked with Synthetic Aperture Radar (SAR). Therefore, it has inherited advantages from SAR, such as the capability to operate in day and night, and in different weather conditions.

Although the InSAR technique can be used to estimate the topography (e.g., Farr et al., 2007), atmospheric modelling (e.g., Hanssen, 1999), or for the detection of sub-surface features (e.g., McCauley et al., 1982; Elachi et al., 1984; Morrison et al., 2013), this technique is most widely used to detect the deformation of the earth's surface. Since the late 1980s, the InSAR technique has been used to evaluate ground stability and has proven its capability to detect small ground motions on the order of centimeters and even millimeters. It uses a differential technique, which achieved prominence when the images were used before and after the Landers earthquake to reveal the spatial distribution of deformation that occurred in that event (Massonnet et al., 1993). More recently, advanced time series approaches have come to prominence involve the processing of many radar images acquired over a long period of time (several years or even decades) to monitor the subtle changes to the Earth's surface (Ferretti et al., 2001; Berardino et al., 2002).

Chaussard et al. (2014) utilized over 600 ALOS PALSAR images from 15 ascending tracks for the period 2007 to 2011 to investigate the land subsidence in Mexico. They identified the land subsidence in 21 areas in central Mexico. The correlation between the land subsidence and land use confirms that the cause of subsidence is mainly due to ground water extraction for agriculture and urban activities. Different SAR sensors by other researchers have also been used to investigate the land subsidence over the same area, such as RADARSAT-2 (e.g., Geudtner, 2014; Lanari et al., 2015), ENVISAT (e.g., Cabral-Cano et al., 2010; Cigna et al., 2011; Osmanoglu et al., 2011; Yan et al., 2012), and Sentinel 1 (Sowter et al., 2016; Wegnüller et al., 2016). Ge et al. (2014) conducted the same research over the Bandung Basin, Indonesia to map the land subsidence for the period 2002 to 2011. They used two data sets: 24 ALOS PALSAR for the period 2002 to 2008, and 30 ENVISAT ASAR for the period 2007 to 2011. The results from independent analysis illustrated good agreement and suggested steady land subsidence in many areas of the basin, which was mainly due to excessive extraction of groundwater and soil consolidation caused by surficial loading. A good correlation was also observed with the annual record of ground water extraction as well as GPS data collected for the period 2002 to 2010.

Schlogel et al. (2015) investigated the potential use of L-band ALOS PALSAR to analyze the deformation of a rapid and large landslide in South East France. Although there was limited availability of SAR data, they found very consistence results in comparison with ground-based measurement (GPS and DEM) and remote results estimated from C and X band satellite SAR sensors. However, they expected better results to be achived with larger datasets

as it will allow the investigation of the evolution of the landslide over a long period and estimation of the relationship with controlling meteorological factors with high accuracy. Likewise, Sun et al. (2015) utilized 16 L-band ALOS PALSAR scenes acquired between January 2007 and June 2010 to study the slow-moving of landslides in Zhougu, China, before a major destructive mudslide on 8 August 2010. Generally, they found good agreement with the field observations regarding the locations and extents of the landslides and demonstrated that the multi-temporal InSAR technique and L-band SAR data could be used to measure the slow-moving landslide adequately in most of the area.

Tang et al. (2016) used 20 scenes of COSMO-SkyMed data to assess the deformation of the World Heritage Site of the Summer Palace in Beijing. They found that multi-temporal InSAR techniques are very suitable to monitor cultural heritage sites because they are not invasive like some other traditional techniques; for example, electrical sensors should be installed in structures for data acquisition. Also, InSAR techniques can provide deformation maps with high spatial and temporal coverages which are suitable to monitor and detect the deformation of structures as well as their surroundings. This assists in the early identification of the potential risks and enables effective planning for conservation of these sites. The techniques are also inexpensive and work better in detecting subtle change due to the high precision (up to mm accuracy). InSAR also has a proven capability to investigate complex deformation (Yang et al., 2016). The cross correlation between regional ground subsidence, underground water level and fault activity have been analyzed over Linfen- Yuncheng Basin, China using 8 Envisat ASAR images acquired between February 2009 to October 2010 and processed using StaMPS technique (Hooper et al., 2004; Hooper, 2008).

Most InSAR Techniques have been limited to urban and bare/rocky land cover types due to the fact that these techniques require pixels to display high coherence consistently over a long period. Consequently, this almost completely precludes the detection and interpretation of subsidence (and indeed surface uplift) over rural and vegetated areas, as vegetation cover, almost by definition, exhibits highly variable coherence due to changes over seasonal cycles and diffuse scattering of the radar signal. Therefore, some techniques have been developed specifically to address this limitation, such as SqueeSAR (Ferretti et al., 2011), and Intermittent Small Base Line Subset (Sowter et al., 2013; Bateson et al., 2015). The latter technique was developed in-house at Nottingham University and appears particularly well suited to monitor low-resolution, broad area deformation over a broad range of land cover classes, including forested areas, agriculture and grasslands (Cigna et al., 2014; Sowter et al., 2016). Such

temporal decorrelation has been addressed by Milillo et al. (2015) by analyzing a X-band COSMO-SkyMed dataset using short repeat-pass interferometry over the rural and vegetated area in the southern part of Italy. With such a technique, they found 180% improvement in usable pixels, which allowed them to extend the spatial coverage and highlight the important features related to the areas subjected to landslide activity. Also, they concluded that short repeat-pass interferometry permits the measurement of seasonal dynamics deformation.

With the new mission of Sentinel-1, a new exciting opportunity has been offered for InSAR studies. The mission consists of two satellites: Sentinel-1A was launched on 3 April 2014, and Sentinel-1 B was launched on 25 April 2016. The data for an interferometric wide (IW) images is collected using the novel Terrian Observation with Progressive Scans (TOPS) SAR imaging mode (Holzner and Bamler, 2002; Yague-Martinez et al., 2016), which poses some challenges to the processing of the interferometry, mainly related to the preparation of IW images and then their co-registration processes. The required accuracy of co-registration for Sentinel-1 TOPS InSAR is one thousandth of one pixel (De Zan et al., 2014), which is more rigorous than other stripmap products, and thus it has the highest effect on the processing. Notwithstanding this, the Sentinel-1 satellites provide considerable benefits for long-term land motion monitoring and offer continuity to the C-band satellites of the ERS-1/2 and ENVISAT missions. Rapid deformation can be monitored and measured owing to regular acquisitions of Sentinel-1 with a short repeat cycle of only 12 days (by using one satellite in the constellation) (Torres et al., 2012), which is reduced to 6 days by using the two satellites in the constellation. Therefore, a significant stack of images can be collected in a much shorter time, which will be useful for routine long-term monitoring applications (Attema et al., 2010; De Zan et al., 2014). In addition, the large swath width of Sentinel-1 IW product, which is about 250 km, allows the monitoring of large areas with fewer acquisitions. A large swath width and a short revisit cycle mean that Sentinel-1 IW products can provide a very high level of support to routine, operational and monitoring applications (Sowter et al., 2016).

Despite the remarkable features of InSAR, its applications for monitoring peatland subsidence are relatively few, due to the decorrelation over these areas which represents the main limitation of InSAR (Zebker and Villasenor, 1992). Most InSAR studies focus on deforestation (Ribbes et al., 1997; Suga and Takeuchi, 2000; Deutscher et al., 2013) and ground biomass estimation (Santos et al., 2004; Morel et al., 2011; Basuki et al., 2013). Zhou et al. (2010) investigated the seasonal peatland surface fluctuation and long-term peatland subsidence over Flanders Moss, Britain using PS-InSAR technique. Two tracks of ENVISAT

ASAR images (seven images from both ascending and descending tracks) with C-band for the period April 2003 to July 2006 have been used for the analysis. For three small areas which, were chosen to investigate the evolution of the surface movement, they found that these areas subsided, but the rate of subsidence was greater when measured using the ascending track rather than the descending which may be due to the difference in the satellite geometries of these two tracks. In addition, they concluded that PS-InSAR could provide encouraging results to detect peatland surface fluctuation with comparable magnitude; however, the loss of coherence is proving challenging. To improve the coherence, they suggested using longer wavelength SAR images such as L-band JERS and ALOS data sets, and / or installing corner reflectors in the study area. Similarly, in 2016, the capability of InSAR using the SBAS technique has been reported to map and monitor peatland subsidence in Central Kalimantan, Indonesia using two independent ALOS L-band tracks SAR images for the period December 2006 to September 2010 (Zhou et al., 2016). Although there is a lack of ground truth data for validation, the correlation in output between two independent tracks provided confidence in the results and suggested that the surface subsidence over this area can be up to 7.65 cm/year due to the loss of stored C.

Most InSAR studies report limited spatial coverage in their study area due to the low coherence, as expected in peatlands. Although the result can improve with the use of additional SAR data sets, this option is not always feasible. Therefore, this research investigates the possibility of using the ISBAS technique, built in-house at Nottingham University, which offeres a potential way around this problem that might open up long-term peatland deformation monitoring and the evaluation of peat conditions.

3.11 Limitations summary

Taking into consideration, the review presented in the previous sections, the limitations summary can be outlined as follows:

- There is very little research using InSAR techniques for long-term peatland monitoring and this represents a clear gap in the research.
- Research involving the use of InSAR to evaluate peat condition for a long period is non-existent and requires investigation.
- Research involving the use of InSAR for long-term peatland monitoring in both coastal and inland areas is non-existent and likewise is ripe for study.

- ISBAS InSAR is a useful tool for studying ground motion over different land cover classes and so it warrants, further work and validation over peatland, as it may solve some of these challenges.

3.12 Summary

Peatlands represent a diverse group of ecosystems which exhibit a large variation in form and function. Therefore, the characteristics of peatland and its importance to many ecosystem services are outlined in this Chapter with a fundamental overview on peatland distribution, functions and its relationship with climate. In addition, the root causes of peatland degradation (subsidence) and their consequences are discussed. Various monitoring techniques over these areas are briefly reviewed, highlighting their advantages and their drawbacks. These include field surveys and remote sensing techniques such as aerial photographs, aerial Lidar, optical satellite images and radar images. Following that, an advancement in the field of renowned space-geodetic techniques (InSAR) is introduced, explaining its ability to measure the deformation with millimeter accuracy for coherent reflectors. This InSAR approach will be adapted in this study by using the ISBAS technique to monitor the deformation over less coherent peatland areas.

CHAPTER 4

THE STUDY SITES

This chapter discusses the choice of the study areas chosen as test areas for this research. The details relevant to each test site are discussed. This includes general information about the area, its topography, geology, hydrology, climate, the availability of SAR data and the ground data measurements.

4.1 Introduction

Peatlands represent the most important carbon storage in the world as they contain 30% of Earth's terrestrial carbon (Charman et al., 2008). Currently, peatlands are highly vulnerable to economic and societal pressure and change of climate (Kimmel and Mander, 2010) which causes their degradation. The degradation of peatland causes organic matter loss and erosion, which have a detrimental impact on water quality, flood regulation and carbon sequestration. It is essential, therefore, to be able to measure and monitor peat degradation in order to manage such consequences. Due to the large extent and relative inaccessibility of these areas, the feasibility of remote sensing techniques, particularly ISBAS DInSAR, has been examined in this study for long term peatland monitoring and evaluation of the peat conditions.

Through investigation of peatland areas particularly sensitive to perturbation in conjunction with the availability of SAR data, two peatland sites having different environments were selected for this research. Specifically, these sites were the Flow Country, Scotland (the largest expanse of blanket bogs in Europe) and Zennare basin in the south of Venice Lagoon, Italy (drained coastal peatland area). The following sections provide details of each chosen site and the reason for their selection.

4.2 Flow Country

Flow Country of Caithness and Sutherland, Northern Scotland, UK is the largest expanse of blanket bog in Europe (Lindsay, 1987; Shotbolt et al., 1998; Holden, 2005) covering about 4,000 Km^2 (**Figure 4.1**). This area represents a complex ecosystem where it is covered with a deep layer of peat (**Appendix A**, **Figure A1**). The surface of this peaty area is mostly a spongy mass, with a living layer of *Sphagnum* bog-moss which continuously constructs its level higher through upward growth; however, in many places it is thrown into strange and distinctive patterns by large groups of small peaty pools (Lindsay et al., 1988). Numerous large lochs also

exist in this area, some of them mainly peaty but some with stony or sandy margins and many streams with different size and character drain the moorlands. The combination of two essential conditions (suitability of climate and topography) has assisted the extreme development of blanket bog over this area. The extensive occurrence of blanket bogs combined with the availability of the sufficiently large SAR datasets essential for this study make this area suitable to investigate the feasibility of using Interferometric SAR for long-term deformation monitoring and in turn to evaluate peat condition.

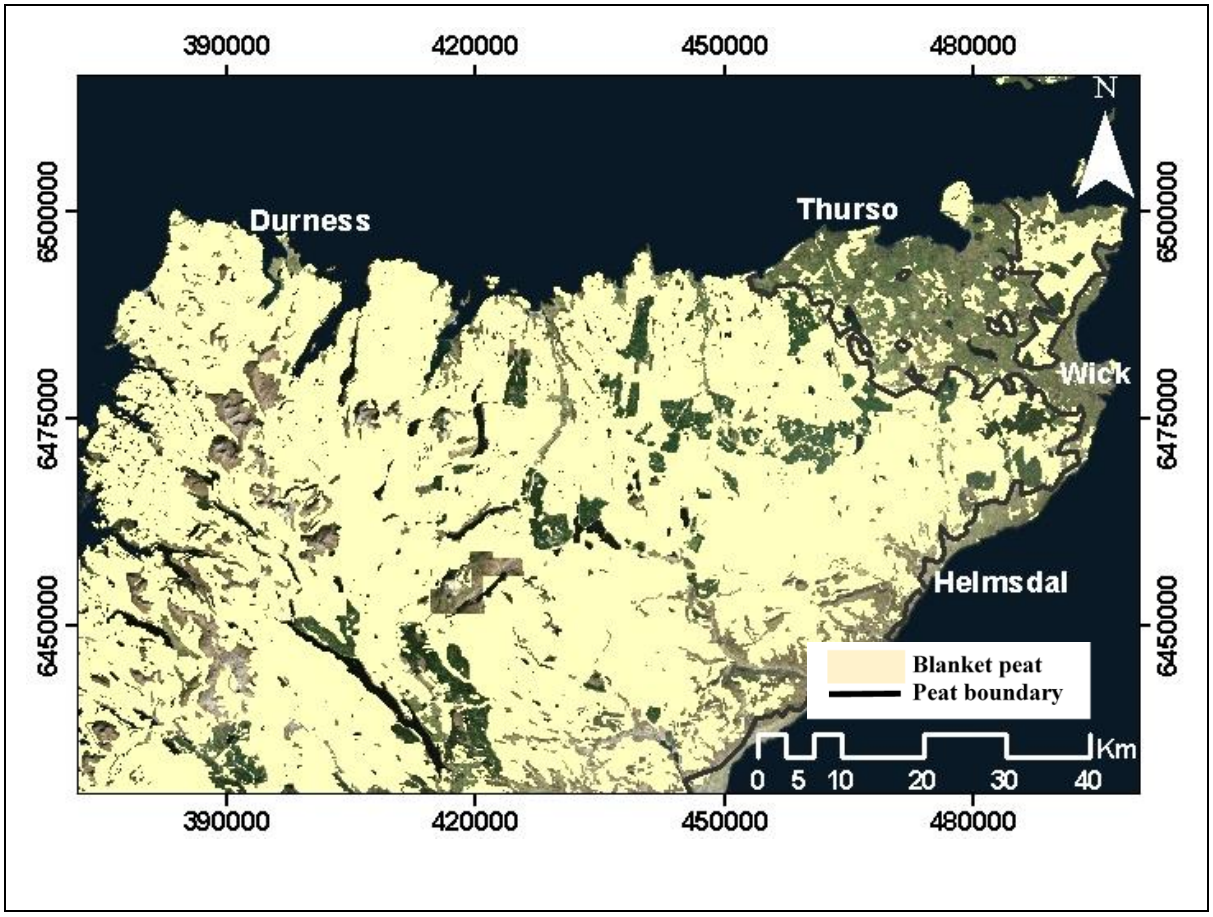


Figure 4.1: The distribution of blanket peat in the Flow Country of Caithness and Sutherland, adapted from (Bruneau and Johnson, 2014). Projection: WGS_1984_UTM_Zone 30

4.2.1 Topography and geology

The Flow Country is characterized by the extreme development of blanket bogs. The key feature of the eastern half of the region (Caithness) is the large extent of gently contoured low land or mostly flat upland (**Figure 4.2**). Sutherland also has a great expanse of such ground in the eastern part, but to the west, the undulating moorlands are increasingly interrupted with

high mountain peaks and ranges until breaking down to an Atlantic coastal region with rugged low ancient foreland (Lindsay et al., 1988; McKirdy and Crofts, 1999).

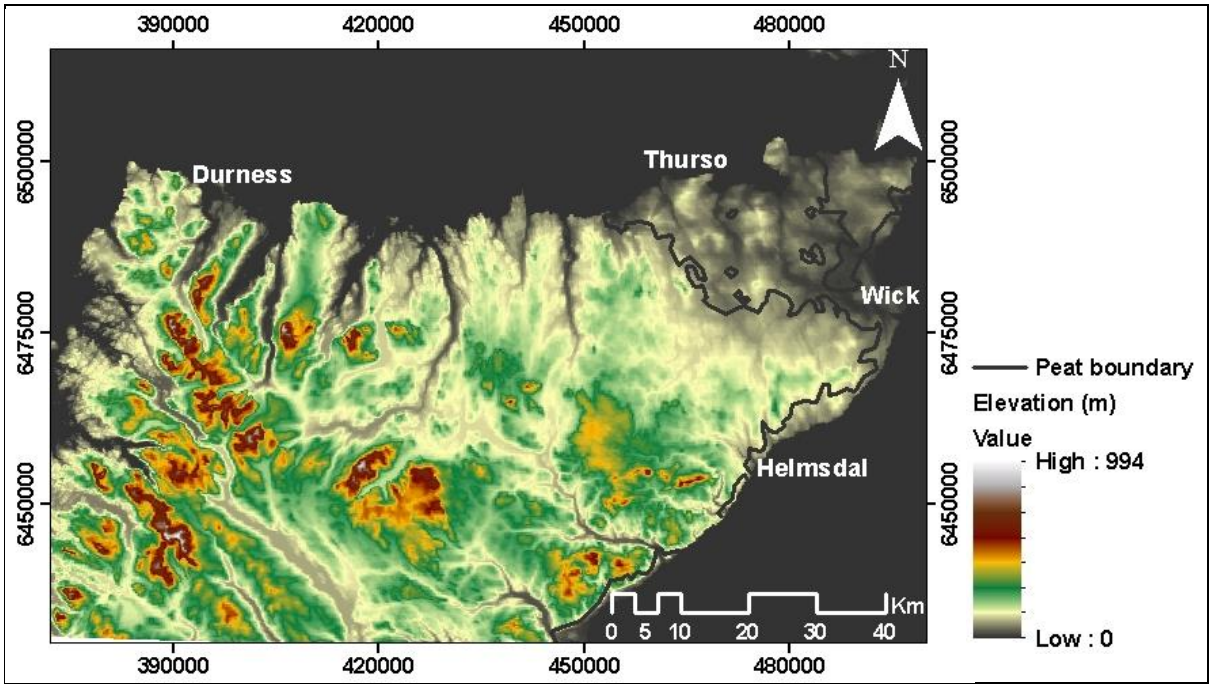


Figure 4.2: A map showing the elevation of the Flow Country (Digital Elevation Model from SRTM at 30 m resolution). Projection: WGS_1984_UTM_Zone 30.

It can be seen from the simplified geological map of the Flow Country of Caithness and Sutherland (**Figure 4.3**) that the geological changes run in an east west direction. However, blanket bogs are found over all areas and are not confined to specific rock formations. The largest areas of blanket bog extend over the Old Red Sandstone of Caithness, the granitic intrusion along the boundary of Caithness and Sutherland, and approximately cover half of the Moine Granulites and Schists of Sutherland (Lindsay et al., 1988).

For the Eastern part of Caithness, the low moorland and coastal plain are formed over the Old Red Sandstone, which is covering most of the region, and the calcareous shell material represents the main element of the drift deposits in this area, brought in from the east at the last glaciation. Further west, the boulder clay is more sandy and free of lime. This geological variation and gentle elevation provide good quality land for agricultural use (Futty and Towers, 1982), with much of this land being covered in peat. However, for more than a millennium of human habitation, this land has been cut and reclaimed. Apart from this, most of Caithness is covered with a large and almost continuous expanse of peat.

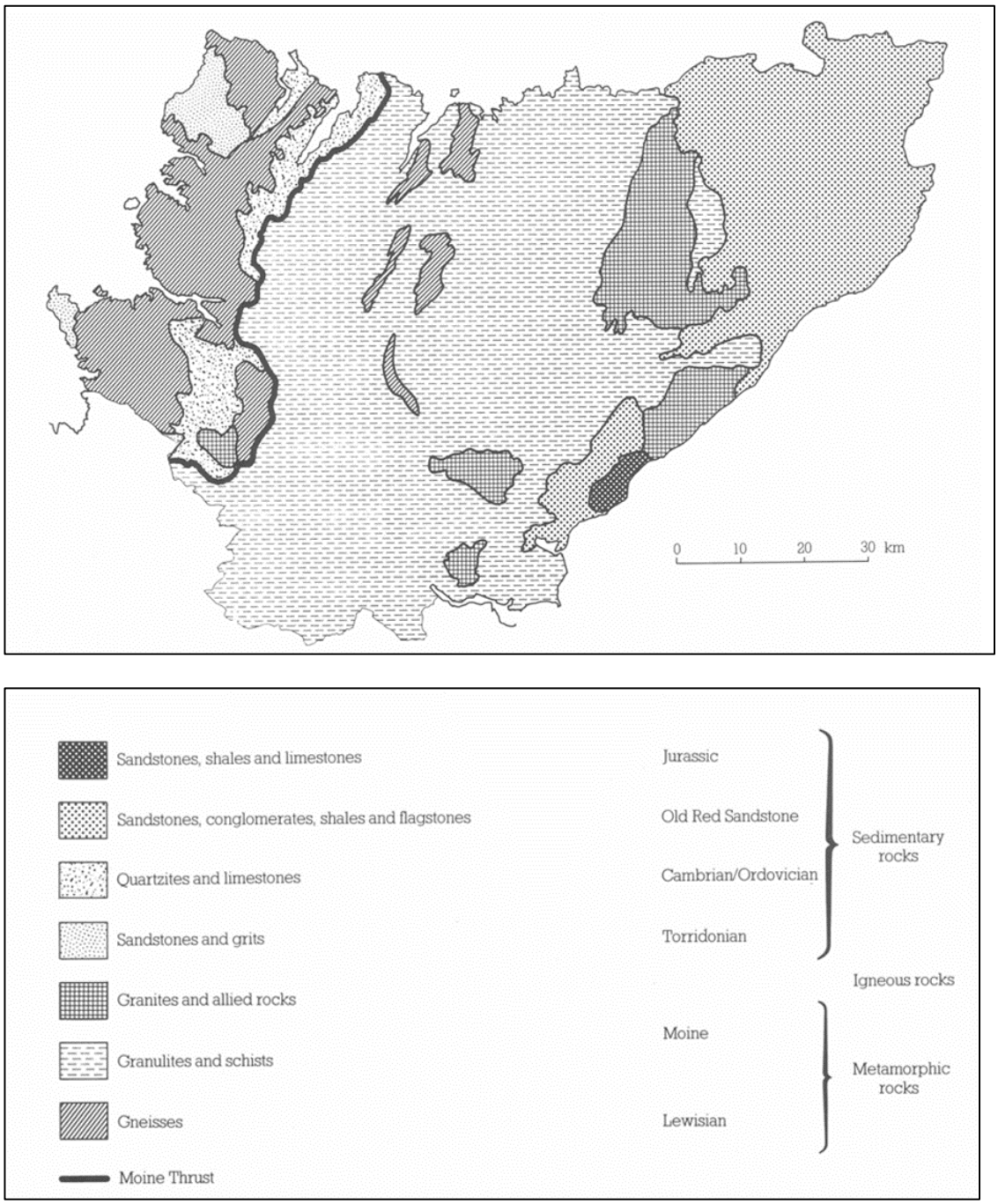


Figure 4.3: The geological map of the Flow Country (Caithness and Sutherland). Adapted from (Lindsay et al., 1988).

The Moine granulites and schists form most of the central part of the Flow Country. The terrain of this section, particularly in the eastern half, is a series of low summits less than 650m. Between the hills there is gentle sloping ground covered with different size of water bodies, most of them lying over a large extent of peat, which covers much of this landscape. The same occurs in Caithness, the gentle gradient of the topography assisting the large areas

of peat to develop. Westwards, many high upland massifs rise above the general level of the plain, but these peaks occur as isolated landmarks within an otherwise almost level and waterlogged landscape (Lindsay et al., 1988).

To the west, the high continuous steep and rugged massifs with the variable composition of Moine rock, Cambrian quartzites and Lewisian gneiss create an extensive break in the development of peatland, though there are small areas of peat bogs distributed there. This variability in topography and underlying geology provide an extremely variable development of blanket bogs.

4.2.2 Climate

Climate is of the highest importance in the development of blanket bog. In the Flow Country of Caithness and Sutherland, the combination of regular and high amounts of precipitation, high humidity in the atmosphere and the relatively cool mean temperature suggests that the climate of the whole area is suitable for the development of blanket bog (Lindsay et al., 1988; Lindsay 2010).

The predominant westerly airstreams from the Atlantic impose a climatic gradient in terms of wetness from west to east. The western mountainous part of Sutherland produces very high rainfall, which is up to 2500mm, and then the rainfall decreases eastwards so that the precipitation falls to 1200 mm in the centre of Sutherland and is only 700 mm at north-east of Caithness.

Although the heaviest rainfall occurs in the high mountain topography (west Sutherland), it has the least extent of blanket bogs. Broad scale development of blanket bog occurs in the eastern part of Sutherland and Caithness under lower rainfall but optimal topography and geology (Lindsay et al., 1988). Therefore, the suitability of both climate and topography is essential in the development of blanket bogs. This research is focused on the eastern part of the Flow Country (Caithness and east of Sutherland) due to the extensive occurrence of blanket bogs there.

4.2.3 Hydrology and ecology

In intact blanket peatlands, the living vegetation protects the peatland surface from weathering and erosion and assists the process of peat accumulation (Parry et al., 2014). Both hydrology and ecology of blanket peatland are closely related to each other and they represent essential components to infer the development and condition of blanket peat. Blanket peatlands are

ombrotrophic, which means that they receive their water and nutrients solely from precipitation (Charman et al., 2008). The flow production on blanket peatland is dominated by saturation-excess overland flow or very shallow throughflow, resulting in flashy stream hydrographs, whereas the deeper peat layer of low hydraulic conductivity holds the remaining water within the peat, resulting in minimal baseflow provision (Holden and Burt, 2002; Parry et al., 2014). Networks of micropores (Holden, 2009) and pipes can also assist the rapid movement of water through the peat profile (Holden and Burt, 2002). Hydrological conditions, for example water table and stream velocity are variable due to the varying topography (Holden et al., 2006). The vegetation of blanket peatland tends to be dominated by *sphagnum*, sedges and dwarf shrubs which are adapted to waterlogged and nutrient-poor conditions (Parry et al., 2014). The vegetation communities of blanket peatland are sensitively adapted to small scale hydrological niches and this variation together with auto-genic processes results in the zooming of peatland vegetation (Lindsay 2010). Species over peatland areas have varying resistance to decay and sensitivity to change. Consequently, the interaction between both hydrology and ecology controls the both development of peatland and its sensitivity to change and degrade (Belyea and Clymo, 2001).

4.2.4 Deformation in Flow Country

As discussed earlier (**Chapter 3, Section 3.6**), peatlands can be deformed or changed in a number of ways and to varying degrees. The primary drivers causing change in these areas are drainage, managed burning, wildfire, atmospheric deposition, agriculture, afforestation and peat extraction (Parry et al., 2014). These drivers can alter the vegetation composition and cause a reduction in the cover of *Sphagnum.* The loss of *Sphagnum* can alter the natural hydrology by lowering the water tables and losing of microtopography and patterning (Evans et al., 1999; Holden et al., 2008). The peat in some areas of the Flow Country was damaged between 1979 and 1987 through the planting of non-native conifer forests and the cutting of thousands of miles of drains. Drains permit the rapid diversion of water off site by intercepting overland flow and increasing drainage density which has been linked to enhancing the risk of flooding. Stewart and Lance (1991) provided clear evidence of reduced water tables within a few meters of drains. Therefore, drainage can result in considerable drying of the peat, where a small reduction in the water table of just a few centimetres can lead to a dramatic effect on bog vegetation (Robroek et al., 2007) and increase GHGs emission. **Figure 4.4** illustrates the effect of drainage on active peat bogs, which causes large areas of peat surface layer to be emptied of water. Subsequent falls of the water table can have an extreme impact on the

vegetation causing a switch from *Sphagnum* dominated to shrubs and grasses (Tallis, 1998; Evans et al., 1999; Charman 2002; Robroek et al., 2007; Lindsay 2010). These drivers of change over peatlands were considered worthy of note when considering potential areas of ground motion that may be visible in InSAR studies. **Figure A2** in **Appendix A** illustrates three examples of degraded peatland due to moor-grips, erosion and peatslide.

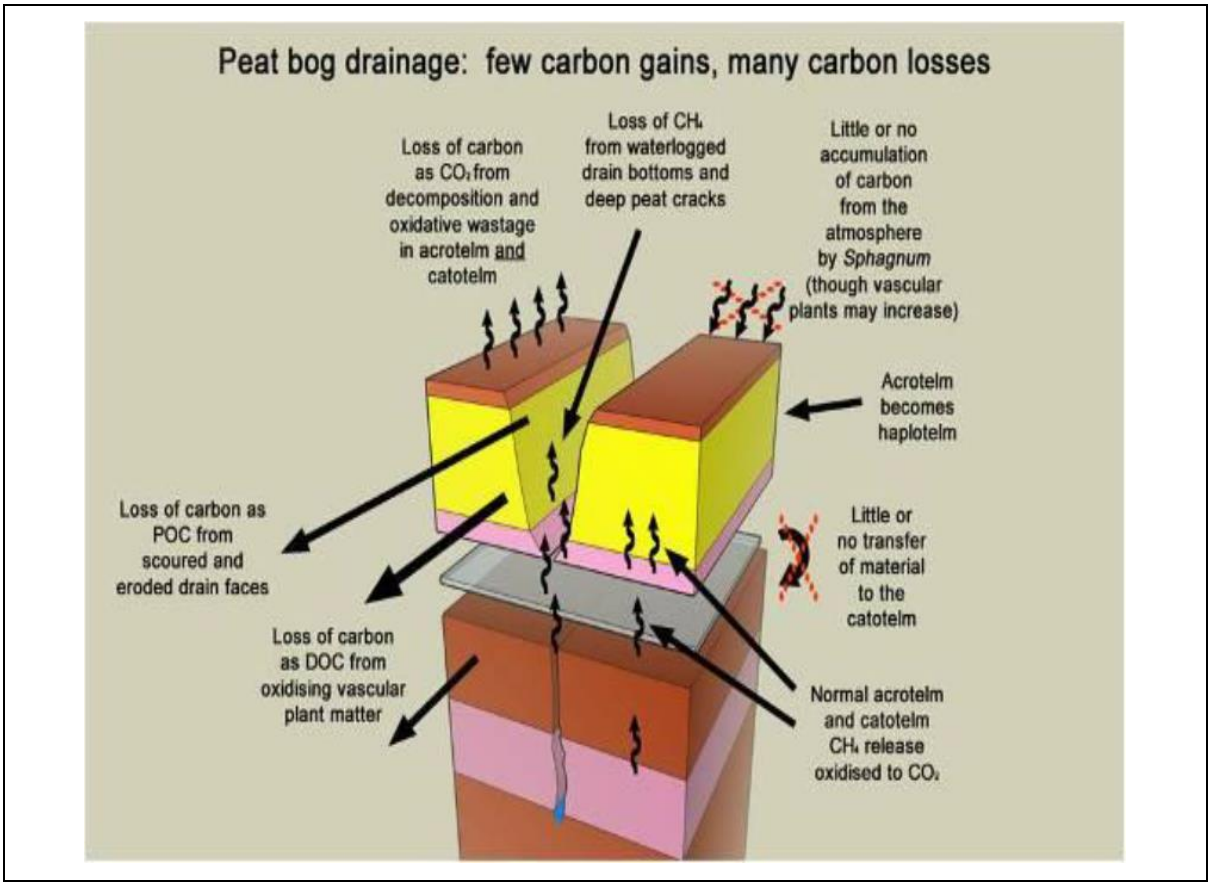


Figure 4.4: Cross section of degraded blanket bog illustrates the amount of carbon losses due to the drainage channel. Reduction of water table causes oxidative of peat layer and loss of carbon. Adapted from (Lindsay 2010).

4.2.5 List of data sources

In the past, long-term deformation monitoring studies over the Flow Country were hindered by the lack of data due to the significant cost involved to carry out a continuous measurement over such a large area. InSAR techniques open new possibilities for such kind of monitoring owing to the long record of SAR images acquired over the past years by different platforms. Evaluation of the deformation over long periods in the Flow Country is made possible as a consequence of this data availability. The InSAR technique is very useful to investigate the

deformation at landscape scales and as such makes it an ideal candidate to explore for the assessment of the deformation in Flow Country. Ground data such as land cover and field measurements of surface motion such as levelling, as well as water table depth which had been collected concurrently to the SAR data, are used to validate InSAR results as appropriate.

4.2.5.1 SAR dataset

Remotely sensed data from two SAR satellite systems were used in this research, namely European Remote Sensing Satellite (ERS) 1/2, and Sentinel 1A. These satellites operate in C-band frequency with approximately 5.6 cm wavelength. ENVISAT data have not been used in the analysis due to the lack of the archived data.

4.2.5.1.1 ERS dataset

The ERS satellite represents the first program in the European Space Agency (ESA) for Earth observation to provide environmental monitoring in the microwave spectrum. Two ERS satellites, i.e., ERS-1 and ERS-2, were launched in 1991 and 1995 respectively into the same orbit at an altitude of approximately 785 km. The payloads of these satellites consisted of synthetic aperture radar imaging, radar altimeter and other instruments for measuring ocean surface temperature and wind fields. Moreover, ERS-2 has additional sensors for monitoring the atmosphere and ozone. The standard operational mode of these satellites provided a 35-day repeat orbit. The mission of the ERS-1 satellite ended on March 2000 due to the failure of the control system for onboard altitude, whereas, the mission of ERS-2 ended on September 2011 after the altitude of the satellite lowered to approximately 573 km. More information about ERS 1/2 satellites is available at the ESA website: *https://earth.esa.int/web/sppa/mission-performance/esa-missions* (accessed on 28.02.2018).

The availability of ERS 1/2 data over the study area can be identified using the Eoli-SA software. This software is a catalogue to help the users to browse the metadata and preview the earth observation data acquired by different satellites, such as ERS, ENVISAT, ALOS, Landsat, IKONOS, SPOT, Kompsat, DMC, Proba, IRS, and SCISAT. Users with a registered account can order and download their products at various processing levels, depending only on their submission of a short proposal.

Table 4.1 illustrated the category-1 (Cat-1) proposal submitted to ESA for ERS 1/2 data acquisition over Flow Country. The proposal was presented to acquire fifty-one ERS 1/2 images in descending orbit in track 495. The requested data in the proposal cover the period from 1 May 1992 to 04 December 2000.

Table 4.1: List of the proposal submitted to ESA for ERS 1/2 data acquisition over Flow Country.

Project ID 32049: Monitoring eroding extent of peatland surface over Flow Country using ISBAS DInSAR technique								
No.	**Mission**	**Date**	**No.**	**Mission**	**Date**	**No.**	**Mission**	**Date**
1	ERS-1	01/05/1992	**19**	ERS-1	24/03/1996	**37**	ERS-2	04/05/1998
2	ERS-1	05/06/1992	**20**	ERS-2	29/04/1996	**38**	ERS-2	08/06/1998
3	ERS-1	23/10/1992	**21**	ERS-2	12/08/1996	**39**	ERS-2	13/07/1998
4	ERS-1	27/11/1992	**22**	ERS-2	16/09/1996	**40**	ERS-2	17/08/1998
5	ERS-1	05/02/1993	**23**	ERS-2	21/10/1996	**41**	ERS-2	21/09/1998
6	ERS-1	12/03/1993	**24**	ERS-2	25/11/1996	**42**	ERS-2	04/01/1999
7	ERS-1	16/04/1993	**25**	ERS-2	30/12/1996	**43**	ERS-2	06/09/1999
8	ERS-1	25/06/1993	**26**	ERS-2	03/02/1997	**44**	ERS-2	11/10/1999
9	ERS-1	09/04/1995	**27**	ERS-2	10/03/1997	**45**	ERS-2	15/11/1999
10	ERS-1	18/06/1995	**28**	ERS-2	14/04/1997	**46**	ERS-2	20/12/1999
11	ERS-2	19/06/1995	**29**	ERS-2	19/05/1997	**47**	ERS-2	28/02/2000
12	ERS-2	24/07/1995	**30**	ERS-2	23/06/1997	**48**	ERS-2	03/04/2000
13	ERS-1	27/08/1995	**31**	ERS-2	28/07/1997	**49**	ERS-2	12/06/2000
14	ERS-2	28/08/1995	**32**	ERS-2	01/09/1997	**50**	ERS-2	17/07/2000
15	ERS-1	01/10/1995	**33**	ERS-2	06/10/1997	**51**	ERS-2	04/12/2000
16	ERS-2	02/10/1995	**34**	ERS-2	10/11/1997			
17	ERS-2	11/12/1995	**35**	ERS-2	15/12/1997			
18	ERS-2	19/02/1996	**36**	ERS-2	19/01/1998			

4.2.5.1.2 Sentinel-1 dataset

The Sentinel-1 satellite belongs to the family of Sentinel satellites (**Table 4.2**) that were developed to provide for the specific needs of the Copernicus programme. This programme is headed by the European Commission and aims to collect information to improve environmental management, climate change assessment and civil security. The Sentinel-1 mission comprises of two satellites, the first satellite in the constellation is Sentinel-1 A which launched on 03 April 2014, and the second satellite is Sentinel-1 B which launched on 25 April 2016. Both Sentinel-1 satellites were placed in a near-polar, Sun-synchronous orbit at approximately 693km altitude, and operate in the C-band frequency at 5.405 GHz. The repeat cycle for one

satellite in the constellation is 12 days and this was reduced to 6 days with the launch of the second satellite. The expected lifespan of the satellites is 7 years, with consumables for 12 years.

Table 4.2: Sentinel satellites with a brief description of their mission objectives. Adapted from *http://www.copernicus.eu/main/sentinels* (accessed on 01.03.2018).

Satellite	Brief description
Sentinel-1	Sentinel-1provides all-weather, day-and-night radar imagery for land and ocean services.
Sentinel-2	Sentinel-2 provides high-resolution optical imagery for land monitoring, for example, the vegetation imagery, soil and water cover, inland waterways and coastal areas. Also, it can deliver information for emergency services.
Sentinel-3	Sentinel-3 provides optical, radar and altimetry data with high-accuracy by measuring the variables such as sea-surface topography, sea- and land-surface temperature, ocean colour and land colour with high-end accuracy and reliability. This will support ocean forecasting systems, environmental monitoring and climate monitoring as well.
Sentinel-4	Sentinel-4 payload devoted to assisting atmospheric composition monitoring that will be embarked on a Meteosat Third Generation-Sounder (MTG-S) satellite.
Sentinel-5	Sentinel-5 payload will monitor the atmosphereic composition from a MetOp Second Generation satellite.
Sentinel-5 Precursor	Sentinel-5P is developed to reduce the gap in the data until the launch of Sentinel-5. This mission will be dedicated to atmospheric monitoring.
Sentinel-6	Sentinel-6 provides high accuracy altimetry for measuring global sea-surface height, primarily for operational oceanography and for climate studies.

The Sentinel-1 satellite mission is designed to provide continuity of C-band SAR images after both ERS 1/2 and ENVISAT satellites, which offer several advantages for monitoring the deformation. Moreover, with Sentinel-1 satellites, more rapid deformation rates can be monitored due to the shorter repeat cycle (Torres et al., 2012). As a result, there is a possibility to gather a sufficient stack of images within a shorter time (Attema et al., 2010; De Zan et al., 2014) which will help for routine long-term monitoring applications. In addition, the large swath width of the IW product, which is approximately 250 km, permits monitoring a large area with fewer acquisitions. The IW product represents the primary mode of Sentinel-1 satellites over land. **Table 4.3** illustrates some basic specifications of IW product. More

information about Sentinel-1 satellites can be found on the ESA website, as follows: *https://sentinels.copernicus.eu/web/sentinel/missions/sentinel-1* (accessed on 01.03.2018). This research provides the first evaluation of the feasibility of Sentinel-1 for monitoring the deformation over peatland areas.

Table 4.3: The basic specification of Sentinel -1 interferometric wide (IW)single look complex product (SLC)

Spatial Resolution	5m (ground range) x 20m (azimuth)
Pixel Spacing	2.3m (slant range) x 14.1m (azimuth)
Incidence Angle	29° - 46°
Polarisations	HH+HV, VH+VV, HH, VV
Total Swath Width	250km

Contradictory to ERS 1/2 and ENVISAT, Sentinel-1 data are freely available for the users without any requirement for the submission of a proposal. The data can be gathered from Sentinel Scientific Data Hub (**Figure 4.5**). Over the Flow Country, 47 images acquired from satellite A in ascending orbit for the period between 12 March 2015 to 7 December 2016 were used in the processing. The images are separated by 12 days intervals, and seven images are missing from the Sentinel-1 Scientific Data Hub, i.e., 03.08.2015, 14.10.2015, 26.10.2015, 07.11.2015, 06.03.2016, 18.03.2016, 22.06.2016. The list of the available Sentinel-1 data is summarised in **Table 4.4**.

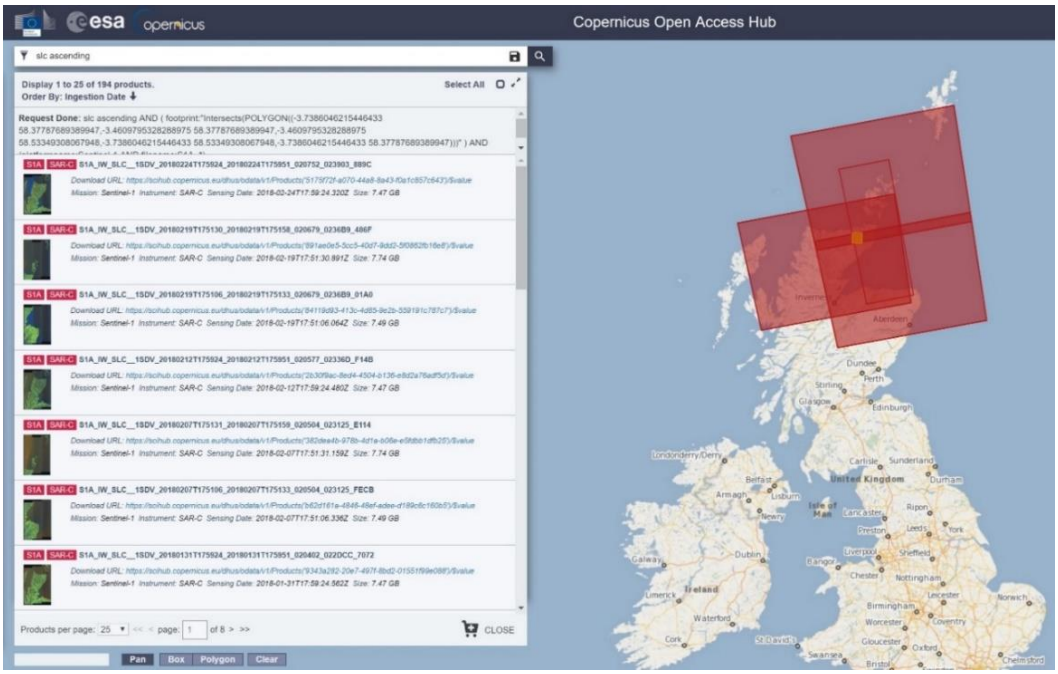


Figure 4.5: Interface of Sentinel-1 Scientific Hub.

Table 4.4: List of Sentinel-1 images used in this study.

No.	Date	No.	Date	No.	Date	No.	Date	No.	Date
1	12/03/2015	**11**	10/07/2015	**21**	25/12/2015	**31**	29/05/2016	**41**	26/09/2016
2	24/03/2015	**12**	22/07/2015	**22**	06/01/1889	**32**	10/06/2016	**42**	08/10/2016
3	05/04/2015	**13**	15/08/2015	**23**	18/01/2016	**33**	17/05/2016	**43**	20/10/2016
4	17/04/2015	**14**	27/08/2015	**24**	30/01/2016	**34**	04/07/2016	**44**	01/11/2016
5	29/04/2015	**15**	08/09/2015	**25**	11/02/2016	**35**	16/07/2016	**45**	13/11/2016
6	11/05/2015	**16**	20/09/2015	**26**	23/02/2016	**36**	28/07/2016	**46**	25/11/2016
7	23/05/2015	**17**	02/10/2015	**27**	30/03/2016	**37**	09/08/2016	**47**	07/12/2016
8	04/06/2015	**18**	19/11/2015	**28**	11/04/2016	**38**	21/08/2016		
9	16/06/2015	**19**	01/12/2015	**29**	23/04/2016	**39**	02/09/2016		
10	28/06/2015	**20**	13/12/2015	**30**	05/05/2016	**40**	14/09/2016		

4.2.5.2 Field data measurements

In this research, different field data measurements have been considered to validate the ISBAS DInSAR technique over the Flow Country, such as the following:

- **Levelling data**

Field data on the surface motion had been collected concurrently to the SAR data, fortuitously, at the UK Forestry Commission's Bad a' Cheo Research Area (Shotbolt et al., 1998; Anderson et al., 2000) by repeated optical levelling (Anderson et al., in prep). The details of the survey are presented in **Chapter 5**.

- **Water table depth**

Water table (WT) depths from five dataloggers for the period 15 March 2015 to 07 December 2016 were used to validate the surface motion recorded by ISBAS DInSAR using Sentinel-1 data set over Flow Country. The WT depth was recorded every 30 minutes.

- **Meteorological data**

Metrological data recorded by Wick airport weather station, managed by the Met Office provided two years of daily historical archived record of climate regime in the Flow Country for the period 15 March 2015 to 07 December 2016 free of charge.

- **Land cover classification**

Image classification has been applied to estimate the vegetation composition map of the Flow Country for 22 sites with 103 ISBAS points that have been selected based on ISBAS deformation map (linear results) (**Chapter 6, Figure 6.2**). The aim of image classification is to demonstrate an association between the vegetation composition map and a bog's condition. The results of the classification are presented in **Chapter 6**.

4.3 Zennare Basin

The second test site is the Zennare Basin, which is an agricultural area located in the southern part of the Venice Lagoon catchment (45˚10′ E, 12˚9′N), approximately 10 km from the Adriatic Sea and 1 km south of the margin of the Lagoon (**Figure 4.6**). The average annual rainfall is approximately 700mm and average annual air temperature is 15˚ C (Zanello et al., 2011). This basin represents one of the 32 hydraulic basins composing the district which is managed by the Adige-Bacchiglione Reclamation Authority and is located at the eastern part of the district, just south of the Venice Lagoon margin. Until the nineteenth century, the basin

was occupied by swamps and marshes, and it was reclaimed completely in the late 1920's (Gambolati et al., 2005; Gambolati et al., 2006; Zanello, 2011).

A detailed description of the Basin's evolution and peatland formation over the Holocene can be found in Rizzetto et al. (2003). At present, the basin is covered by alluvial sediments where the sandy and silty soils represent the remnants of ancient fluvial ridges and the organic material (peaty soils) are produced by the decomposition of the reeds in the interdistributary lowlands that are occupied by marshes and swamps. After reclamation of the basin for agriculture activities, soil ploughing enhanced the oxidation process of the organic material with the consequent formation and emission of carbon dioxide, mass loss and land subsidence (Gatti et al., 2002). Currently, the Zennare Basin which is almost completely dedicated to corn growing (Camporese et al., 2008) is entirely below mean sea level (**Figure 4.7**) and it is sinking progressively, which increases the vulnerability and geological hazard (Tosi et al., 2000).

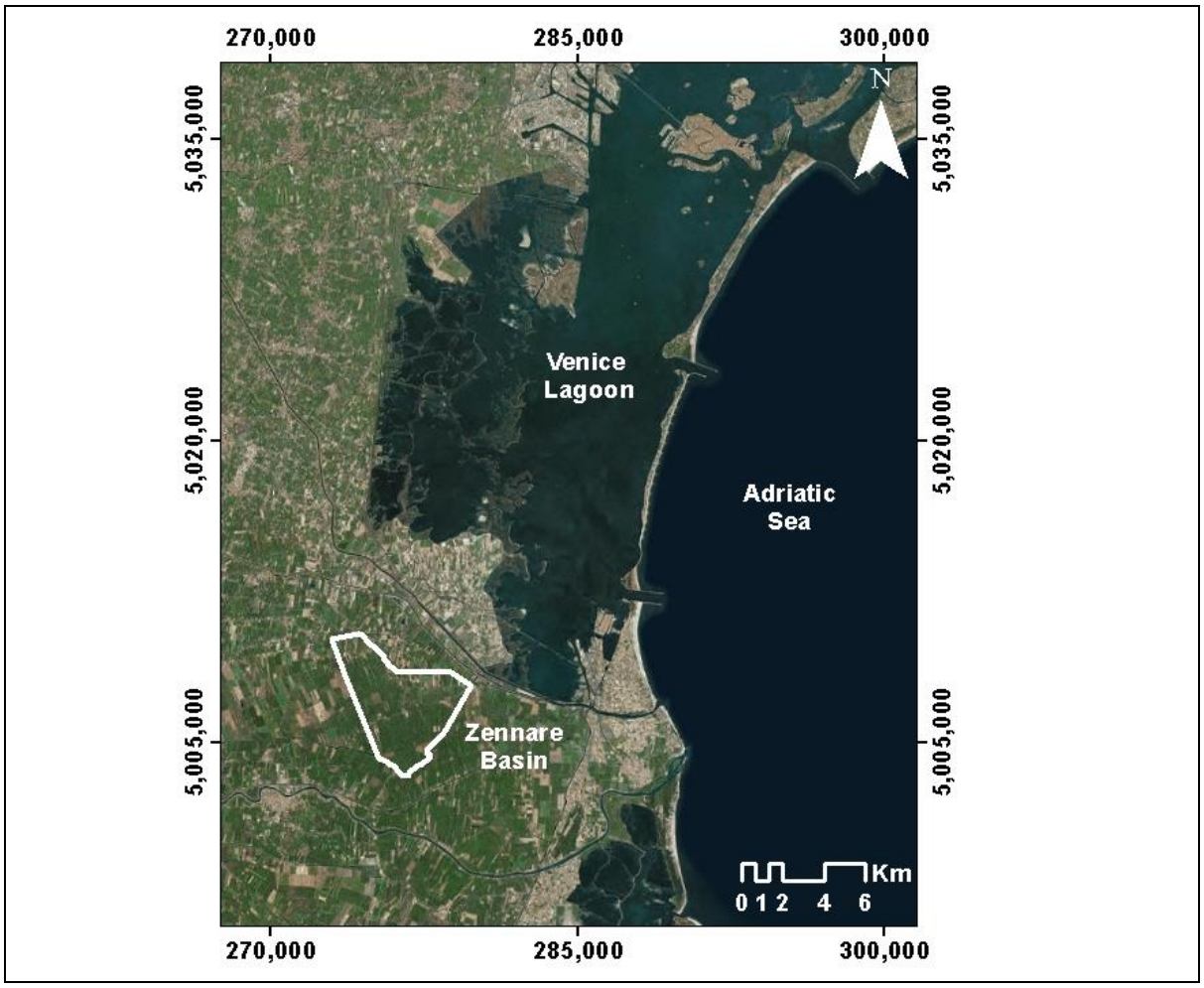


Figure 4.6: Location of Zennare Basin in the South of Venice Lagoon.(WGS-1984-UTM-Zone-33).

The basin is hydrologically well defined; it is bounded by roads and or channel embankments that are higher than the surrounding cultivated plain by at least 2m, with many constructed levees to prevent the flooding from the sea. A dense drainage network the conveys the surplus water to the Zennare pumping station, which has been used to control the water table depth (Gambolati et al., 2006) at between 0.4-0.5 m, as is required by the local agricultural practices.

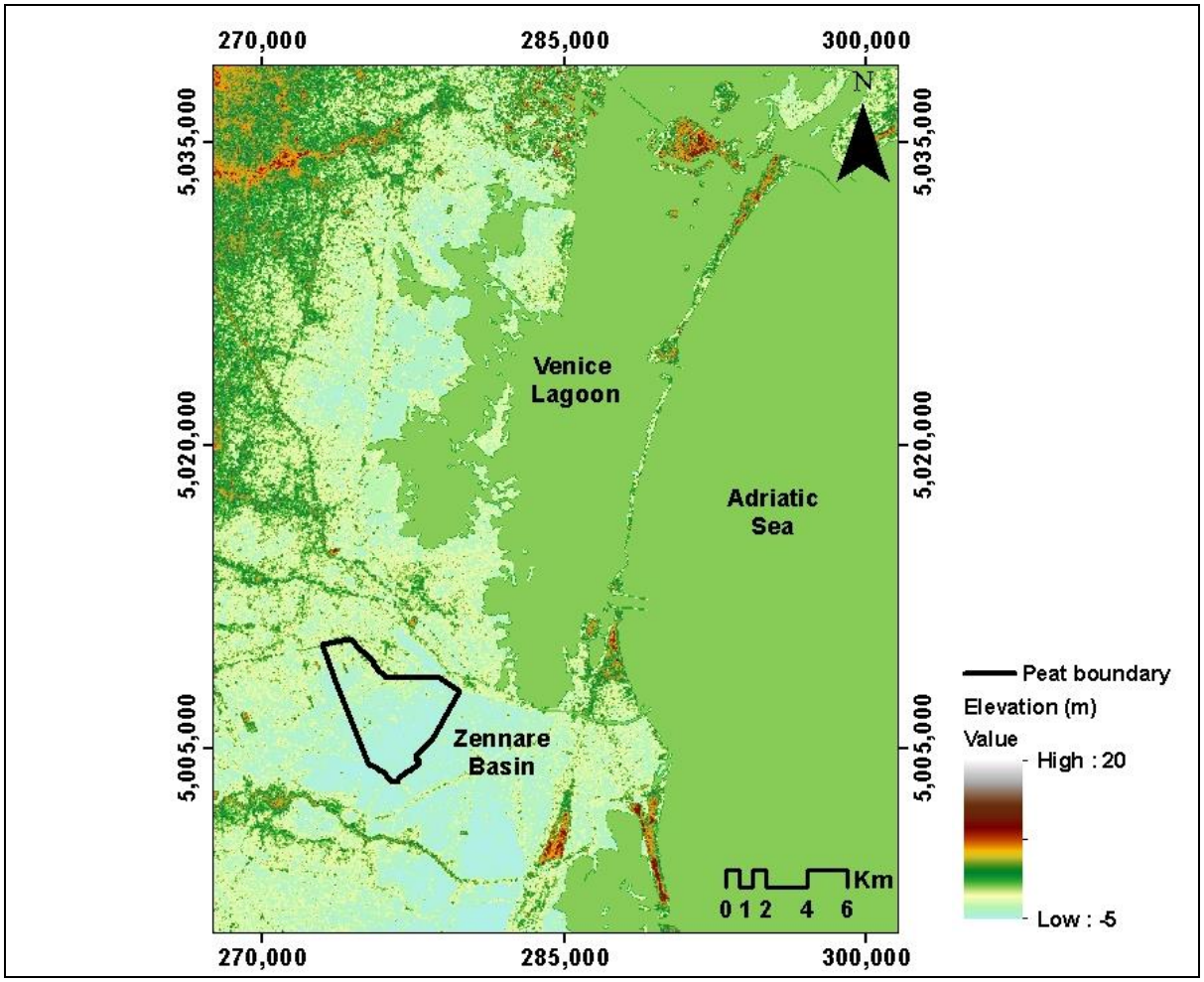


Figure 4.7: Digital Elevation Model from SRTM at 30 m resolution of the Zennare Basin

4.3.1 Land subsidence due to peat oxidation

Many field campaigns such as field surveys, remote sensing analysis and geophysical investigations have been used to map the thickness and extent of peat deposits in Zennare Basin (Nicoletti et al., 2003). **Figure 4.8** illustrates the geomorphological map of the basin, which shows that the peat is located mainly in the southern part of the Basin, is reported to be 1 m thick and results from the decomposition of reed vegetation (Zanello et al., 2011).

Although ad hoc campaigns have never been performed to measure the land subsidence in this area before 2000, records of historical subsidence can be assessed from some old hydraulic structures found on the soil underlying the outcropping peat. In addition, the reduction of the water table level at the pumping station entry provides further evidence of an average subsidence rate of about 2-3 cm /year for the last 70 years (Zanello, 2011). Similar results were found by comparing the DEM obtained in 1983 based on aerial photogrammetric survey and kinematic DGPS that was carried out in 2002 (Gambolati et al., 2005).

Land subsidence due to peat oxidation represents a major environmental hazard. The peatland surface elevation can be lowered by an amount that can reach several meters with systematic drainage, thus increasing the flooding risk (Mount and Twiss, 2005) and cost of the land drainage (Gambolati et al., 2006) or levee integrity maintenance. In this regard, the choice of instruments to monitor the degradation over drained coastal peatland areas such as the Zennare basin and the methods used are extremely important to characterize the deformation and to evaluate possible mitigation strategies. The availability of large SAR datasets over the Zennare basin which has different environments from Flow Country, make this area suitable to investigate the feasibility of using Interferometric SAR to monitor the deformation over this drained coastal peatland area.

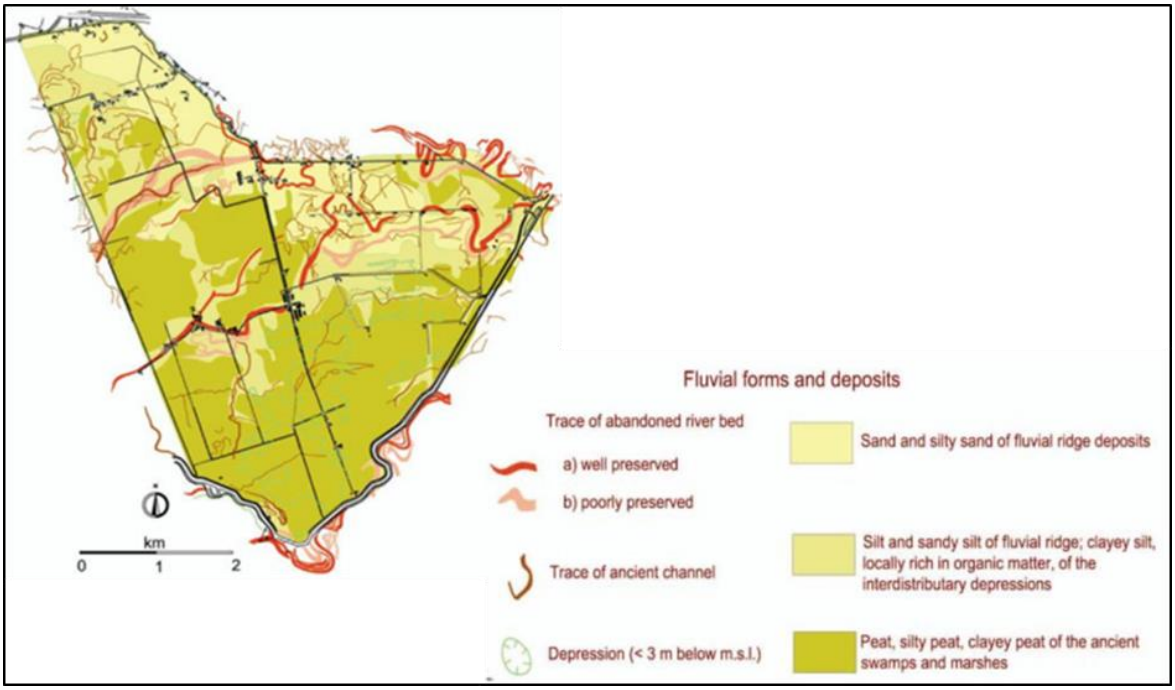


Figure 4.8: Geomorphological map of Zennare Basin extracted from remote sensing data. The map adapted from (Nicoletti et al., 2003).

4.3.2 List of SAR datasets

Assessment of long-term deformation in the Zennare basin using the InSAR technique is made possible as a consequence of the availability of a long record of SAR images acquired over the past years through different platforms. The SAR images that have been used in this study were acquired from three satellites mission, ERS 1/2, ENVISAT and Sentinel-1 A. These satellites operate in C-band frequency with approximately 5.6cm wavelength.

4.3.2.1 ERS 1/2 dataset

A category-1 proposal was submitted to ESA to acquire seventy-four ERS 1/2 SAR images in the track 394. All images were in descending orbit and cover the period from 24 May 1992 to 01 January 2001. **Table 4.5** showed the proposal submitted to ESA for ERS data acquisition in Venice Lagoon (Italy). Only 61 images have been used in the processing.

Table 4.5: List of submitted proposal to ESA to request ERS1/2 images in Venice Lagoon (Italy).

Project ID 32651: Long-term deformation monitoring in peat-land areas by using DInSAR techniques.								
No.	**Mission**	**Date**	**No.**	**Mission**	**Date**	**No.**	**Mission**	**Date**
1	ERS 1	24/04/1992	**26**	ERS 1	26/05/1996	**51**	ERS 2	28/12/1998
2	ERS 1	29/05/1992	**27**	ERS 2	27/05/1996	**52**	ERS 2	07/03/1999
3	ERS 1	03/07/1992	**28**	ERS 1	30/06/1996	**53**	ERS 2	08/03/1999
4	ERS 1	07/08/1992	**29**	ERS 2	09/09/1996	**54**	ERS 1	11/04/1999
5	ERS 1	11/09/1992	**30**	ERS 2	14/10/1996	**55**	ERS 2	12/04/1999
6	ERS 1	16/10/1992	**31**	ERS 2	23/12/1996	**56**	ERS 1	16/05/1999
7	ERS 1	20/11/1992	**32**	ERS 2	27/01/1997	**57**	ERS 2	17/05/1999
8	ERS 1	29/01/1993	**33**	ERS 2	03/03/1997	**58**	ERS 2	21/06/1999
9	ERS 1	05/03/1993	**34**	ERS 2	07/04/1997	**59**	ERS 2	26/07/1999
10	ERS 1	09/04/1993	**35**	ERS 2	12/05/1997	**60**	ERS 1	29/08/1999
11	ERS 1	18/06/1993	**36**	ERS 2	16/06/1997	**61**	ERS 2	30/08/1999
12	ERS 1	23/07/1993	**37**	ERS 2	21/07/1997	**62**	ERS 2	04/10/1999
13	ERS 1	27/08/1993	**38**	ERS 2	25/08/1997	**63**	ERS 1	07/11/1999
14	ERS 1	01/10/1993	**39**	ERS 2	29/09/1997	**64**	ERS 2	08/11/1999
15	ERS 1	10/12/1993	**40**	ERS 2	03/11/1997	**65**	ERS 2	13/12/1999
16	ERS 1	07/05/1995	**41**	ERS 2	08/12/1997	**66**	ERS 2	17/01/2000
17	ERS 1	11/06/1995	**42**	ERS 2	12/01/1998	**67**	ERS 2	27/03/2000
18	ERS 2	12/06/1995	**43**	ERS 2	16/02/1998	**68**	ERS 2	05/06/2000
19	ERS 2	17/07/1995	**44**	ERS 2	23/03/1998	**69**	ERS 2	10/07/2000
20	ERS 2	21/08/1995	**45**	ERS 2	27/04/1998	**70**	ERS 2	14/08/2000
21	ERS 2	30/10/1995	**46**	ERS 2	01/06/1998	**71**	ERS 2	18/09/2000
22	ERS 1	07/01/1996	**47**	ERS 2	06/07/1998	**72**	ERS 2	23/10/2000
23	ERS 2	08/01/1996	**48**	ERS 2	10/08/1998	**73**	ERS 2	27/11/2000
24	ERS 1	21/04/1996	**49**	ERS 2	14/09/1998	**74**	ERS 2	01/01/2001
25	ERS 2	22/04/1996	**50**	ERS 2	23/11/1998			

4.3.2.2 ENVISAT ASAR dataset

Environmental Satellite (ENVISAT) was launched on 1 March 2002 with ten sophisticated optical and radar instruments. The main instrument of ENVISAT on board was Advanced Syenthetic Aperture Radar (ASAR), operating in C-band and ensuring ERS satellite data continuity. This satellite was equipped with a phased-array antenna which provided independent control of both phase and amplitude of the received signal at different regions of the antenna (ESA, 2002). This feature permitted the ASAR instrument to operate in different modes. The other improvements of ASAR include beam flexibility, steering to acquire images at different incidence angles and altering the polarization mode (co-polar and cross-polar). The main objectives of launching ENVISAT were to contribute to environmental and climate

change studies as well as to ensure the ERS data continuity. The mission of the ENVISAT satellite ended on 8 April 2012 due to a lost connection with the satellite after the tenth anniversary of its launch.

The availability of ENVISAT ASAR images over the study area also can be identified using Eoli-sa software. A category-1 proposal was submitted to ESA for ENVISAT data acquisition over Venice Lagoon (Italy) to acquire fifty-four images in the track 122; however, only fifty-one images have been used in the processing. The images were in descending orbit and cover the period from 2 April 2003 to 31 December 2008. **Table 4.6** illustrates the submitted proposal to ESA for ENVISAT data acquisition over Venice Lagoon (Italy).

Table 4.6: List of the proposal submitted to ESA for ENVISAT ASAR data acquisition over Vennice Lagoon (Italy).

Project ID 32188: Long-term deformation monitoring in drained peatland areas using DInSAR techniques					
No.	**Date**	**No.**	**Date**	**No.**	**Date**
1	02/04/2003	**19**	15/06/2005	**37**	16/05/2007
2	24/09/2003	**20**	20/07/2005	**38**	20/06/2007
3	29/10/2003	**21**	24/08/2005	**39**	25/07/2007
4	07/01/2004	**22**	28/09/2005	**40**	29/08/2007
5	11/02/2004	**23**	02/11/2005	**41**	03/10/2007
6	17/03/2004	**24**	07/12/2005	**42**	07/11/2007
7	21/04/2004	**25**	11/01/2006	**43**	12/12/2007
8	26/05/2004	**26**	22/03/2006	**44**	16/01/2008
9	30/06/2004	**27**	26/04/2006	**45**	20/02/2008
10	04/08/2004	**28**	31/05/2006	**46**	26/03/2008
11	08/09/2004	**29**	05/07/2006	**47**	30/04/2008
12	13/10/2004	**30**	09/08/2006	**48**	04/06/2008
13	17/11/2004	**31**	18/10/2006	**49**	09/07/2008
14	22/12/2004	**32**	22/11/2006	**50**	13/08/2008
15	26/01/2005	**33**	27/12/2006	**51**	17/09/2008
16	02/03/2005	**34**	31/01/2007	**52**	22/10/2008
17	06/04/2005	**35**	07/03/2007	**53**	26/11/2008
18	11/05/2005	**36**	11/04/2007	**54**	31/12/2008

4.3.2.3 Sentinel-1 dataset

Over Venice lagoon (Italy), eighty-eight Sentinel-1 images have been collected from Sentinel-1 data Hub. All images were acquired from Satellite A in a descending orbit for the period 4 January 2015 to 1 March 2018. The images are separated by 12 days intervals, and nine images are missing from the Data Hub, i.e., 16/01/2015, 28/05/2015, 21/06/2015, 27/07/2015, 25/09/2015, 07/10/2015, 19/10/2015, 27/06/2016 and 17/01/2017. Also one Sentinel-1 image (23/03/2016) has been excluded from the processing due to technical problem The list of the available Sentinel-1 data is summarized in **Table 4.7**.

Table 4.7: List of Sentinel-1 images used in the processing over Venice Lagoon (Italy).

No.	Date	No.	Date	No.	Date	No.	Date	No.	Date
1	04/01/2015	**19**	31/10/2015	**37**	03/06/2016	**55**	29/01/2017	**73**	02/09/2017
2	28/01/2015	**20**	12/11/2015	**38**	15/06/2016	**56**	10/02/2017	**74**	14/09/2017
3	09/02/2015	**21**	24/11/2015	**39**	09/07/2016	**57**	22/02/2017	**75**	26/09/2017
4	21/02/2015	**22**	06/12/2015	**40**	21/07/2016	**58**	06/03/2017	**76**	08/10/2017
5	05/03/2015	**23**	18/12/2015	**41**	02/08/2016	**59**	18/03/2017	**77**	20/10/2017
6	17/03/2015	**24**	30/12/2015	**42**	14/08/2016	**60**	30/03/2017	**78**	01/11/2017
7	29/03/2015	**25**	11/01/2016	**43**	26/08/2016	**61**	11/04/2017	**79**	13/11/2017
8	10/04/2015	**26**	23/01/2016	**44**	07/09/2016	**62**	23/04/2017	**80**	25/11/2017
9	22/04/2015	**27**	04/02/2016	**45**	19/09/2016	**63**	05/05/2017	**81**	07/12/2017
10	04/05/2015	**28**	16/02/2016	**46**	01/10/2016	**64**	17/05/2017	**82**	19/12/2017
11	16/05/2015	**29**	28/02/2016	**47**	13/10/2016	**65**	29/05/2017	**83**	31/12/2017
12	09/06/2015	**30**	11/03/2016	**48**	25/10/2016	**66**	10/06/2017	**84**	12/01/2018
13	03/07/2015	**31**	23/03/2016	**49**	06/11/2016	**67**	22/06/2017	**85**	24/01/2018
14	15/07/2015	**32**	04/04/2016	**50**	18/11/2016	**68**	04/07/2017	**86**	05/02/2018
15	08/08/2015	**33**	16/04/2016	**51**	30/11/2016	**69**	16/07/2017	**87**	17/02/2018
16	20/08/2015	**34**	28/04/2016	**52**	12/12/2016	**70**	28/07/2017	**88**	01/03/2018
17	01/09/2015	**35**	10/05/2016	**53**	24/12/2016	**71**	09/08/2017		
18	13/09/2015	**36**	22/05/2016	**54**	05/01/2017	**72**	21/08/2017		

4.4 Summary

Information regarding the suitability of each study site that could fulfil the aims and objectives of this study has been presented. The presence of peat bogs with different conditions in the Flow Country combined with the availability of SAR data and ground-based measurements make this area ideal for the study of ground motion and evaluation of the peat conditions using InSAR. However, a second test site is needed to examine the feasibility of ISBAS technique over a different peatland environment. Therefore, the drained coastal peatland (Zennare basin) was selected as a second test site. This site was selected for a few reasons, mainly due to the availability of large SAR data sets with some previous works explaining the deformation and the fact that it has completely different environment from the Flow Country.

CHAPTER 5

METHODOLOGY AND RESULTS FOR LONG-TERM PEATLAND CONDITION ASSESSMENT VIA SURFACE MOTION USING ISBAS DINSAR TECHNIQUE

5.1 Introduction

The previous chapter discussed how the Flow Country in Scotland (the largest expanse of blanket bogs in Europe) and the Zennare basin in the south of Venice Lagoon, Italy (farm coastal peatland area) were selected as the most suitable test sites for this research. This chapter, therefore, presents the processing methodologies and final results of the long-term deformation monitoring in both sites using the ISBAS DInSAR technique. The LOS velocity maps over these sites are presented, drawing attention to their respective quality and internal consistency. The datasets are also compared with other sources of data wherever possible which naturally leads into the next chapter.

5.2 SAR data processing over Flow Country (Scotland)

5.2.1 Site overview

As explained in **Chapter 4**, the Flow Country of Caithness and Sutherland, Northern Scotland, UK is the largest expanse of blanket bog in Europe, covering about 4,000 square kilometres (**Figure 5.1**). Peatlands in the UK have developed under peat forming vegetation, and along with contemporary land management, this has resulted in a myriad of land cover classes and peat depths (and status) across the area (Bruneau and Johnson, 2014). The peat in some areas of the Flow Country was damaged between 1979 and 1987 through the planting of non-native conifer forests and the cutting of thousands of miles of drains. This has now been stopped and the area is under restoration. In the central eastern part of the Flow Country is the UK Forestry Commission's Research Reserve at Bad a Cheo (475066 E, 6476417 N (WGS-1984-UTM-Zone-30N)), a site situated on wet, infertile blanket bog about 90 m above sea level, with mean annual precipitation of 930mm (Shotbolt et al., 1998; Anderson et al., 2000) and featuring afforested plots. The area contains plots afforested in 1968, plots afforested in 1989, a few plots drained in 1989 but otherwise undisturbed and some areas that have been neither drained nor afforested. This reserve was used for the focused quantitative analysis of the ISBAS outputs, with the remaining 4,000 km^2 of peatland analysed contextually, providing qualitative analyses of the outputs from the processing of the SAR data.

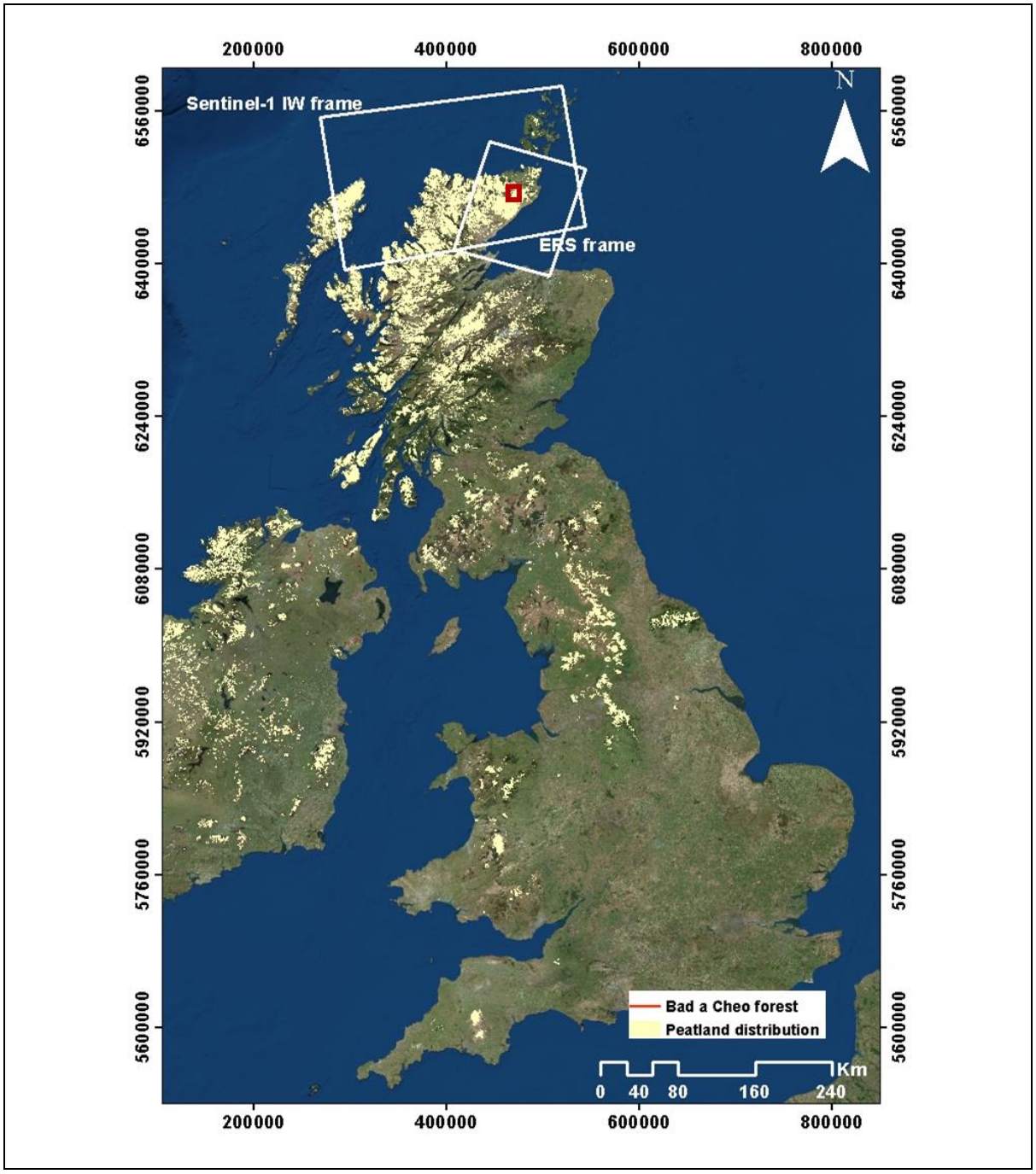


Figure 5.1: The distribution of blanket peat of the United Kingdom and Ireland, adapted from the 2012 CORINE (Co-ordinated Information on the Environment) along with the boundary of Bad a Cheo forest Reserve and the footprints of the ERS and Sentinel-1 SAR image frames. (WGS-1984-UTM-Zone-30N).

5.2.2 Data

As determined by SAR data availability over the study area, remotely sensed data from two SAR satellite systems were used in this study (refer to **Chapter 4**, **section 4.2.5**); this allowed for a different set of measurement scenarios to be investigated, principally related to the monitoring periods and temporal and orbital baseline constraints (Cigna and Sowter, 2017). As determined by availability, dataset one was comprised of fifty-one ERS 1/2 C-band VV polarised SAR images from a descending orbit acquired for a long monitoring period between May 1992 and December 2000 (**Chapter 4, Table 4.1**). Dataset two (again determined by availability) was comprised of forty-seven Sentinel-1 Interferometric Wide (IW) SLC images acquired from satellite A in an ascending orbit over a much shorter monitoring period between March 2015 and December 2016 (see **Chapter 4**, **Table 4.4**). **Figure 5.1** illustrates the footprints of ERS and Sentinel-1 image frames. Both datasets were separately processed using the ISBAS DInSAR technique (Sowter et al., 2013; Bateson et al., 2015) (refer to **Chapter 2, Section 2.3**) to calculate annual surface motion velocities (m/year) and their standard errors during the respective monitoring periods across the Flow Country.

Field data on surface motion (refer to **Chapter 4, Section4.2.5.2**) had been collected at the UK Forestry Commission's Bad a Cheo Research Area (Shotbolt et al., 1998; Anderson et al., 2000) by repeated optical levelling (Anderson et al., in prep). Although temporally concurrent to the SAR data, these field surface motion data were not collected for the purpose of comparison with the InSAR surface motion outputs; however, they have been used here due to the absence of any other field data on surface motion of the Flow Country. From 1989 to 1994 the levelling measurements were repeated twice per year, once in spring and once in autumn. Then for 1994-1999, the frequency of the levelling measurements reduced to once per year, in the autumn. The next repetition was in spring 2005. Four blocks of a randomised block afforestation experiment had been surveyed here between 1989 and August 2016 (after which the reserve was clear-felled and no further measurements were taken) (**Figure 5.2**), which more-or-less covers the same time period as the ERS and Sentinel-1 observations.

Each block contains four 42 x 20 m plots; in each case, one of the plots is drained but unplanted and the other three are drained, ploughed and planted. Observations of peat height were made along a longitudinal mid-line transect of each plot with measurements at a fixed set of 85 locations related to the ploughing pattern, including drain bases, bases of furrows, tops of ridges and the original surface mid-way between ridges and beside them. In the drained but

unplanted plots, 42 measurements were made including drain bases and the original surface at 1 m intervals along the transects. A local benchmark had been established beside each block in 1988 by pushing a metal rod vertically through the peat and hammering it into the mineral substratum (Shotbolt et al., 1998). These benchmarks by each of the four blocks were installed to act as local benchmarks against which to detect changes in the ground surface level due to peat consolidation, shrinkage, compression and oxidation and tree root growth. These were sufficiently well anchored in the mineral substrate to be used for this purpose and our assumption is that (though no measurement was made to verify this) any vertical motion of the mineral substrate is negligible compared to vertical motion of the ground surface due to processes in the peat. Before and after surveying the points on each transect, which were all done from a single tripod position, the appropriate local benchmark was surveyed from the same tripod position so that heights on the transect could be expressed as heights relative to these benchmarks. These measurements of the local datum were also a check to confirm that the automatic level had not inadvertently moved during the transect survey, which it never had. The observations of the heights were surveyed with a Topcon AT-F6 automatic level and rounded to the nearest 1 cm (Anderson et al., 2000). The mean height change of each transect was then used for comparison with the ERS and Sentinel-1 derived surface motion data sets, estimated by fitting a linear trend through the plot mean levelling heights. Twelve measurements for each levelling transect from 1991 to 2001 were used with the ERS data set (28/04/92 -04/12/2000); however, due to the timing of this study, only two measurements were available to compare with the Sentinel-1 data set (28/01/15 - 03/08/2016). To supplement this, qualitative comparisons to site condition were made on several sites across the Flow Country as a whole, on the basis of land cover and use (e.g. drained, forested, clear felled, presence of pool systems, bare peat, mineral soil), as delineated via visual interpretation of optical satellite images available from the Google Earth geobrowser (Gorelick et al., 2017).

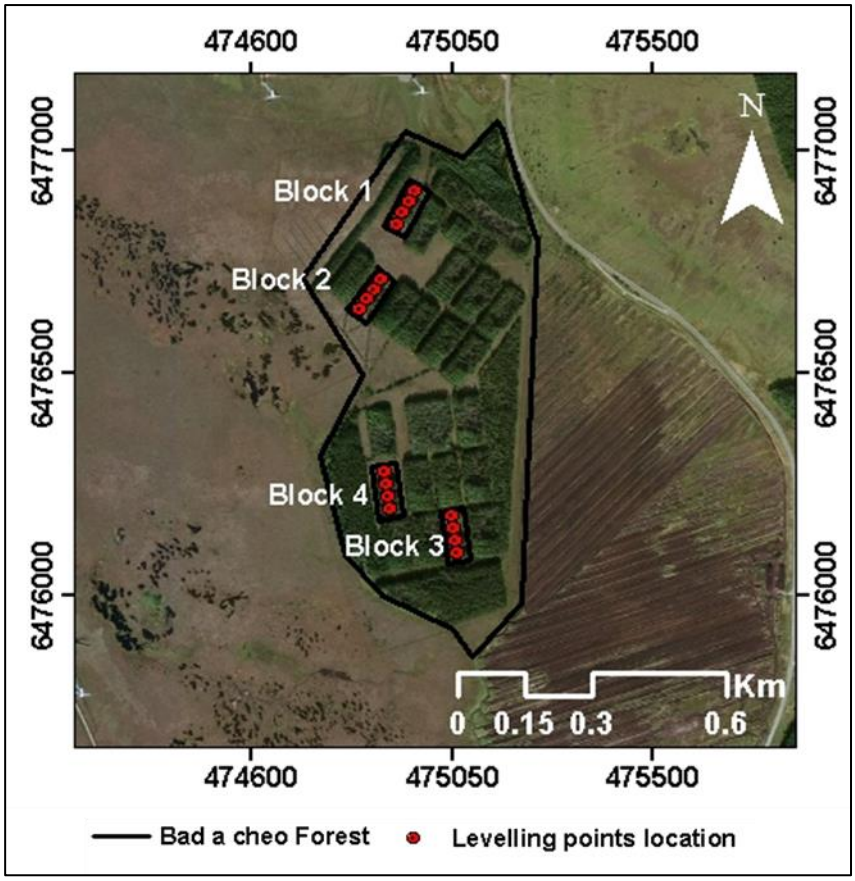


Figure 5.2: A very high resolution RGB image of the UK Forestry Commission's Bad a' Cheo Forest Research Reserve (outlined in black, centered on 475066 E, 6476417 N (WGS-1984-UTM-Zone-30N)) showing the mid-point locations of the levelling transects from which the levelling measurements were taken (red dots). Note there are four forest blocks, each with four levelling measurements transects. In the quantitative assessment of the InSAR surface velocity outputs, these levelling measurements are used for comparison and context.

5.2.3 SAR data processing using ISBAS technique

All ERS and Sentinel-1 images were processed using the ISBAS DInSAR technique (refer to **Chapter 2, Section 2.3**), using temporal and orbital baseline constraints that allow for the maximisation of spatial coherence and a reduction of the contribution of DEM errors in the generation of the differential interferograms. In order to increase the quality of the phase estimation and reduce the noise of the radar signal in the scene, the interferograms were multi-looked using a window size of 4x20 (range x azimuth) pixels for the ERS data and 22x5 pixels for the Sentinel-1 data, giving a final pixel dimension of approximately 100x100m in ground range for ERS and 80x70m for Sentinel-1. In both cases, the points that were derived from ISBAS processing were considered coherent when the average coherence was greater than or equal to 0.25, in accordance with the SBAS technique (see **Chapter 2, Section 2.3.1.4**).

ISBAS processing was then performed only for coherent points as defined above. As reported in Gee et al. (2016), areas with sustained coherence over all interferograms, such as in urban areas, have a low standard error; over areas for which coherence is more intermittent, such as in rural areas, the standard error increases. Therefore, care was taken to limit the minimum number of interferograms contributing to a coherent pixel to control the standard error. Differential interferograms were generated (**Chapter 2, Section 2.3.1.3**) through calculating the phase difference between a pair of images and subtracting off a simulated phase calculated using the image geometry and a digital elevation model from the SRTM mission. After generation of the differential interferograms, close attention by way of visual inspection was paid to identify any anomalies (i.e. atmospheric interference). No clear errors were observed, or they had been removed through the processing that had been applied.

Phase unwrapping was implemented using a statistical cost network flow algorithm described by Chen and Zebker (2001), to individually unwrap all the ISBAS points within each interferogram (**Chapter 2, Section 2.3.1.6**). Numerous previous studies using ISBAS have used one reference point and this was the case here. The same stable reference point, located in Dounreay on the northern coast at 58°34’44’’N 3°44’23’’W, was used for both datasets image stacks (**Figure 5.3**). The selection of the reference point is extremely important because all the velocity results are relative to this point. Therefore, the reference point is expected to be stable, with zero velocity. The choice of the reference point was made subject to a statistical consideration relating to the coherence of the signal and the minimum standard deviation of the phase in all interferograms (i.e., the reference point has a high coherence and displays a low phase standard deviation across all interferograms) (**Chapter 2, Section 2.3.1.5**). Dounreay is used since this is a stable high-coherence area and thus a low noise, zero-mean, neighbourhood. Through this choice of location of the reference point any chance of erroneously choosing an unstable point has been minimized and the phase can thus be easily unwrapped and related to other stable areas surrounding it. Note that the resultant reference point is very close to a Thurso (THUS) Global Navigation Satellite System (GNSS) station (less than 1 km distance between them) (**Figure 5.3**).

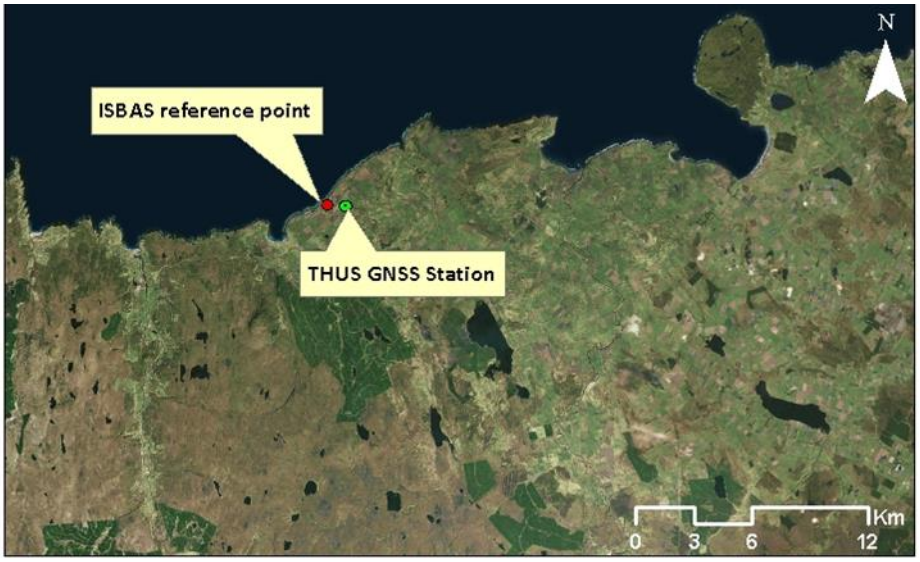


Figure 5.3: Relative location of ISBAS reference point used and the nearby THUS GNSS station: comparison of the motion data from the two indicates stability of the reference point.

All ISBAS velocity results are in the line of sight (LOS) direction, towards or away from the satellite. In order to enable an equivalent comparison between LOS velocity (VelLOS) results and the field acquired levelling data, all the velocity results were converted to an equivalent vertical (Velvert) velocity by:

$$Vel_{vert} = Vel_{LOS}/cos\theta \qquad \textbf{Eq. 5.1}$$

where Θ is the incidence angle from the surface normal. Here, the incidence angle was explicitly calculated for each coherent point using the satellite and image geometry. It should be noted that the correction that was applied assumes that the ground displacement is wholly in the vertical direction only, which is a reasonable assumption given that analyses of the data from the THUS Global Navigation Satellite System (GNSS) station in Thurso reports a vertical velocity for the period 2007 to 2014 was 0.6±0.5 mm/year using ITRF 2008 reference frame (http://www.bigf.ac.uk/). The vertical velocity for the reference point as measured by the ISBAS technique was -0.17±0.34 mm/year. Given that the geology is the same across the study, this stability should be case for the Bad a Cheo reserve too. However, in cases where horizontal motion is anticipated, it is possible to resolve the vertical and lateral components of motion using a stereo analysis of separate results from ascending and descending orbits, as demonstrated by Lanari et al. (2007). It is useful to note here that all pixel values in a multilooked, unfiltered interferogram are independent of each other and therefore errors in one pixel have no connection to the errors of its neighbours. Phase unwrapping merely adds an

integer number of cycles to a pixel value and therefore does not propagate random errors or biases in any individual measurements. A 'stable' reference point simply means that its motion is so small that it does not require phase unwrapping (i.e. there are no integer cycle errors). As long as this condition is met, none of its intrinsic motion or noise will be propagated to any other pixels in the unwrapped phase. Note that the GNSS station observations are only used to confirm that the pixel location is stable - at no point is the pixel value adjusted to agree with the GNSS velocity.

5.2.3.1 ERS ISBAS processing

The fifty-one ERS C-band VV polarised SAR images were processed using constraints of a maximum 250m perpendicular baseline and four years temporal baseline between any interferometric pair used. This follows previous studies (Berardino et al., 2002; Casu et al., 2006; Cigna and Sowter, 2017) and ensured limited spatial decorrelation and topographic errors and that interforemetretic coherence was preserved. The resultant interferograms (pairs) are depicted in **Figure 5.4 a**; the total number of generated interferograms was 249, corresponding approximately to over 19% of the possible pair combinations of the ERS data set. However, a threshold value of 72 interferograms was used as the minimum point threshold. The point threshold is an indication of the minimum number of coherent interferograms that contribute to the analysis of each pixel. As indicated in Cigna and Sowter (2017), a high point threshold indicates a low standard error, which is a preferred outcome, but at the cost of poor coverage. For example, if the point threshold is at a maximum, equal to the number of interferograms, the coverage is very close to that of a standard SBAS or PSI survey with most points over hard targets such as buildings or infrastructure and very few points over vegetated peatland areas. Therefore, the approach here was to successively lower the point threshold from its maximum value until an acceptable coverage was reached, but with an acceptable compromise to the standard error. This rule allows the ISBAS algorithm to accept points that may not be high quality in all interferograms (N) (i.e., intermittent coherence pixels), which is a characteristic of vegetated sites such as peatlands.

5.2.3.2 Sentinel-1 ISBAS processing

The forty-seven Sentinel-1 Interferometric Wide (IW) SLC images were processed with a maximum normal perpendicular baseline of 200m. With this perpendicular baseline two different temporal baselines were used: 6 months and approximately 2 years (i.e., the entire period of the observations). The longer baseline was determined by the Sentinel-1 record at the

time of data analyses. The shorter baseline of 6 months was chosen to examine if this had any impact on potential phase ambiguity, particularly in this dynamic peatland environment. With the 6 months temporal baseline, 493 differential interferograms were formed which corresponds to 45% of the possible pair combinations (**Figure 5.4 b**); with the 2 years temporal baseline the number of resultant differential interferograms was 1071 (**Figure 5.4 c**), corresponding to over 99% of the possible pair combinations. The point threshold values for the 6 months and 2 year temporal baselines were 246 and 420 interferograms respectively.

5.2.4 Data analysis

The resultant vertical velocity maps produced from the processed ERS and Sentinel-1 data were evaluated both qualitatively (i.e., through comparisons with known peat subsidence and accumulation patterns over the study area, mainly related to land cover and site history) and quantitatively (i.e., through comparison with the field levelling data). Prior to evaluation, the vertical velocity outputs from the ERS and Sentinel-1 ISBAS processing were output as raster layers and orthorectified using nearest neighbour interpolation to provide pixels at a uniform 50m spacing in a UTM map projection.

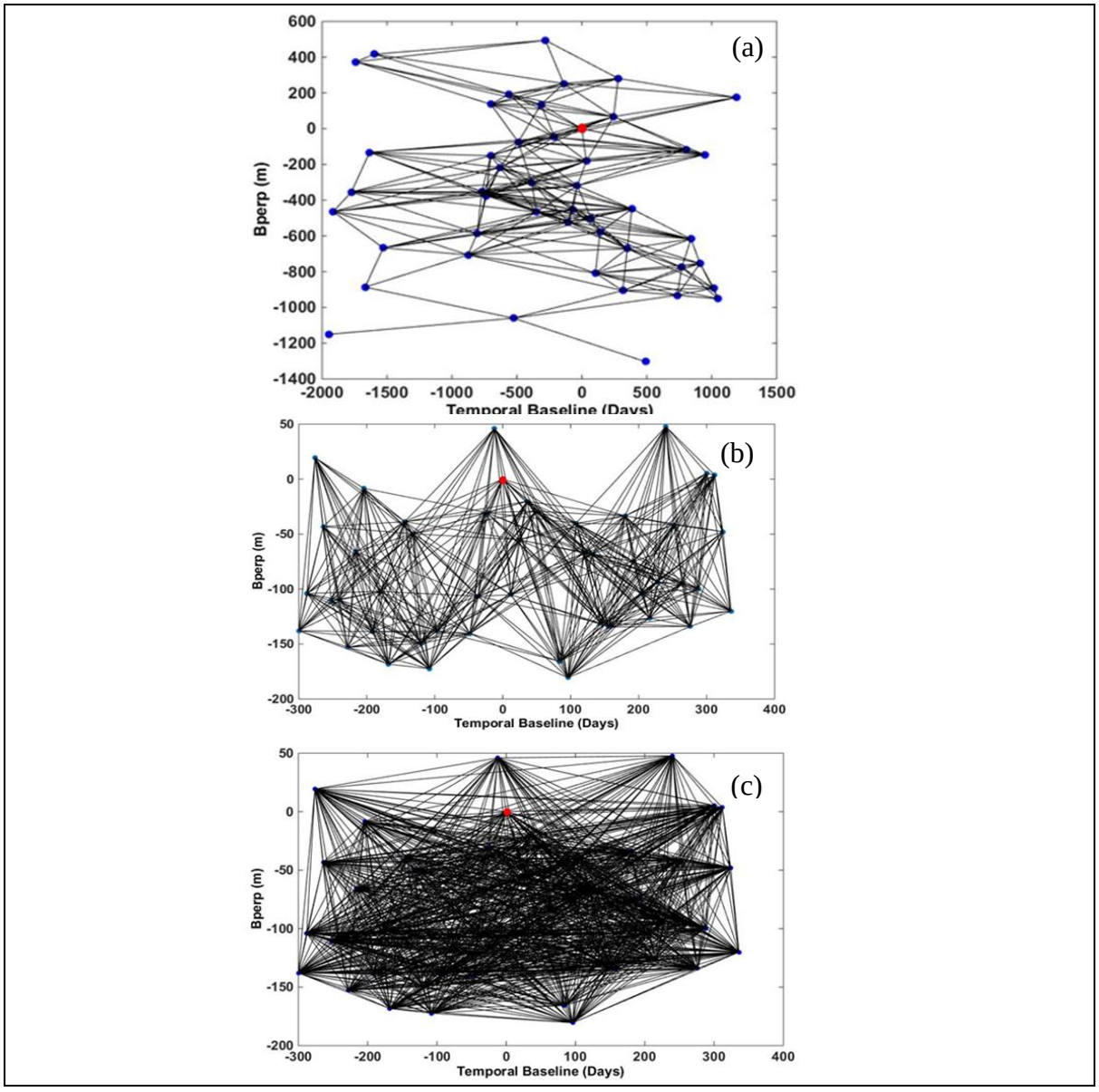


Figure 5.4: Perpendicular and temporal baselines of the image pairs relative to the master scene (a) ERS SAR (master: 1st September 1997) (b and c) Sentinel-1 SAR 6 months and 2 years temporal baselines respectively (master: 6th January 2016). Red point is the master SAR image.

The fortuitous nature of the availability of the levelling data meant that only general patterns in surface motion were extracted and compared with the InSAR outputs. Although a useful ground dataset, it could not be used for a validation exercise per se - a key issue was that the output spatial resolution of the ISBAS velocity maps is clearly much larger than the individual field levelling transect means (4 transect means per block – see **Figure 5.2**). As a result, all levelling points from each block and all raster cells of the ERS or Sentinel-1 outputs within each block were extracted for the simultaneous time period and used for further

analyses. Moreover, the surface motion outputs for all the raster cells in reserve as a whole were also extracted. It should be noted that this meant that the measurements for each of the four blocks are from both peatland that had forests for the entire study period but also peatland that had been drained at the same time but not planted. Analysis was undertaken through comparison between the levelling data and the InSAR velocity maps and this took two forms. The first was to plot the mean and standard error of the ground motion graphically for each of the four blocks separately, for each of the four blocks as a whole (i.e., all together) and also for the reserve as a whole. The second was to conduct a Wilcoxon-Mann-Whitney U-test at the scale of the blocks. This non-parametric method compares the arithmetic means of two samples (i.e., levelling data and InSAR data) to see if they are different or not. For clarity, we should stress that in this comparison the levelling measurements are relative to the relevant separate benchmarks and the InSAR measurements relative to the reference point at Thurso.

5.2.5 Results

For both the ERS and Sentinel-1 datasets, the spatial coverage of vertical velocity maps over the peatland area of the Flow Country attained a significant proportion of total coverage (over land). A measure of the coverage provided by the ISBAS method over this predominantly rural area is the solution density: the ratio between the number of pixels providing a solution and the total number of processed pixels over land (Cigna and Sowter, 2017). On the ERS ISBAS velocity map, ISBAS points cover more than 70% of the total land area; on the Sentinel-1 velocity map they cover 87% of the area (**Figure 5.5**, **Figure 5.6, Figure 5.7**).

The ERS derived vertical velocity maps and histograms (**Figure 5.5**) illustrate the spatial and statistical distribution of velocities and their standard errors for the period 1992 to 2000. Negative LOS velocities indicate subsidence, while positive values indicate uplift. The mean vertical velocity of all ERS ISBAS points across the entire scene was -0.0006 ± 0.0012 m/year, with values ranging from -0.0081±0.0024 m/year to 0.0071±0.0015 m/year. Over the open peatland areas, the standard error is very low due to a large number of coherent pixels per point. Over agricultural and forested areas the standard error increases due to the intermittent coherence. Sentinel-1 derived vertical velocity maps and histograms (**Figure 5.6** and **Figure 5.7**) illustrate the spatial and statistical distribution of velocities and their standard errors calculated using temporal baselines of 6 months (**Figure 5.6**) and 2 years (**Figure 5.7**) for the time period 2015 to 2016. These velocity maps overlap with those obtained with the ERS data apart from a transect that dissects the study area along-track direction. This was due to the

swaths that made up the IW images not overlapping in all images. Notwithstanding this missing data, the 6 months temporal baseline generated a mean vertical velocity of -0.0072±0.003 m/year for the entire scene with values ranging from -0.048 ± 0.005 m/year to 0.019 ± 0.004 m/year. The 2 year temporal baseline generated a mean vertical velocity of -0.0048 ± 0.002 m/year with values ranging from -0.0223 ± 0.0017 m/year to 0.008 ± 0.0014 m/year. As was evident with the ERS data, the standard error of the Sentinel-1 velocities also increases over agricultural and forested areas due to intermittent coherence.

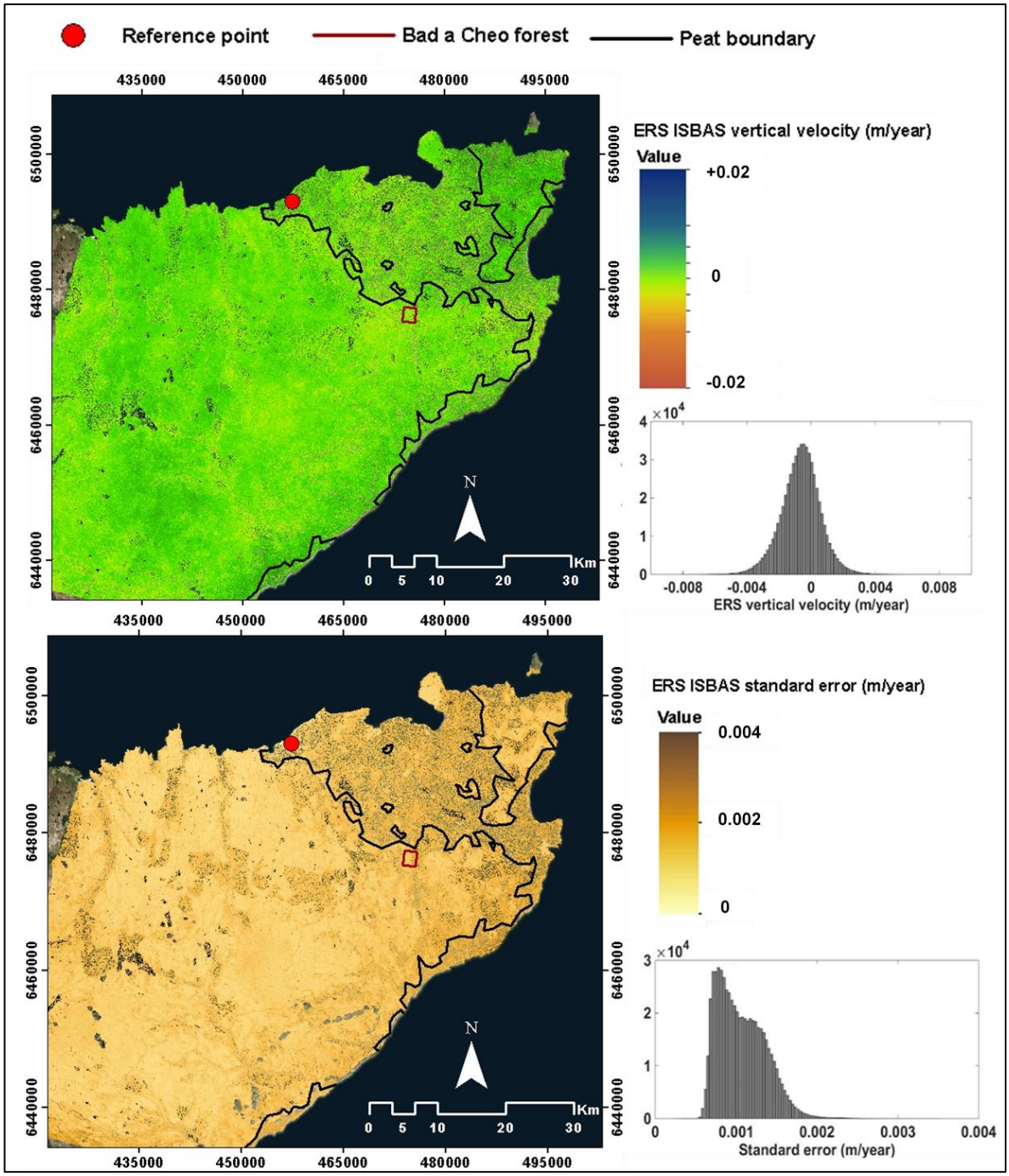


Figure 5.5: ERS ISBAS vertical velocity map with standard error map and their statistical distribution. The red dot represents the location of the stable reference point (location - Dounreay on the Northern coast at 456984 E, 6493400 N) used in the ISBAS processing. Black line shows the boundary of peatland over Flow Country. Red rectangle represents the location of the Bad a Cheo forest Reserve. Projection: WGS_1984_UTM_Zone 30.

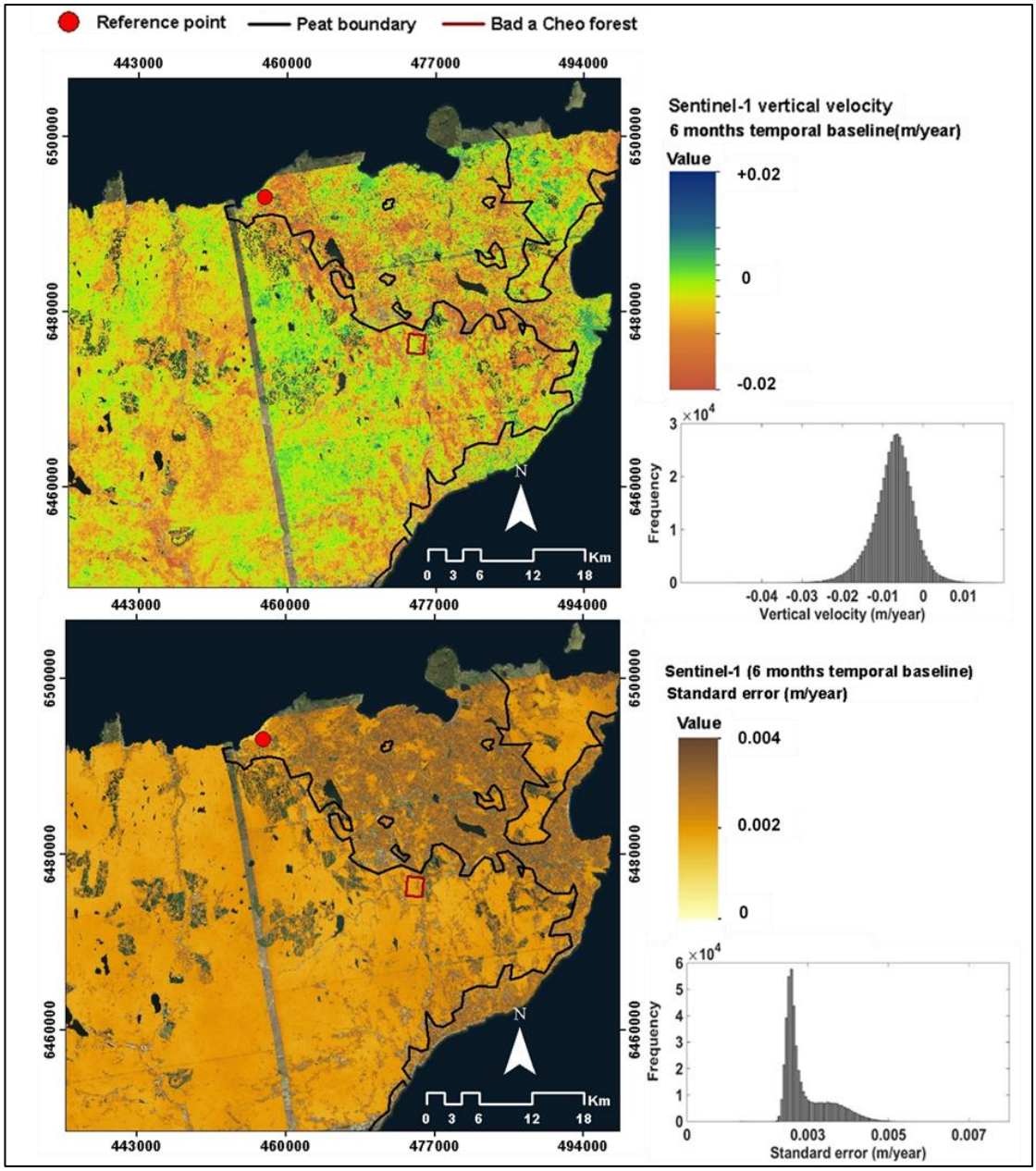


Figure 5.6: Sentinel-1 ISBAS (6 months temporal baseline) vertical velocity map with standard error map and their statistical distribution. The red dot represents the location of the stable reference point (location - Dounreay on the Northern coast at 456984 E, 6493400 N) used in the ISBAS processing. Black line shows the boundary of peatland over Flow Country. Red rectangle represents the location of the Bad a Cheo forest Reserve. The transect that dissects the study area along the track direction is due to the swaths that made up the IW images not overlapping in all images. Projection: WGS_1984_UTM_Zone 30.

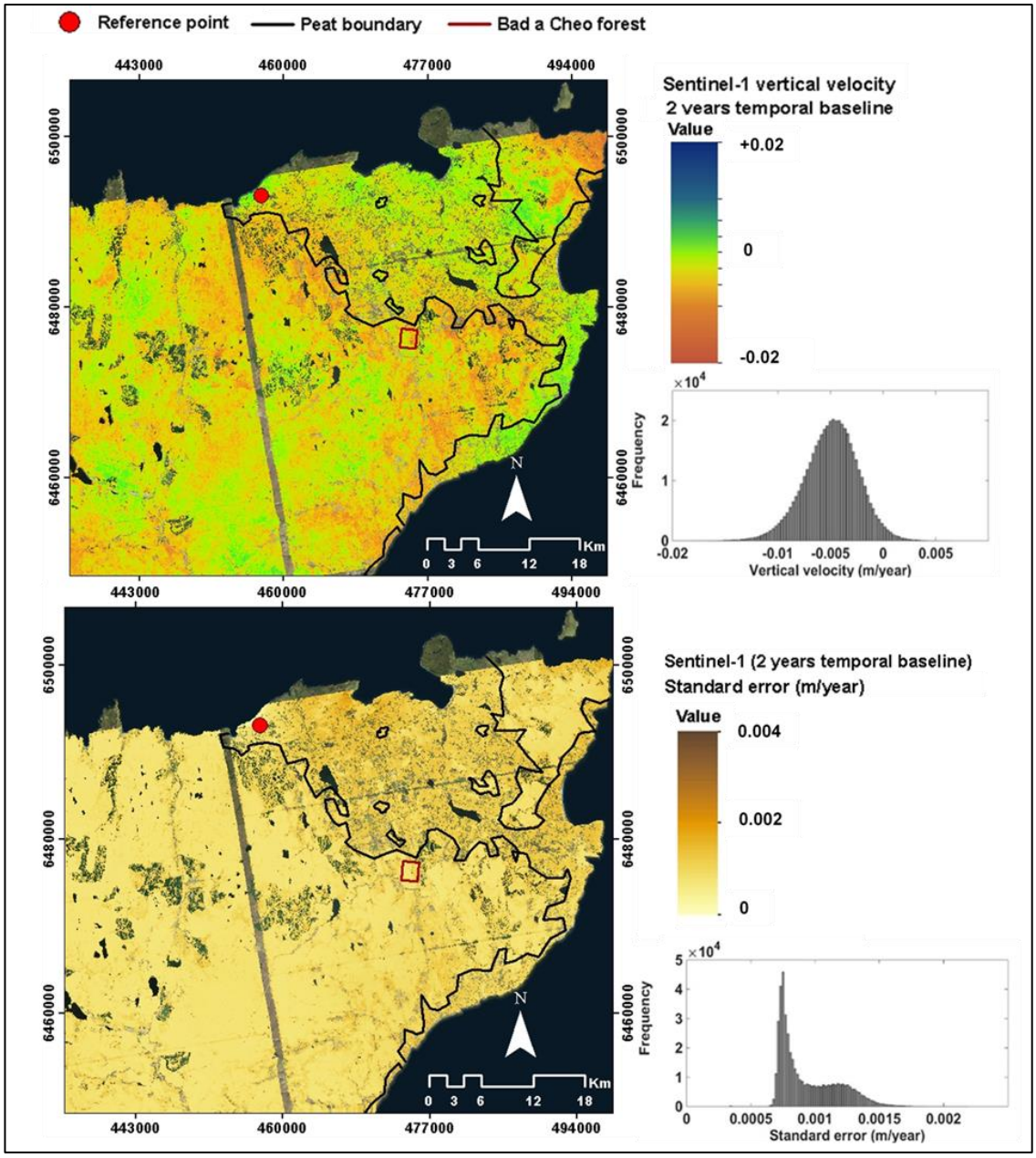


Figure 5.7: Sentinel-1 ISBAS (2 years temporal baseline) vertical velocity map with standard error map and their statistical distribution. The red dot represents the location of the stable reference point (location - Dounreay on the Northern coast at 456984 E, 6493400 N) used in the ISBAS processing. Black line shows the boundary of peatland over Flow Country. Red rectangle represents the location of the Bad a Cheo forest Reserve. The transect that dissects the study area along the track direction is due to the swaths that made up the IW images not overlapping in all images. Projection: WGS_1984_UTM_Zone 30.

5.2.5.1 Qualitative analysis

At the scale of the whole scene, the qualitative analysis indicates that the highest rates of subsidence occur at the margins of the peatlands where the peatland intercalates with agricultural land. This is most obvious along the eastern margin of the Flow Country, which is also the area that receives the lowest precipitation (www.metoffice.gov.uk). High values of subsidence are also associated with plantation forestry and, in upland areas, with bare peat. Four areas of interest are highlighted to illustrate the qualitative relationships to land cover/use at higher spatial resolution (**Figure 5.8**). These areas show that peatland pool systems are clearly associated with areas of stability or uplift, as are areas of peatland far from lines of drainage. Plantation forest and clear-felled forest are clearly associated with subsidence, although within forested areas this relationship is not uniform. The main effect of the plantations is to reduce the water content of the underlying peat and thus cause subsidence. The Flow country extract indicates that the north east is dominated by subsidence rates of more than 0.005 m/year and this is a forested area. The one stable area of the scene to the southwest is that showing healthy peat as indicated by the pool systems. The Bowside Lodge extract is a classic peatland area - dominated by stability or slight uplift – with minimal drainage and pool systems evident; the one area of high subsidence rates through the centre-left of the scene intersects with forestry. The Loch Sletill extract is one dominated by subsidence and features bare peat, forest and clear felled forest (in the south west). Lastly, the south Westerdale scene is mixed in terms of surface motion. Those areas dominated by stability or uplift (central area and to the southeast) are far from lines of drainage and/or feature a peatland pool system. These described observations between surface motion and land cover/use align entirely with the expected peatland condition of the Flow Country as a landscape and indicate that the InSAR data provides a meaningful, qualitative and relative indicator of peatland condition. Further and robust utility of these data would be provided if the velocities obtained had absolute meaning.

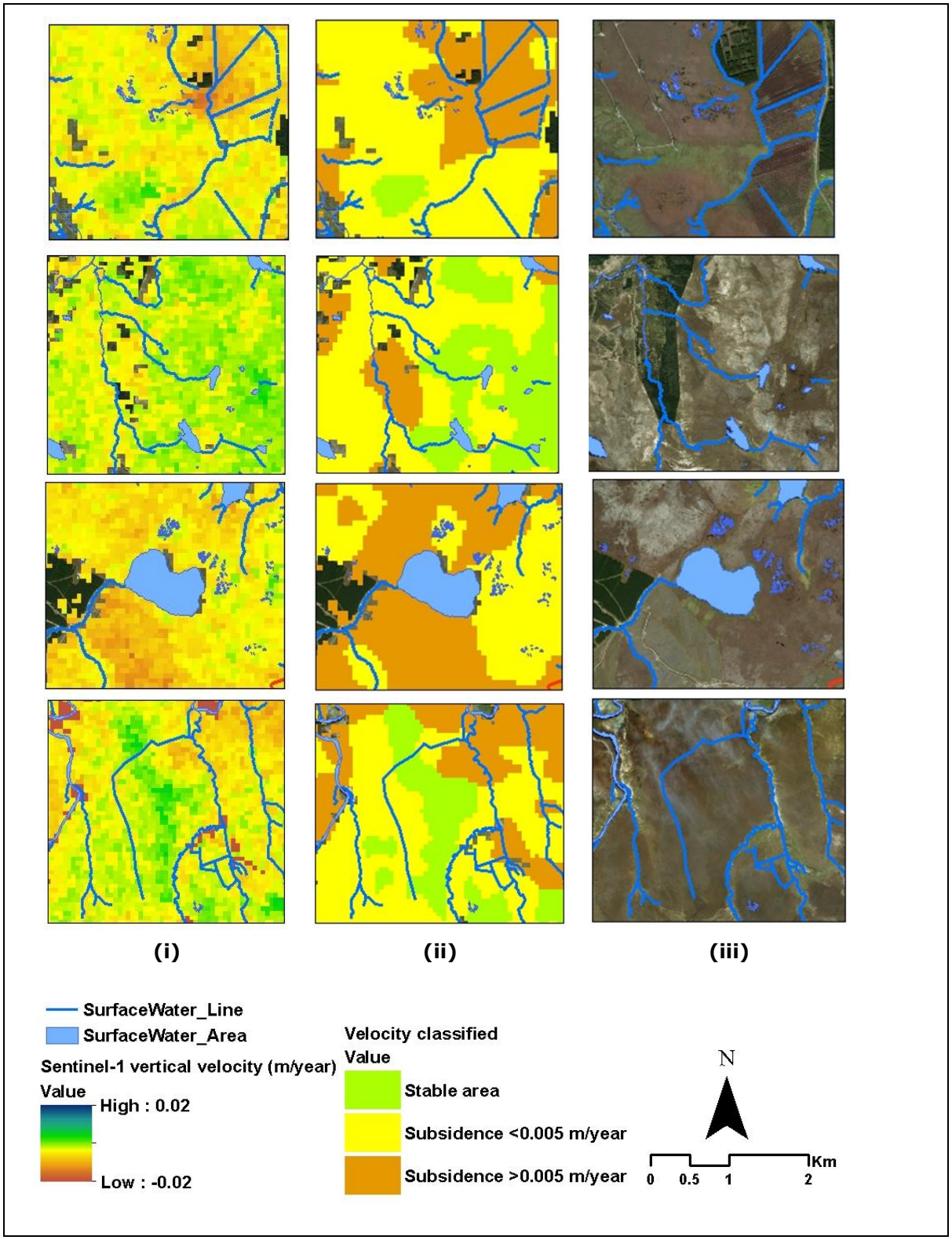


Figure 5.8: Sentinel-1 ISBAS vertical velocity maps (i) along with their outputs having undergone unsupervised segmentation (ii) to illustrate three main classes of (stable areas, subsidence at rates less than 0.005 m/year and subsidence at rates of more than 0.005 m/year. Corresponding Google Earth VHR imagery (iii) to aid interpretation over the same area for four different locations (from top to bottom): Flow Country; Bowside Lodge Loch; Sletill and South Westerdale.

5.2.5.2 Quantitative analyses

At the scale of the whole Bad a Cheo Forest Reserve the overall trend of motion as captured by the InSAR data was of subsidence; this was the case for the both ERS and Sentinel-1 data (for both 6 months and 2 year temporal baselines) (**Figure 5.9**). The ERS satellite measured a mean rate of subsidence across the period 1992 to 2000 was of -0.0019 m/year with an associated standard error of 0.0001 m/year. For Sentinel-1 ISBAS data using 6 months and 2 year temporal baselines the mean rates of subsidence across the period of March 2015 to December 2016 were -0.009 m/year and -0.006 m/year respectively. The associated mean standard error was 0.001 m/year respectively.

At the scale of the four blocks as a whole within the Reserve, the overall trend of motion as captured by the InSAR was of subsidence; this was the case for both the ERS and Sentinel-1 data for both temporal baselines used across the period under investigation (**Figure 5.9**). The mean rate of subsidence for the blocks as a whole for ERS ISBAS points was -0.002 m/year and the associated mean standard error was 0.0004m/year. The Mann-Whitney U test analyses comparing this ERS measure with that measured by the levelling (n1) illustrates that while the ERS data (n2) correctly predicts the direction of ground motion (i.e., subsidence) its magnitude (**Figure 5.9 a** and **Figure 5.10 a)** is different to that measured by the levelling data (at the 95% level of confidence) (n1 = 16; n2 = 12). For the exact same time period, the mean of the levelling measurements was -0.01 m/year and its standard error 0.001 m/year. For the Sentinel-1 data, it was the case that the mean of the levelling measurement for the period of comparison was -0.016 m/year and its standard error 0.009 m/year. Comparing this (n1) with the Sentinel-1 ISBAS (n2) mean and SE using the Mann-Whitney U test reveals that for both the 6 month and 2 year temporal baseline there was no difference at 95% level of confidence in the measurements. The Sentinel-1 data (using a 6 month baseline) had a mean rate of movement of -0.007 m/year with a standard error of 0.001 m/year and the Sentinel-1 (using a 2 year baseline) had a mean rate of movement of -0.005 m/year with a standard error of 0.001 m/year.

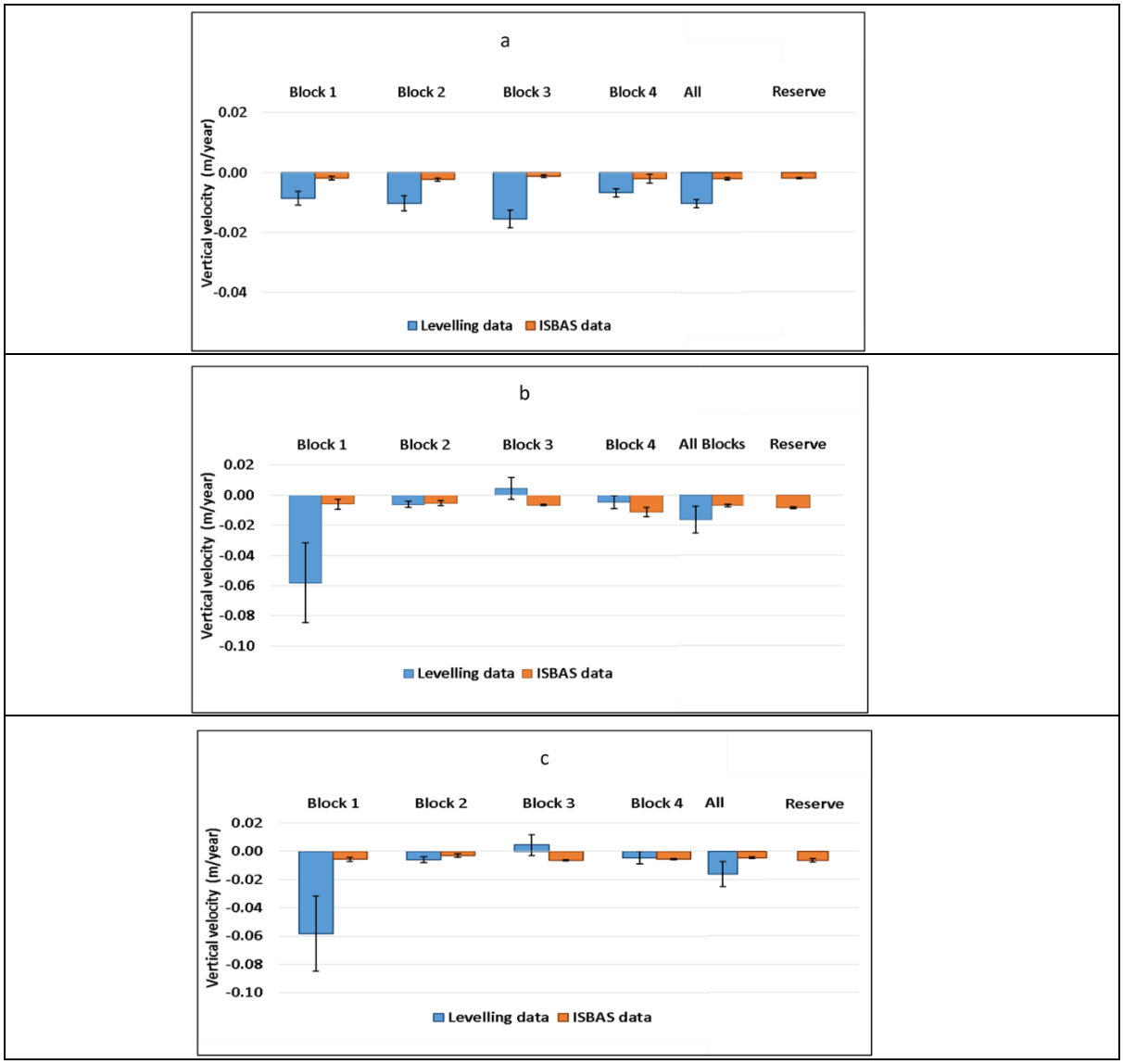


Figure 5.9: (**a**) The rate of the deformation between ERS ISBAS points and levelling transect block means over Bad a Cheo forest Reserve for each block individually, for the blocks combined and for the Reserve as a whole. The average rates of surface motion with the standard error of the mean are used to plot both levelling (blue bars) and ISBAS measurements of displacement occurring during the relevant time periods (orange bars); (**b**) the rate of the deformation between Sentinel-1 (with a six-month baseline) ISBAS points and levelling transect block means over Bad a Cheo forest Reserve for each block individually, for the blocks combined and for the Reserve as a whole. The average rates of surface motion with the standard error of the mean are used to plot both levelling (blue bars) and ISBAS measurements of displacement occurring during the relevant time periods (orange bars); (**c**) the rate of the deformation between Sentinel-1 (2 year baseline) ISBAS points and levelling transect block means over Bad a Cheo forest Reserve for each block individually, for the blocks combined and for the Reserve as a whole. The average rates of surface motion with the standard error of the mean are used to plot both levelling (blue bars) and ISBAS measurements of displacement occurring during the relevant time periods (orange bars).

By looking at **Figure 5.10** and **Figure 5.11**, it is evident that, although the general trend of the Reserve measured by both the InSAR ISBAS and the levelling methods is that of subsidence, there is spatial variability within the Reserve with some of the ISBAS output points showing uplift, and the pattern of variability differs between that captured by the ERS and Sentinel-1 satellites. Taking each Block individually, it is the case that the levelling data shows an approximately linear trend of motion in all four blocks (**Figure 5.10 a** and **b**); however, the variability of the velocity is greater than the variability in velocity measured with the InSAR ISBAS data. As a case in point, during the 2 year period covered by the Sentinel-1 data, the average of the levelling measurements per block indicate that 3 blocks were subsiding (block 1 with 0.04 m/year, block 2 with 0.004 m/year and block 4 with 0.003 m/year) and one block (block 3) experienced uplift of about 0.003 m/year (**Figure 5.10 b**). Although caution is required here as levelling measurements were only made on two occasions and also the final measurement made was prior to the end date of the Sentinel-1 acquisitions, it is the case that comparison with the Sentinel-1 measurements (**Figure 5.10 b** and **Figure 5.11b**, **c**) indicates a mismatch with block 3, with both temporal baseline outputs showing subsidence, albeit at small rates, rather than uplift during this period.

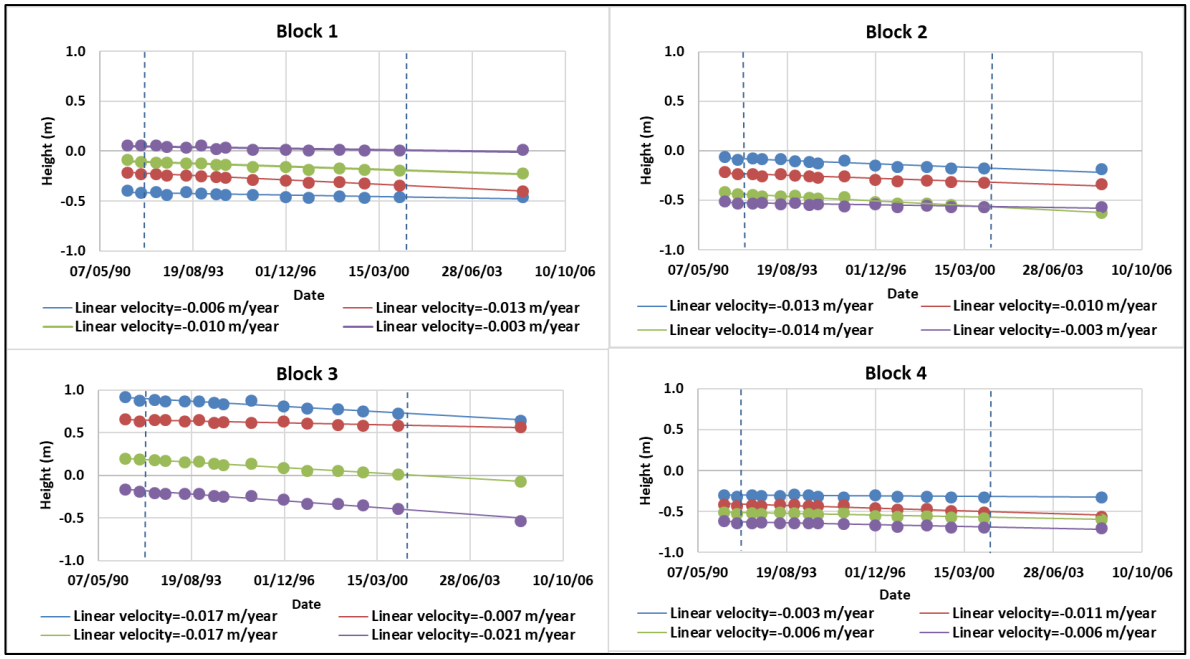


Figure 5.10 a: The 4 levelling transect mean heights in each block. The vertical dashed lines represent the start and end of ERS acquisitions.

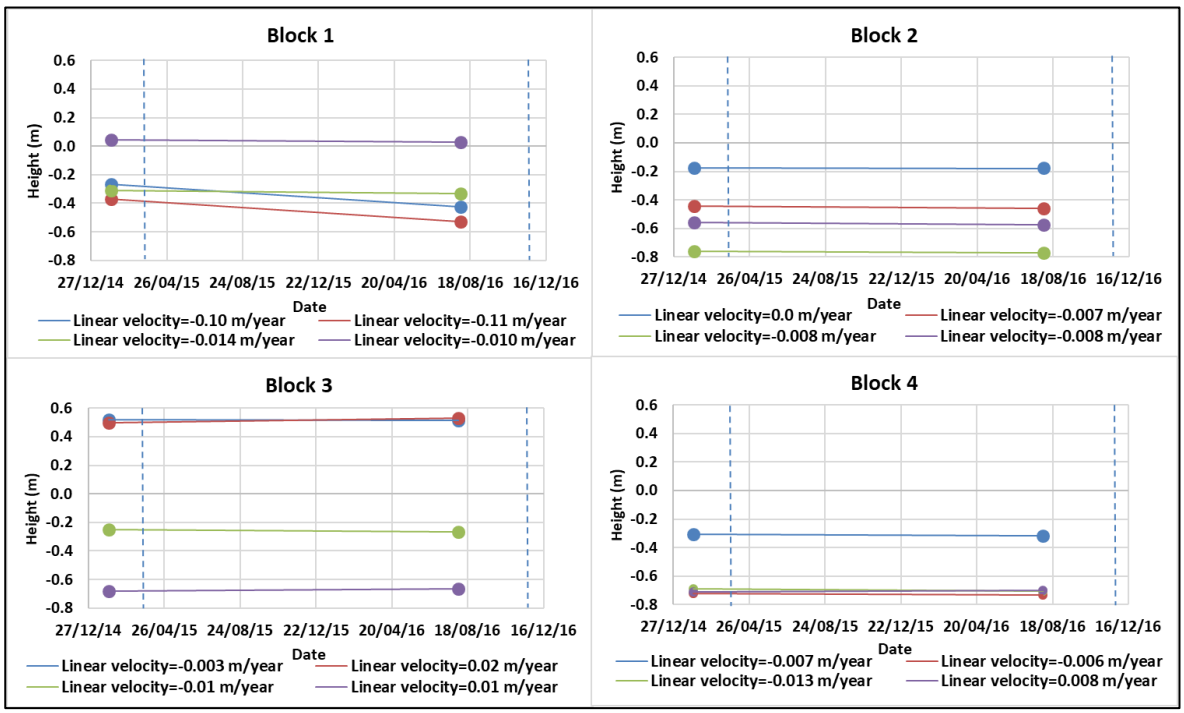


Figure 5.10 b: The 4 levelling transect mean heights in each block. The vertical dashed lines represent the start and end of Sentinel-1 SAR acquisitions

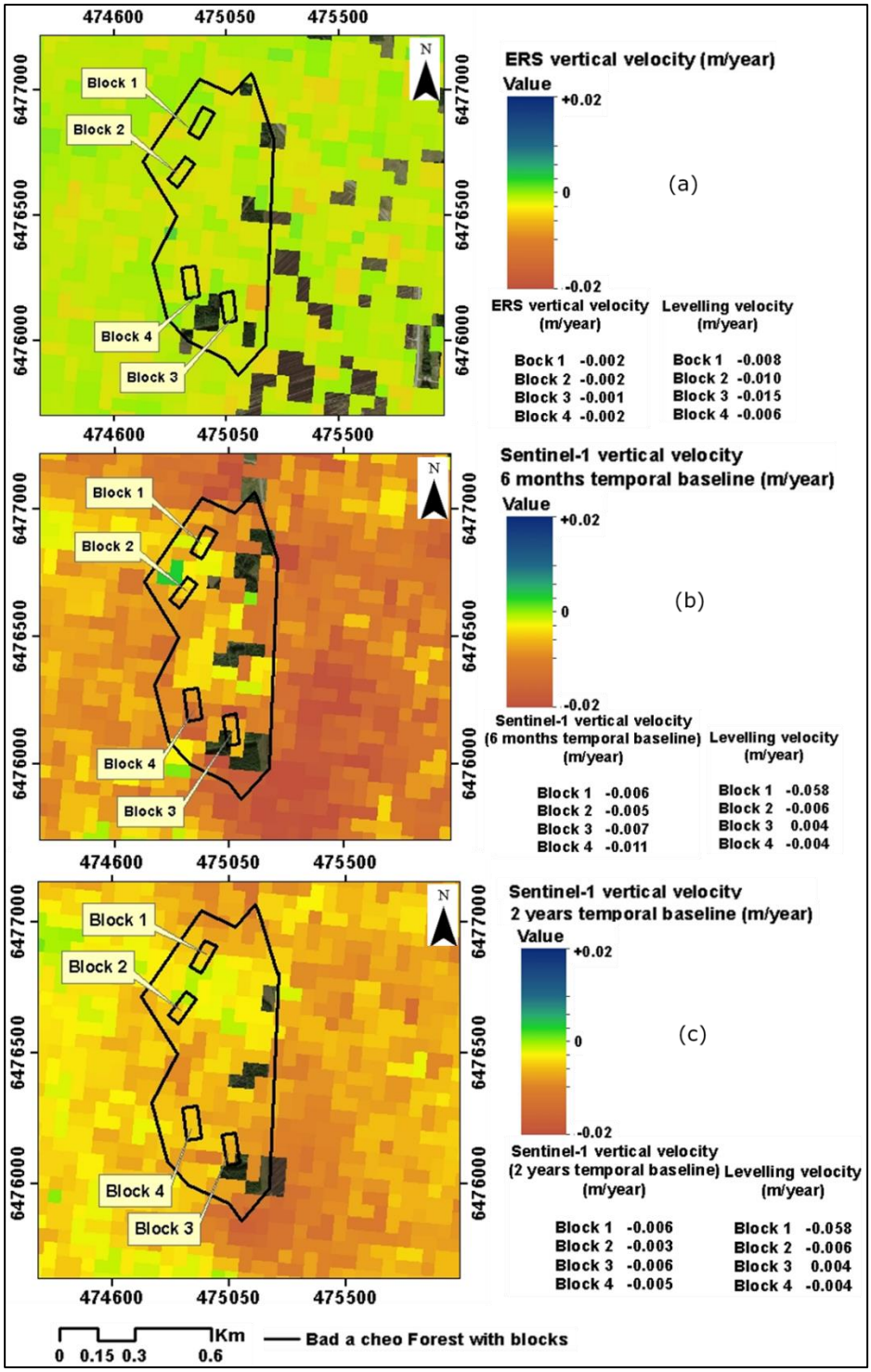


Figure 5.11: ISBAS vertical velocities maps with levelling benchmarks overlaid. (a) ERS ISBAS vertical velocity map. (b) Sentinel 1 ISBAS vertical velocity map (6 months temporal baseline). (c) Sentinel 1 ISBAS vertical velocity map (2 years temporal baseline). Projection: WGS_1984_UTM_Zone 30.

5.2.6 Discussion

The ISBAS maps of surface motion output for Flow Country of Scotland, UK represent the first contiguous maps of peatland surface motion. Using knowledge of peatland surface motion as provided by ground data, i.e., through interpretation of land cover shown on high spatial resolution optical satellite data and best available levelling measurements, the real potential of using satellite InSAR data processed using the ISBAS method has been demonstrated. This is much needed mapping given the links between peatland condition and ecosystem services and, although it is difficult to fully explain from this work the exact magnitudes in the differences and uncertainties, the results presented here indicate that further investigation of this methodology should be undertaken. Full validation of this remote sensing method for this application is required, particularly given that the levelling measurements were not designed for the validation of such mapping. Further work could pay dividends and would build upon previous studies that have only alluded to the possibility of peatland surface motion being measured by InSAR/ISBAS but had much less evidence from ground observations to support conclusions e.g., (Shimada et al., 2013; Cigna et al., 2014; Cigna and Sowter, 2017). This study over temperate peatland is also a useful addition to the literature on InSAR for peatlands. All previous, albeit few InSAR studies undertaken to date have been in very different peatland environments to that of the Flow Country. Moreover, these studies have used different SAR data and processing techniques. Subsidence of up to 7.65 cm/year was reported in Central Kalimantan, Indonesia using the SBAS technique applied to ALOS L-band data (Zhou et al., 2016) and up to 1 cm/year in the Zennare Basin in Venice Lagoon Italy using ERS data in Interferometric Point Target Analysis (IPTA) (Teatini et al., 2007).

5.2.6.1 Qualitative discussion

Qualitatively, the results obtained seem to present a meaningful account of peatland condition in terms of its growth, stability or subsidence across the entire region that would appear to match expectations in areas where the conditions are either known or can be reasonably derived from interpretation of optical satellite data. The overall trend of peat surface subsidence for the Flow Country revealed by the InSAR outputs concurs with expectations, based on the fact that much of the area of peatland is drained, afforested or eroding. It is reasonable to assume that, in the case of drained or eroding ground, there is a net of greenhouse gas emissions. This assumption cannot be made for afforested ground which is thought to be a net source initially due to peat disturbance and drainage, becoming a net sink as tree growth sequesters carbon and

reverting to a net source after 50 to 200 years as carbon dioxide release from the breakdown of timber products starts to exceed sequestration of the trees (Cannell et al., 1993). On this basis, the values of the InSAR outputs are considerable in their landscape spatial resolution and this should enable identification of areas undergoing change and support more effective monitoring, management and intervention. Thus, the results obtained are encouraging and suggest that, in this era of BigInSAR (Cigna and Sowter, 2017), this study is timely; it indicates the value in using InSAR data to support a monitoring system of peatland at all spatial scales (Kim et al., 2017). The need for the increase in InSAR data via higher temporal resolution afforded by constellations is demonstrated by the ERS results here, which were comprised by the gaps in the time series-this meant using a four-year temporal baseline, resulting in the measurement of small deformation rates in comparison to what the Sentinel-1 data measured (due to ambiguity). Regular acquisitions of Sentinel-1 with a short repeat cycle of 12 days made it possible to decrease the temporal baseline and measure greater rates of deformation.

5.2.6.2 Quantitative discussion

Quantitatively, as already stated, there is, however, further work to be conducted to fully understand the value of InSAR/ISBAS output maps, particularly, given that the quantitative accuracy of the ISBAS method over peatland is hard to fully establish on the basis of this study. The results of the quantitative analyses come with the limitation that recognises that the levelling data were not collected for the purpose of comparison with the satellite-derived measurements of surface motion. Hence, results are to be treated with some caution, with only general patterns noted. In both levelling and InSAR measurements, there will be some degree of error propagation that will need to be fully quantified in future studies. For example, an error analysis on the levelling data reveals sources of error during transect reading (e.g., telescope instability, curvature, and rounding error) that could be up to ±18 mm and further that, during local datum level reading, another ±18 mm of error could be introduced. This combined with an estimated error of -0.17 mm/year due to a different reference point being used for the InSAR (i.e., the InSAR vertical velocity at the reference point) and levelling measurements, indicates the need for further work, particularly focused on the quantitative validation of the InSAR vertical velocity outputs.

For future validation studies, several issues need to be considered. One issue concerns the temporal mismatch between the levelling measurements and Sentinel-1 data. Unfortunately, the Sentinel-1 dataset for this study was constrained by the periods for which

the levelling results were collected (and the project in the Bad a Cheo reserve ended) so could not extend this time period. Another issue is that the levelling transect, which is typical of peatland studies, lacked the systematic spatial coverage to adequately validate the InSAR. Nevertheless, this has been useful in building upon the qualitative comparison in demonstrating that forested areas on peatland have an overall trend of subsidence. At the scale of the reserve as a whole, both the levelling measurements and the InSAR ISBAS outputs for both ERS and Sentinel-1 (six-months and two-years temporal baseline) satellites agree that the peatlands of the Bad a Cheo reserve are subsiding. Given that the peatland in this particular area is covered with trees, which lowers water tables and makes the peat compact, this is encouraging. Furthermore, spatial variations seen in the ISBAS DInSAR outputs may be explained by the fact that earlier levelling work at the Bad a Cheo Reserve has shown high spatial variability in surface level change related to the layout of the forest plots and other unknown causes (Shotbolt et al., 1998). Within the forest plots, variability in surface level change relates to the tree species or species mixture, the different surfaces of the ploughing micro-relief and the deep drains and associated spoil ridges.

Nonetheless, the accuracy of the InSAR measurements shows differences and uncertainties when compared with the levelling measurements. This could be a result of questions around the suitability of levelling measurements made along transects at 42 × 20m resolution to compare against a pixel size of approximately 100 m × 100 m. Any further validation campaign should adopt calibration and validation methods designed for measuring contiguous mapping (i.e., be randomly located) and consider intra-pixel deployment of levelling measurements. That said, however, peatland is predominantly water (typically about 95% in volume) and surface motion both short and long term is predominantly driven by changes in the mass of water within the peat body (e.g., Kennedy and Price, 2005). Hydraulic continuity operates on scales much greater than 100 m, the scale of mire units (mesotopes) and mire complexes (macrotopes) (Lindsay et al., 2016). As the mass of water within the peat increases the pressure increases and the surface expands; as water is removed, the peat collapses. Long-term bog growth results from the accumulation of both carbon (plant matter) and water. Given that hydraulic continuity operates on scales greater than 100 m, it could therefore be a reasonable assumption that independent measures of surface motion should display the same trends and rates over long periods of time.

Notwithstanding these known shortcomings of the levelling measurements, they are indicative of the range of vertical movement that could be present at this site—up to −0.11

m/year. Within the Reserve, neither of the satellites measured motion that extreme. This is due to the limitation imposed by the radar and the chosen temporal baseline relative to the actual rate of surface motion. The smoothing of displacements when averaging the information present in the SAR data by heavy multi-looking might also explain the findings. Phase unwrapping has the greatest influence on the quantitative measurement of deformation on an individual interferogram. Phase unwrapping is applied to determine the phase ambiguity that occurs whenever there is a fringe in an interferogram (i.e., when the phase jumps from + to − radians or vice versa). When fringes are well-defined and there is no noise, this can be a simple task; however, when there is noise and coherent pixels are sparse, such as in vegetated areas, this can be very difficult and lead to an underestimation of fringes and, consequently, an underestimation of the deformation. Another limitation imposed by radar is the atmospheric signal (a predominant InSAR error source). Although this signal is well removed using ISBAS technique for data acquired over long epochs (Cigna and Sowter, 2017; Gee et al., 2017) ERS in this study, using data over a short time period may reduce the ability to accurately retrieve the underlying velocity signal (Sowter et al., 2016; Gee et al., 2017). This is the most likely reason for ISBAS underestimating the magnitude of peatland subsidence in the Reserve (Alshammari et al., 2018).

5.3 SAR data processing over Zennare Basin (Venice Lagoon, Italy)

5.3.1 Site overview

As explained in chapter four, the Zennar basin is a subsiding area of the Lagoon lying below mean sea level. It was completely reclaimed in the 1930s for agricultural use and at present is characterized by the presence of bogs with a large fraction of outcropping peat soil (less than 2m thick) which provide evidence of the existence of ancient swamps (Rizzetto et al., 2003). The area is progressively sinking due to the bio-oxidation of the peats in the upper aerated zone (Gambolati et al., 2005; Teatini et al., 2007) which increases the vulnerability and geological hazard such as river flooding, riverbank stability and intrusion of seawater in the aquifer system (Tosi et al., 2000). **Figure 5.12** illustrates the land cover classification map of the Lagoon adapted from CORINE 2012 which shows that the agricultural land is the most dominant class within the Lagoon and within the basin.

5.3.2 Data

As determined by the availability of SAR data over the study area, remotely sensed data from three SAR satellite systems were used in this study (refer to **Chapter 4, Section 4.3.2**); this

permits for a different set of measurement scenarios to be examined. As determined by availability, dataset one was comprised of sixty-one ERS 1/2 C-band VV polarised SAR images from a descending orbit acquired for a long-monitoring period between May 1992 and January 2001 (see **Chapter 4, Table 4.5**). Dataset two (determined by availability) was comprised of fifty-one ENVISAT ASAR scenes from a descending orbit also acquired for a long-monitoring period between April 2003 and December 2008 (see **Chapter 4**, **Table 4.6).** The last dataset which is also determined by the availability was comprised of eighty-seven Sentinel-1 Interferometric Wide (IW) SLC images acquired from satellite A in a descending orbit over a much shorter monitoring period between January 2015 and March 2018 (**Chapter 4, Table 4.7**). **Figure 5.13** shows the footprints of the ERS, ENVISAT and Sentinel-1 SAR image frames. The three datasets were processed separately using the ISBAS DInSAR technique (refer to **Chapter 2, Section 2.3**) to calculate annual surface motion velocities (m/year) and their standard errors during the respective monitoring periods across Venice Lagoon, and particularly the Zennare basin.

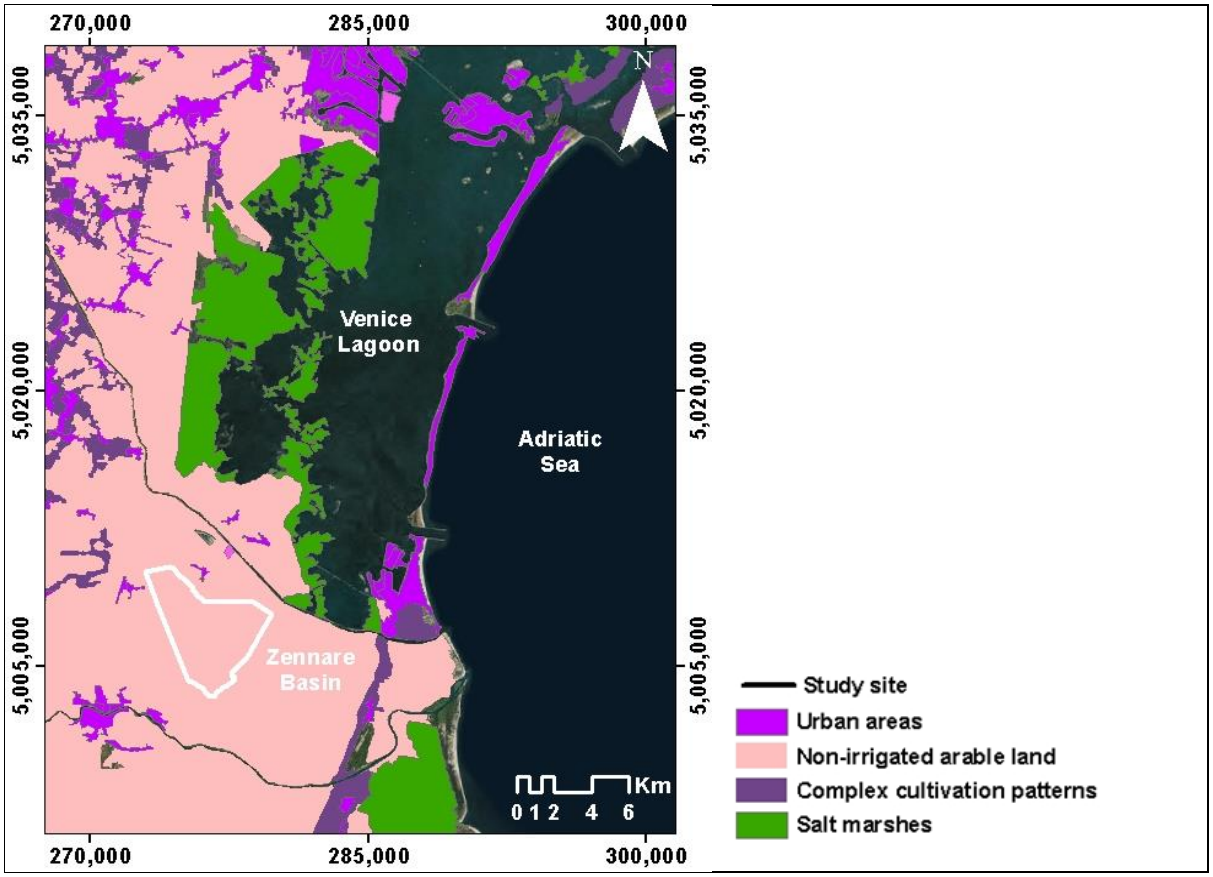


Figure 5.12: A land cover classification map of the Venice Lagoon, Italy taken from the CORINE 2012 (Co-ordinated Information on the Environment) Land cover inventory. (WGS-1984-UTM-Zone-33N).

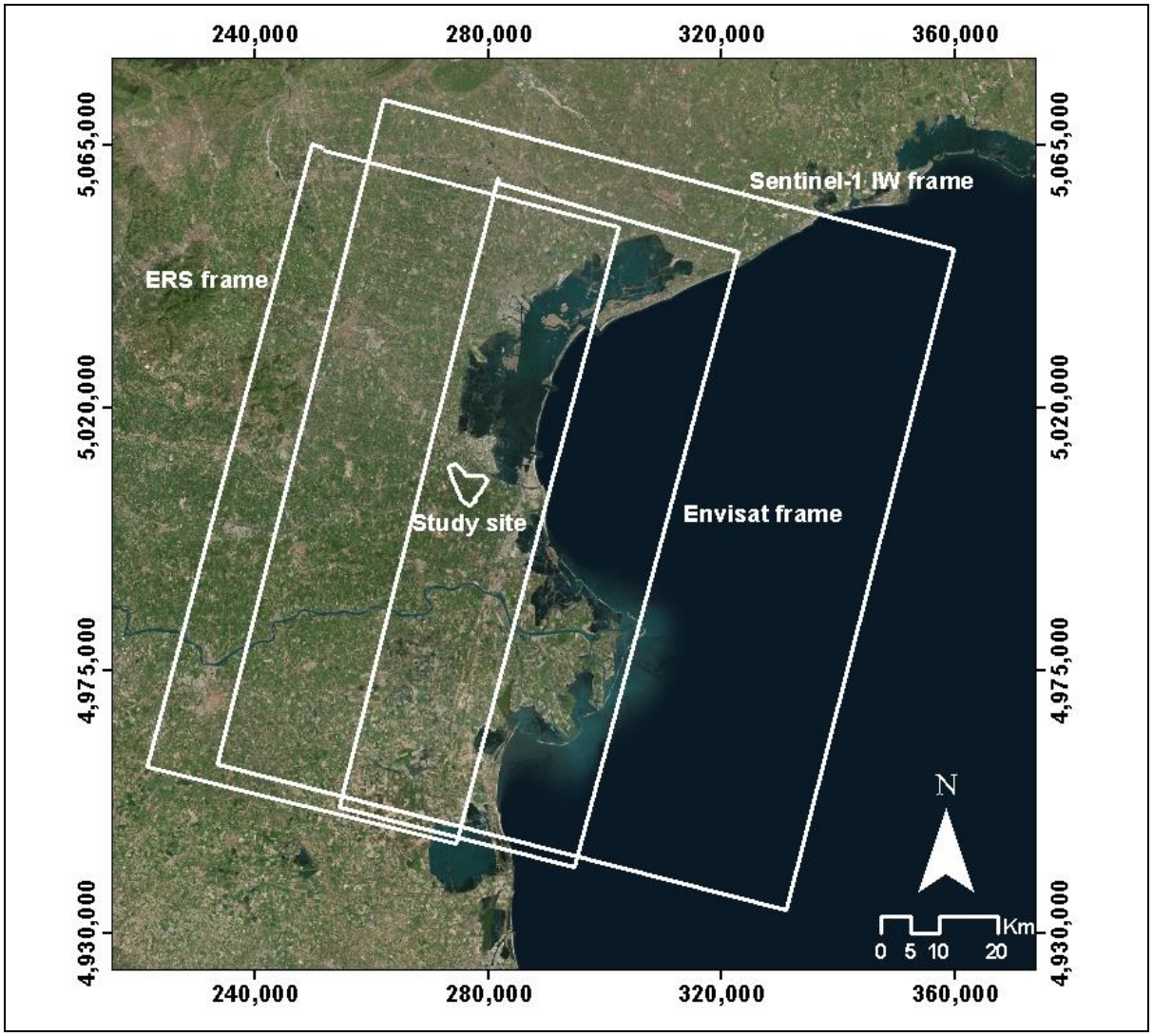


Figure 5.13: Footprints of the ERS, ENVISAT and Sentinel-1 SAR image frames. (WGS-1984-UTM-Zone-33).

5.3.3 SAR data processing using ISBAS technique

The same procedures explained in **Section 5.2.3** (refer to **Chapter 2, Section 2.3)** have been followed to process the three datasets. The ISBAS technique was used for the processing with temporal and orbital baseline constraints to maximize the spatial coherence and to minimize the contribution of DEM errors in the generation of interferograms. To reduce the noise in the radar signal, the scenes were multi-looked in both rang and azimuth using factors of 4 X 20 pixels for ERS and ENVISAT datasets and 22 X 5 pixels for Sentinel-1 to produce a final pixel dimension of about 100 X 100m in ground range for ERS and ENVISAT and 80 X 70m for Sentinel-1. Then the ISBAS processing was performed for coherent points only that had average coherence greater than or equal to 0.25 in a minimum number of interferograms. Differential interferograms were generated by calculating the phase difference between a pair

of images and subtracting off a simulated phase calculated using the image geometry and a digital elevation model from the SRTM mission. Phase unwrapping was then implemented using a statistical cost network flow algorithm described by Chen and Zebker (2001) for unwrapping all the ISBAS points within each interferogram using the same stable reference point located in the south west of Sottomarina at 45°11'50''N 12°16'59''E for all datasets. The selection of the reference point was made subject to a statistical consideration relating to the coherence of the signal with the minimum standard deviation of the phase in all interferograms (i.e., the reference point has a high coherence and displays a low phase standard deviation across all interferograms) and the subsidence history over the study area. Sottomarina is used since is a high coherence area with low noise and is suggested as being stable, in agreement with the previous regional studies (Teatini et al., 2005; Teatini et al., 2007).

5.3.3.1 ERS ISBAS processing

The sixty-one ERS C-band VV polarised SAR images were processed using constraints of a maximum 250m perpendicular baseline and four years temporal baseline between any interferometric pair used. The resultant interferograms (pair) are illustrated in **Figure 5.14 a**, where the total number of the generated interferograms using a threshold value of 120 (minimum number of interferograms) was 369, corresponding approximately to 20% of the possible pair combinations of ERS dataset.

5.3.3.2 ENVISAT ISBAS processing

Same as ERS ISBAS processing, the fifty-one ENVISAT ASAR images were processed using constraints of a maximum 250 perpendicular baseline and four years temporal baseline between any interferometric pair, which resulted in 396 interferograms (**Figure 5.14 b**) corresponding to 28% of the possible pair combinations of the ENVISAT dataset. The threshold value of 120 interferograms was used as a minimum point threshold.

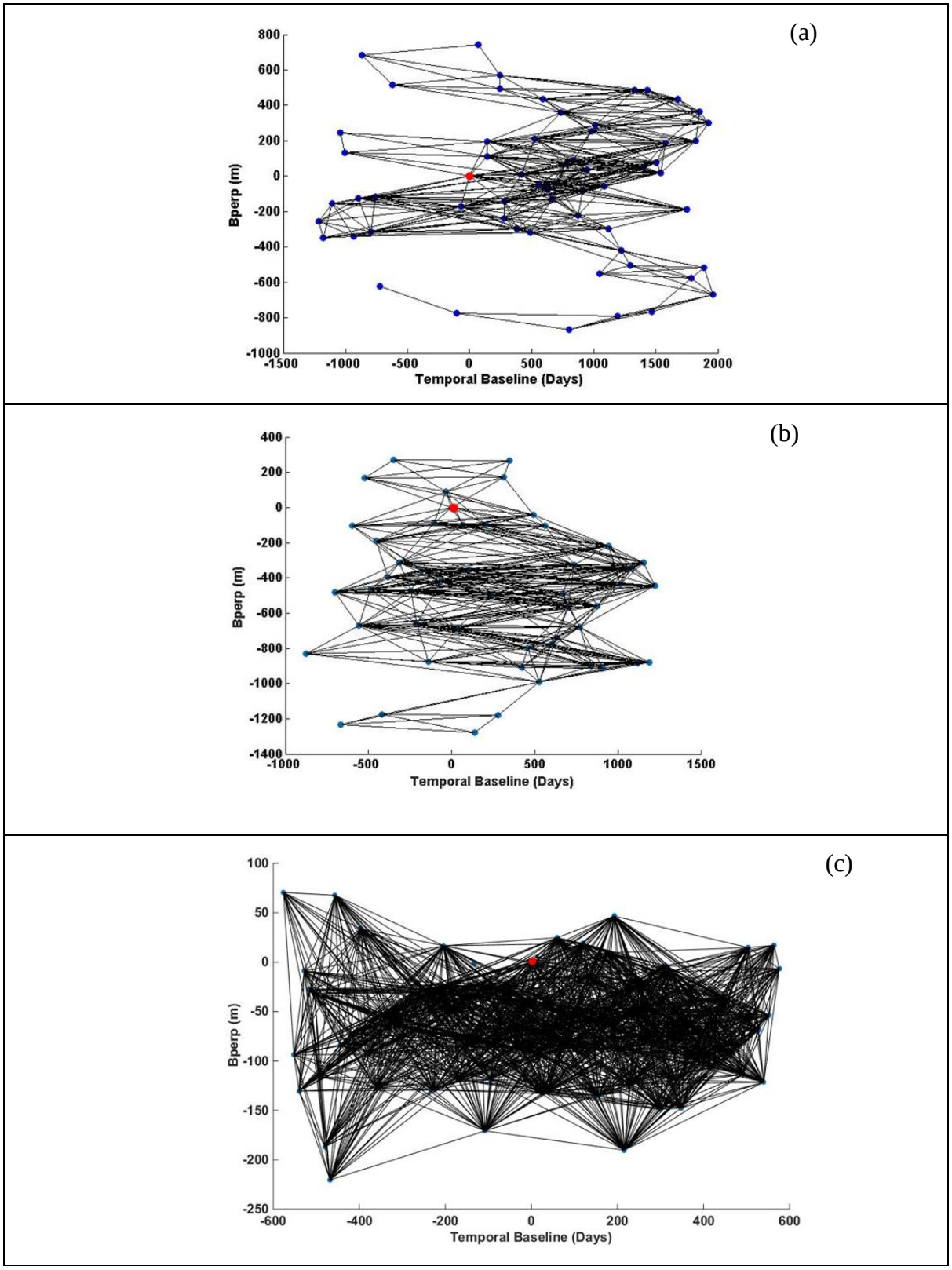


Figure 5.14: Perpendicular and temporal baselines of the image pairs relative to the master scene (a) ERS SAR with four-years temporal baseline (master: 21 August 1995) (b) ENVISAT ASAR with four-years temporal baseline (master: 24 August 2005) (c) Sentinel-1 SAR with one-year temporal baseline (master: 2 August 2016). Red point is the master SAR image.

5.3.3.3 Sentinel-1 ISBAS processing

The eighty-seven Sentinel-1 Interferometric Wide (IW) SLC images were processed with a maximum normal perpendicular baseline of 200m and one-year temporal baseline to reduce the phase ambiguity over this farm peatland environment. The generated interferograms were 1958 which corresponds to 52% of the possible pair combinations (**Figure 5.14** c). The point threshold value was 684 interferograms.

5.3.4 Data analysis

The resultant LOS velocity maps produced from the processed ERS, ENVISAT and Sentinel-1 data were evaluated qualitatively through comparisons with previously published studies used InSAR over the same area. LOS ISBAS velocity outputs from the three datasets were output as a raster layer and orthorectified using nearest neighbour interpolation to provide pixels at a uniform 50m spacing in UTM map projection.

5.3.5 Results

For the three datasets (ERS, ENVISAT and Sentinel-1), the spatial coverage of LOS velocity maps over the vegetated area of the Venice Lagoon provided significant coverage over land. As explained previously, the ISBAS coverage over rural and vegetated areas represents a solution density: the ratio between the number of the ISBAS pixels providing a solution density and the total number of pixels on land (Cigna and Sowter, 2017). For ERS ISBAS, the coherent points covered approximately 75% of the of the total land cover classes in the processed frame **Figure 5.15**. For ENVISAT and Sentinel-1 datasets, they covered approximately 81% and 88% of the processed scene respectively (**Figure 5.16** and **Figure 5.17**). The distribution of ISBAS coherent points was densest in urban areas as well as in rural and vegetated areas. However, the best quality of ISBAS points occurs when the points are coherent in all interferograms, where these points represent SBAS points and they are limited over vegetated areas and they account for only 7% for ERS dataset, 8% for ENVISAT and 11% for Sentinel-1 (**Figure 5.15**, **Figure 5.16** and **Figure 5.17**).

The ERS derived LOS velocity maps and histograms (**Figure 5.15**) show the spatial and statistical distribution of velocities and their standard errors for the period 1992 to 2001. Negative LOS velocities indicate subsidence, while positive values indicate uplift. The mean LOS velocity of all ERS ISBAS points across the entire scene was -0.00097±0.001 m/year,

with maximum subsidence of about -0.0064±0.0013 m/year and maximum uplift of +0.004±0.0014 m/year. Over agriculture areas including the peatland area (**Figure 5.15**), the standard error is very high due to the intermittent coherence. ENVISAT derived LOS velocity maps and histograms (**Figure 5.16**) illustrate the spatial and statistical distribution of velocities and their standard errors for the period 2003 to 2008. These velocity maps overlap with those obtained with the ERS data. The mean LOS velocity of all ENVISAT ISBAS points was -0.001±0.0009 m/year with values ranging from -0.0066±0.001 m/year to 0.004±0.001 m/year. Sentinel-1 derived LOS velocity and histograms (**Figure 5.17**) show the spatial and statistical distribution of velocities and their standard errors calculated using a temporal baseline of one year for the period 2015 to 2018. The velocity maps overlap from the south with those obtained from both ERS and ENVISAT datasets, so they all cover the farm peatland area (Zennare Basin). For the Sentinel-1 dataset, the mean vertical velocity for the entire scene was -0.0002±0.001 m/year with values ranging from -0.009±0.0004 m/year to 0.004±0.0009 m/year. As was evident with ERS data, the standard error of both ENVISAT and Sentinel-1 velocities increases over agriculture areas due to intermittent coherence.

5.3.5.1 Qualitative analysis

At the scale of the whole scene, qualitative analysis of both ERS and ENVISAT ISBAS maps shows the general stability of the central part of the Lagoon for the period of 1992 to 2008 which is confirmed by other studies (Teatini et al., 2007; Teatini et al., 2012), whereas the subsidence rates increase in the northern and southern part of the Lagoon (**Figure 5.15** and **Figure 5.16**). Sentinel-1 ISBAS maps, on the other hand, show a clear pattern of the deformation with lower standard errors of the velocities in comparison with ERS and ENVISAT datasets for the southern part of the Lagoon (**Figure 5.17**).

At the scale of the whole farm peatland area (Zennare Basin), the overall trend of motion as captured by InSAR technique was almost stable; this was the case in all three of the datasets (**Figure 5.18**). The ERS satellite measured a mean rate of motion of -0.0008±0.0009 m/year with values ranging from -0.003±0.001 m/year to 0.002±0.001 m/year. For the ENVISAT dataset, the mean rate of surface motion was -0.0005±0.0009 with values ranging from -0.004±0.001 m/year to 0.002±0.0009 m/year. For the Sentinel-1 satellite, the measured mean rate of motion was -0.0003±0.001 m/year with values ranging from -0.005±0.0005 m/year to 0.003±0.001 m/year respectively. However, a published multi-temporal DInSAR study using ERS IPTA technique found that the subsidence rate at the north part of the basin

was up to -0.01 m/year, which was likely caused by the consolidation process for the remnants of the organic soil (Teatini et al., 2007).

It is evident from **Figure 5.18** that, although the general trend of the farm peatland area (Zennare Basin) measured by the three InSAR datasets was almost stable, there is a clear spatial variability and lack of coverage within the ISBAS output points. It should be noted that all ISBAS points over the Zennare Basin from the three datasets are intermittent coherent points with a minimum number of interferograms (**Figure 5.15**, **Figure 5.16** and **Figure 5.17**); therefore, the noise in the output results is expected to be high. Due to the lack of ground observations over this site, the application of ISBAS using ESA Sentinel-1 C-band to evaluate peat condition using InSAR time-series has not been applied in the next chapter.

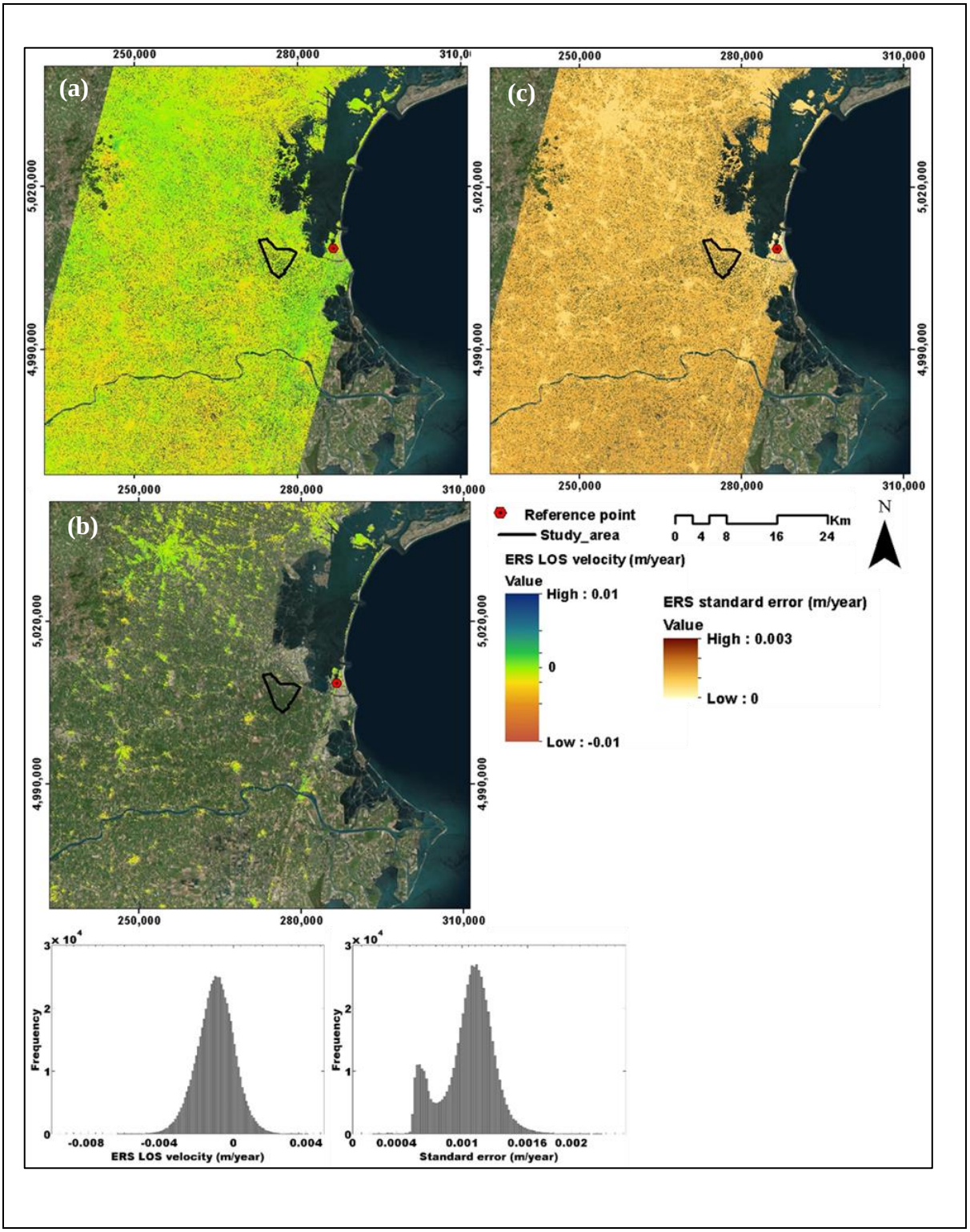


Figure 5.15: (a and b) ERS ISBAS and SBAS LOS velocity maps respectively. (c) ISBAS standard error map along with the frequency distributions of ISBAS velocity and ISBAS standard error. The red dot represents the location of the stable reference point (location: south-west of Sottomarina) used in ISBAS processing. The black line represents the location of the peatland area (Zennare Basin). WGS-1984_UTM_Zone_33.

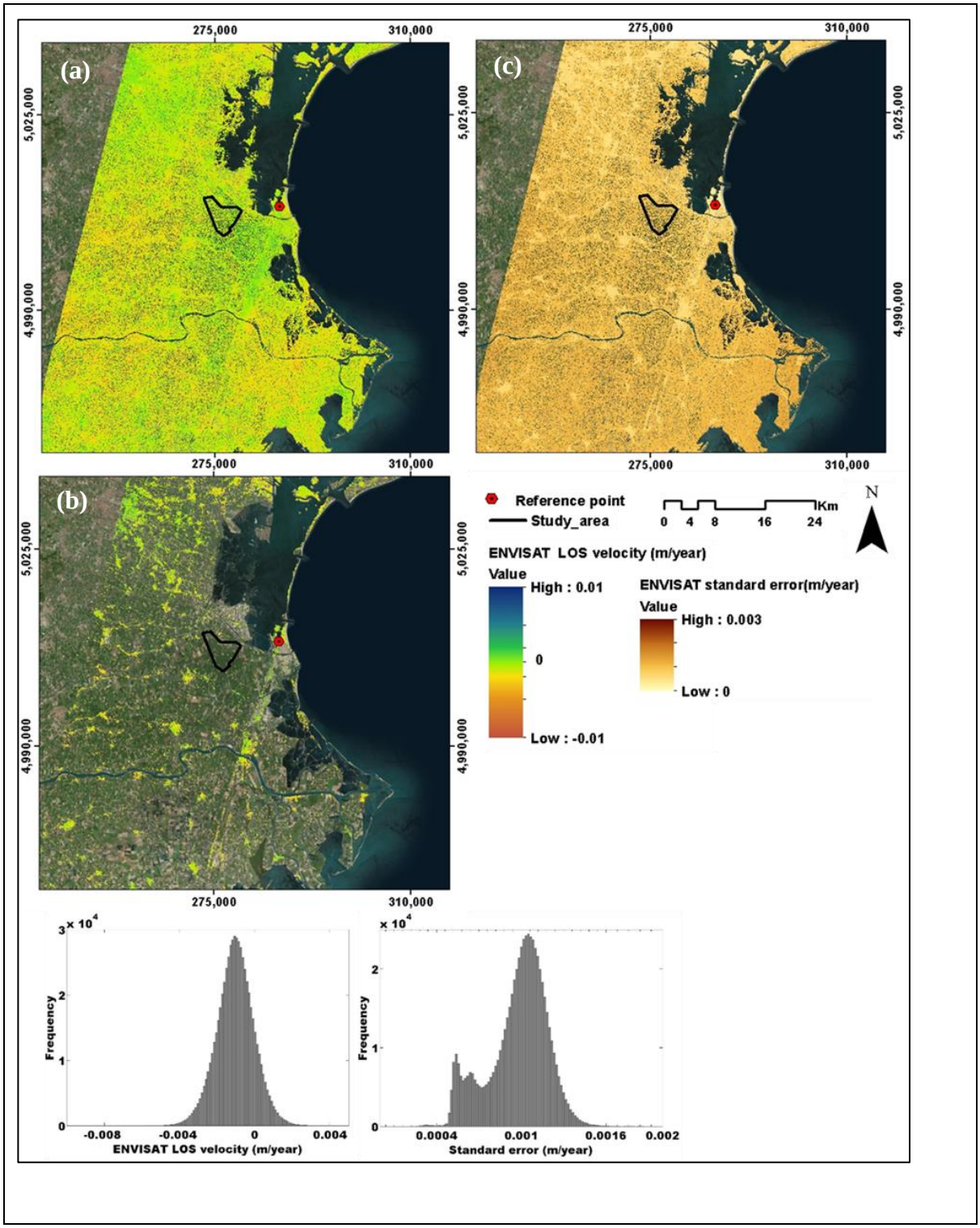


Figure 5.16: (a and b) ENVISAT ISBAS and SBAS LOS velocity maps. (c) ISBAS standard error map along with the frequency distributions of ISBAS velocity and ISBAS standard error. The red dot represents the location of the stable reference point (location: south-west of Sottomarina) used in ISBAS processing. The black line represents the location of the peatland area (Zennare Basin). WGS-1984_UTM_Zone_33.

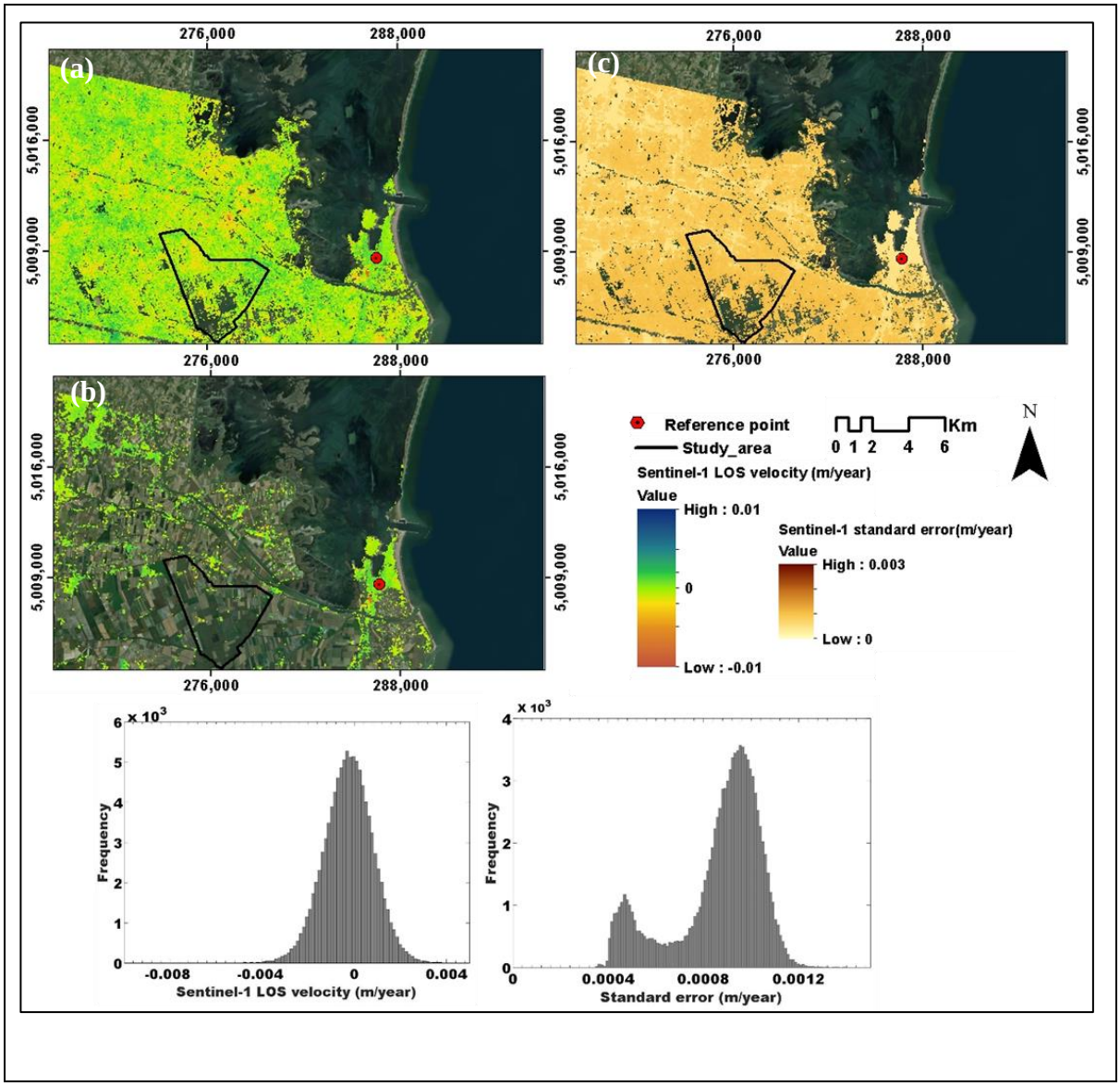


Figure 5.17: (a and b) Sentinel-1 ISBAS and SBAS LOS velocity maps. (c) ISBAS standard error map along with the frequency distributions of ISBAS velocity and ISBAS standard error. The red dot represents the location of the stable reference point (location: south-west of Sottomarina) used in ISBAS processing. The black line represents the location of the peatland area (Zennare Basin). WGS-1984_UTM_Zone_33.

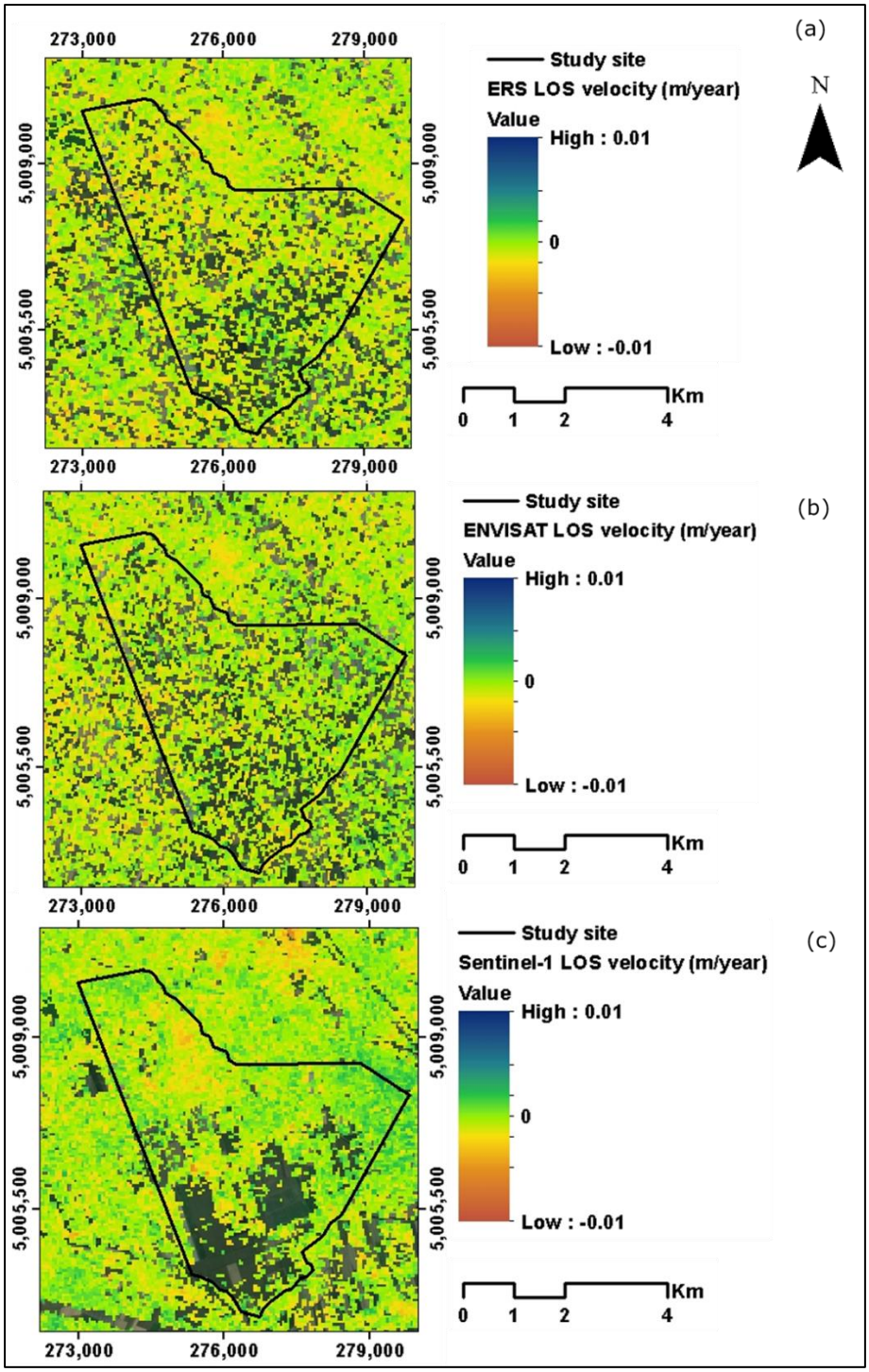


Figure 5.18: ISBAS LOS velocity maps over farmed peatland area (Zennare Basin). (a) ERS ISBAS velocity map. (b) ENVISAT ISBAS velocity map. (c) Sentinel-1 ISBAS velocity map. WGS_1984_UTM_Zone_33.

5.3.6 Discussion

The LOS velocity maps generated from the three SAR datasets show the real potential of using ISBAS DInSAR technique to provide surface motion over the Venice Lagoon, where the arable land class (unfavourable for InSAR) represents the dominant class over this area. These maps enable quantification of surface deformation over a wide area in the LOS direction.

The LOS velocity maps from both ERS and ENVISAT processing almost matched in their overlapping area. The central part of Venice Lagoon showed a stable trend, while the subsidence rates increased in the northern and southern part of the Lagoon, which is preserved in both results and correlated with ERS-IPTA result from Teatini et al. (2007). However, the estimated rate of deformation from ERS-IPTA result is much higher than ISBAS results from both ERS and ENVISAT processing, which can be attributed to the difference in spatial resolution of the results; the ISBAS technique uses multi-looking, whereas the IPTA technique works on full resolution pixels. For the Sentinel-1 dataset, the LOS velocity map overlapped from the south with those obtained from both ERS and ENVISAT processing, so that they have all covered the farm peatland area (Zennare Basin). The estimated LOS velocity map using Sentinel-1dataset is more consistence and the distribution of the deformation is less noisy in comparison with ERS and ENVISAT ISBAS maps. This can be assigned to the regular acquisitions of the Sentinel-1 satellite with a short repeat cycle of 12 days, which made it possible to gather a large stack of images in short temporal period and also made it possible to decrease the temporal baseline to one year to preserve the coherence over this vegetated area. However, evaluation of the accuracy of all ISBAS maps is hindered due to the absence of the ground measurement data in the area.

As suggested from the comparison between the ISBAS and SBAS maps, the Zennare Basin (farm peatland area) is dominated by low coherence targets that are characterized by high standard errors due to the limited number of interferograms used in the ISBAS analysis; consequently, the maps from the three datasets are somewhat noisy with lack of coverage. It should be noted that the LOS velocity is estimated assuming monotonic motion of the target. However, this farm peatland area is an agriculture area which is cultivated continuously (Camporese et al., 2008). In these areas, the surface is always changed due to the ploughing or harvesting between the observations, which therefore contributes to increasing the error in the estimated phase (Gabriel et al., 1989). Moreover, errors imposed by radar as explained in

Section 5.2.5.2 above are also expected to propagate into the results due to sparse coherence points.

The spatial variability of the ISBAS LOS velocity results from the Sentinel-1 satellite over the Zennare Basin is less in comparison with the two other datasets (ERS and ENVISAT) over the same area. However, the lack of both coverage, particularly in the southern part of the Basin (where the peat layer is located) and validation hindered the use of Sentinel-1 ISBAS DInSAR time-series to evaluate the peat condition over this agriculture area. It should be noted that with the Sentinel-1 dataset, it is possible to decrease the point threshold of the minimum number of the coherent interferograms that contribute to the analysis of each ISBAS pixel to get acceptable coverage over this vegetated area; however, this increases the uncertainty, in turn, increases noise of the output results. Moreover, this area is dedicated to corn growing (Camporese et al., 2008); therefore, the peat condition over this area cannot be quantified using plant functional type to be compared with ISBAS time-series of surface motion like in the Flow Country (Scotland) because it is managed peatland area. But the peat surface motion over this area can be quantified, for example, using the hydrological field measurements (Zanello et al., 2011) and linking them with InSAR time-series. Therefore, the ISBAS results processed using Sentinel-1 data over the Zennare Basin have not been used for further analysis (i.e., to evaluate peat condition using Sentinel-1 ISBAS time-series).

5.4 Summary of the limitation of using ISBAS technique over peatland

Taking into consideration the discussion of using ISBAS methodology over both the Flow Country in the north east of Scotland and the Zennare Basin in the south of Venice Lagoon (Italy), the summary of the limitations of applying this technique can be outlined as follows:

1. Temporal decorrelation: peatland areas exhibit a generally dynamic and variable temporal behaviour with changing environmental conditions. Moreover, management of these areas causes a continuous change of the surface motion due to ploughing and harvesting which decreases the coherence between the interferometric pairs. The occurrence of temporal decorrelation (low coherence) over these areas represents a significant challenge during the processing, mainly with the use of C-band InSAR. Although these effects can be usually mitigated through using SAR pairs with small temporal separation, the gaps in ERS and ENVISAT time-series, in particular with long revisite cycle of 35 days, preclude to decrease the temporal baseline to less than 4 years

which enhances the decorrelation and causes under estimation of the deformation for the areas with high deformation rates due to phase ambiguity.

2. Phase unwrapping errors: temporal decorrelation over these vegetated areas and steep phase gradient due to, for example, sudden slide movement triggered by intense rainfall can easily lead to phase unwrapping error.
3. Atmospheric phase components: in the linear analysis, the estimation of the deformation (LOS-velocity) and the DEM error for each coherent target is made assuming the atmospheric signal is random over time and thus has zero mean. This assumption can be considered valid for a large stack of interferograms that are properly distributed over a long period of time.

5.5 Summary

The processing strategies and the final results of the long-term deformation over two different peatland areas as quantified from Synthetic Aperture Radar (SAR) measurements have been presented. The analysis of ISBAS results over the Flow County indicates that the InSAR technique can provide a meaningful qualitative result which can be used as an indicator of peatland condition in terms of its accumulation, stability or subsidence. The ISBAS results over the Zennare Basin (farm peatland area in Venice Lagoon, Italy) on the other hand, are less correlated and show a clear spatial variability and lack of coverage within the area. Moreover, the scarcity of the ground measurements made it not possible to use ISBAS results from Sentinel-1 data for further analysis. The next chapter addresses the feasibility of ISBAS time-series (non-linear part) to evaluate peat condition through its surface motion.

CHAPTER 6

METHODOLOGY AND RESULTS FOR QUANTIFYING PEATLAND CONDITION FROM INSAR TIME-SERIES DATA VIA ITS SURFACE MOTION CHARACTERISTICS

6.1 Introduction

Despite the numerous advancements that have been achieved in the InSAR field, linking InSAR techniques with the oscillations of the peatland surface as an indicator of peatland condition has not been attempted. This chapter aims to investigate the application of InSAR, particularly the ISBAS technique, to evaluate peat condition. It uses the non-linear part of Sentinel-1 ISBAS DInSAR results processed in **Chapter 5** to quantify peat condition over the site that has been identified in the previous chapters to satisfy the aims and objectives laid out in **Chapter 1**. It begins with a brief introduction of peatland surface motion and the processes that may cause this motion. This is followed by a description of the processing methodologies used to process the SAR data and the analytical methods used to process the resultant data from the InSAR processing: Univariate Singular Spectrum Analyses (SSA) and Multivariate Singular Spectrum analyses (MSSA). The focus of this research is the Flow Country in Scotland.

6.2 Peatland surface motion

Peatland surfaces are highly dynamic and move in response to a range of processes, including peat growth due to accumulation of peat (Kennedy and Price, 2005; Fritz et al., 2008); long-term irreversible subsidence due to biological oxidation and decay of the organic material in drained peatland; short-term reversible subsidence (shrinkage/swelling process) due to the elastic response of the peat matrix to drying/wetting or freezing/thawing cycles (Price and Schlotzhauer, 1999; Kennedy and Price, 2005; Camporese et al., 2008; Fritz et al., 2008); biogenic gas release (Rosenberry et al., 2003; Glaser et al., 2004); variation in water table or water storage (Fritz et al., 2008) and buoyancy forces (Kellner et al., 2005; Strack et al., 2006a). Each of these processes can be related to the condition of the peat. Long-term steady growth is indicative of carbon sequestration and peat in good condition. Conversely, long-term subsidence is indicative of carbon loss and poor peat condition, and irreversible seasonal deformation is sensitive to the elastic properties of the peat matrix (Kennedy and Price, 2005).

To some extent the relationship between peat condition and surface motion is intuitive. For example, a degraded drained dense peat would be expected to display a markedly different response in surface motion to that of a low-density water and gas saturated pristine sphagnum peat. However, due to the lack of research, the sensitivity of the measured deformation to environmental change within a peatland landscape is not known and detailed studies of surface motion over high temporal resolutions are confined only to small geographical scales (Fritz et al., 2008; Reeve et al., 2013) on account of the logistical and financial challenges posed by large scale field survey. Recently InSAR, particularly the ISBAS technique, may provide a means of overcoming these difficulties (Sowter et al., 2013) and extending surface motion measures over whole regions and countries (Bateson et al., 2015). However, the mismatch between the scale of observation, accuracy and precision of InSAR and field observations makes it extremely difficult to validate the accuracy of the InSAR results. An alternative validation approach is to abandon concerns of absolute accuracy and focus on the capacity of the characteristics of the InSAR surface motion time-series to quantify peat condition, in effect using the InSAR time-series as an operationally defined measure. Therefore, this chapter assesses this more feasible approach by comparing the characteristics of ISBAS DInSAR surface motion time-series to readily obtained vegetation and land use based measures of peat condition. The underpinning hypothesis here is that the ISBAS DInSAR results are representative of the surface motion (at high temporal resolution) of the peatland and in turn that surface motion is representative of peat condition.

6.3 Application of univariate SSA to analyse peatland surface motion from ISBAS DInSAR time-series over the Flow Country, Scotland

A time-series provides useful information about the dynamics of a system that produces it. The main purpose of analysing the time-series is to identify some of the system's key properties by determining certain features of the time-series which can then help to understand and predict the future behaviour of that system (Ghil et al., 2002). Singular Spectrum Analysis represents a novel and powerful technique to analyse time-series data (Ghil et al., 2002; Hassani, 2007) and it has been used in different applications, such as mathematics, physics, economics, metrology, oceanology, social science and market research (Hassani, 2007). This method permits the decomposition of an original time-series of data into the sum of a small number of individual and interpretable components (e.g., slowly varying trend, oscillatory components and noise).

6.3.1 Sampling strategies of InSAR

This section describes a systematic methodology for analysing ISBAS DInSAR time-series of peatland surface motion using Univariate SSA tools. The proposed methodology can be used to extract seasonal trends from InSAR time-series and link it to the peat condition.

6.3.1.1 Location and site selection

After estimation of the linear deformation over the Flow Country, using the Punnet software (**Chapter 2, Section 2.3**), 22 sites have been selected based on this output to cover a spectrum of peat conditions. **Figure 6.1** shows the locations of the selected sites and **Figure 6.2** illustrates the linear deformation pattern from the ISBAS DInSAR technique over each site selected along with Google Earth Very High Resolution (VHR) imagery, to aid interpretation of peat condition over the same area for the 22 sites. Site selection was based on two approaches: 15 sites were chosen to cover different ranges of subsidence and uplift and the rest were chosen based on account of having detailed field measurements of peat condition. The resulting sites are widely dispersed and cover a broad range of altitude, peatland hydrological settings and conditions. An analysis was made for each site in order to classify its condition and this was done using optical satellite data (Sentinel-2 and Google Earth provided VHR data) and field observations of plant functional type (**Appendix C**, **Table C1**).

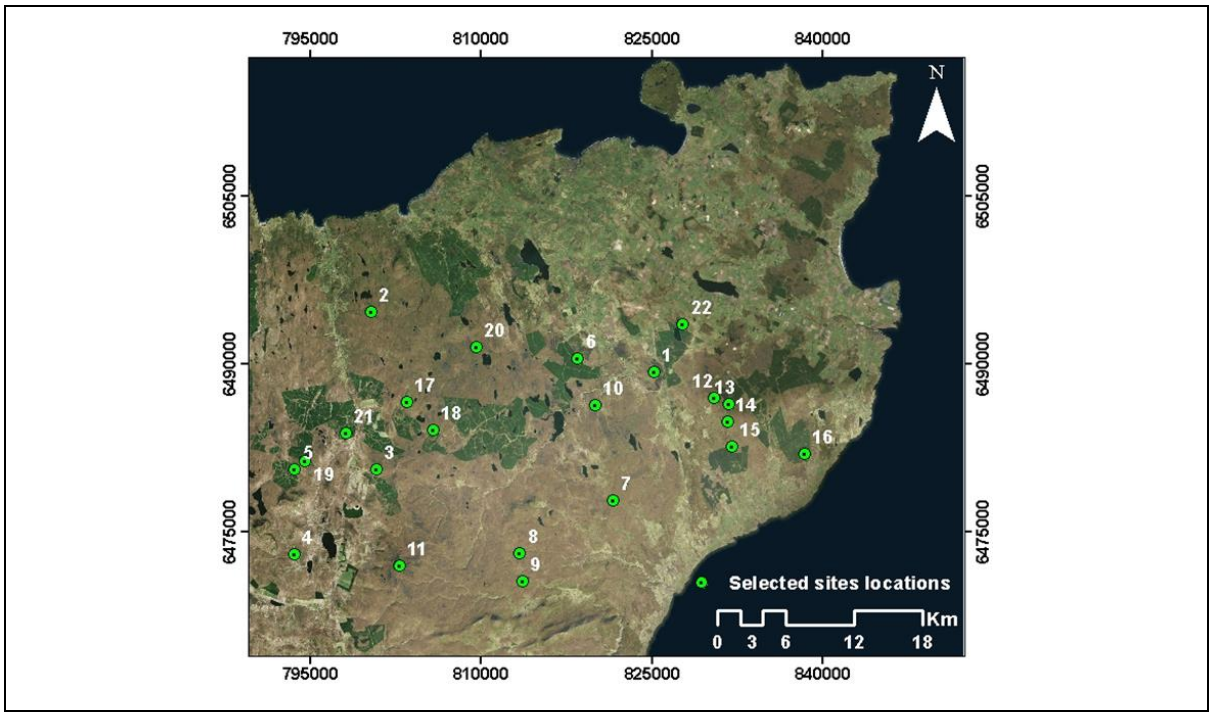
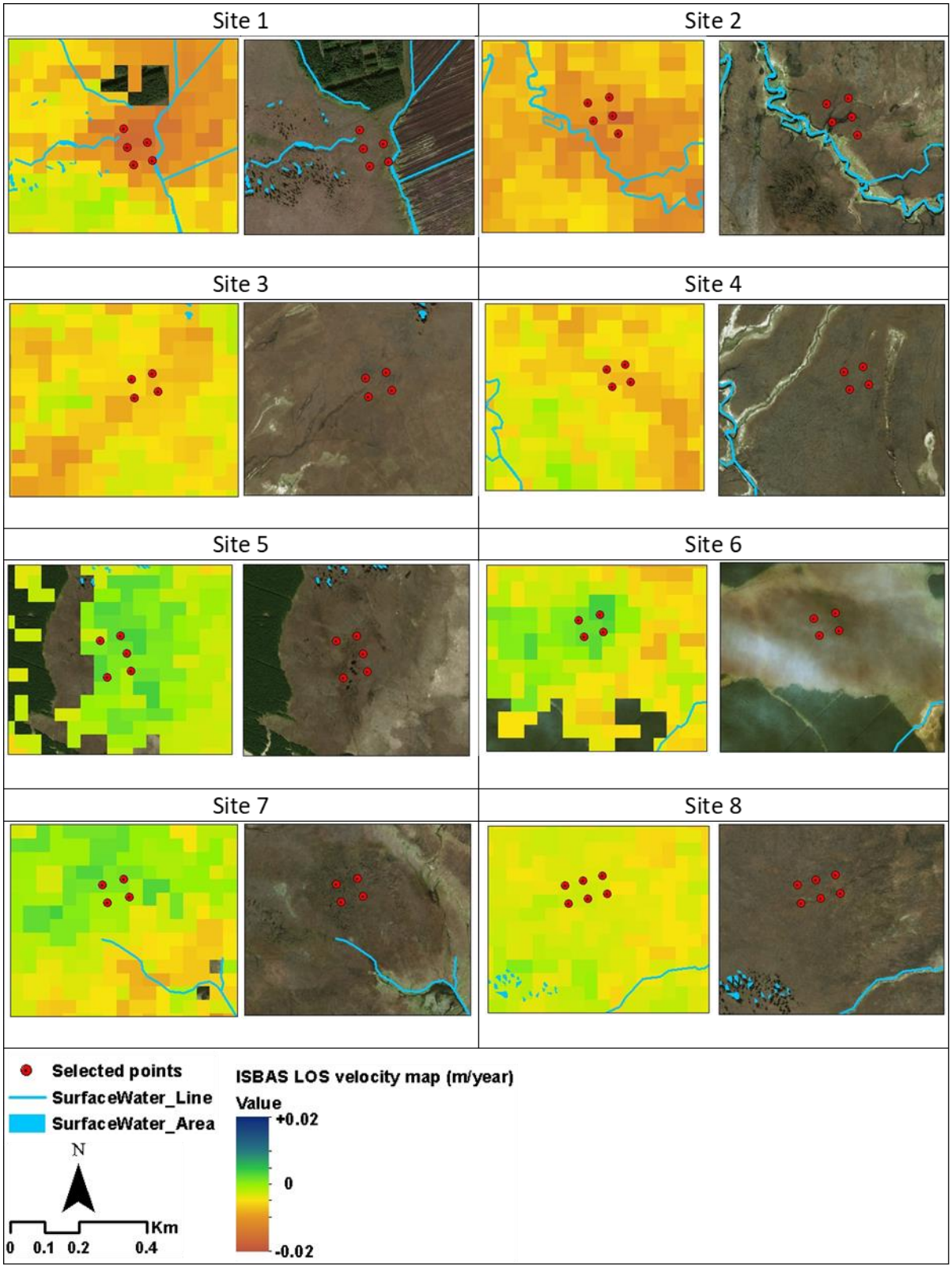
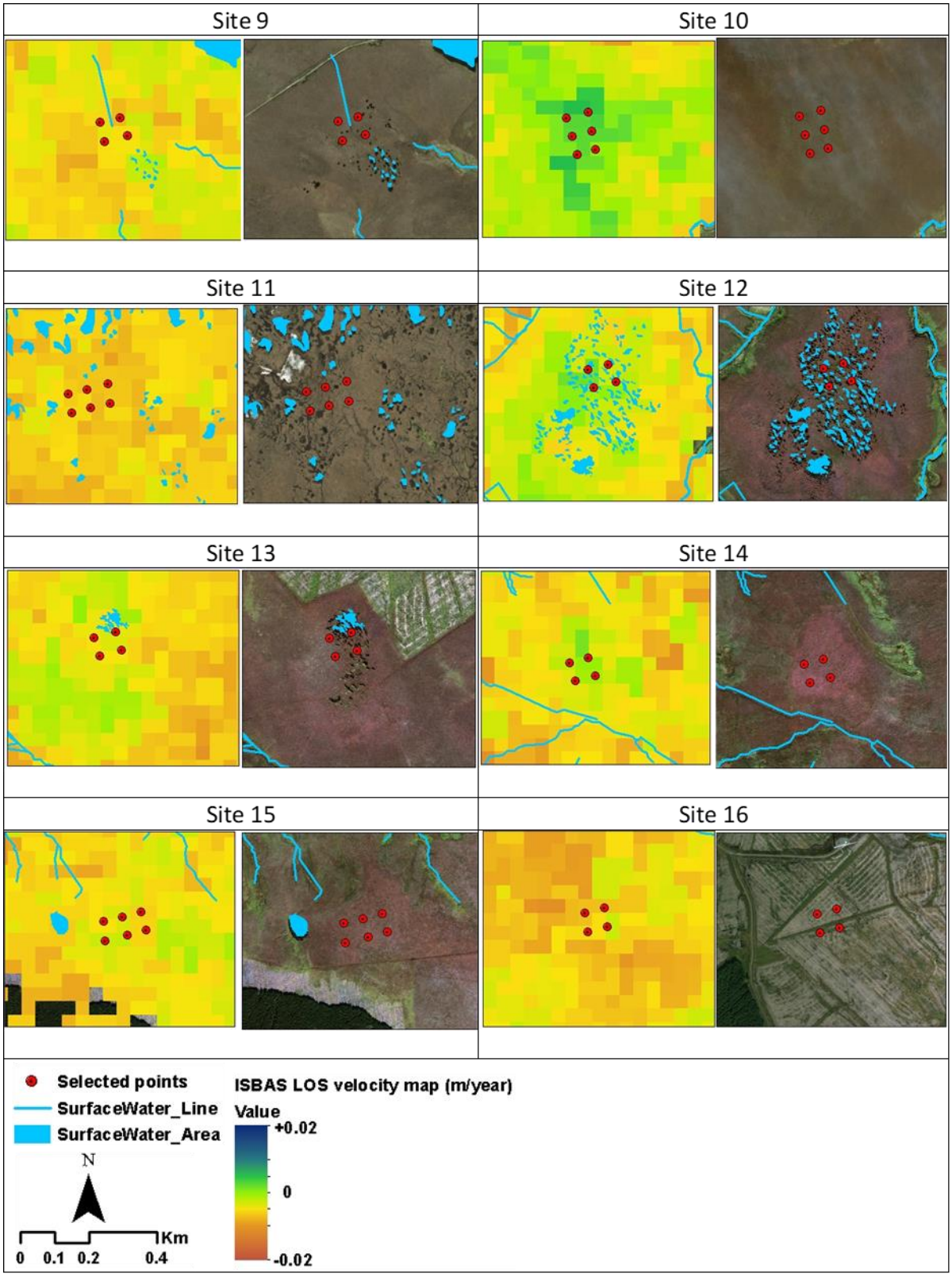


Figure 6.1: Locations of the selected sites for quantifying peat condition from InSAR time-series. Projection: WGS_1984_UTM_Zone 30.


Site 1
Site 2
Site 3
Site 4
Site 5
Site 6
Site 7
Site 8
Selected points
SurfaceWater_Line
SurfaceWater_Area
N
0 0.1 0.2 0.4
Km
ISBAS LOS velocity map (m/year)
Value
+0.02
0
-0.02


Site 9
Site 10
Site 11
Site 12
Site 13
Site 14
Site 15
Site 16
Selected points
SurfaceWater_Line
SurfaceWater_Area
N
0 0.1 0.2 0.4
Km
ISBAS LOS velocity map (m/year)
Value
+0.02
0
-0.02

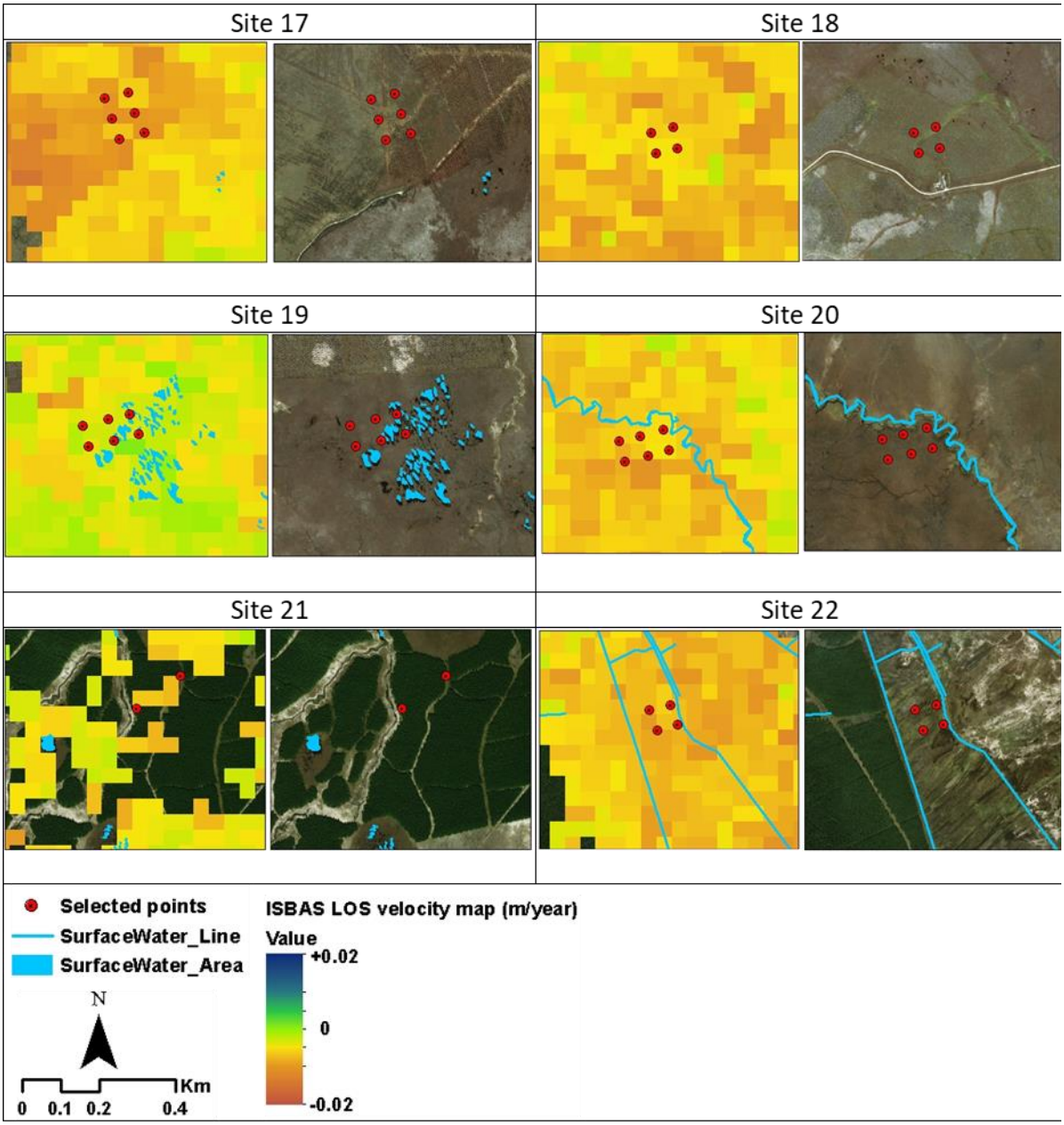


Figure 6.2: Shows the deformation pattern from Sentinel-1 ISBAS DInSAR technique for each selected site (this map is generated in **Chapter 5**). Corresponding Google Earth VHR imagery to aid interpretation over the same area for each selected site. Red dots represent the ISBAS time-series points that have been stacked in each site to improve the signal to noise ratio and provide a more representative spatial average.

6.3.1.2 Stacking of time-series

For each site, the ISBAS DInSAR time-series from an average five adjoining pixels (Red points in **Figure 6.2**) have been stacked because they exhibited very similar trends and amplitudes. The average time series for each site is considered as representative of peatland motion for that site (**Appendix C**, **Figure C1**). The gained benefit from stacking at each site is to improve the signal to noise ratio and provide a more representative spatial average of measurement.

6.3.1.3 ISBAS DInSAR time-series gap filling

Referring to **Section 2.4.4** in **Chapter 2**, time-series input data for SSA analysis must be at equal intervals in time, i.e., sampled evenly. However, some of the potential SAR images to be used were missing or had been excluded from the entire processing due to technical problems. As a result, the InSAR time-series were rarely equally distributed in time, exhibiting some gaps (**Figure 6.3**). Therefore, the gap filling method based on SSA using KSpectra-Toolkit software (Ghil et al., 2002) was used to fill the missing observations in the InSAR time-series. This method uses temporal correlations in the dataset by specifying the size of the SSA window (M) which should be large enough to cover the largest temporal periodicity in the data set. As peatland surfaces change seasonally (Kennedy and Price, 2005; Fritz et al., 2008), the window length in this study was set to 15 which is equivalent to 6 months. Only the leading SSA components that capture most of the variance in the time-series have been used in the reconstruction to estimate the missing measurements. The main idea of using the minimum number of components is to discard higher-ranked components corresponding to noise (**Figure 6.4**). Note that for a Sentinel-1 data set, the gap filling method using SSA does not introduce any artificial modulation in amplitude due to the few missing observations in the time-series in comparison with the total length of the data. This has been confirmed by comparing the SSA gap filling method with gap filling using a linear interpolation method, where the variance of the SSA components that are used in the reconstruction process to extract the non-linear trend (seasonal trend) are almost the same between the two methods (**Figure 6.5**).

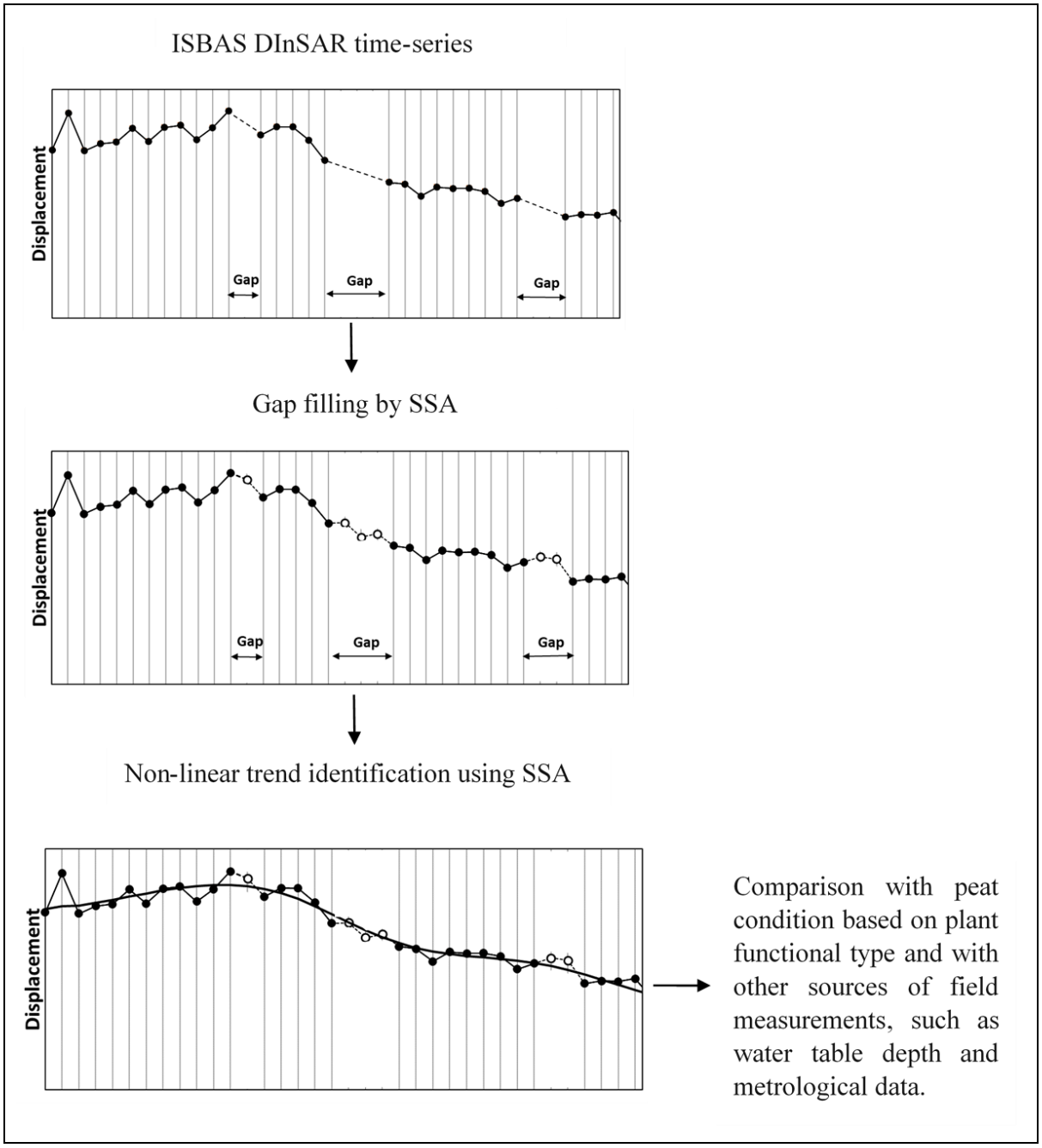


Figure 6.3: The flow chart of the proposed methodology for the analysis of ISBAS DInSAR time-series using SSA.

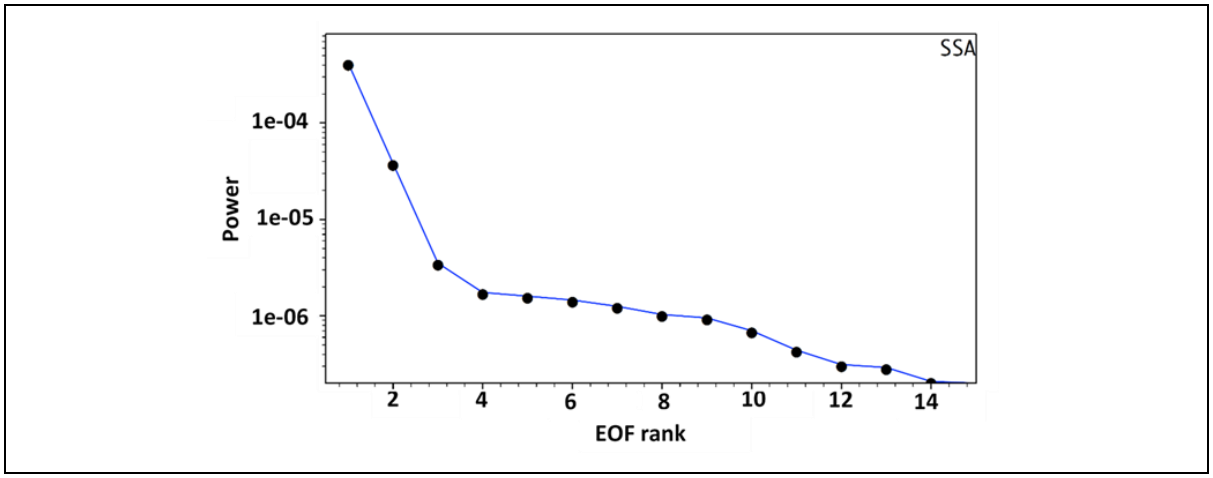


Figure 6.4: Example of SSA spectrum of filled ISBAS time-series record over Flow Country, with a window size of 6 months. The optimum number of components in this example corresponds to the two leading SSA components that have the long-term trend and oscillatory signal only. Break in the slope between the first two leading EOFs and the other components indicates the separation of oscillatory modes from noise.

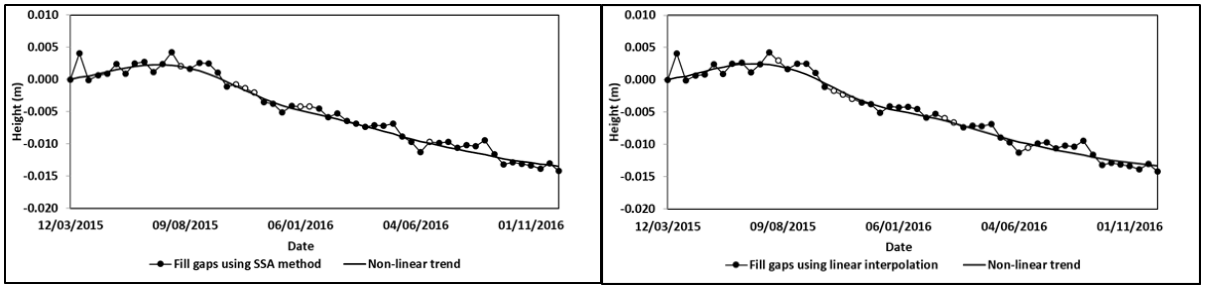


Figure 6.5: Comparison between the non-linear trend (seasonal trend) extracted using (a) linear interpolation to fill the gaps and (b) using SSA method. White dots represent the missing observations in the time-series which has been filled using the methods explained above.

6.3.1.4 Trend identification using SSA

Seasonal trends (non-linear trends) for each site have been extracted using SSA and Kendall's tau nonparametric trend test in KSpectra-Toolkit software (Ghil et al., 2002). As mentioned in **Section 2.4.1** in **Chapter 2**, the window length M is the only parameter in the decomposition process. The size of the window defines the ability to distinguish between two spectral peaks (Rangelova et al., 2012). If the window size is too small, this may cause several neighbouring peaks to be present in the spectrum (Vautard et al., 1992), while using a large window size will split the peak into a number of components with neighbouring frequencies (Gruszczynska et

al., 2017). The appropriate selection of the window length M depends on the lengths and preliminary information of the time-series. Theoretically, the window length should be large enough but not greater than the length of the time-series (N)/2 for a higher degree of statistical confidence (Ghil et al., 2002). Furthermore, if the time-series have a seasonal component such as peatland, it is advisable to take the window length (M) proportional to that period. Therefore, the choice of M=15 allows the periodicities as long as six months to be captured with reasonable statistical confidence.

After determination of the eigenelements (eigenvalues λ_k and eigenvectors $\rho_k$which are also called EOFs: k=1,……,M) of the lag covariance matrix C_X, a Monti Carlo significance test has been used to evaluate them. **Figure 6.6** shows an example of a Monti Carlo singular spectrum of the transformed ISBAS DInSAR time-series over site 1. Eigenvalues are plotted against frequency, along with the error bars representing the 95% and 5% noise percentiles. Hence, the eigenvalues lying outside this interval are relatively unlikely to be due to the red noise process. However, both EOFs in the low frequency domain which have the slowly varying component (non-linear trend) at the frequencies 0.035 and 0.067 (cycle/month) that have the highest variance in the time-series (approximately 91%) are uncertain. This case usually happens for the dominant frequency, especially in the low frequency domain due to unharmonicity of the EOFs (Ghil et al., 2002). Finally, partial reconstruction has been applied for the slowly varying components of the time-series (the first two leading eigenvalues in the example above) that captures the seasonal behaviour with its distinct near-periodicity. **Figure 6.7** illustrates the first two slowly varying EOFs that have been used in the reconstruction process to retrieve the seasonal trend over site 1.

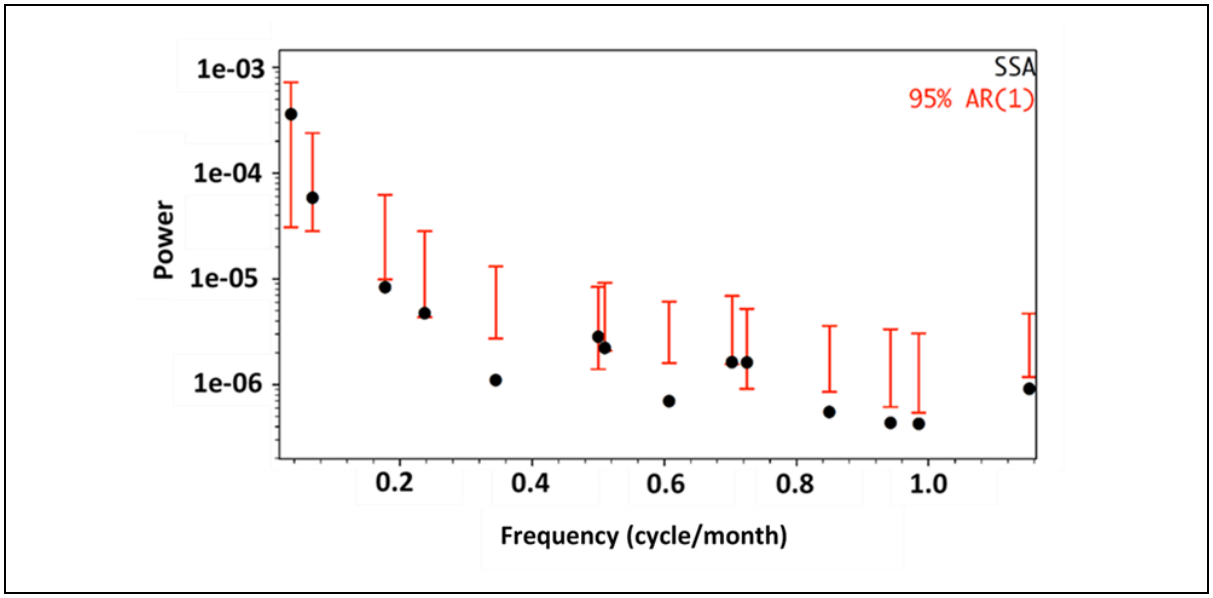


Figure 6.6: Monte Carlo singular spectrum of the ISBAS DInSAR time-series over site 1. The dots represent the eigenvalues, and the error bars represent the 95% confidence level.

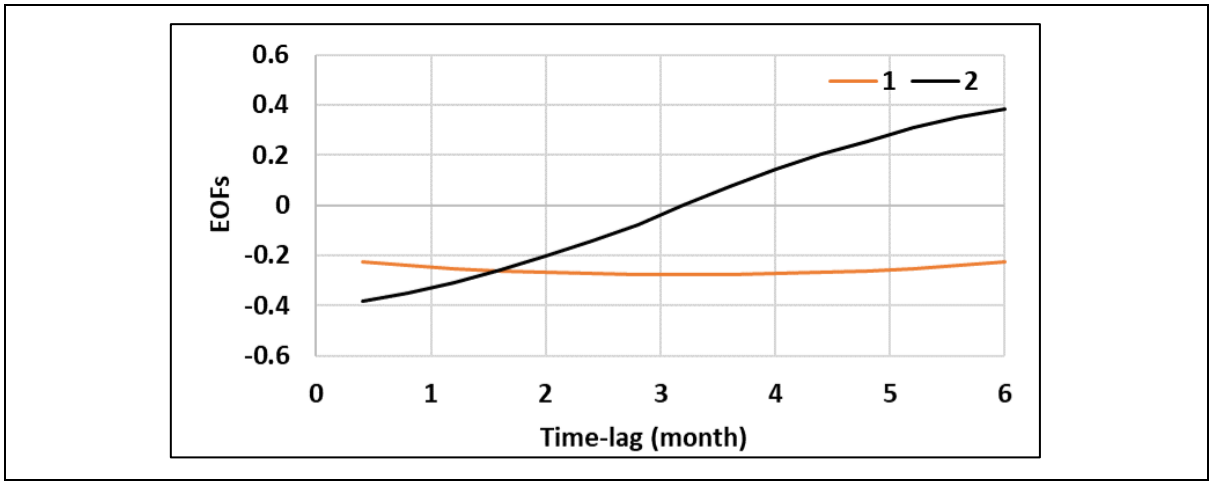


Figure 6.7: The first two leading Empirical Orthogonal Functions (EOFs) of ISBAS DInSAR time-series over site 1 that have been used in the reconstruction process (seasonal trend components).

6.3.1.5 Normalising the time-series

For more effective comparison between the trends of the time-series, the time-series were normalised by subtracting the mean and dividing by the standard deviation.

$$x\ (normalised) = x - mean/std(x) \qquad \textbf{Eq. 6.1}$$

6.3.2 Field data

As mentioned in **Section 4.2.5.2** in **Chapter 4**, different field measurements have been considered to describe the peat condition over Flow Country, which are then used to validate the InSAR results on the assumption that the ISBAS DInSAR time-series results are representative of the surface motion and that surface motion is representative of peat condition.

6.3.2.1 Land cover classification

6.3.2.1.1 Field survey

Within each InSAR pixel, 4-6 10 x10m areas (equivalent to, and centered on Sentinel-2 pixels; see below) were selected for vegetation surveys. In the field, a 10 x 10m square was centered on the GPS coordinate of the chosen Sentinel-2 pixels (**Appendix B**). In total, 14 sites were visited over a period of 7 days in the peak of the growing season. The remaining 8 sites could not be visited due to an access restriction (and these were classified as per **Section 6.3.2.1.2** below). In the field, the four sides of each square were aligned with the cardinal points and thus in the same orientation as the Sentinel-2 pixels. In each square, the percent cover of key plant functional groups (*Sphagnum* mosses, other mosses, lichen, ericaceous shrubs, sedges, grasses) as well as key features associated with peat condition and with the potential influence of the spectral signature of the Sentinel-2 pixel (bare peat, open water and vegetation litter) were estimated using the Braun-blanquet scale (Poore, 1955). For each functional group identified, dominant species were also noted. Each square was photographed from the South-East corner, facing North, and vegetation patterns reflecting density and spread of dominant plant functional groups were drawn and annotated for future reference. For each site, general condition was further assessed by noting the presence of drains, tracks, evidence of deer trampling or browsing, presence of natural pools, restoration activity, and estimated the distance to road, forestry or infrastructure within a 100 x 100m area around the groups of squares. Land-use history was documented by a discussion with land-owners.

This information was put together to establish 4 condition categories that represent a gradation in peatland condition. Condition 1 represents what is generally considered to be wet peatland with a shallow water table in good condition that is dominated by *Sphagnum* moss species (≥ 50%) forming large continuous carpets and sedges (also ≥ 50%, largely dominated by *Eriophorum angustifolium* and *Tricophorum germanicum*), with some shrubs (mostly *Erica tetralix*). Condition 2 represents wet peatland in relatively good condition with some patches of Sphagnum mosses (25-50%) and sedges (25-75%), but signs of disturbance or lower water

table, e.g., increased shrubs, particularly *Calluna vulgaris* and lichen, small patches of bare peat or evidence of deer activity. Condition 3 represents sites with small clumps of *Sphagnum* mosses (10-25%) often including species associated with disturbance (e.g. *S. tenellum, S. fallax*), high sedge cover (20-75%) combined with shrub and lichen dominance, presence of grasses (e.g. *Molinia caerulea* and *Deschampsia flexuosa*) and indication of disturbance at the wider scale e.g. drainage ditches, areas of bare peat, deer trampling or known past disturbance (hill drains, grazing, fire). Finally, condition 4 is generally considered to be peat in poor condition with a low water table and includes large areas of bare peat (>25%), has a predominance of shrubs that are almost exclusively C. vulgaris fewer sedges and less than 10% *Sphagnum* confined to small isolated clumps, also including clear disturbance both within the squares and in the wider area. In addition to these two categories, two additional categories were defined: condition 5 for clear-felled conifer plantation on peat and condition 6 for commercial conifer plantation on peat.

6.3.2.1.2 Satellite optical data

Using the afore mentioned Sentinel-2 Multi Spectral Instrument (MSI) cloud-free image (dated from September 2015; downloaded from earthexplorer.usgs.gov and pre-processed using the Sentinel-2 toolbox from ESA to resample all wavebands to 10m spatial resolution), a series of land cover classifications were conducted using the 14 visited sites as training data. The classifiers used were (i) support vector machine; (ii) spectral angle mapper and (iii) spectral information divergence, and the resultant classified pixels for the 8 remaining sites determined by way of an ensemble decision rule (Foody et al., 2007). This combination of detailed field observations and spectral discrimination using the Sentinel-2 imagery afforded the description of the peatland condition of each of the 22 sites used in all subsequent analyses (**Appendix C**, **Table C1**).

6.3.2.2 Water table depth

Water table depths are only available for four sites (two dataloggers in site 12, and one in sites 13, 14, and 15), but they do cover the same period of Sentinel-1 ISBAS time-series over the Flow Country. However, the WTD time-series present a shorter time sampling interval (daily and every 30 mins) than that available from the InSAR time-series. Consequently, the WTD time-series have been resampled to the revisiting time interval of the Sentinel-1 satellite (every 12 days). For this task, the average daily values of WTD corresponding to the acquisition dates of SAR images have been used for the resampling process. For site 12, because there are two

dataloggers in the same site, the average time-series is used for the processing. Following the procedure described in **Section 6.3.1.4**, the seasonal fluctuations have been extracted using SSA for each WTD time-series (**Figure 6.8**) to be used for the comparison with InSAR time-series at each specific site. It should be noted that the shift in WTD over site 13 in July-16 is caused by moving the position of the logger.

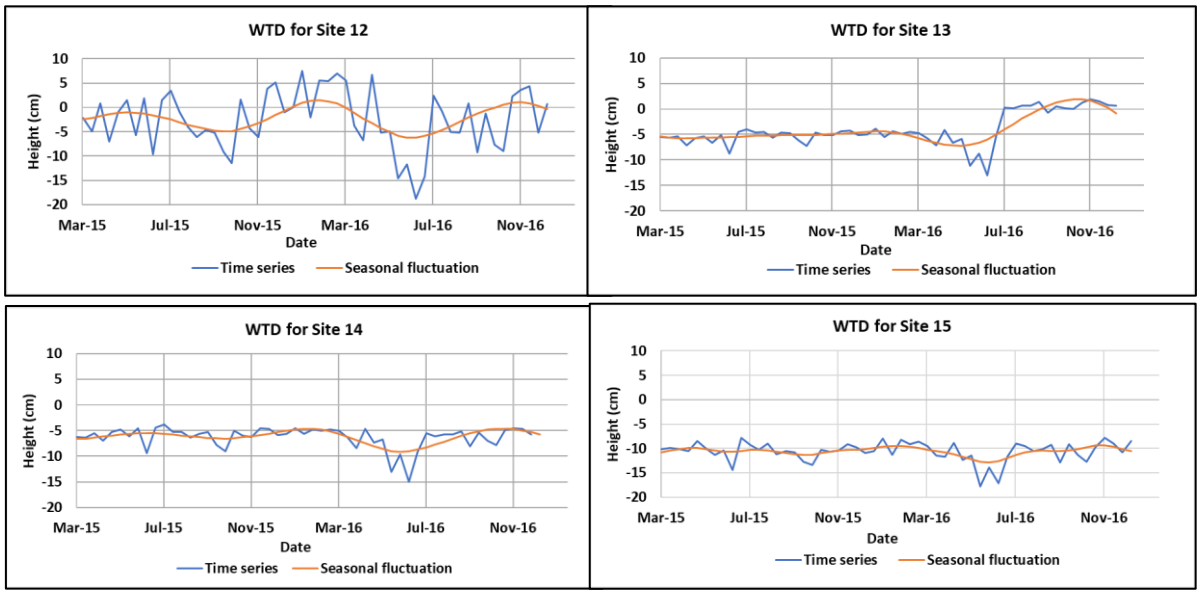


Figure 6.8: WTD time-series along with seasonal fluctuations extracted using SSA over site 12, 13, 14, and 15.

6.3.3 Results

6.3.3.1 ISBAS DInSAR linear trend and peat condition

ISBAS DInSAR linear deformation rates for 103 ISBAS points distributed across the 22 sites (**Figure 6.2**) were compared with peat condition as determined by the field data (**Figure 6.9**). The comparison shows that the areas with poor peat condition (degraded areas, e.g., conditions 3, 4, 5 and 6 in **Figure 6.9**) display higher subsidence rates (i.e., a larger negative mean LOS rate) than the areas in good condition (conditions 1 and 2). Indeed those sites having a poor condition all had a similar mean LOS rate. The same was the case for those having good condition. Although encouraging this would only allow for the mapping of two broad classes of peat condition. The next stage was to investigate if the non-linear trends in the InSAR time-series afforded more classes of peat condition to be discerned.

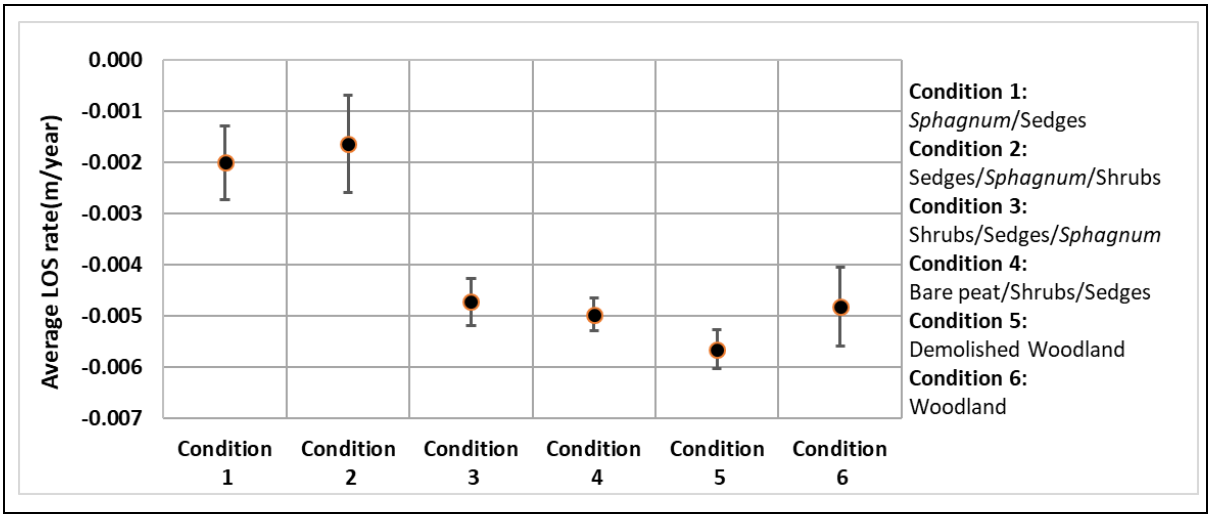


Figure 6.9: Comparison of the linear trend of 103 ISBAS points distributed in 22 sites with the peat condition for each point, based on the average subsidence rate corresponds to each condition. The error bars represent the standard error of the mean.

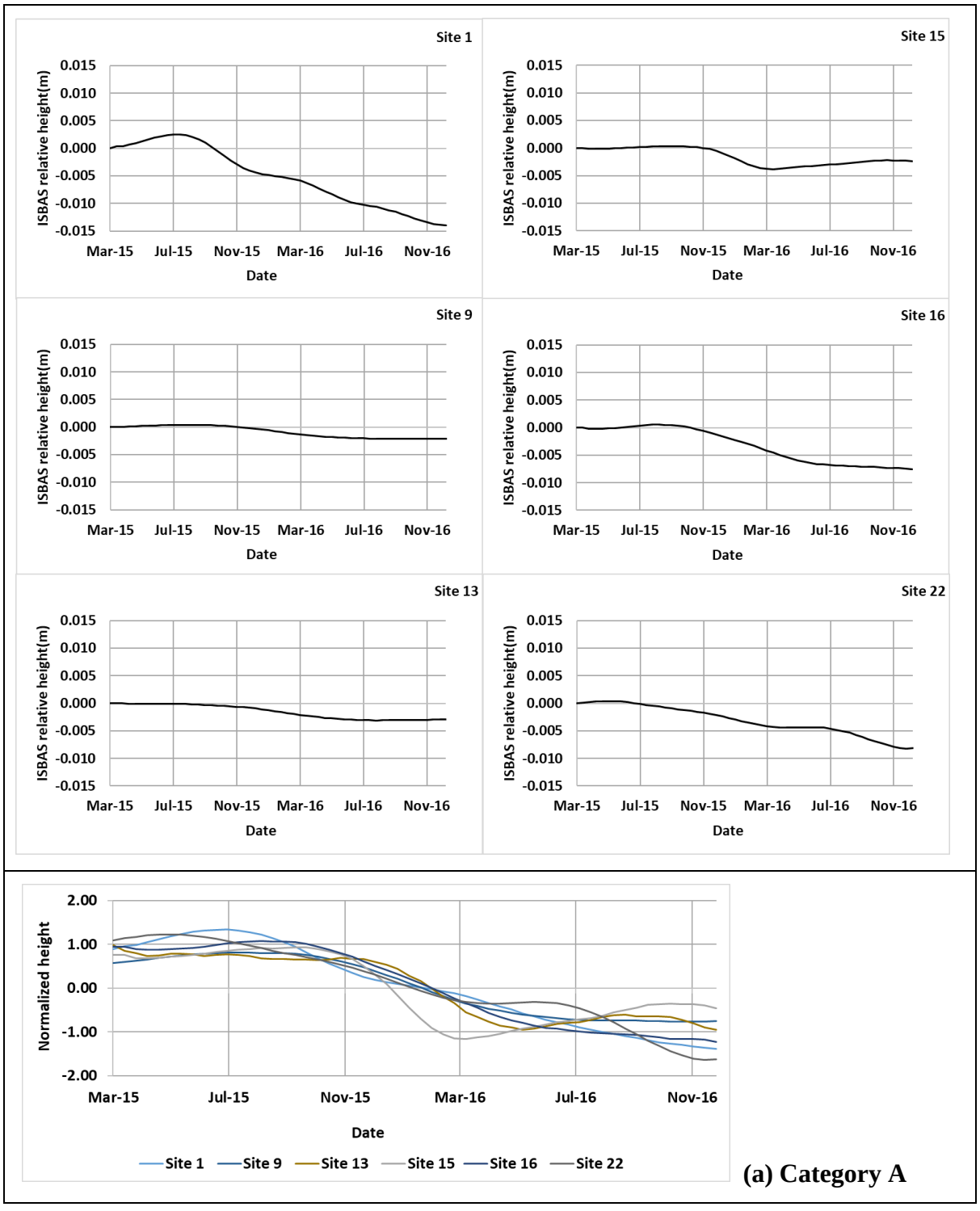
6.3.3.2 ISBAS DInSAR time-series and peat condition

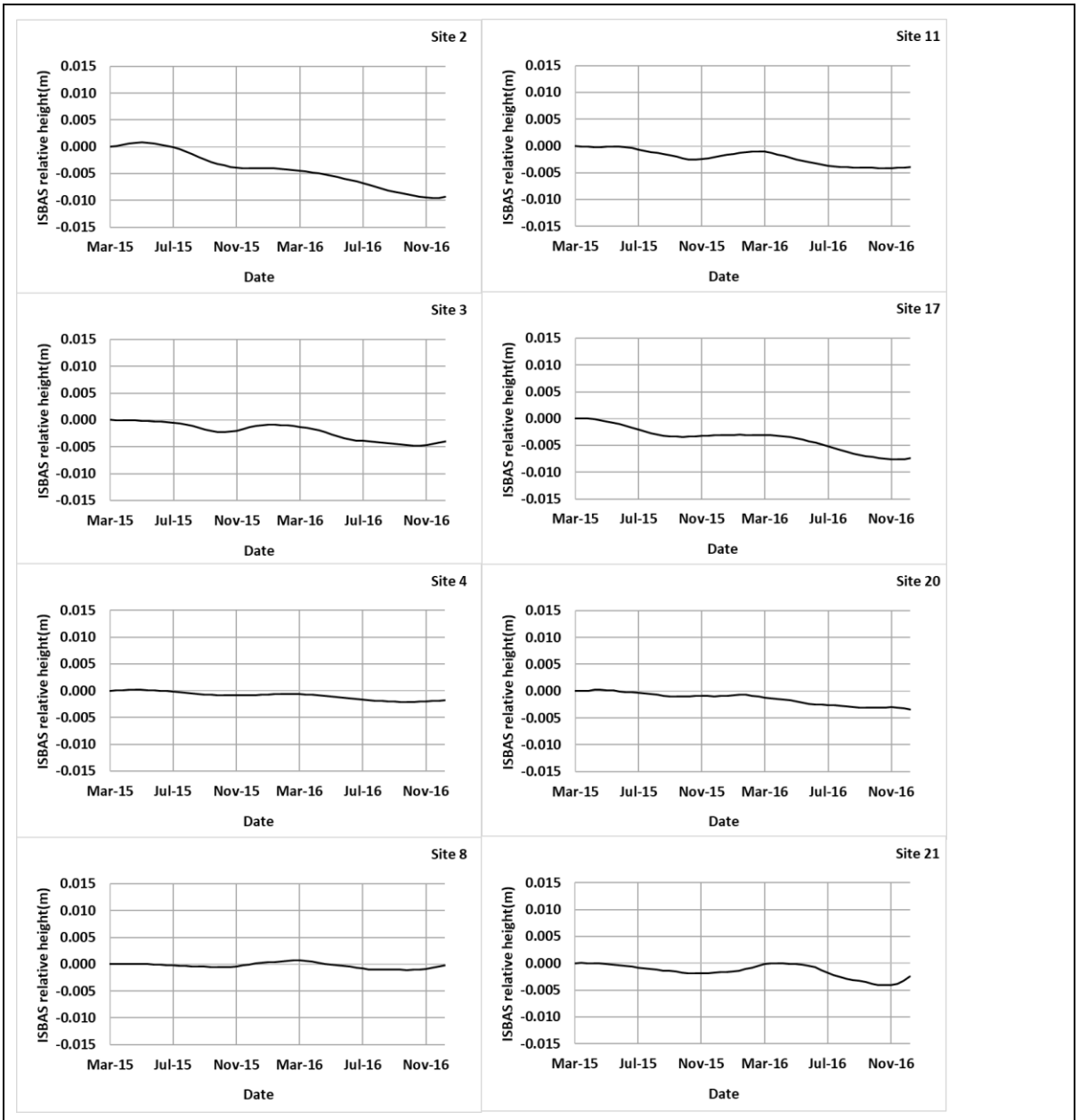
Based on the similarities of the non-linear trends extracted using SSA from ISBAS DInSAR time-series of surface motion for 22 sites (**Figure 6.10**), most sites can be assigned to one of four distinct categories:

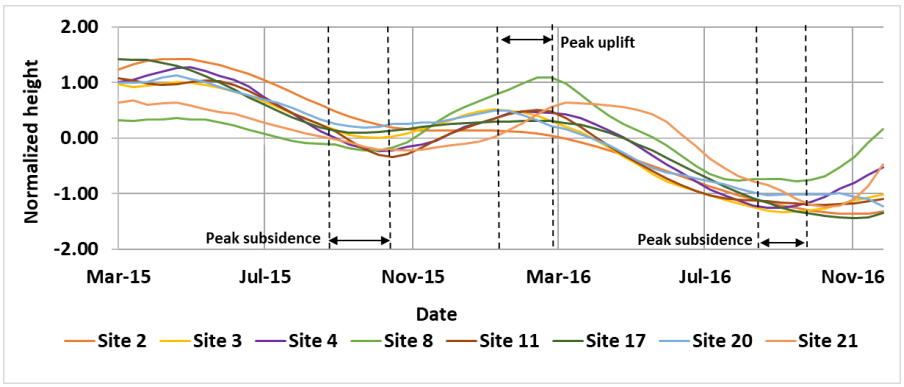
- **Category A:** represents sites with a predominant subsidence trend and little or no seasonal oscillations (**Figure 6.10** A).
- **Category B:** represents sites with strong seasonal oscillations with peak subsidence in late summer-mid autumn (Aug-Oct) and peak uplift in late winter-early spring (Feb-April) (**Figure 6.10** B), except site 21, for which the peaks shifts by approximately 1 month.
- **Category C:** represents sites with strong seasonal oscillations with peak subsidence in late-spring/ mid-summer (April-June) and peak uplift in mid-winter (Nov-Jan) (**Figure 6.10** C) for all sites except site 12, where the peaks again shift by about 1 month.
- **Category D:** represents only site 18 which is undergoing rewetting remediation and it does not assign to any category, but the time-series displays attributes of both category A and category C (**Figure 6.10** D).

A strong correlation exists between the trend categories and peat condition categories based on plant functional group type classification (**Figure 6.11**). Sites under category A are the most degraded sites, where shrub vegetation (condition 3) is the dominant class over these

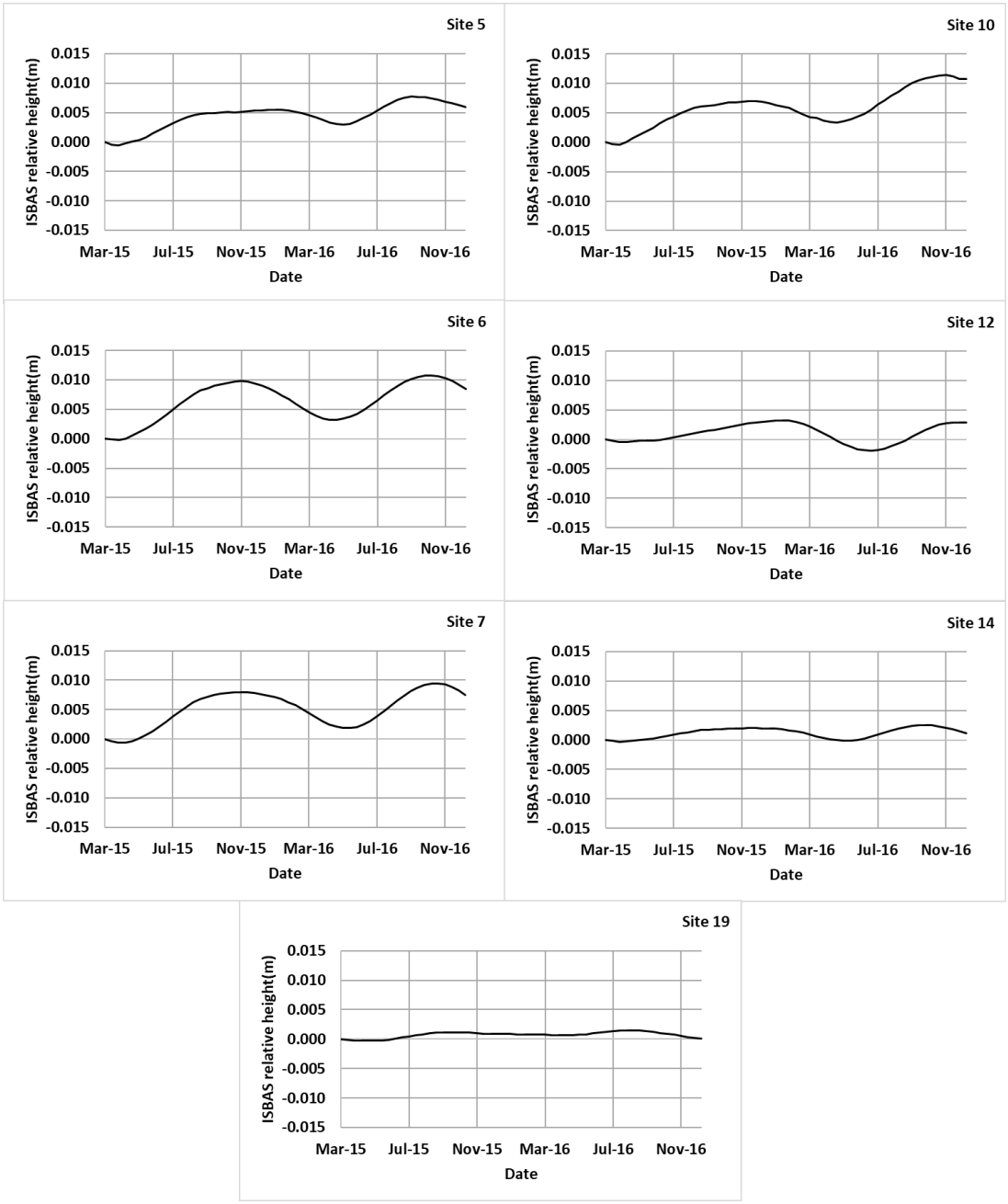
sites composed with sedges (condition 2), bare peat (condition 4) and clear-felled conifer plantation (condition 5). Category B sites contain the broadest mix of conditions but are predominantly composed with condition 3 and 4. Category C sites, on the other hand, are the most pristine sites with a predominance of *sphagnum* and sedge species (**Figure 6.11**).

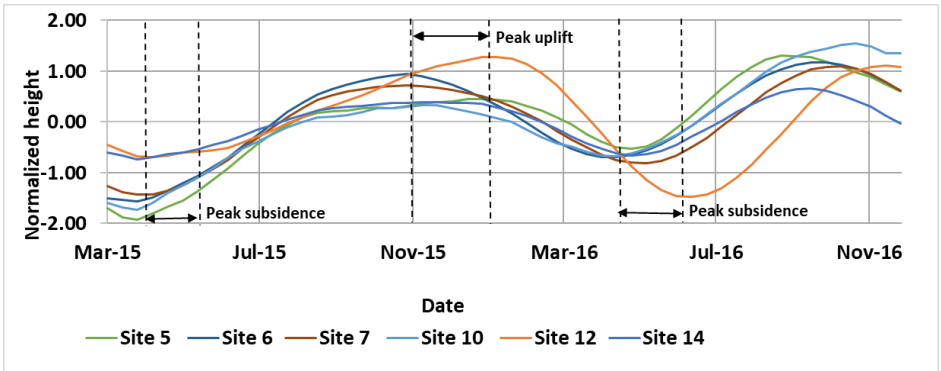



Site 2
Site 11
Site 3
Site 17
Site 4
Site 20
Site 8
Site 21
ISBAS relative height(m)
0.015
0.010
0.005
0.000
-0.005
-0.010
-0.015
Mar-15
Jul-15
Nov-15
Mar-16
Jul-16
Nov-16
Date


Normalized height
2.00
1.00
0.00
-1.00
-2.00
Peak uplift
Peak subsidence
Peak subsidence
Mar-15
Jul-15
Nov-15
Mar-16
Jul-16
Nov-16
Date
Site 2
Site 3
Site 4
Site 8
Site 11
Site 17
Site 20
Site 21

(b) Category B


Site 5
Site 10
Site 6
Site 12
Site 7
Site 14
Site 19
ISBAS relative height(m)
0.015
0.010
0.005
0.000
-0.005
-0.010
-0.015
Mar-15
Jul-15
Nov-15
Mar-16
Jul-16
Nov-16
Date


Normalized height
2.00
1.00
0.00
-1.00
-2.00
Peak uplift
Peak subsidence
Peak subsidence
Mar-15
Jul-15
Nov-15
Mar-16
Jul-16
Nov-16
Date
Site 5
Site 6
Site 7
Site 10
Site 12
Site 14

(c) Category C

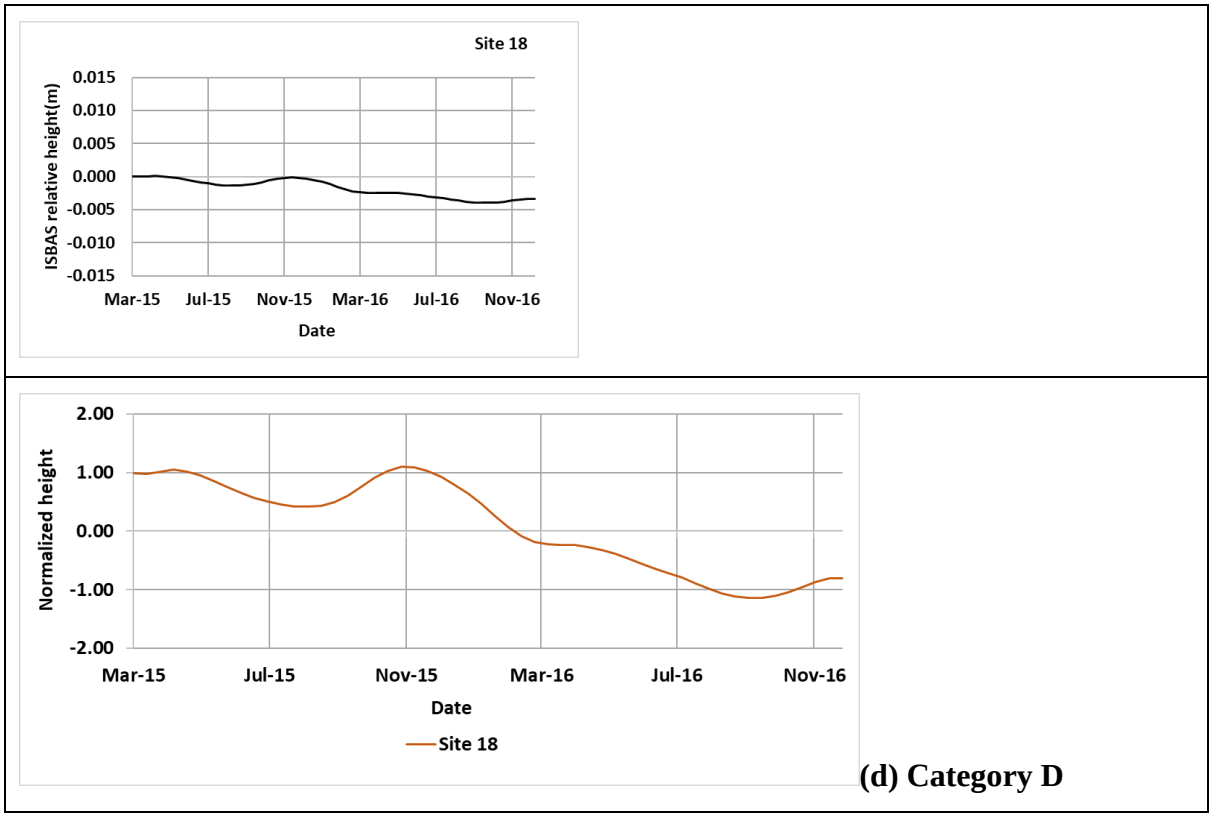


Figure 6.10: The non-linear trend derived from ISBAS DInSAR time-series using SSA. (a) Category A trends display sustained subsidence and minimal seasonal oscillations. (b) Category B trends display long-term subsidence, peak subsidence in late summer-early autumn (Sept-Nov) and peak uplift in late winter (Feb-April). (c) Category C trends display long term uplift, peak subsidence in late-spring/ mid-summer (April-June) and peak uplift in mid-winter (Nov-Jan). (d) Category D trend display combined trend between category A and C.

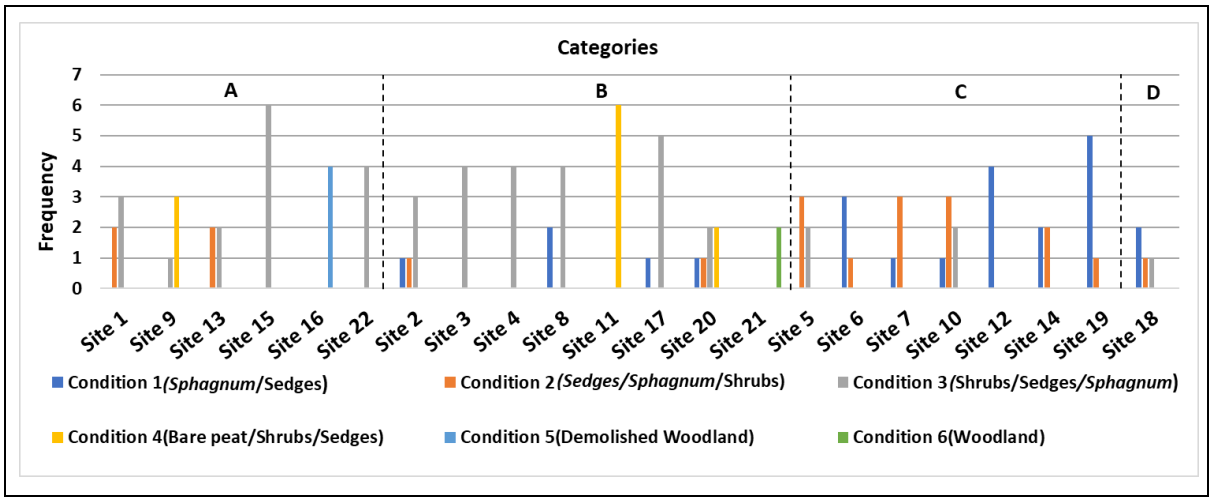
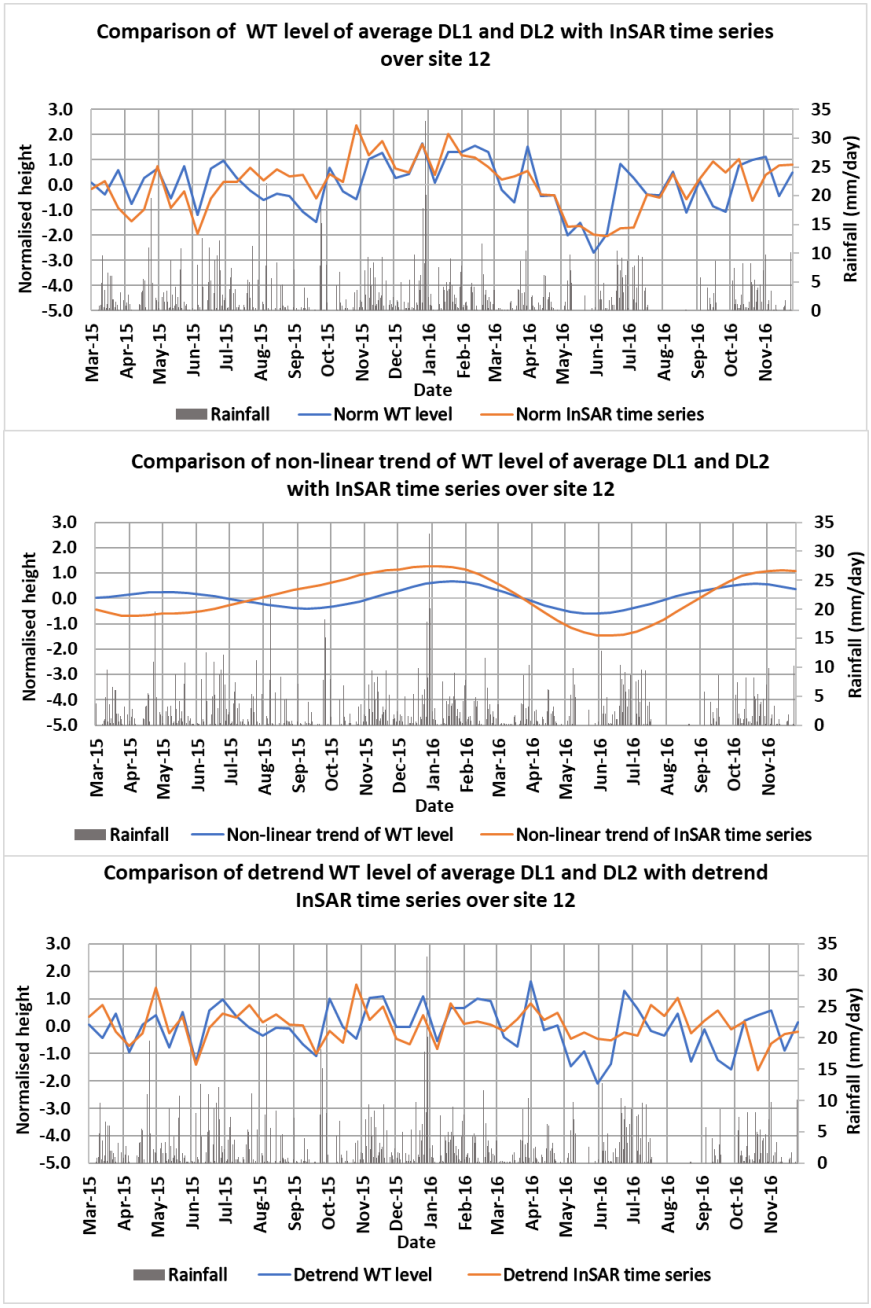
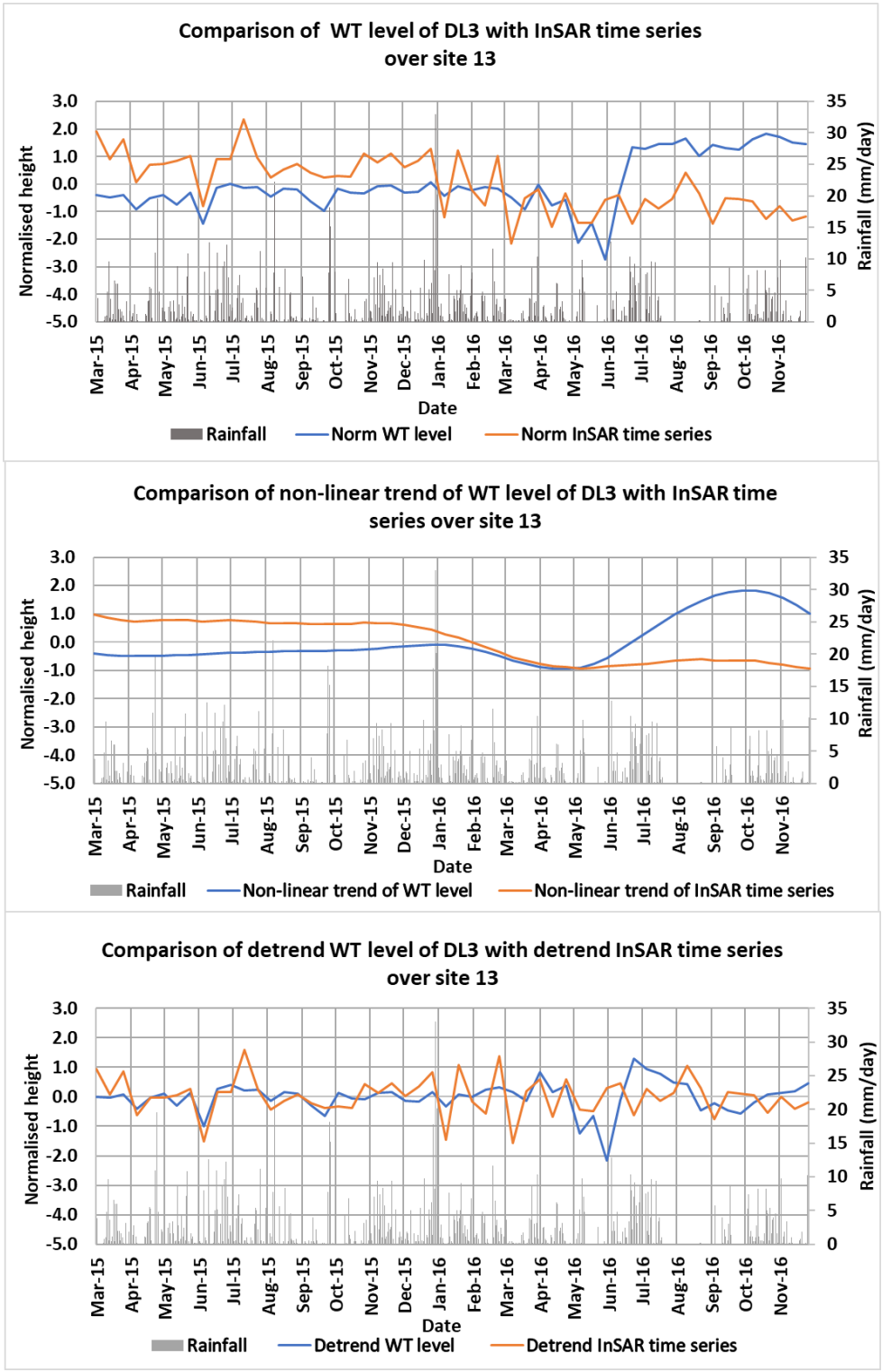


Figure 6.11: Peat condition over each 22 sites. Condition had been quantified using optical satellite data calibrated by field observation of plant functional type. The frequency on the Y-axis shows the number of ISBAS points having the same condition in each site

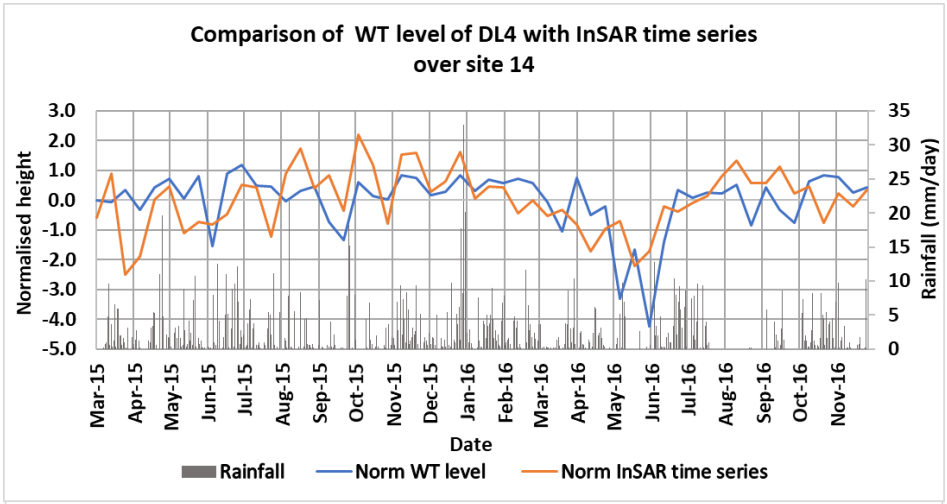
Examination of further indicators of peat condition and the time-series further supports the hypothesis that the InSAR time-series can be used to indicate peat condition. The comparison between normalised WTD and ISBAS DInSAR surface motion over sites number 12, 13, 14 and 15 (**Figure 6.12**) indicates that for sites in good condition (i.e., *sphagnum* and sedge dominated), there is a strong correlation between oscillations in the water table and oscillations of the peat surface and rainfall (sites 12 and 14, under Category C and condition 1 & 2, **Figure 6.11**). In the most degraded sites the correlation between WTD and ISBAS DInSAR time-series decreases, where the inter-seasonal oscillations appear to be out of phase and the time-series do not display clear a seasonal trend particularly over site 15. However, over site 13, there is a clear correlation between the WTD oscillations and InSAR time-series before moving the position of the logger in July-16.

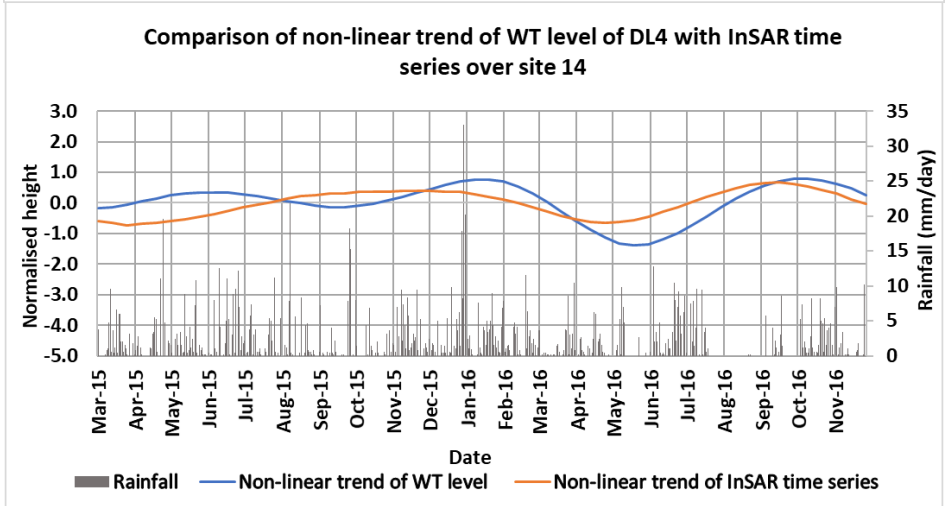

Comparison of WT level of average DL1 and DL2 with InSAR time series over site 12
Normalised height
Rainfall (mm/day)
Date
Rainfall
Norm WT level
Norm InSAR time series
Comparison of non-linear trend of WT level of average DL1 and DL2 with InSAR time series over site 12
Normalised height
Rainfall (mm/day)
Date
Rainfall
Non-linear trend of WT level
Non-linear trend of InSAR time series
Comparison of detrend WT level of average DL1 and DL2 with detrend InSAR time series over site 12
Normalised height
Rainfall (mm/day)
Date
Rainfall
Detrend WT level
Detrend InSAR time series

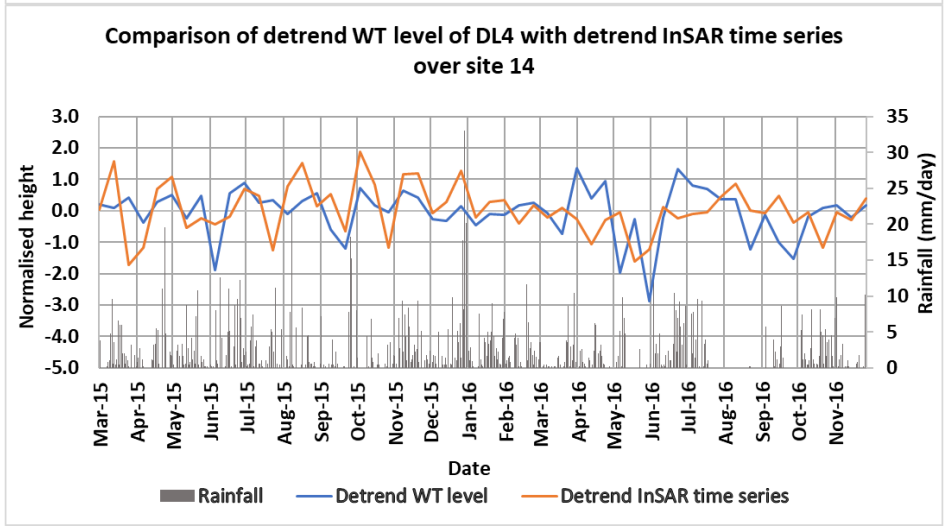
(a)


Comparison of WT level of DL3 with InSAR time series over site 13
Normalised height
Rainfall (mm/day)
Date
Rainfall
Norm WT level
Norm InSAR time series
Comparison of non-linear trend of WT level of DL3 with InSAR time series over site 13
Normalised height
Rainfall (mm/day)
Date
Rainfall
Non-linear trend of WT level
Non-linear trend of InSAR time series
Comparison of detrend WT level of DL3 with detrend InSAR time series over site 13
Normalised height
Rainfall (mm/day)
Date
Rainfall
Detrend WT level
Detrend InSAR time series

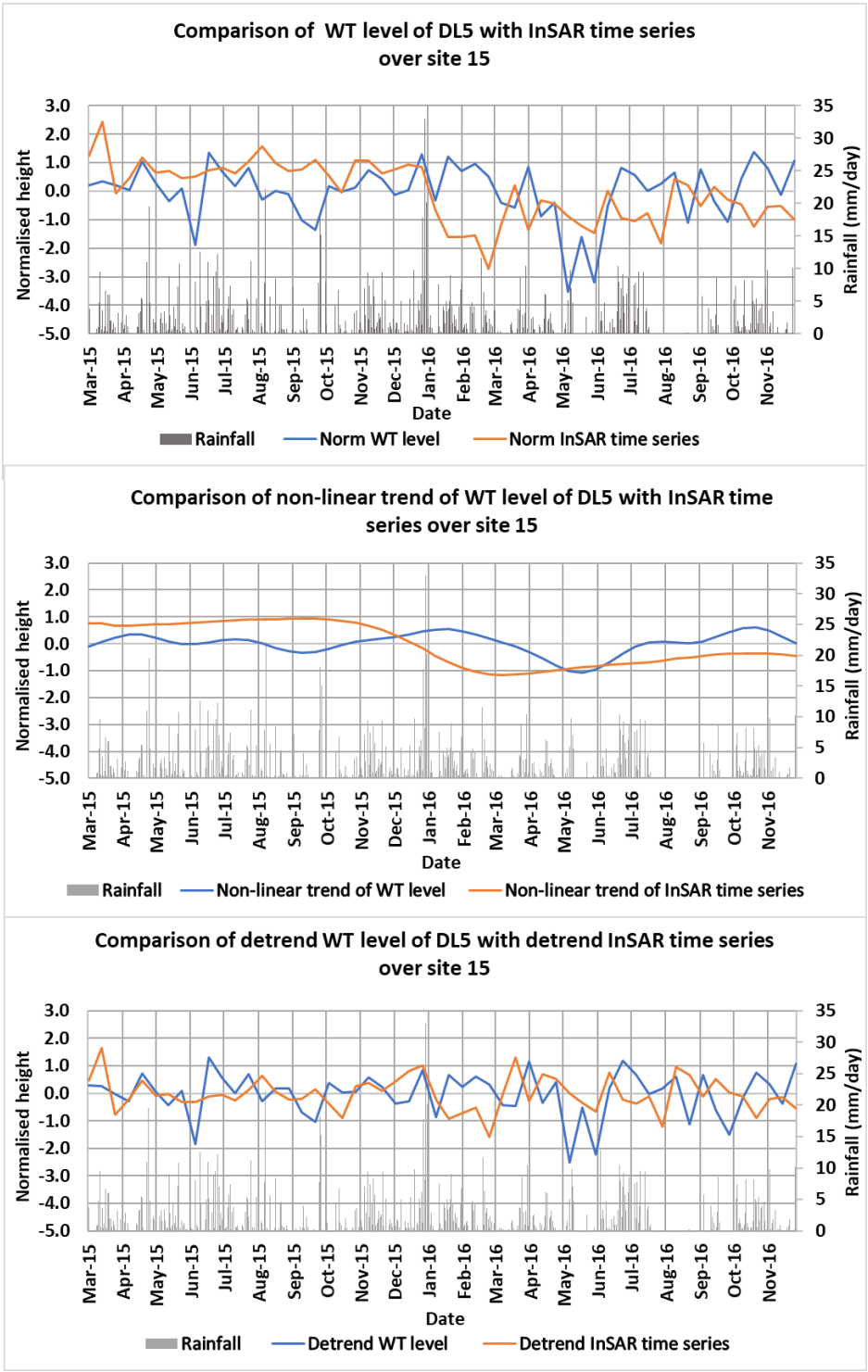
(b)


Comparison of WT level of DL4 with InSAR time series over site 14
Normalised height
Rainfall (mm/day)
Date
Rainfall
Norm WT level
Norm InSAR time series


Comparison of non-linear trend of WT level of DL4 with InSAR time series over site 14
Normalised height
Rainfall (mm/day)
Date
Rainfall
Non-linear trend of WT level
Non-linear trend of InSAR time series


Comparison of detrend WT level of DL4 with detrend InSAR time series over site 14
Normalised height
Rainfall (mm/day)
Date
Rainfall
Detrend WT level
Detrend InSAR time series

(c)



(d)

Figure 6.12: Comparison of WT level and rainfall with ISBAS DInSAR time-series. (a) over site 12 (Category C). (b) over site 13 (Category A). (c) over site 14 (Category C). (d) over site 15 (Category A).

6.3.3.3 Interpretation of the results

The above results give clear evidence that there is a strong correspondence between the inferred peat condition and ISBAS DInSAR time-series of surface motion. Comparison between WT level and ISBAS DInSAR indicates that for the sites in good condition (sites 12 and 14 in **Figure 6.12**) the peat surface oscillates corresponding to the oscillations of the water table, and this is consistent with the field observations of other studies such as Fritz et al. (2008) and Reeve et al. (2013). It is likely that the most influential factor on the InSAR time-series is the mechanical response of the peat to the variations in water storage in both saturated and unsaturated zones. This response can be split into two components which can be considered either irreversible or reversible for the entire period of the observation: the long-term irreversible changes in the mass of organic material and water stored in the peat matrix; and short-term reversible seasonal or higher frequency oscillations in response to the drying and wetting cycle (Camporese et al., 2006). Therefore, the variation in WTD may explain the shifted peaks between site 12 and the remaining sites in category C (**Figure 6.10** c).

Category A sites are the most degraded due to drainage and they contain no sphagnum (**Figure 6.11**). They display sustained subsidence and lack seasonal oscillations (**Figure 6.10** a). The lack of seasonal oscillations could be due to a combination of the low permeability of compacted, highly humified peat and or the presence of fracture porosity which in combination do not permit significant water storage within the peat matrix. It is also known that highly degraded peat loses its compressibility on account of the of the long term irreversible changes caused by decay (Waddington and McNeil, 2002; Kennedy and Price, 2005).

Category B sites are partially drained sites but less degraded than Category A sites. These sites include a greater matrix of plant functional types, are dominated by vascular plants but do include some areas of sphagnum (**Figure 6.11**) and are interpreted to be generally wetter with a greater capacity for seasonal water storage. Unlike category A sites, the seasonal oscillations are distinct but generally of lower amplitude than those observed in category C sites. This can be interpreted as indicating that the water table is shallower than at category A sites and deeper than at category C sites with variations occurring within less degraded peat with greater porosity, elasticity and specific storage (S) than category A sites. The predominance of deep rooted vascular plants (mainly heather and sedge) that exercise a strong evapotranspiration drawdown on water level throughout the growing season may explain why water levels reach a minimum at the end of the growing season in the late summer-early

Autumn and recover to a maximum ahead of the growing season in late winter-early spring (Bourgault et al., 2017). It is clear from **Figure 6.10** b that most sites within category B have almost the same peak of subsidence and uplift, except site 21 (commercial conifer plantation, condition 6), where the peaks are shifted from the other sites. This may be due to the characteristics of the site itself, as it is a woodland area with only two ISBAS points available for stacking, and the amount of noise on the returned radar signal over this site.

Category C sites are sphagnum dominated with a shallow water table. Unlike category A and B sites, the dominance of the non-vascular sphagnum species means the predominant seasonal control on the water budget is evaporative demand (Lapen et al., 2000) not vascular evapotranspiration and this shifts the maximum drawdown and recharge of the water and associated surface motion to a summer/ winter pattern that aligns with seasonal variations in evaporative demand in the UK (Robinson et al., 2017). Furthermore when subject to evaporative stress sphagnum acts to conserve water (Kettridge et al., 2016) possibly limiting sustained loss into the late summer.

Site 18 which has undergone remediation work following forest clearance by ditch blocking and rewetting, displays surface motion characteristics that are a combination of Category C and Category A. The category C component is best interpreted as evidence of shallow water table and probable colonisation by sphagnum; however, the strong category A component indicates that despite rewetting the site is still losing mass, possibly over more elevated areas, resulting in rapid subsidence. Following two decades under forestry management (conifer plantation), management at the site included tree felling and drain blocking in 2003-2004, with further blocking of furrows to smoothen the surface completed in 2016-17. Therefore, it is not surprising to see rapidly localised rewetting, which would precede longer-term sustained recovery. However, continued loss of mass could indicate that the surface peat was severely damaged and much of the peat mass is still vulnerable to aerobic degradation.

It can be seen from **Figure 6.10** that the seasonal trends for all sites in each category are not identical with each other and they have slightly different seasonal oscillations. This can be interpreted due to the stacking of an average 5 adjoining pixels (ISBAS points) over each site (**Figure 6.2**), since these pixels have different condition as quantified using optical satellite data calibrated by field observation of plant functional type.

As the application of SSA technique to evaluate peat surface motion from a single time-series of InSAR provides a potential study to monitor the change in peat condition, the MSSA technique for thousands of time-series of InSAR has been used in the next section (**Section 6.4**) to evaluate peat surface motion in regional scale.

6.4 Application of multivariate SSA (MSSA) to analyse seasonal variation from ISBAS DInSAR time-series

Monitoring the earth's surface using multi-temporal satellite based methods could play an important role in quantifying a spatio-temporal phenomenon that cannot be elucidated using conventional mapping (Rawat and Kumar, 2015). With the availability of increasingly large amounts of data, contemporary methods are required for processing with careful interpretation. Multi-channel SSA (MSSA) is an extension to univariate SSA (Broomhead and King, 1986b) that analyses multiple sets of time-series data (multiple channel) with the aim of specifying and extracting the predominant spatio-temporal structures of the underlying stochastic process, particularly the common oscillatory patterns for the time-series in the data set sample, i.e., the non-linear periodicities to most channels. This study, therefore, presents the results of MSSA applied for the first time to InSAR time-series data (Sentinel-1). The focus of study (as with the employment of SSA) was the Flow Country, Scotland, UK (the largest expanse of blanket bog in Europe). The sequence of SAR images for InSAR processing was considered as a time variable, whose one component (channel) represents the time-series for one pixel. Applying this method to ISBAS DInSAR time-series allows regional evaluation of peat condition through its surface motion and understanding the seasonal peat volume change, which has important implications for restoration methods.

6.4.1 Methodology

6.4.1.1 ISBAS DInSAR time-series gap filling using MSSA

The gap filling method based on multivariate SSA (MSSA) using Ksepctra-Toolkit software (Ghil et al., 2002) was applied to fill the missing ISBAS DInSAR observations (refer to **Section 2.4.4** in **Chapter 2**). This method is similar to univariate SSA, but it takes advantage of both spatial and temporal correlations in the dataset by specifying the MSSA window size and the number of MSSA components for filling. Due to the enormous number of spatial channels (ISBAS DInSAR pixels) over the processed scene, a reduced covariance matrix with window length 27 (approximately 11 months) was used in the processing, which provides maximum spectral resolution $(M = N' = N/2)$ (Ghil et al., 2002) (refer to **Section 2.4.2** in **Chapter 2**).

The number of MSSA components used to fill the missing observations depends on the dataset, and on the amount of noise present. It is the same idea as with univariate SSA, which is in principle able to reject the higher ranked components corresponding to noise. With MSSA, only the four leading MSSA components that captured 43% of the variance have been used to estimate the missing observations. **Figure 6.13** illustrates the MSSA spectral estimate of filled-in data. The break represents the separation of the first four leading components from the noise.

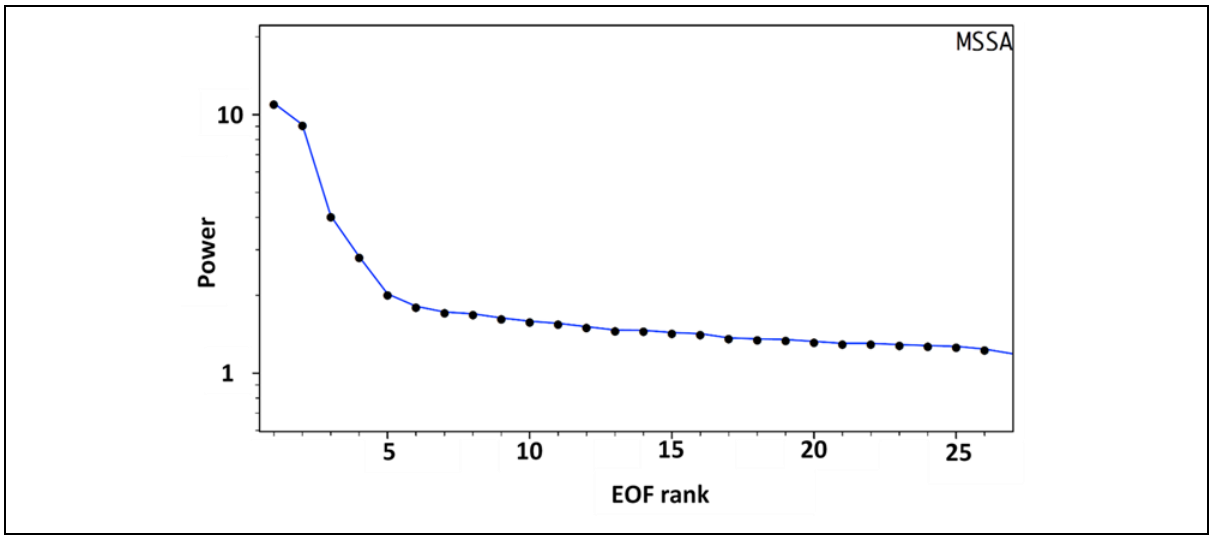


Figure 6.13: MSSA estimate of filled in ISBAS data over Flow Country with a window size of approximately 11 months. The first four leading components have been used for gap filling. The break in the slope between the first four leading EOFs and the other components indicate the separation of oscillatory modes from noise.

6.4.1.2 Seasonal trend identification using MSSA

The common seasonal oscillation (seasonal trend) for thousands of ISBAS points in the processed scene is then extracted using PCA->MSSA Kspectra-Toolkit software (Ghil et al., 2002). This method is the MSSA method, but it is done on data compressed by PCA. As explained in the previous section, the temporal window length has been set to 27 corresponding approximately 11 months to maximize the spectral resolution for thousands of channels and to yield the M and N' windows both approximately equal to $N/2$ ($M = N' = N - M + 1$). Here, the $ML > N'$ (where L is the number of channels and M is the window length), therefore, the reduce covariance matrix (**Section 2.4.2, Chapter 2**) is used rather than (ML X ML) matrix. Then the MSSA has been applied to 10 leading PCA components of the ISBAS spatial data to extract detailed temporal and spectral information from ISBAS DInSAR time-series. These 10 leading spatial PCs describe 95% of the variance of the time-series and they contain common characteristics for all utilized time-series and noise. This property makes it possible to compute

the common seasonal signals for all time-series. As explained in **6.3.1.4** peatland surfaces change seasonally (Kennedy and Price, 2005; Fritz et al., 2008) and this represents the curves of interest in this study, the seasonal trend (non-linear trend) for thousands of ISBAS time-series is modelled from a combination of four leading PCs in the low frequency domain that correspond to the non-linear trend. These four PC components have a frequency of 0.047, 0.017, 0.097 and 0.135 (cycle/month) respectively and the minimum frequency corresponds to 7.5 months with the total variance of about 91%. **Figure 6.14** (a) shows the variance of the data for the 10 leading PCs using a window size of 27 (the first four leading PCs with the highest variance represent the seasonal trend as discussed above).

It should be noted that the selection of different temporal window size (for example $M = 40$, which yields $N' = 15$ roughly 6 months as it is used in univariate SSA (**Figure 6.14** b) using reduced covariance matrix) splits the peak into a number of modes with neighbouring frequencies. As can be easily noticed from **Figure 6.14** b, there is no capability to sufficiently resolve between the non-linear trend (1, 2, 3, 4 and 5) and the noise. This difference in selection of different window size arises because the rank of the reduce covariance matrix in both cases are different, where for the first case **Figure 6.14** (a) is 27 and for the second case, which is equivalent to univariate SSA window, **Figure 6.14** (b) is 40.

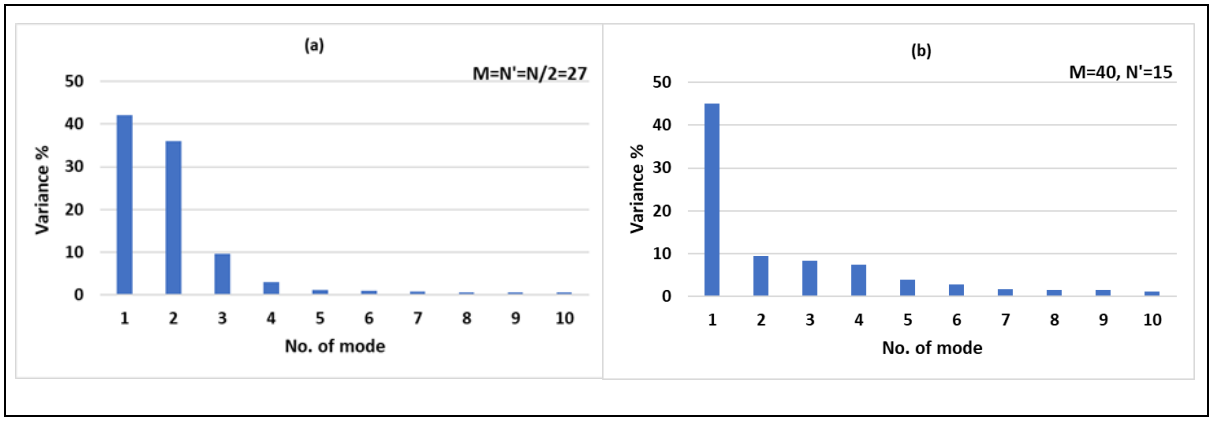
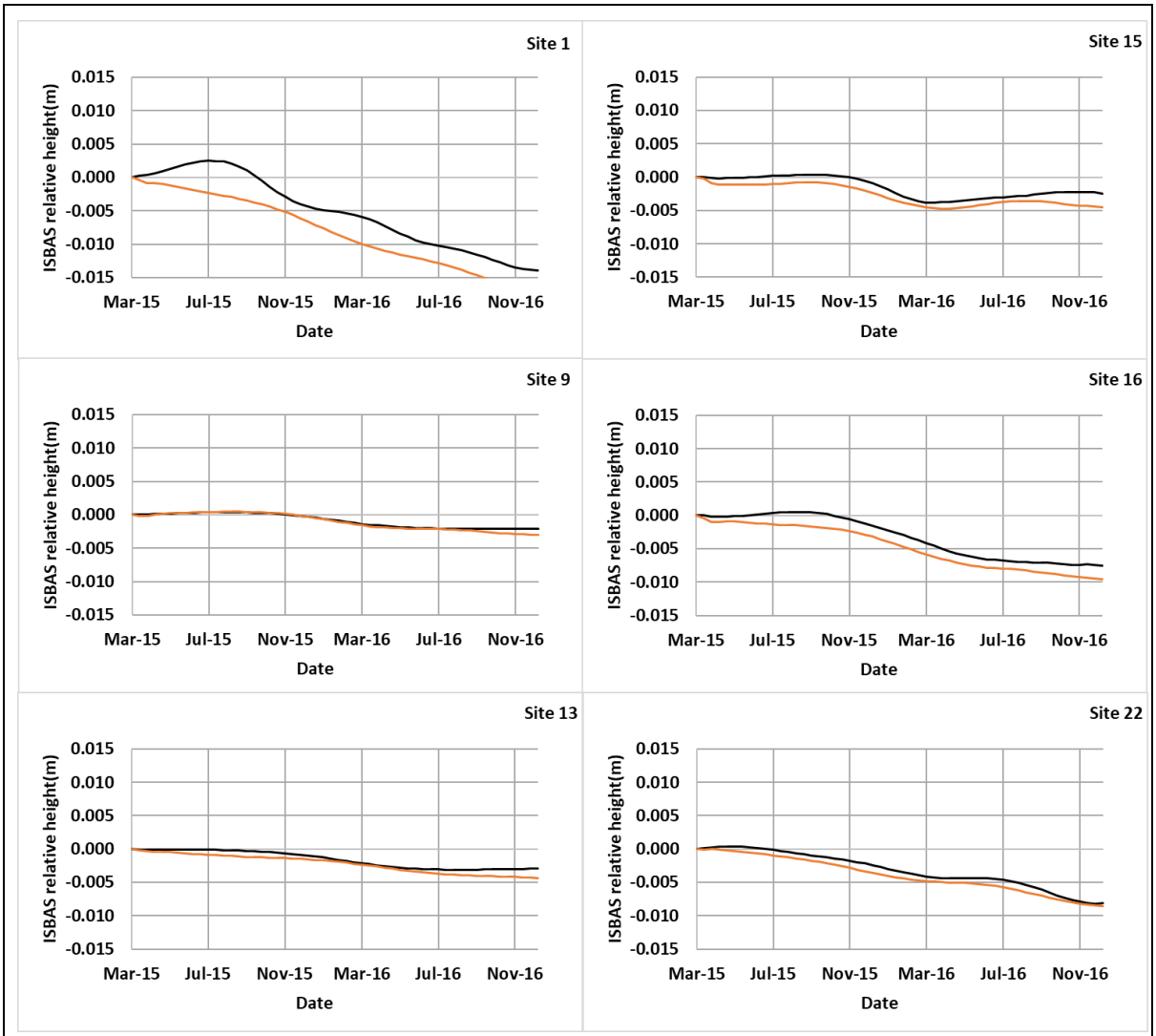


Figure 6.14: Variance of data explained by certain modes of MSSA for thousands of channels using two different window sizes with reduce covariance matrix. (a) window Size M=N'=N/2 =27 corresponding roughly 11 months, and (b) M=40, which yields N′=15 corresponding 6 months as it is used in univariate SSA.

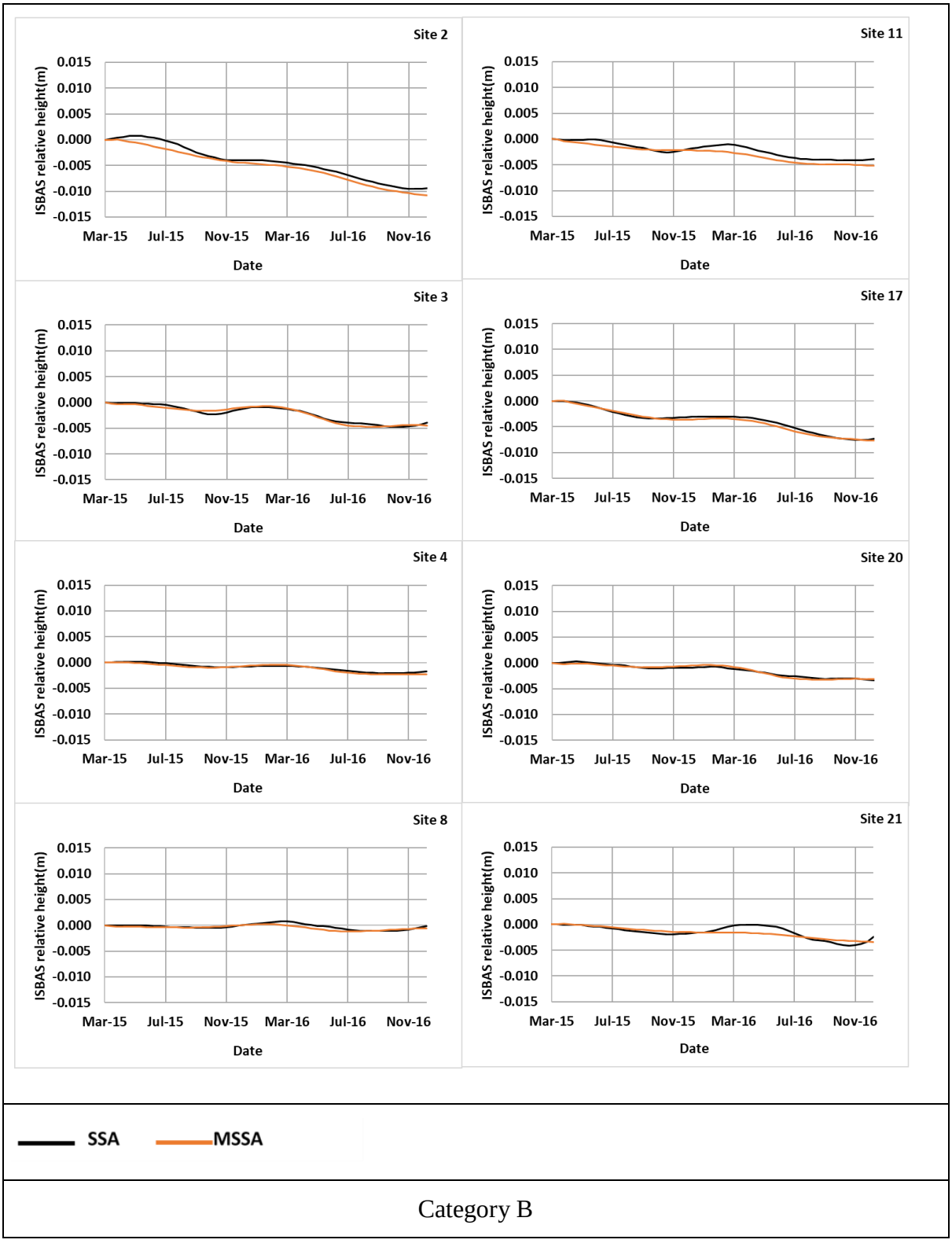
6.4.2 Results

6.4.2.1 Comparison with univariate SSA

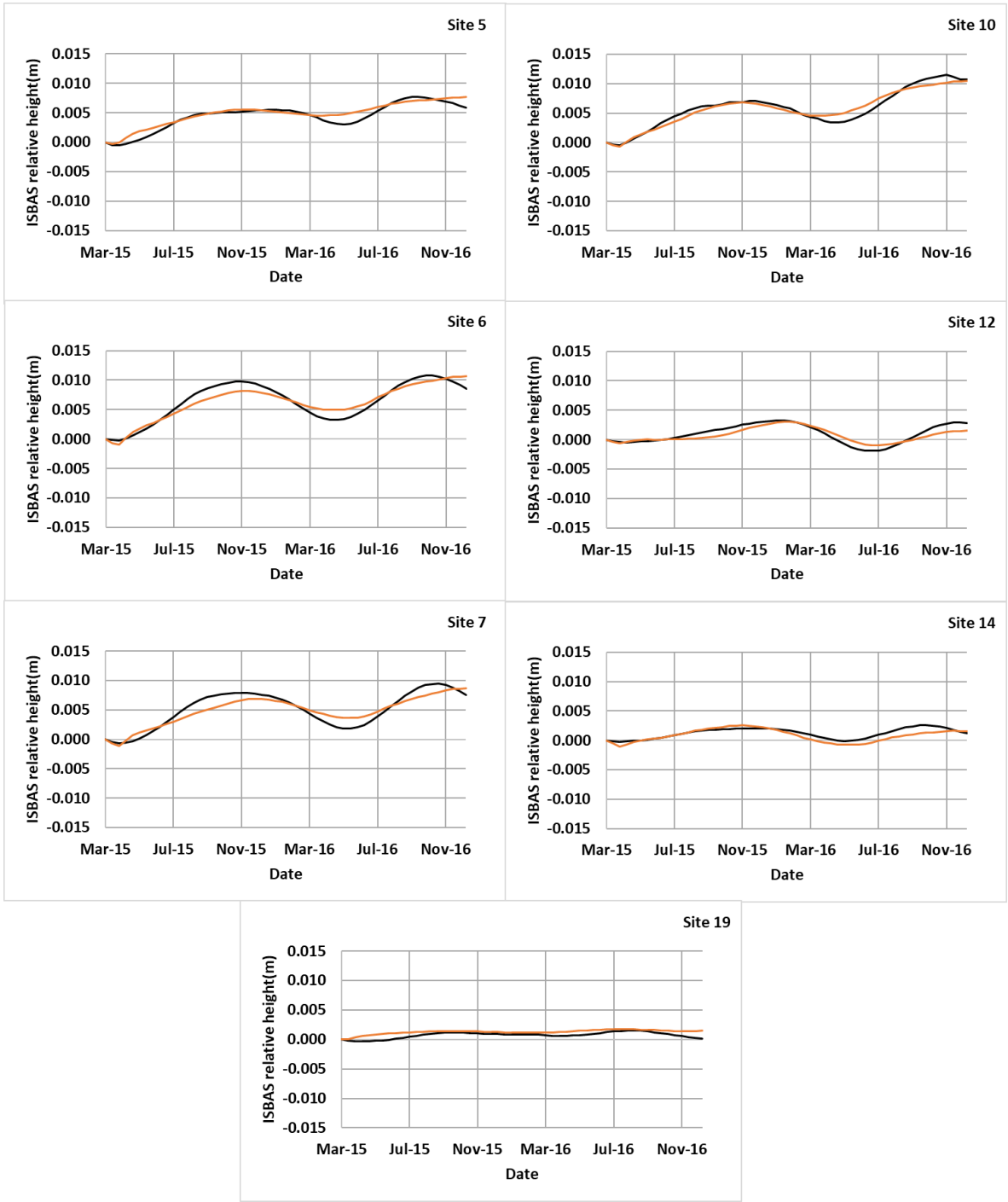
MSSA represents an extension to univariate SSA processing. The majority of the MSSA algorithm steps are similar to those of the univariate method. However, the difference between the two methods is the trajectory matrix structures and its approximation (Zhang et al., 2014). Referring to **Section 6.3.1**, the SSA has been applied to extract the non-linear trend (seasonal trend) of the ISBAS DInSAR time-series after stacking an average of 5 adjoining pixels over 22 sites. MSSA, on the other hand, provides the seasonal trends for all ISBAS points (thousands of pixels). For better comparison between the seasonal trends that were extracted using both methods, the seasonal trends from MSSA have been averaged for those ISBAS points that have been stacked over each 22 sites (**Section** 6.3.1.2). **Figure 6.15** shows the trends that were extracted for each site using SSA method and MSSA method for ISBAS DInSAR time-series. The seasonal trends resulting from both SSA and MSSA over each of the 22 sites are almost similar. However, small differences are noticed between them. These differences arise from a number of factors, for example, the difference in window size length and the number of components used to retrieve the seasonal trend. However, for both methods, the minimum frequency used to model the trend corresponds to 6 months and any components below the minimum have been discarded in the reconstruction stage. In addition, the modelled seasonal trend using SSA may contain real seasonal changes that are common for the entire data set, but may also be influenced by local oscillations, which cannot be distinguished between the selected components for the reconstruction process. MSSA, on the other hand, contains only the common signals that are varying within the time due to, for instance, real large scale geophysical changes (Gruszczynska et al., 2017). For example, over site 5 the percentage of the variance modelled as a non-linear trend (seasonal signal) using SSA is approximately 84% and the percentage of the variance modelled as a non-linear trend for all the time-series using MSSA is about 91% (**Figure 6.14** a) which means that the difference in variance (7%) may represent a site specific or local variation due to for example local hydrology. Summing up, the non-linear trend using SSA matches all time varying changes for individual time-series over each site but may include some noise. The modelled seasonal trend using MSSA, on the other hand, is not affected by site specific or local changes noise and therefore contains only the joint seasonal change for all the time-series.


Site 1
Site 15
Site 9
Site 16
Site 13
Site 22
ISBAS relative height(m)
0.015
0.010
0.005
0.000
-0.005
-0.010
-0.015
Mar-15
Jul-15
Nov-15
Mar-16
Jul-16
Nov-16
Date
SSA
MSSA

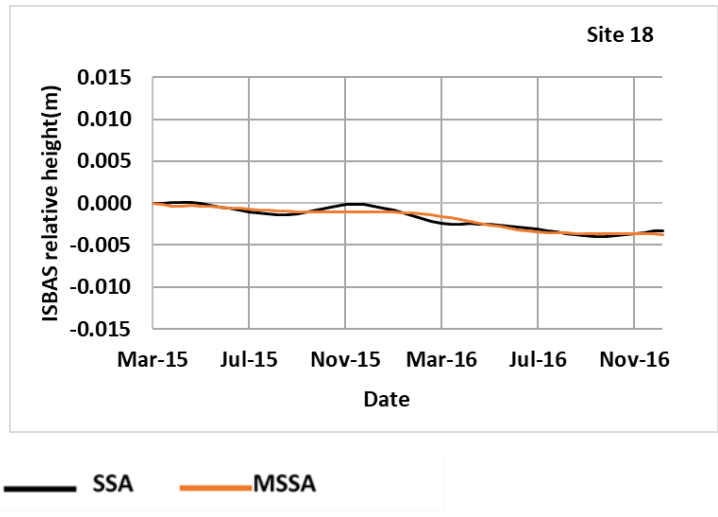
Category A


Site 2
Site 11
Site 3
Site 17
Site 4
Site 20
Site 8
Site 21
ISBAS relative height(m)
0.015
0.010
0.005
0.000
-0.005
-0.010
-0.015
Mar-15
Jul-15
Nov-15
Mar-16
Jul-16
Nov-16
Date
SSA
MSSA

Category B


Site 5
Site 10
Site 6
Site 12
Site 7
Site 14
Site 19
ISBAS relative height(m)
0.015
0.010
0.005
0.000
-0.005
-0.010
-0.015
Mar-15
Jul-15
Nov-15
Mar-16
Jul-16
Nov-16
Date
SSA
MSSA

Category C



Category D

Figure 6.15: Comparison of the non-linear trend (seasonal trend) extracted from SSA and MSSA for each category over each site.

6.4.2.2 Comparison of MSSA trends with peat condition

Time-series surface motion for 97 ISBAS points distributed over 20 sites (**Figure 6.1** and red dots in **Figure 6.2**) have been assessed by comparing the non-linear trend extracted using MSSA for each ISBAS point with peat condition for that point (condition 5 and 6 corresponding to site 16 and 21 are excluded from the comparison because they represent characteristics of specific sites (e.g., forest and cleared forest)). For example, 23 out of 97 ISBAS points are under condition 1 (classified using field survey and optical data (refer to **Section 6.3.2.1**)) (**Figure 6.16**); however, 16 out of them share the same trend (same peak of subsidence and uplift) (**Figure 6.17** a).

It is evident from **Figure 6.16** that most of the ISBAS DInSAR trends for 97 points have a significant correlation with peat condition. However, based on the similarity between the extracted seasonal trends, two distinct seasonal trends have been recognized (**Figure 6.17**). The first trend is for sites in good condition (condition 1 and 2). The sites under these conditions have a distinct seasonal oscillation with peak subsidence in late spring/mid-summer (April-June) and peak uplift in mid-winter (Nov-Jan) (small shift in peaks can be noticed between the sites under these conditions of approximately 1 to 1.5 month, which may be due to the variation of WTD between the sites, **Section 6.3.3.3**) (**Figure 6.17** a and b), which corresponds Category C in SSA, **Section 6.3.3.2**. The second seasonal trend is for sites under conditions 3 and 4,

where these sites display a subsidence trend with little or no seasonal oscillation (**Figure 6.17** b and c) and they correspond to Category A in SSA.

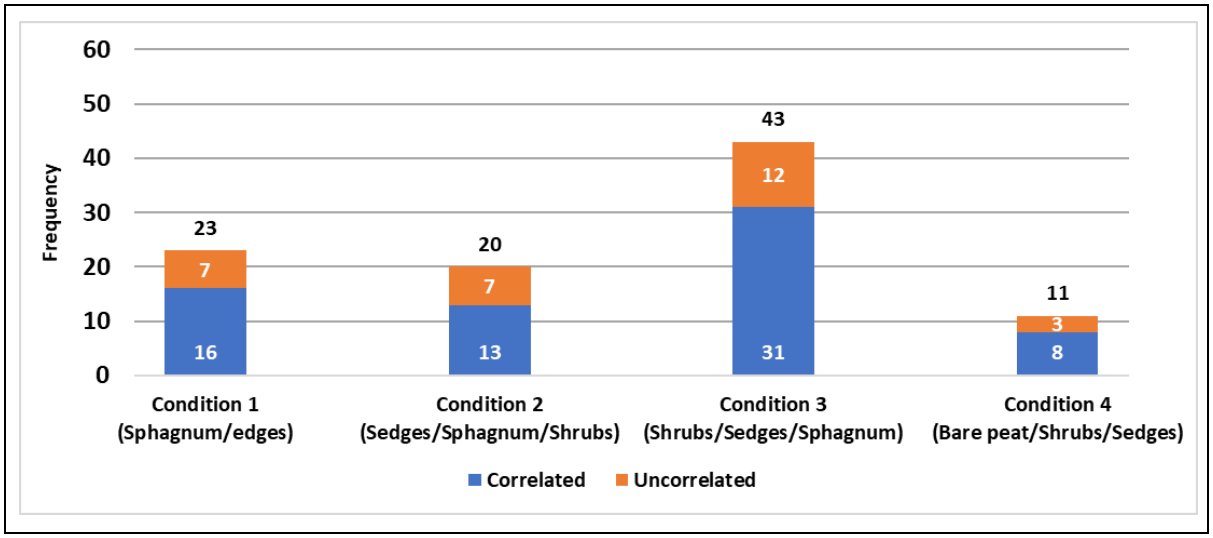
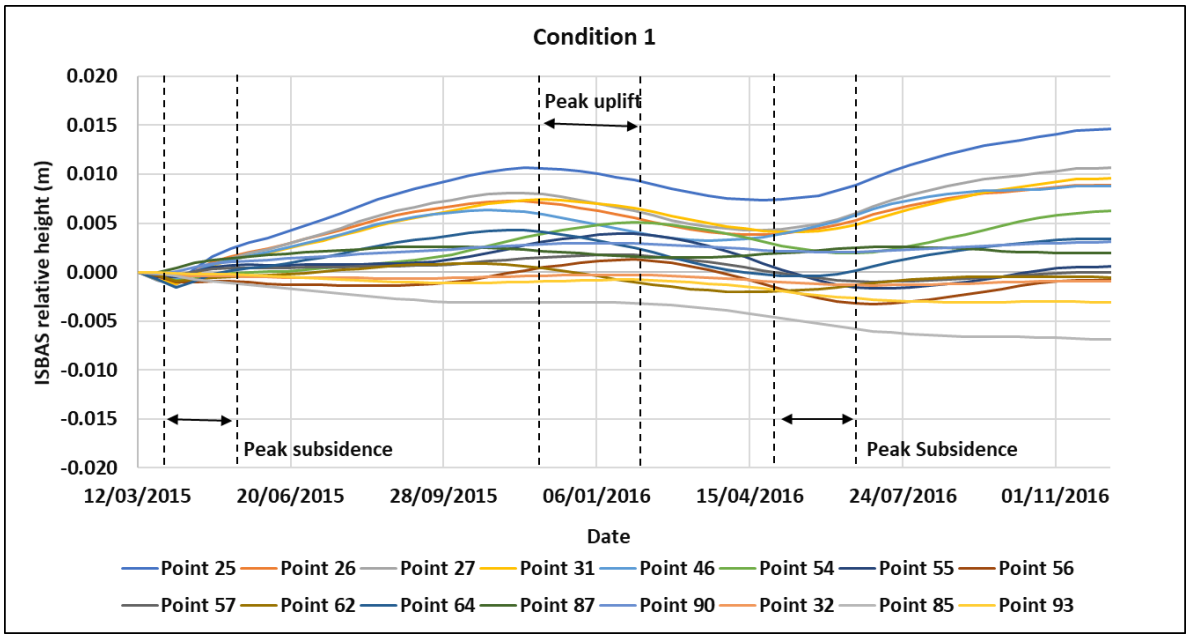
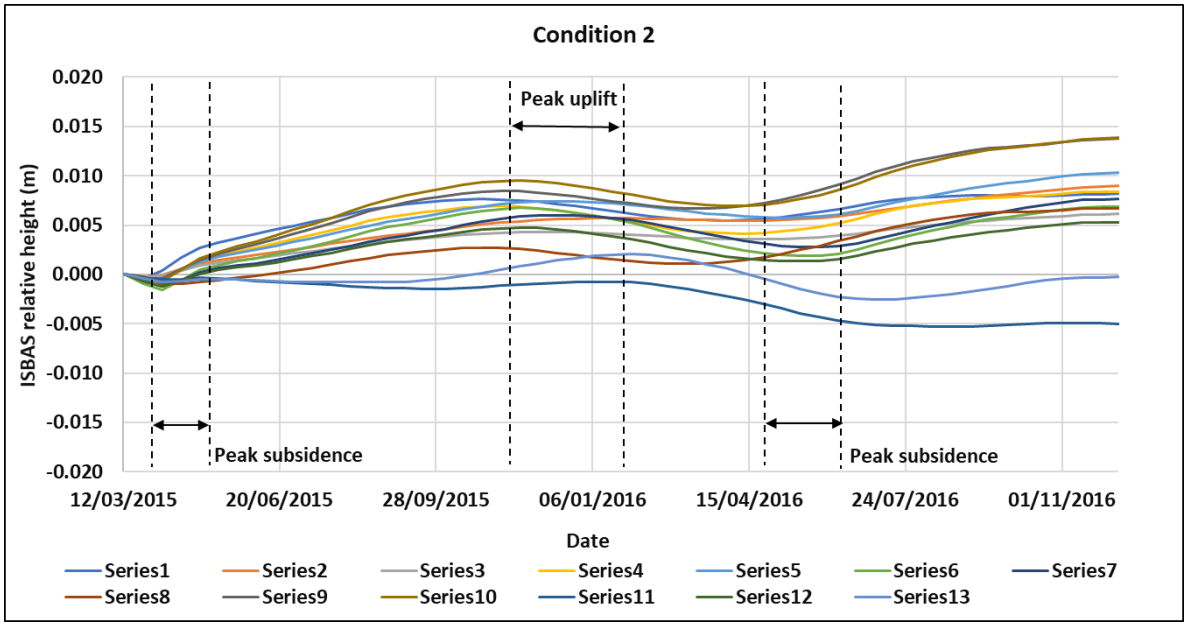


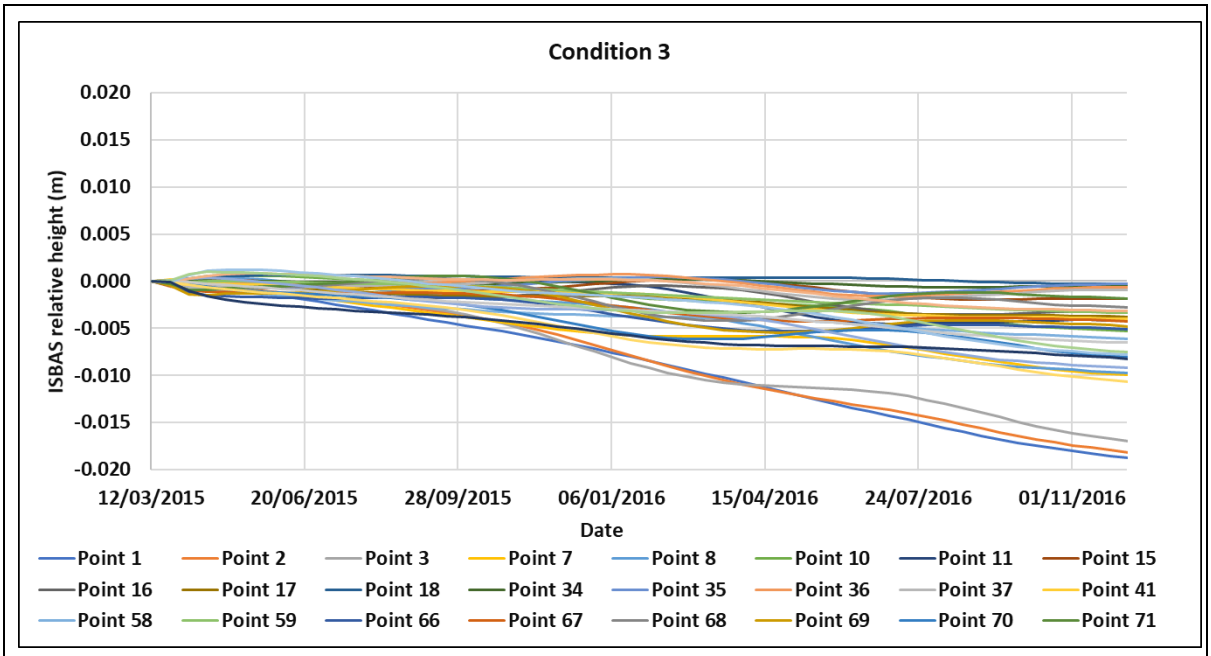
Figure 6.16: Comparison between the non-linear trend extracted using MSSA for 97 ISBAS points distributed over 20 sites with the peat condition for each point. Condition 5 and 6 excluded from the analysis because they are related to the forest and cleared forest, where the coherence of ISBAS points is very low and the standard error is very high.


Condition 1
ISBAS relative height (m)
0.020
0.015
0.010
0.005
0.000
-0.005
-0.010
-0.015
-0.020
Peak uplift
Peak subsidence
Peak Subsidence
12/03/2015
20/06/2015
28/09/2015
06/01/2016
15/04/2016
24/07/2016
01/11/2016
Date
Point 25
Point 26
Point 27
Point 31
Point 46
Point 54
Point 55
Point 56
Point 57
Point 62
Point 64
Point 87
Point 90
Point 32
Point 85
Point 93

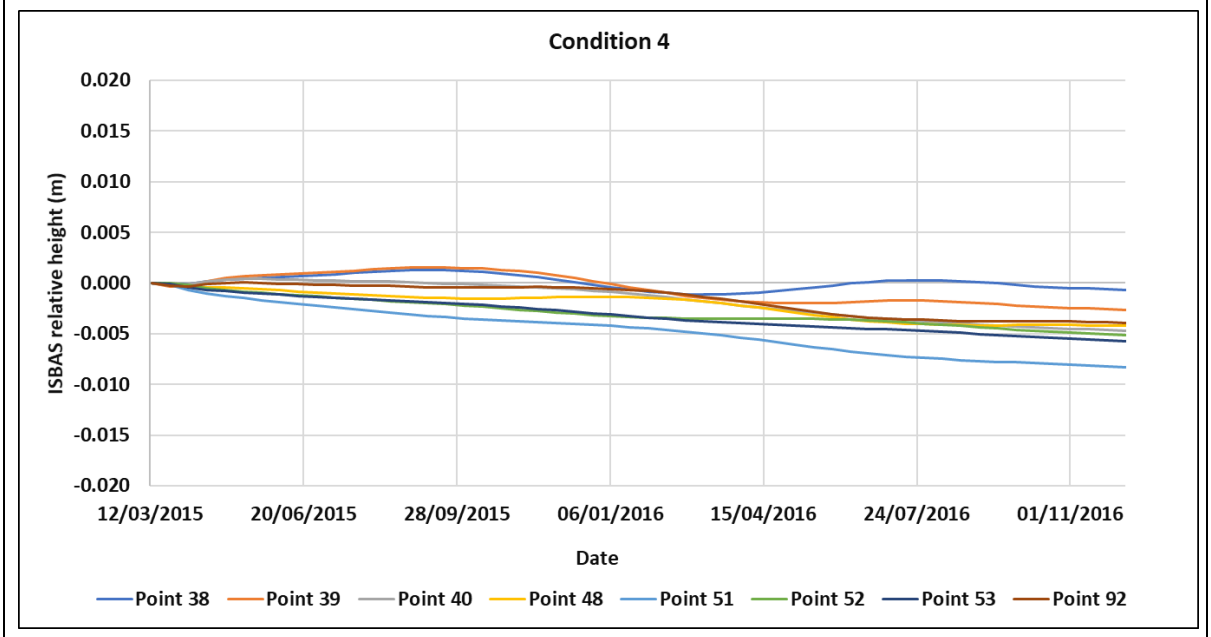
(a)


Condition 2
ISBAS relative height (m)
0.020
0.015
0.010
0.005
0.000
-0.005
-0.010
-0.015
-0.020
Peak uplift
Peak subsidence
Peak subsidence
12/03/2015
20/06/2015
28/09/2015
06/01/2016
15/04/2016
24/07/2016
01/11/2016
Date
Series1
Series2
Series3
Series4
Series5
Series6
Series7
Series8
Series9
Series10
Series11
Series12
Series13

(b)



(c)



(d)

Figure 6.17: Comparison between the non-linear trend extracted using MSSA for each ISBAS point over 20 sites with the peat condition. It shows only the correlated trend with the peat condition (**Figure 6.16**). (a) Display the non-linear trends extracted using MSSA for 16 ISBAS points sharing the same condition (Condition 1). (b) Display the non-linear trend for 13 ISBAS points under Condition 2. (c) Display the non-linear for 31 ISBAS points under Condition 3. (d) Display the non-linear trend for 8 ISBAS points under Condition 4.

6.4.2.3 Spatial variation of peat condition

After extracting the long-term seasonal trend from reconstruction of PCs 1, 2, 3 and 4 using MSSA method (with window length W=27 corresponding to approximately 11 months) for each ISBAS DInSAR time-series in the processed scene, the linear trend is removed (**Figure 6.18**). This process helps to investigate the spatial correlation between ISBAS points that are sharing the same condition and hydrology by means of seasonal changes (peak subsidence and peak uplift). Then the average non-linear trend for correlated points in each condition (**Figure 6.17** in **Section 6.4.2.2**) has been calculated (**Figure 6.19**) to aid interpretation of seasonal changes for thousands of ISBAS points. Therefore, areas in good condition (condition 1 and 2) with *sphagnum* and sedge dominated and shallow water table are anticipated to follow the seasonal trend in **Figure 6.19 a** and degraded sites under condition 3 and 4 are anticipated to follow the seasonal trend in **Figure 6.19 b**.

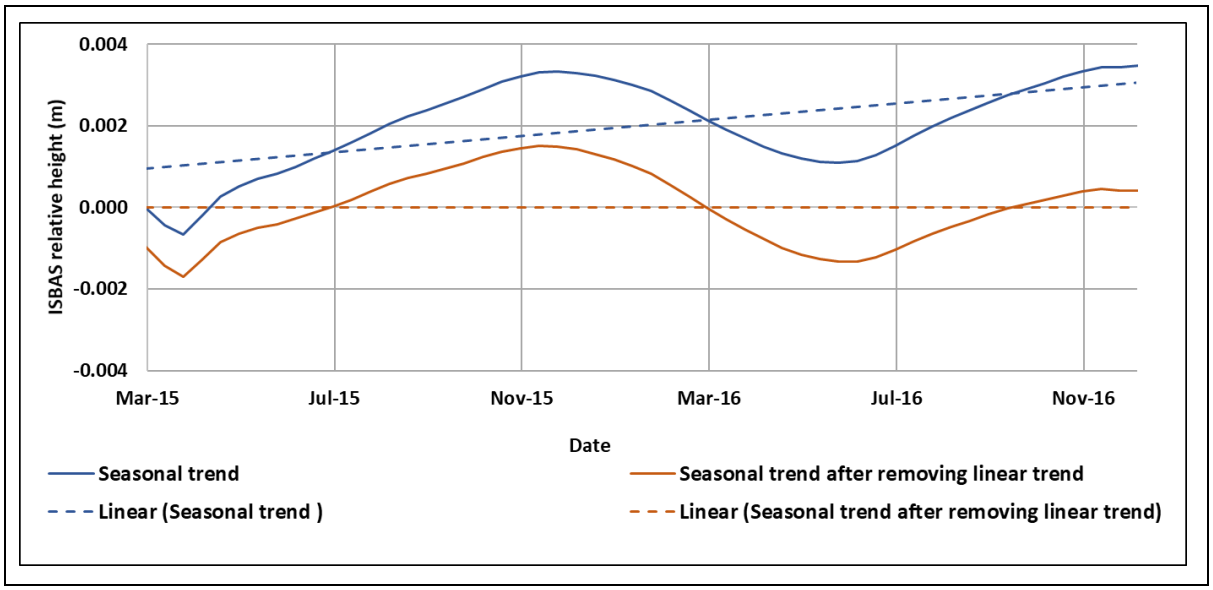


Figure 6.18: Example of seasonal trend extracted for each ISBAS DInSAR time series using MSSA before and after removing the linear trend.

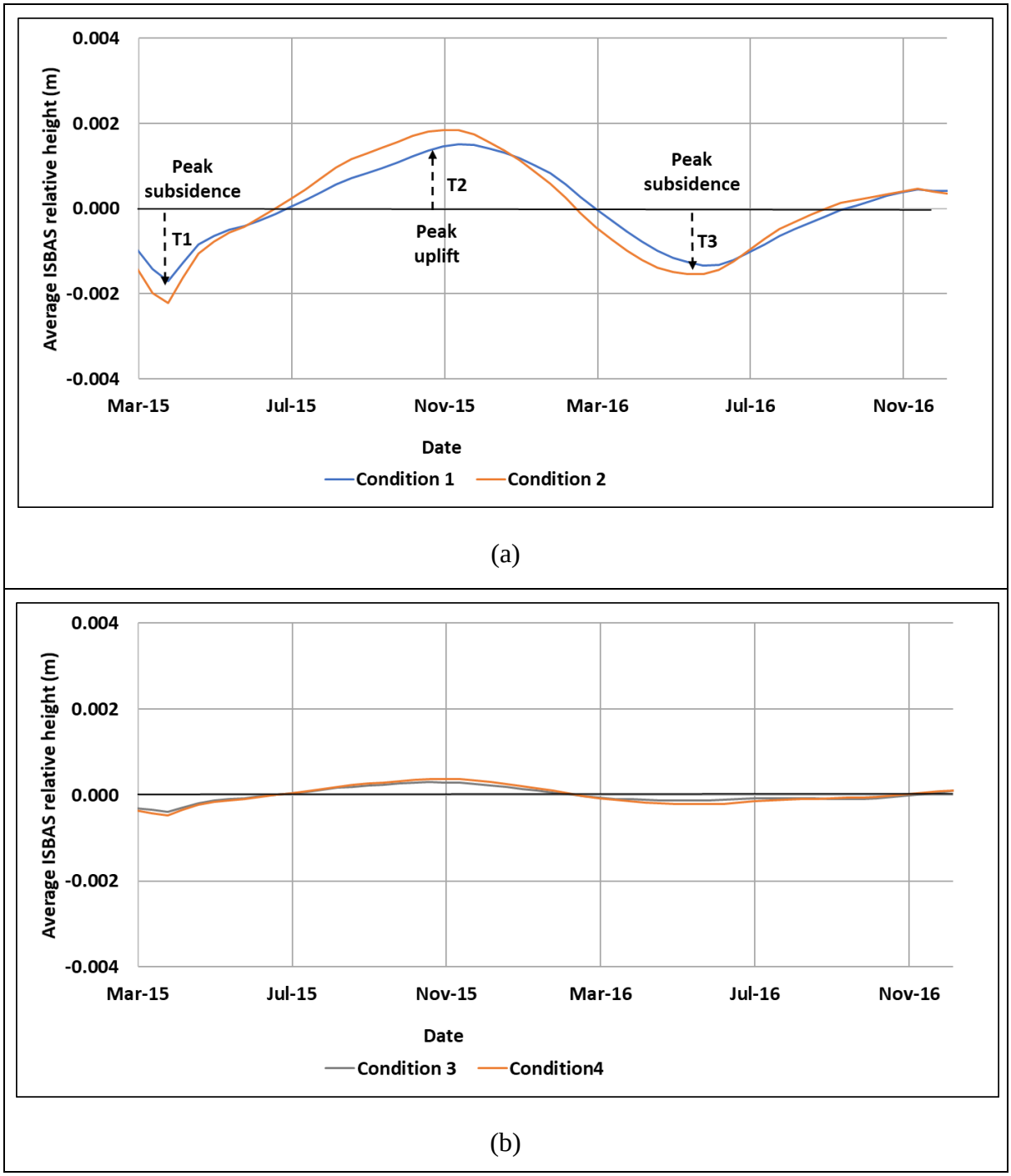
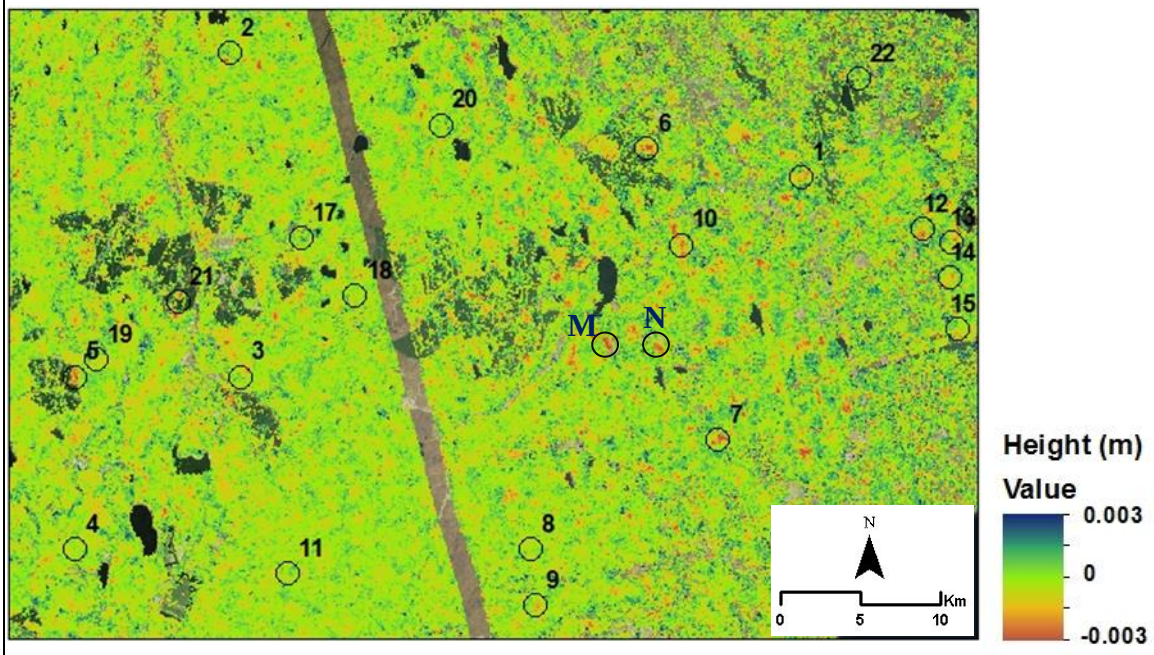
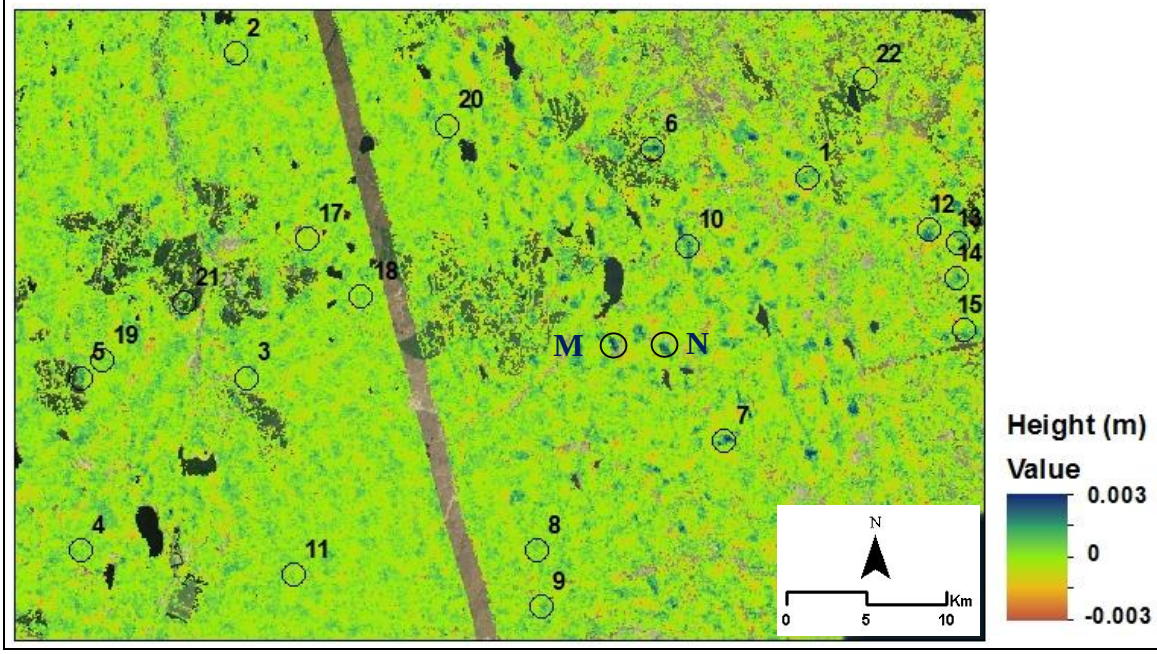


Figure 6.19: Average non-linear trend for correlated ISBAS points under each condition to aid interpretation of seasonal changes (peak subsidence and peak uplift) in regional scale. (a) Seasonal changes for areas in good condition (condition 1 and 2) with peak subsidence in late-spring/mid-summer (T1 and T3) and peak uplift in mid-winter (T2). (b) Seasonal trend for degraded areas (condition 3 and 4) with lack of seasonal oscillations.

(a) Spatial distribution of ISBAS DInSAR time-series for T1 in **Figure 6.19 a**



(b) Spatial distribution of ISBAS DInSAR time-series for T2 in **Figure 6.19 a**



(c) Spatial distribution of ISBAS DInSAR time-series for T3 in **Figure 6.19 a**

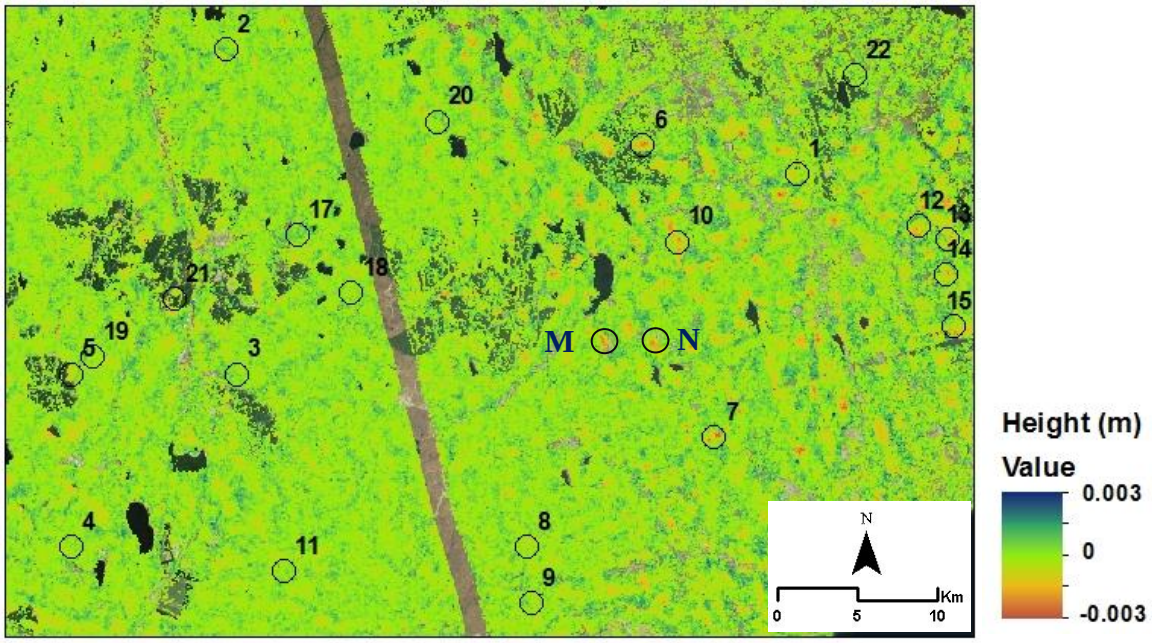
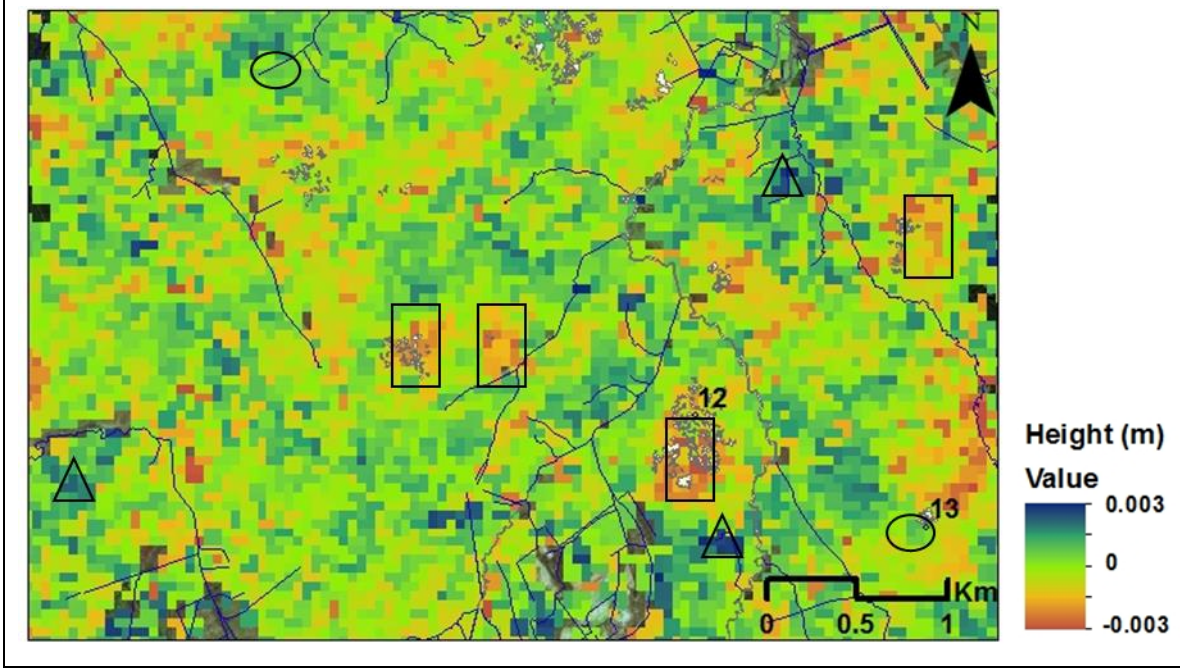


Figure 6.20: Regional seasonal trend maps obtained from the reconstruction of PCs 1, 2, 3 and 4 using W=27 which is approximately 11 months for each ISBAS point over peatland Scotland for the period (12/03/2015 to 7/12/2016). (a) Spatial distribution of ISBAS DInSAR time-series for T1 in **Figure 6.19 a** corresponds 5/04/2015. (b) Spatial distribution of ISBAS DInSAR time-series for T2 (19/11/2015) in **Figure 6.19 a**. (c) Spatial distribution of ISBAS DInSAR time-series for T3 (17/05/2016) in **Figure 6.19 a**. Dark circles represent the selected 22 sites over Flow Country. Peat condition over each selected site is explained in **Figure 6.11**. M and N expected wet sites in good condition (sphagnum and sedge dominated).

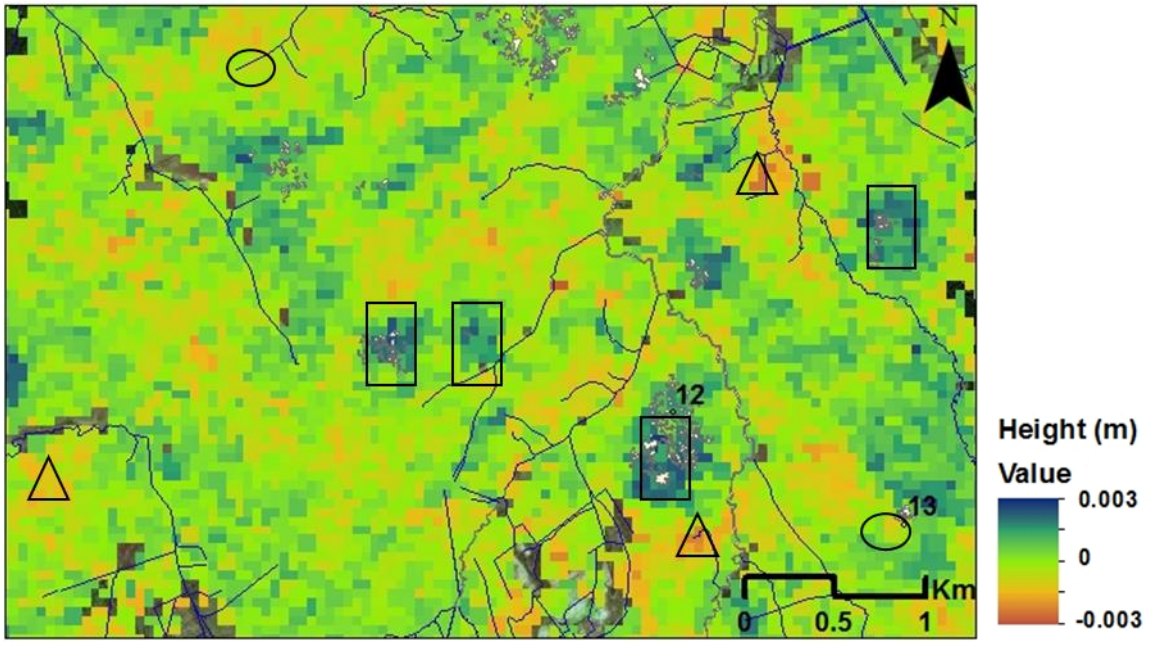
From regional scale ISBAS DInSAR trend maps (**Figure 6.20**), it can be seen that the regional spatial variation of surface motion displays two distinctive seasonal trends. First, sites with high seasonal oscillation (sites under condition 1 and 2) with peak subsidence in late spring/mid-summer (April-June) and peak uplift in mid-winter (Nov-Jan) follow the seasonal trend in **Figure 6.19 a** (category C in section **6.3.3.2)**. Moreover, sites with little or no seasonal oscillation follow the trend in **Figure 6.19 b** (category A in **Section 6.3.3.2**). According to the classification of peat condition using optical data and field survey, sites 5, 6, 7, 10, 12, and 14 have strong seasonal oscillation and this is evident in **Figure 6.20**. The high amplitude seasonal cycles with maximum subsidence between April and June (**Figure 6.20** a and c) and maximum uplift between Nov and Jan (**Figure 6.20 b**) are most likely due to the predominance of *sphagnum* and sedge species with a shallow, near surface water table (wet sites). Only site 19 under these conditions displays a low amplitude seasonal cycle and this may be due to the water

table being very close to the surface, high specific yield and open pore structure that promotes rapid drainage and minimal variations in water table depth. Consequently, all sites over the Flow Country which have the same seasonal trend as the sites above are expected to be *sphagnum* rich sites in good condition like sites M and N in **Figure 6.20**. The remaining classified sites (site 1, 9, 13, 15, 22, 2, 3, 4, 8, 11, 17, and 20) under condition 3 and 4 have a lack of seasonal oscillation (**Figure 6.19** b) as it is evident in **Figure 6.20**. Where most sites oscillate around 0 (**Figure 6.19 b**, green colour in **Figure 6.20**) and this can be explained due to low permeability of highly decomposed peat, the presence of fracture porosity that does not allow significant water storage within the peat matrix and low compressibility due to long term irreversible changes (Kennedy and Price, 2005).

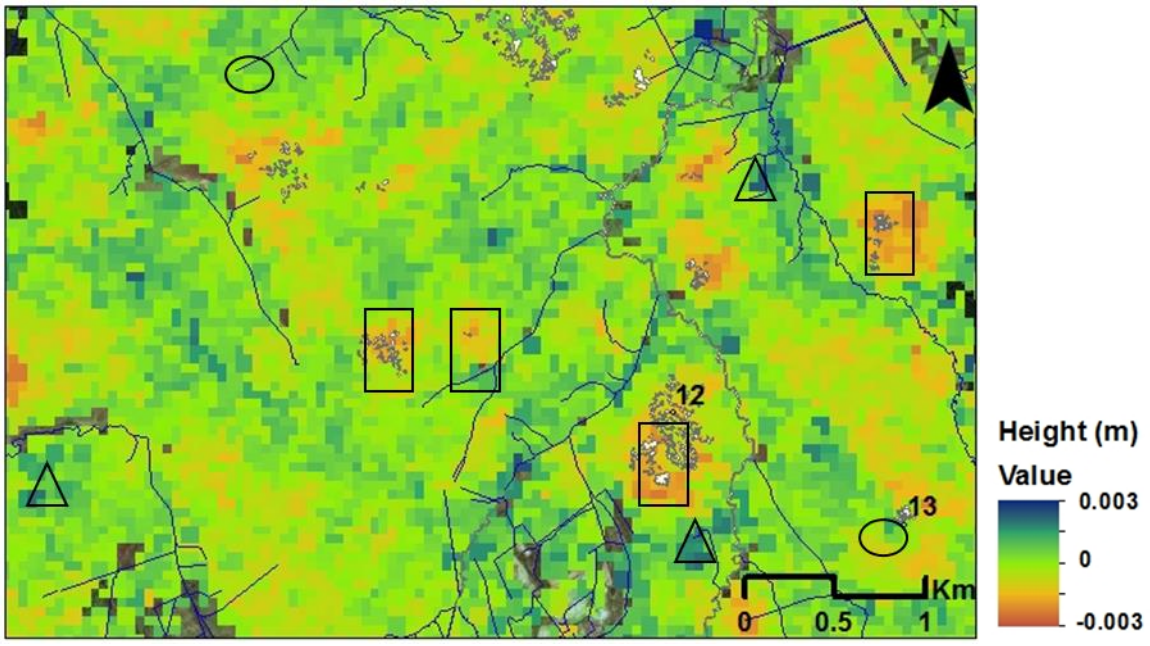
(a) Spatial distribution of ISBAS DInSAR time-series for T1 in **Figure 6.19 a**



(b) Spatial distribution of ISBAS DInSAR time-series for T2 in **Figure 6.19 a**



(c) Spatial distribution of ISBAS DInSAR time-series for T3 in **Figure 6.19 a**



(d) Linear LOS velocity map

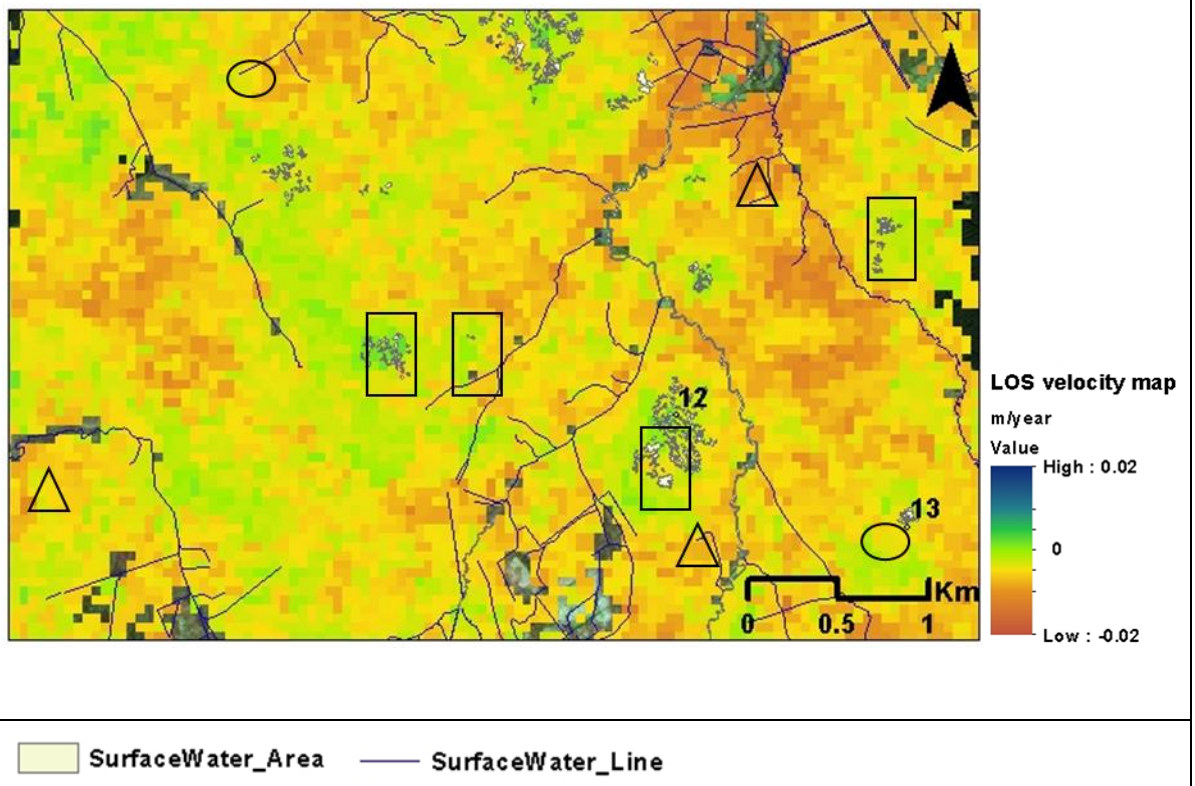


Figure 6.21: Local scale ISBAS DInSAR trend maps obtained from the reconstruction of PCs 1, 2, 3 and 4 using W=27 which is approximately 11 months for each ISBAS point over peatland Scotland for the period (12/03/2015 to 7/12/2016). (a) Spatial distribution of ISBAS DInSAR time-series for T1 in **Figure 6.19** a corresponds 5/04/2015. (b) Spatial distribution of ISBAS DInSAR time-series for T2 (19/11/2015) in **Figure 6.19** a. (c) Spatial distribution of ISBAS DInSAR time-series for T3 (17/05/2016) in **Figure 6.19** a. (d) Linear deformation map for the same area. Dark two circles show the condition of site 12 and 13 over Flow Country. Rectangles show the groups of points having almost the same condition and they follow the seasonal trend for sites in good condition (**Figure 6.19** a). Circles show sites in bad condition (follow the seasonal trend in **Figure 6.19** b). Triangles show the sites having opposite seasonal trend with the sites in good condition.

In contrast, smaller scale ISBAS DInSAR trend maps (**Figure 6.21)** (after zooming in) show the spatial variation of surface motion (peak subsidence and peak uplift) for each ISBAS point. It can be seen that each group of ISBAS points follow different trends; for example, the group of points under rectangle shapes follow the same seasonal trend for sites in good condition (condition 1 and 2 in **Figure 6.19 a**) and the group of ISBAS points under circle shapes follow the same trend for sites in bad condition (condition 3 and 4). However, the group of points under triangle shape has the opposite seasonal trend direction in comparison with the sites in good condition. This may be due to the predominance of vascular plants that exercise

strong evapotranspiration, which shifts the seasonal trend (peak subsidence and peak uplift) into the opposite direction to the sites having good condition, and can be interpreted as areas having an intermediate condition.

Comparison between InSAR trend maps (**Figure 6.21 a**, **b** and **c**) and the linear deformation map (**Figure 6.21 d)** illustrates that the linear deformation map can provide the level of degradation; however, the trend maps represent complementary maps to evaluate the peat condition through the characteristic of surface motion. For further clarification, site 1, for example, is the highly degraded site from the linear deformation map with maximum subsidence rate of about 2cm/year (**Figure 6.22 a**) due to afforestation (see **Chapter 5**, **Section 5.2.5.1**). However, the selected ISBAS points in this site are mixed between condition 3 (poor condition) which is predominant and condition 2 (good condition) based on the optical data calibrated by field observation of plant functional type which is not clear from the linear deformation map (**Figure 6.22 a**) but is evident from the seasonal maps (**Figure 6.22 b**, **c** and **d**). Therefore, using the seasonal trend maps from the ISBAS time-series will help to understand the seasonal behaviour for the selected site for future management particularly after removing the linear trend from the time-series (**Figure 6.18**) to investigate the spatial correlation between ISBAS points that are sharing the same seasonal trend using peak subsidence and peak uplift.

Although this study presents the capability of the ISBAS DInSAR technique to quantify the peat condition through InSAR time-series, more advanced analysis is needed to understand the variability and sensitivity of measurements to local peat conditions and whether or not this variability lies firmly within the realms of noise.

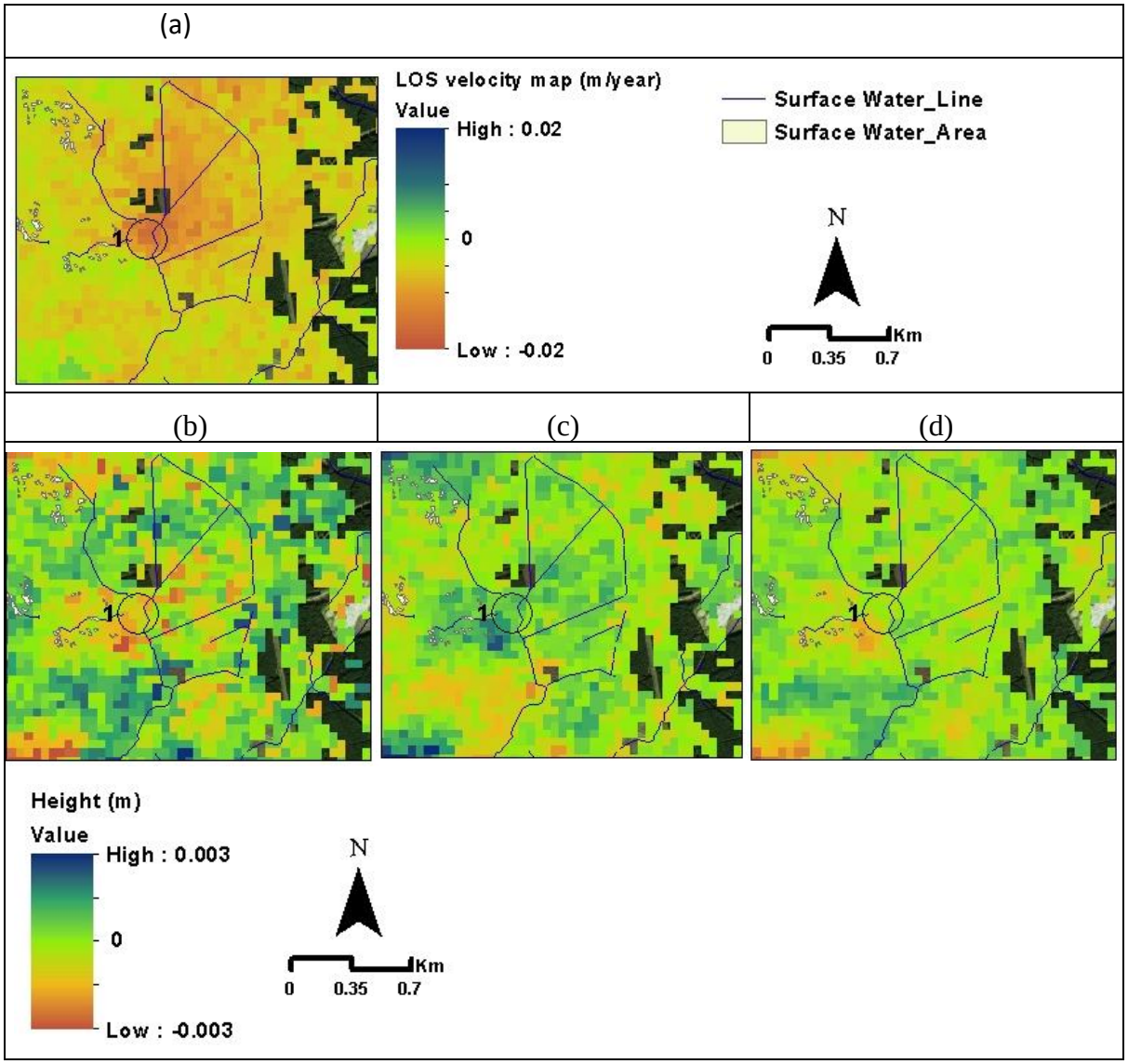


Figure 6.22: ISBAS DInSAR LOS velocity map along with the trend maps over site 1 and the surrounding area. (a) Shows the linear deformation rates over site1 which provide the level of degradation. (b, c and d) illustrate the seasonal trend maps correspond T1, T2 and T3 in **Figure 6.19a** which explain the peat condition and hydrology through the characteristic of surface motion.

6.4.3 Discussion

This study demonstrated that the seasonal trend differences estimated from both SSA and MSSA might be affected by the difference in window size length and the number of modes used to retrieve the seasonal trend. For SSA the window size length was 15 which corresponds to 6 months to get a higher degree of statistical confidence. However, with the MSSA the window size length was set to 27 corresponding to approximately 11 months to maximise the spectral resolution for thousands of ISBAS channels. Moreover, SSA may affect the stochastic

part of the ISBAS DInSAR data and artificially removes some part of the power (explained by the variance). The estimated variance explained by seasonal trend over site 5 using SSA is approximately 7% lower than the one estimated using the MSSA over the same site.

The results from both methods provide clear evidence that the differences in the surface motion characteristics quantified by InSAR are indicative of differences in peat condition and plant functional type. Sites in good condition (wet with sphagnum dominate) display markedly different long-term trends in comparison to sites in poor condition over the same period.

Comparison to water level indicates that for wet sites in good condition, the surface oscillations measured by InSAR correspond to oscillations in water level which is consistence with the field observation that the peat surface motion tracks the water level (Fritz et al., 2008; Reeve et al., 2013). Therefore, it appears that InSAR time-series provide a measure of the mechanical movement of the surface as it responds to the changing of water storage within the peat. By applying this explanation, the InSAR time-series can be considered as being composed of long-term irreversible changes in the mass of organic matter and water stored in the peat and short-term reversible changes in response to drying and wetting cycles (Camporese et al., 2006).

Using SSA to analyse the seasonal variations from ISBAS DInSAR time-series data distributed over 22 sites (the InSAR time-series for each site represents an average of about 5 adjoining ISBAS pixels), four different categories have been identified. **Category A** sites represent the most degraded sites. These sites display sustained subsidence with lack of sphagnum and seasonal oscillations. As explained in **Chapter 6, section 6.2.3.3,** the lack of seasonal oscillations may result from several factors associated with peat degradation. Loss of compressibility within the peat is an irreversible consequence of enhanced decay at the more degraded sites (Waddington and McNeil, 2002; Kennedy and Price, 2005). Low permeability of the compacted, humified peat combined with the possible presence of fracture porosity because of shrinkage does not permit significant water storage within the peat matrix. **Category B** sites are interpreted as degraded but not as severely degraded as category A sites. These sites include a greater mixture of plant functional types, which are dominated by vascular plants but do include some areas of *Sphagnum* and are interpreted to be generally wetter with a greater capacity for seasonal water storage. In contrast to category A sites, there are clear seasonal oscillations but with lower amplitude than the sites observed under category C. This can be interpreted that the water-level for these sites is shallower than the sites under category

A and deeper than the sites under category C. In addition, these sites are less degraded with greater porosity, elasticity and water storage than sites under category A. The presence of vascular plants cause reduction in the water level during the growing season due to the strong evapotranspiration process which may explain the behaviour of seasonal oscillations for the sites under this category (minimum water level in late summer-mid autumn (Aug-Oct) and maximum water level in late winter-early spring (Feb-April)). **Category C** sites are Sphagnum and sedge dominated with a shallow, near-surface water table. Evaporation through Sphagnum is directly linked to the evaporative demand of the atmosphere and depth to water table. The high amplitude seasonal cycles and mid-summer/mid-winter minima and maxima are most likely due to the predominance of the non-vascular Sphagnum species in which potential evaporation exercises a greater or equal control on the total evapotranspiration (Lapen et al., 2000). The physiology of Sphagnum, therefore, shifts maximum drawdown and recharge of the water table and associated surface motion to a mid-summer/mid-winter pattern that aligns with seasonal variations in evaporative demand in the UK (Robinson et al., 2017). The surface motion of **category D** site represents a mixture between category A and category C. The category C component is interpreted as evidence of a shallow water table and probable colonisation by Sphagnum in areas of ditch blocking; however, the strong subsidence more typical of category A sites is interpreted to indicate that despite rewetting the site is still losing mass, possibly over more elevated areas resulting in overall rapid subsidence.

Using MSSA to analyse the seasonal variations from ISBAS DInSAR time-series data for each single ISBAS pixel (the assessment has been made for only 97 ISBAS points distributed over 20 sites due to the availability of ground data measurements from optical data and field survey), two distinct categories have been identified. The first category is for sites in good condition which corresponds to the sites under category C in SSA. The second category is for sites in bad condition, which corresponds to sites under category A in SSA. However, for both categories, variations in ISBAS relative seasonal amplitude and shift in peaks for approximately 1 to 2 months have been noticed, which can be interpreted due to the variation of water table depth WTD between the sites under the same category and composition of plant functional type that cover each ISBAS point. Therefore, it can be concluded that the seasonal trends for sites under category B and D using SSA represents the consequence of the averaging process between category A and category C; i.e., stacking of an average 5 ISBAS time-series with the different condition for each site (combined trend). In addition, the spatial variations of the seasonal trend over time in ISBAS DInSAR time-series that may arise from large scale

hydrological changes have been assessed using MSSA. It has been found that these seasonal maps can provide the extent of surface motion of the peat body that has as a single hydrological entity or coalesce into large composite units. In turn, these maps can be used as classification maps to indicate the functional hydrology levels to assist future management by identifying, for example, the potential restoration sites and prioritizing them using ecological and hydrological (by means of the seasonal trend from InSAR time-series) and economic criteria which are not a simple task.

This analysis carries important implications as peatland surface motion can be attributed to changes in water budget, water table depth, carbon balance and net ecosystem exchange (Moore et al., 1998; Laine et al., 2007; Mezbahuddin et al., 2017). Hence if the InSAR time-series capture meaningful characteristics of the surface motion, this will open up a new view of peatland dynamics on an unprecedented scale that would not be practical using standard field-based techniques. As changes in water storage due to drainage or restoration should precede ecological change, InSAR time-series characteristics also have the potential to offer a sensitive monitoring tool that can be used to quantify evolving peatland condition. InSAR time-series also have a high spatial density that enables a new approach to regional peatland monitoring through the application of MSSA (e.g., principle component analysis and extend empirical orthogonal functions) more typically deployed in climatology and oceanography. However, the analysis of InSAR time-series using the techniques described above (SSA and MSSA) is sensitive to the quality of InSAR data itself. Moreover, any error related to the processing of InSAR time-series can lead to bad reconstruction of the time-series, in turn, provide meaningless characteristics of surface motion.

In this research, the empirical relationship between the InSAR measures and the site condition is considered. The accuracy of the InSAR measure or the sensitivity of the InSAR approach to change has not been addressed. There is also a question as to the representativeness of the InSAR signal in particular whether wet *Sphagnum* covered surfaces in hollows and adjacent mounds with more vascular plant function types contribute equally to the InSAR signal. By addressing these questions, a far greater understanding of the radar response may be obtained. To achieve a true assessment of accuracy will be difficult as single points or short transects do not replicate the totality of the InSAR response from a 100x100 m area and where peatland field data is available the error in field measurements is a major source of uncertainty. However, despite this validation difficulty, the precision of the measurement is clearly sufficient to produce a meaningful signal that relates to the peatland process and condition.

6.5 Limitations of using ISBAS time-series to quantify peat condition

It should be noted that there are two potential errors could be presented in the processing of ISBAS DInSAR time-series:

1. Additional phase unwrapping errors: there are two phase unwrapping steps required to retrieve the deformation at SAR acquisition dates using ISBAS algorithm. The first is presented previously in **Chapter 2**, **Section 2.3.1.6**, that made on the differential interferograms to retrieve and estimate the linear deformation rates and topographic errors. The second phase unwrapping step is performed on the residuals from the first processing (**Chapter 2**, **Section 2.3.2)** to calculate the non-linear deformation along with the atmospheric delay components (the atmospheric phase screen (APS)).

2. Atmospheric delay error: in the linear model using Punnet software, the atmospheric delay is eliminated using the assumption that the stratified troposphere is random over time, thus has mean zero. This assumption is considered to be valid for stacking a large number of interferograms that are appropriately distributed over a long period. Then the phase contribution from the linear model is subtracted from the original unwrapped phases. The residuals, in this case, are assumed to have the non-linear component, atmospheric delay (also called APS) and noise. In this stage, the non-linear deformation component can be separated from APS using custom filters (**Chapter 2**, **Section 2.3.2**) based on the assumption that the atmospheric signal is correlated in space, while the deformation component is correlated in time. The performance of these filters is dependent on the validity of the assumptions such as the atmospheric signal is correlated within 5 km radius and on the number and distribution of the interferograms. Moreover, separating the non-linear deformation component from APS will be more challenging for the area having a slow deformation rate as it can be masked out by noise. Therefore, the quality of the InSAR time-series should be examined first before using them for further analysis.

6.6 Summary

This chapter is focused on the research undertaken to address the capability of InSAR to evaluate peat condition and hydrology by applying the ISBAS technique to characterise peat deformation over 18 months at 103 ISBAS points distributed across 22 discrete peatland sites in the Flow Country, Northern Scotland. Peat condition at each single point in each site was determined using plant functional types quantified via field survey and optical satellite imagery. Using univariate SSA, the seasonal trends from an average of 5 adjoining ISBAS points under three categories were compared with the average peat condition for each category. Extending Univiriate SSA to MSSA to extract the common seasonal trends and noises for all time time series represents the main advantage of the MSSA (Gruszczynska et al., 2017). With multivariate SSA (MSSA), the peat condition was compared to surface motion trends for each ISBAS point distributed in all sites. The results indicate that the InSAR technique can provide a meaningful description of peat condition and its hydrology through surface motion, based on the seasonal trend. Three distinct trends under category A, B, and C were observed through applying SSA to an average ISBAS DInSAR time-series at each site. However, by applying MSSA, two distinct trends were observed (corresponding to category A and C), in addition to other less consistent trends.

CHAPTER 7

CONCLUSIONS AND RECOMMENDATIONS

This chapter presents the conclusions on the various aspects of the research restating the aims and objectives and summarising how each was achieved, which leads to a list of suggestions and recommendations for future work.

7.1 Review of the aims and objectives

Chapter 1 contains the aims and objectives of the research. The stated aims were to:

- Conduct background research regarding the application of InSAR over peatland areas.
- Analyse what value the ISBAS technique, in particular, might bring to peatland monitoring.
- Consider how the ISBAS technique might be used to infer peat condition.

And the objectives were to:

- Identify gaps in the use of InSAR for peatland deformation monitoring.
- Investigate the potential of using the ISBAS DInSAR technique for long-term peatland monitoring.
- Investigate the potential of using the ISBAS DInSAR time-series to quantify peat condition.
- Determine how other sources of data might be used to validate ISBAS results.

These are discussed in the following sections to demonstrate what was achieved in this research and what could be improved in future research endeavours.

7.2 Research gaps

The basic principles of all techniques relevant to this research were presented in **Chapter 2**. Research relating to the importance of peatlands in ecosystem services, peatland distribution and the causes and consequences of peatland degradation were discussed in **Chapter 3**. This naturally led to the research motivation involving the techniques used for monitoring change in these areas, with a review of the difficulties in monitoring them. The capability of InSAR to map and analyse the dynamics of the Earth's surface was also discussed. This chapter ended with a summary of limitations relating to these subjects.

7.3 Using ISBAS DInSAR technique for long-term peatland monitoring

Two case studies have examined the feasibility of using the ISBAS DInSAR technique for long-term peatland monitoring:

1. In the case of open peatland areas (Flow Country, northern Scotland), two C-band SAR datasets (ERS 1/2 spanning the period from 1992 to 2000 and Sentinel-1 SAR data for the period between March 2015 and December 2016) have been used to investigate the feasibility of ISBAS technique for long-term peatland monitoring. Although C-band SAR data has limited capability to penetrate the vegetation canopies, the ISBAS velocity maps over this peatland area from both datasets provided a meaningful account of peatland condition in terms of peat growth, stability or subsidence which enabled the identifications of areas undergoing changes. This suggests that over open peatland area, the ISBAS DInSAR technique can be used as a more effective technique for peatland surveying that would reduce the long-term monitoring cost by assessing the relative magnitude and spatial pattern of the deformed areas that are caused by, for example, drainage, afforestation or erosion which in turn provides key information for guiding future management.
2. In the case of a drained coastal peatland area farmed for agriculture (Zennare Basin, south of Venice Lagoon, Italy) three C-band SAR datasets (ERS 1/2 for the period 1992 to 2001, ENVISAT from2003-2008 and Sentinel-1 for the period between 2015 to 2018) were used to assess the capability of ISBAS technique to monitor the deformation over this area. The spatial coverage of the ISBAS maps over this agricultural area was significant in comparison with other InSAR techniques, but the results were somewhat noisy with a lack of coverage (not like the results over open peatland area, such as the Flow Country). This suggests that ISBAS results over manged farmed peatland area are less consistent in comparison with open peatland area as a result of farming practices, which contribute to the decorrelation of the interferometric phase between the image pairs. This has been treated using the regular acquisitions of the Sentinel-1 data with a short repeat cycle of 12 days which provide potential for mapping a surface motion over this farmed peatland area. However, the limited ground data hindered the complete understanding of the deformation and a true assessment of the ISBAS accuracy.

Combining these two case studies suggest that ISBAS technique is feasible for long-term peatland monitoring using C-band Sentinel-1 SAR data in particular by virtue of gathering a significant stack of images in short time. This provides the opportunity to reduce the temporal

baselines to ensure good coherence between the interferometric pairs but still retain a high number of observations, which increase the confidence in the ISBAS results. The accuracy of the estimated linear velocity rate is inversely propotional to the time span covered by the InSAR observations.

7.4 Using ISBAS time-series to quantify peat condition

A novel analysis of the ISBAS DInSAR time-series was applied, which linked the characteristics of surface motion derived by InSAR and peat condition. This was applied to the Sentinel-1 ISBAS time-series over the Flow Country through the application of SSA and MSSA. The results suggest that:

- Analysing InSAR time-series using these applications helps to understand the seasonal kinematic behaviour of peatland from local to regional scales.
- Due to the strong correlation between the surface motion recorded by InSAR and peat condition (**Chapter 6**), successful application of InSAR over these open peatland areas will decrease the cost for long-term monitoring, help rapid and unbiased evaluation of these areas for future management and assist quantification of peat condition in remote areas.
- The analysis of InSAR time-series suggests that the changes over peatland area can be noticed in the short-term; i.e., seasonally every six months particularly in wet areas with *Sphagnum* and sedge dominated during the growing season (peak amplitude of seasonal cycle) and in the long-term of approximately one year.
- Seasonal maps extracted from InSAR time-series using MSSA can provide the extent of the peat areas that are sharing the same condition. In turn, these maps can be used as classification maps to indicate the functional hydrology levels (from good, intermediate, to bad condition) to assist future restoration. In addition, these maps can be used for risk assessment from, for example, peat landslide hazard, by identifying the degraded areas which are more susceptible to landslide and analysing the relationships between the seasonal behaviour derived from InSAR time-series and triggering factors such as rainfall.
- InSAR trend maps using MSSA represent complementary maps to the linear deformation maps. The latter provides the level of degradation whereas the former allows the evaluation of the peat condition through the characteristics of surface motion.

This synergy between these maps will help to identify suitable sites for future management which can be applied over all wetland areas.

7.5 ISBAS accuracy

True assessment of InSAR accuracy is difficult to achieve through using field observations of single points or short transects due to the mismatch between the scale of observation, accuracy and precision of InSAR and field observations (**Chapter 5**, **section 5.2.5.2**). An alternative validation method was used by comparing the characteristics of ISBAS DInSAR surface motion time series to readily obtained vegetation and land use based on the measurements of peat condition. The underpinning hypothesis here is that the ISBAS DInSAR results are representative of the surface motion (at high temporal resolution) of the peatland and in turn that surface motion is representative of peat condition. This hypothesis is considered to be not valid over farmed peatland area due to farming activities (ploughing and harvesting different types of crops). The peat surface motion over farmed peatland area might be quantified using hydrological field measurements such as soil moisture, water table depth, temperature fluctuations and peat oxidation (Zanello et al., 2011) and linking them InSAR time-series of surface motion. However, differences and uncertainties may introduce between the observations as explaned in **Chapter 5**, **Section 5.2.6.2** due to error propogations.

The fluctuations of water table depth in this research have also been used to validate InSAR time-series. However, the WTD time-series present a shorter time sampling interval (daily and every 30 mins) than that available from the InSAR time series (every 12 days). Therefore, the WTD time-series have been resampled to the revisiting time interval of the Sentinel-1 satellite (every 12 days). The comparison between plant functional type and WTD with ISBAS time-series provides a meaningful estimation of peat condition. This suggests that absolute accuracy is difficult to achieve over these areas; however, alternative approaches (as explained above) can be used to validate InSAR results.

7.6 Limitations of the methodologies

Through assessment of peatland condition using ISBAS technique over two different peatland environments, the primary limitations of applying this technique and analysing the InSAR results can be summarized as follows:

1. InSAR phase unwrapping error: phase unwrapping over this vegetated area where the coherence is highly variable may encounter some difficulties which may cause underestimation of the deformation for the areas undergoing large deformation rates

due to the ambiguity. This can be minimised by having short temporal baselines to reduce the effect of any large deformation on the interferometric phase. Reducing the temporal baseline to less than four years was difficult to achieve with the use of ERS and ENVISAT datasets due to the gaps in the time-series and long revisit cycle of 35 days. However, regular acquisitions of the Sentinel-1 satellite with a short repeat cycle of every 12 days made it possible to decrease the temporal baseline to preserve the coherence between the image pairs and measure greater rates of deformation with high confidence. This suggests that over peatland areas, short temporal baselines are required to ensure good coherence between the interferometric pairs using C-band SAR data, which in turn decrease the probability of underestimation of the deformation for the areas subject to high changes.

2. ISBAS accuracy: from the available ground measurements (levelling data) over Flow Country, the ISBAS accuracy was difficult to achieve due to the temporal and spatial mismatch. This suggests that the archived field observations, if not collected for the purpose of validation of the same study, will show differences and uncertainties between the observations due to error propagations from both ground and InSAR measurements. However, this will allow the direction of surface motion to be compared between them, in turn, observing the entire landscape with certainties in measurements that afford the direction of surface motion to be mapped across the area. To detrmine the absolute accuracy of the ISBAS measurements, the validation campaign for example should adopt calibration and validation methods designed for measuring contiguous mapping (i.e., be randomly located) and consider intra-pixel deployment of the levelling measurements to be compared with the ISBAS results.
3. Using SSA and MSSA to analyse InSAR time-series: although SSA and MSSA represent advanced techniques for processing one-dimensional and multi-dimensional time-series to detect the correlated variable behaviour that helps to classify and interpret the information, the main limitation in applying these techniques on InSAR is the quality of InSAR data itself. The presence of noise in InSAR data may lead one to get modes that are similar to the original modes. Although a hypothesis test was used to discriminate between the modes associated with the signals and the modes associated with the noise, the error related to the processing of InSAR, for example, phase unwrapping error and atmospheric signal delay over this low coherence area can provide bad reconstruction of the time-series. Therefore, before applying SSA and

MSSA it is suggested to minimize the error of InSAR during the processing by, for example, working with SAR satellites that provide regular acquisitions over long periods of time, using appropriate temporal baselines depending on the application, selecting a stable reference point for phase unwrapping, and inspecting the quality of InSAR output visually during the linear and non-linear processing.

7.7 Suggestions and recommendations for future work

The following points are extracted from the conclusions above which suggest that further research may improve and perhaps provide significant results:

1. Reduce the temporal baseline to less than one year using Sentinel-1 C-band SAR data from both satellites A and B (6 days revisiting cycle) or using longer wavelength such as L-band SAR data may improve the coherence over peatlands particularly forest and farmed peatland areas, in turn, increases the precision of the estimated ISBAS LOS velocities.
2. Exploit the availability of Sentinel-1 SAR images from different geometries (ascending and descending), to resolve the complete 3D peatland displacements, i.e. in northing, easting, and height which assists the investigation of surface displacements and their dynamics.
3. Apply the same techniques that have been used in **Chapter 6** (analyse InSAR time-series using SSA and MSSA) to study the dynamic of the Earth's surface and to classify the area depending on its surface motion in different applications such as landslide studies.
4. Predict the deformation over peatland areas from InSAR time-series using SSA and MSSA techniques which is essential for future management.
5. Although this research presents the capability of InSAR technique to quantify the peat condition through InSAR time-series, more advanced analysis is needed to understand the variability and sensitivity of measurements to local peat conditions and whether or not this variability lies firmly within the realms of noise.

References

Adam, E., Mutanga, O. & Rugege, D. 2010. Multispectral and hyperspectral remote sensing for identification and mapping of wetland vegetation: a review. *Wetlands Ecology and Management,* 18**,** 281-296.

Alexandrov , G. A. 1988. A spatially distributed model of raised bog relief. *In Wetland Modelling , ed. W.J. Mitsch , M. Straškraba and S.E. Jorgensen . Amsterdam : Elsevier ,pp. 41 – 53* .

Allen, M. R. & Smith, L. A. 1996. Monte Carlo SSA: Detecting irregular oscillations in the Presence of Colored Noise. *Journal of Climate,* 9**,** 3373-3404.

Allison, F. E. 1973. *Soil organic matter and its roule in crop production*.

Alshammari, L., Large, D., Boyd, D., Sowter, A., Anderson, R., Andersen, R. & Marsh, S. 2018. Long-Term Peatland Condition Assessment via Surface Motion Monitoring Using the ISBAS DInSAR Technique over the Flow Country, Scotland. *Remote Sensing,* 10**,** 1103.

Anderson, A., Ray, D. & Pyatt, D. 2000. Physical and hydrological impacts of blanket bog afforestation at Bad a′ Cheo, Caithness: the first 5 years. *Forestry,* 73**,** 467-478.

Armentano, T. & Menges, E. 1986. Patterns of change in the carbon balance of organic soil-wetlands of the temperate zone. *The Journal of Ecology***,** 755-774.

Attema, E., Cafforio, C., Gottwald, M., Guccione, P., Monti Guarnieri, A., Rocca, F. & Snoeij, P. 2010. Flexible Dynamic Block Adaptive Quantization for Sentinel-1 SAR Missions. *IEEE Geoscience and Remote Sensing Letters,* 7**,** 766-770.

Baghdadi, N. G., S., and King, Ch., 2001. Retrieving surface roughness and soil moisture from SAR data using neural networks. *In: Wilson,A.(ed.) ,Proceedings of the Third International Symposium on Retrieval of Bio- and Geophysical Parameters from SAR Data for Land Applications (11–14 September 2001; Sheffield, UK).* Noordwijk, the Netherlands: ESA.

Bain, C. G., Bonn, A., Stoneman, R., Chapman, S., Coupar, A., Evans, M., Gearey, B., Howat, M., Joosten, H., Keenleyside, C., Labadz, J., Lindsay, R., Lunt, P., Miller, C. J., Moxey, A., Reed, M., Smith, P., Swales, V., Thompson, P. S., Van de Noort, R., Wilson, J. D., Worrall, F. & Edinburgh 2011. IUCN UK Commission of Inquiry on Peatlands. Edinburgh.

Baird, A. J., Belyea, L. R. & Morris, P. J. 2009. Upscaling of peatland-atmosphere fluxes of methane: small-scale heterogeneity in process rates and the pitfalls of "bucket-and-slab" models. *Geophysical Monograph Series,* 184**,** 37-53.

Basuki, T. M., Skidmore, A. K., Hussin, Y. A. & Van Duren, I. 2013. Estimating tropical forest biomass more accurately by integrating ALOS PALSAR and Landsat-7 ETM+ data. *International Journal of Remote Sensing,* 34**,** 4871-4888.

Bateson, L., Cigna, F., Boon, D. & Sowter, A. 2015. The application of the Intermittent SBAS (ISBAS) InSAR method to the South Wales Coalfield, UK. *International Journal of Applied Earth Observation and Geoinformation,* 34**,** 249-257.

Belyea, L. R. & Clymo, R. S. 2001. Feedback control of the rate of peat formation. *Proc Biol Sci,* 268**,** 1315-21.

Berardino, P., Fornaro, G., Lanari, R. & Sansosti, E. 2002. A new algorithm for surface deformation monitoring based on small baseline differential SAR interferograms. *Ieee Transactions on Geoscience and Remote Sensing,* 40**,** 2375-2383.

Billett, M. F., Palmer, S. M., Hope, D., Deacon, C., Storeton-West, R., Hargreaves, K. J., Flechard, C. & Fowler, D. 2004. Linking land-atmosphere-stream carbon fluxes in a lowland peatland system. *Global Biogeochemical Cycles,* 18**,** n/a-n/a.

Bonnett, S. A. F., Ross, S., Linstead, C. & Maltby, E. 2009. A review of techniques for monitoring the success of peatland restoration. *University of Liverpool. Natural England Commissioned Reports,Number 086.*

Bourgault, M. A., Larocque, M. & Garneau, M. 2017. Quantification of peatland water storage capacity using the water table fluctuation method. *Hydrological Processes,* 31**,** 1184-1195.

Brisco, B., Kapfer, M., Hirose, T., Tedford, B. & Liu, J. 2014. Evaluation of C-band polarization diversity and polarimetry for wetland mapping. *Canadian Journal of Remote Sensing,* 37**,** 82-92.

Brisco, B., Schmitt, A., Murnaghan, K., Kaya, S. & Roth, A. 2013. SAR polarimetric change detection for flooded vegetation. *International Journal of Digital Earth,* 6**,** 103-114.

Broomhead, D. S. & King, G. P. 1986. Extracting qualitative dynamics from experimental data. *Physica D: Nonlinear Phenomena,* 20**,** 217-236.

Broomhead, D. S. & King, G. P. 1986b. On the qualitative analysis of experimental dynamical systems. In S. Sarkar (Ed.). *Nonlinear Phenomena and Chaos***,** pp. 113-44. Bristol, England: Adam Hilger.

Bruneau, P. M. C. & Johnson, S. M. 2014. Scotland's peatland - definitions & information resources. *Scottish Natural Heritage Commissioned Report No 701.*

Burgmann, R., Hilley, G., Ferretti, A. & Novali, F. 2006. Resolving vertical tectonics in the San Francisco Bay Area from permanent scatterer InSAR and GPS analysis. *Geology,* 34**,** 221-224.

Cabral-Cano, E., Osmanoglu, B., Dixon, T., Wdowinski, S., Demets, C., Cigna, F. & Diaz-Molina, O. 2010. Subsidence and fault hazard maps using PSI and permanent GPS networks in central Mexico. *Land Subsidence, Associated Hazards and the Role of Natural Resources Development,* 339**,** 255-+.

Camporese, M., Ferraris, S., Putti, M., Salandin, P. & Teatini, P. 2006. Hydrological modeling in swelling/shrinking peat soils. *Water Resources Research,* 42.

Camporese, M., Putti, M., Salandin, P. & Teatini, P. 2008. Spatial variability of CO2efflux in a drained cropped peatland south of Venice, Italy. *Journal of Geophysical Research,* 113.

Cannell, M. G. R., Dewar, R. C. & Pyatt, D. G. 1993. Conifer plantations on drained peatlands in Britain - a net gain or loss of carbon. *Forestry,* 66**,** 353-369.

Canuti, P., Casagli, N., Farina, P., Marks, F., Ferretti, A. & Menduni, G. Land subsidence in the Arno River Basin studied through SAR interferometry. Proceedings of the Seventh International Symposium on Land Subsidence., 2005.

Casu, F., Manzo, M. & Lanari, R. 2006. A quantitative assessment of the SBAS algorithm performance for surface deformation retrieval from DInSAR data. *Remote Sensing of Environment,* 102**,** 195-210.

Charman , D. 2002. Peatlands and Environmental Change. *Chichester , UK: John Wiley* .

Charman, D., Joosten, H., Laine, J., Lee, D., Minayeva, T., Opdam, S., Parish, F., Sirin, A., Silvius, M. & Stringer, L. 2008. Assessment on Peatlands, Biodiversity and Climate Change: Main Report. *Global Environment Centre, Kuala Lumpur and Wetlands International, Wageningen.*

Charman, D. J., Beilman, D. W., Blaauw, M., Booth, R. K., Brewer, S., Chambers, F. M., Christen, J. A., Gallego-Sala, A., Harrison, S. P., Hughes, P. D. M., Jackson, S. T., Korhola, A., Mauquoy, D., Mitchell, F. J. G., Prentice, I. C., van der Linden, M. & De Vleeschouwer, F., et al. 2013. Climate-related changes in peatland carbon accumulation during the last millennium. *Biogeosciences,* 10**,** 929-944.

Chaussard, E., Wdowinski, S., Cabral-Cano, E. & Amelung, F. 2014. Land subsidence in central Mexico detected by ALOS InSAR time-series. *Remote Sensing of Environment,* 140**,** 94-106.

Chen, C. W. & Zebker, H. A. 2000. Network approaches to two-dimensional phase unwrapping: intractability and two new algorithms. *Journal of the Optical Society of America A,* 17**,** 401.

Chen, C. W. & Zebker, H. A. 2001. Two-dimensional phase unwrapping with use of statistical models for cost functions in nonlinear optimization. *Journal of the Optical Society of America a-Optics Image Science and Vision,* 18**,** 338-351.

Chen, C. W. & Zebker, H. A. 2002. Phase unwrapping for large SAR interferograms: statistical segmentation and generalized network models. *IEEE Transactions on Geoscience and Remote Sensing,* 40**,** 1709-1719.

Ching, N. H., Rosenfeld, D. & Braun, M. 1992. Two-dimensional phase unwrapping using a minimum spanning tree algorithm. *IEEE Trans Image Process,* 1**,** 355-65.

Cigna, F., Del Ventisette, C., Liguori, V. & Casagli, N. InSAR time-series analysis for management and mitigation of geological risk in urban area. Geoscience and Remote Sensing Symposium (IGARSS), 2010 IEEE International, 2010. IEEE, 1924-1927.

Cigna, F., Del Ventisette, C., Liguori, V. & Casagli, N. 2011. Advanced radar-interpretation of InSAR time series for mapping and characterization of geological processes. *Natural Hazards and Earth System Sciences,* 11**,** 865-881.

Cigna, F. & Sowter, A. 2017. The relationship between intermittent coherence and precision of ISBAS InSAR ground motion velocities: ERS-1/2 case studies in the UK. *Remote Sensing of Environment*.

Cigna, F., Sowter, A., Jordan, C. J. & Rawlins, B. G. Intermittent Small Baseline Subset (ISBAS) monitoring of land covers unfavourable for conventional C-band InSAR: Proof-of-concept for peatland environments in North Wales, UK. SPIE Remote Sensing, 2014. International Society for Optics and Photonics, 924305-924305-6.

Colesanti, C., Ferretti, A., Prati, C. & Rocca, F. 2003. Monitoring landslides and tectonic motions with the Permanent Scatterers Technique. *Engineering Geology,* 68**,** 3-14.

Costantini, M. 1998. A novel phase unwrapping method based on network programming. *IEEE Transactions on Geoscience and Remote Sensing,* 36**,** 813-821.

Costantini, M., Falco, S., Malvarosa, F. & Minati, F. 2008. A New Method for Identification and Analysis of Persistent Scatterers in Series of SAR Images. II-449-II-452.

Crichton, K. A., Anderson, K., Bennie, J. J. & Milton, E. J. 2015. Characterizing peatland carbon balance estimates using freely available Landsat ETM+ data. *Ecohydrology,* 8**,** 493-503.

Curlander, J. C. & McDonough, R. N. 1991. Synthetic Aperture Radar: systems and signal processing. *John Wiley & Sons, Inc, New York.*

De Zan, F., Prats-Iraola, P., Scheiber, R. & Rucci, A. 2014. Interferometry with TOPS: Coregistration and Azimuth Shifts.In EUSAR 2014; 10th European Conference on Synthetic Aperture Radar. pp. 1–4.

Deutscher, J., Perko, R., Gutjahr, K., Hirschmugl, M. & Schardt, M. 2013. Mapping Tropical Rainforest Canopy Disturbances in 3D by COSMO-SkyMed Spotlight InSAR-Stereo Data to Detect Areas of Forest Degradation. *Remote Sensing,* 5**,** 648-663.

Deverel, S. J. & Leighton, D. A. 2010. Historic, recent, and future subsidence, Sacramento-San Joaquin Delta, California, USA. *San Francisco Estuary and Watershed Science,* 8.

Dorrepaal, E., Toet, S., van Logtestijn, R. S. P., Swart, E., van de Weg, M. J., Callaghan, T. V. & Aerts, R. 2009. Carbon respiration from subsurface peat accelerated by climate warming in the subarctic. *Nature,* 460**,** 616-619.

Drew, S., Waldron, S., Gilvear, D., Grieve, I., Armstrong, A., Bragg, O., Brewis, F., Cooper, M., Dargie, T., Duncan, C., Harris, L., Wilson, L., McIver, C., Padfield, R. & Shah, N. 2013. The price of knowledge in the knowledge economy: Should development of peatland in the UK support a research levy? *Land Use Policy,* 32**,** 50-60.

Elachi, C., Roth, L. E. & Schaber, G. G. 1984. Spaceborne Radar Subsurface Imaging in Hyperarid Regions. *IEEE Transactions on Geoscience and Remote Sensing,* GE-22**,** 383-388.

Englhart, S., Keuck, V. & Siegert, F. 2011. Aboveground biomass retrieval in tropical forests : The potential of combined X- and L-band SAR data use. *Remote Sensing of Environment,* 115**,** 1260-1271.

ESA 2002. Envisat ASAR product Handbook Issue 1.1. *European Space Agency*.

ESA 2013. Sentinel-1 User Handbook. *European Space Agency*.

Euliss, N. H., LaBaugh, J. W., Fredrickson, L. H., Mushet, D. M., Laubhan, M. K., Swanson, G. A., Winter, T. C., Rosenberry, D. O. & Nelson, R. D. 2004. The wetland continuum: A conceptual framework for interpreting biological studies. *Wetlands,* 24**,** 448-458.

Euliss, N. H., Mushet, D. M., Newton, W. E., Otto, C. R. V., Nelson, R. D., LaBaugh, J. W., Scherff, E. J. & Rosenberry, D. O. 2014. Placing prairie pothole wetlands along spatial and temporal continua to improve integration of wetland function in ecological investigations. *Journal of Hydrology,* 513**,** 490-503.

Evans, M., Warburton, J. & Yang, J. 2006. Eroding blanket peat catchments: Global and local implications of upland organic sediment budgets. *Geomorphology,* 79**,** 45-57.

Evans, M. G., Burt, T. P., Holden, J. & Adamson, J. K. 1999. Runoff generation and water table fluctuations in blanket peat: evidence from UK data spanning the dry summer of 1995. *Journal of Hydrology,* 221**,** 141-160.

Evans , M. G. & Warburton , J. 2007. Geomorphology of Upland Peat. *Oxford, UK: Blackwell.*

Farr, T. G. 1993. Radar interactions with geologic surfaces. *In Guide to Magellan image interpretation.*: JPL Publication.

Farr, T. G., Rosen, P. A., Caro, E., Crippen, R., Duren, R., Hensley, S., Kobrick, M., Paller, M., Rodriguez, E., Roth, L., Seal, D., Shaffer, S., Shimada, J., Umland, J., Werner, M., Oskin, M., Burbank, D. & Alsdorf, D. 2007. The Shuttle Radar Topography Mission. *Reviews of Geophysics,* 45.

Ferretti, A. 2014. *Satellite InSAR data: reservoir monitoring from space*, EAGE Publications.

Ferretti, A., Fumagalli, A., Novali, F., Prati, C., Rocca, F. & Rucci, A. 2011. A New Algorithm for Processing Interferometric Data-Stacks: SqueeSAR. *IEEE Transactions on Geoscience and Remote Sensing,* 49**,** 3460-3470.

Ferretti, A., Monti-guarnieri, A., Prati, C. & Rocca, F. 2007. InSAR Principles: Guidelines for SAR Interferometry Processing and Interpretation, ESA Publications.

Ferretti, A., Prati, C. & Rocca, F. 2001. Permanent scatterers in SAR interferometry. *IEEE Transactions on Geoscience and Remote Sensing,* 39**,** 8-20.

Flanagan, L. B. & Syed, K. H. 2011. Stimulation of both photosynthesis and respiration in response to warmer and drier conditions in a boreal peatland ecosystem. *Global Change Biology,* 17**,** 2271-2287.

Foody, G. M., Boyd, D. S. & Sanchez-Hernandez, C. 2007. Mapping a specific class with an ensemble of classifiers. *International Journal of Remote Sensing,* 28**,** 1733-1746.

Fornaro, G., Franceschetti, G. & Lanari, R. 1996a. Interferometric SAR phase unwrapping using Green's formulation. *IEEE Transactions on Geoscience and Remote Sensing,* 34**,** 720-727.

Fornaro, G., Franceschetti, G., Lanari, R. & Sansosti, E. 1996b. Robust phase-unwrapping techniques: a comparison. *Journal of the Optical Society of America A,* 13**,** 2355.

Freeman, C., Lock, M. A. & Reynolds, B. 1993. Climatic change and the release of immobilized nutrients from Welsh riparian wetland soils. *Ecological Engineering,* 2**,** 367-373.

Fritz, C., Campbell, D. I. & Schipper, L. A. 2008. Oscillating peat surface levels in a restiad peatland, New Zealand-magnitude and spatiotemporal variability. *Hydrological Processes,* 22**,** 3264-3274.

Futty, D. & Towers, W. 1982. Soil and Land Capability for Agriculture: Northern Scotland. *Aberdeen: Macaulay Institute*.

Gabriel, A. K., Goldstein, R. M. & Zebker, H. A. 1989. Mapping Small Elevation Changes over Large Areas - Differential Radar Interferometry. *Journal of Geophysical Research-Solid Earth and Planets,* 94**,** 9183-9191.

Gallant, A. 2015. The Challenges of Remote Monitoring of Wetlands. *Remote Sensing,* 7**,** 10938-10950.

Gallant, A., Kaya, S., White, L., Brisco, B., Roth, M., Sadinski, W. & Rover, J. 2014. Detecting Emergence, Growth, and Senescence of Wetland Vegetation with Polarimetric Synthetic Aperture Radar (SAR) Data. *Water,* 6**,** 694-722.

Gallego-Sala, A. V., Booth, R. K., Charman, D. J., Prentice, I. C., Yu, Z., Bonn, A., Allott, T., Evans, M., Joosten, H. & Stoneman, R. 2016. Peatlands and climate change. 129-150.

Gambolati, G., Putti, M., Teatini, P., Camporese, M., Ferraris, S., Stori, G. G., Nicoletti, V., Silvestri, S., Rizzetto, F. & Tosi, L. 2005. Peat land oxidation enhances subsidence in the Venice watershed. *Eos, Transactions American Geophysical Union,* 86**,** 217-220.

Gambolati, G., Putti, M., Teatini, P. & Stori, G. G. 2006. Subsidence due to peat oxidation and impact on drainage infrastructures in a farmland catchment south of the Venice Lagoon. *Environmental Geology,* 49**,** 814-820.

Gatti, P., M., Bonardi, L., Tosi, F., Rizzetto, A., Fornasiero, G., Gambolati, M., Putti, a. & Teatini 2002. The peat deposit of the subsiding Zennare Basin, south of the Venice Lagoon, Italy: Geotechnical classification and preliminary mineralogical characterization. *Scientific Research and Safeguarding of Venice (CORILA Research Program 2001 Results).* Veneto di Sci. Lett. ed Arti, La Garangola, Padua, Italy.

Ge, L. L., Ng, A. H. M., Li, X. J., Abidin, H. Z. & Gumilar, I. 2014. Land subsidence characteristics of Bandung Basin as revealed by ENVISAT ASAR and ALOS PALSAR interferometry. *Remote Sensing of Environment,* 154**,** 46-60.

Gee, D., Bateson, L., Sowter, A., Grebby, S., Novellino, A., Cigna, F., Marsh, S., Banton, C. & Wyatt, L. 2017. Ground Motion in Areas of Abandoned Mining: Application of the Intermittent SBAS (ISBAS) to the Northumberland and Durham Coalfield, UK. *Geosciences,* 7**,** 85.

Gee, D., Sowter, A., Novellino, A., Marsh, S. & Gluyas, J. 2016. Monitoring land motion due to natural gas extraction: Validation of the Intermittent SBAS (ISBAS) DInSAR algorithm over gas fields of North Holland, the Netherlands. *Marine and Petroleum Geology,* 77**,** 1338-1354.

Geudtner, D. 2014. Implementation of the TOPS Mode on RADARSAT-2 in Support of the Copernicus Sentinel-1 Mission. *RADARSAT-2 TOPS SAR Interferometry (InSAR) Scene Pair Data Acquisitions.*: ESA Technical Note.

Ghiglia, D. C. & Romero, L. A. 1994. Robust two-dimensional weighted and unweighted phase unwrapping that uses fast transforms and iterative methods. *Journal of the Optical Society of America A,* 11**,** 107.

Ghiglia, D. C. & Romero, L. A. 1996. Minimum Lp-norm two-dimensional phase unwrapping. *Journal of the Optical Society of America A,* 13**,** 1999.

Ghil, M., Allen, M., Dettinger, M., Ide, K., Kondrashov, D., Mann, M., Robertson, A. W., Saunders, A., Tian, Y. & Varadi, F. 2002. Advanced spectral methods for climatic time series. *Reviews of geophysics,* 40.

Ghodsi, M., Hassani, H. & Sanei, S. 2010. Extracting fetal heart signal from noisy maternal ECG by singular spectrum analysis. *Journal of Statistics and its Interface,* 3 (3). pp. 399-411.

Glaser, P. H., Chanton, J. P., Morin, P., Rosenberry, D. O., Siegel, D. I., Ruud, O., Chasar, L. I. & Reeve, A. S. 2004. Surface deformations as indicators of deep ebullition fluxes in a large northern peatland. *Global Biogeochemical Cycles,* 18**,** n/a-n/a.

Gleason, R. A., Euliss, N. H., Hubbard, D. E. & Duffy, W. G. 2003. Effects of sediment load on emergence of aquatic invertebrates and plants from wetland soil egg and seed banks. *Wetlands,* 23**,** 26-34.

Goldstein, R. M., Zebker, H. A. & Werner, C. L. 1988. Satellite radar interferometry: Two-dimensional phase unwrapping. *Radio Science,* 23**,** 713-720.

Golyandina, N., Nekrutkin, V. & Zhigljavsky, A. 2001. Analysis of Time Series Structure: SSA and related techniques. *Chapman & Hall/CRC, New York - London.*

Gorelick, N., Hancher, M., Dixon, M., Ilyushchenko, S., Thau, D. & Moore, R. 2017. Google Earth Engine: Planetary-scale geospatial analysis for everyone. *Remote Sensing of Environment,* 202**,** 18-27.

Gruszczynska, M., Klos, A., Rosat, S. & Bogusz, J. 2017. Deriving Common Seasonal Signals in Gps Position Time Series by Using Multichannel Singular Spectrum Analysis. *Acta Geodynamica Et Geomaterialia,* 14**,** 273-284.

Guizar-Sicairos, M., Thurman, S. T. & Fienup, J. R. 2008. Efficient subpixel image registration algorithms. *Optics Letters,* 33**,** 156.

Hanssen, R. F. 1998. Atmosperic Hetrogenites From ERS Tandem SAR Interferometry and Sea Surface Images. Delft University Press, Delft, the Netherlands.

Hanssen, R. F. 1999. High-Resolution Water Vapor Mapping from Interferometric Radar Measurements. *Science,* 283**,** 1297-1299.

Hanssen, R. F. 2001. *Radar interferometry: data interpretation and error analysis*, Springer Science & Business Media.

Hassani, H. 2007. Singular Spectrum Analysis: Methodology and Comparison. *Journal of Data Science,* Vol. 5, No. 2**,** pp. 239-257.

Hassani, H., Heravi, S. & Zhigljavsky, A. 2013. Forecasting UK Industrial Production with Multivariate Singular Spectrum Analysis. *Journal of Forecasting,* 32**,** 395-408.

Hemond, H. F., Nuttle, W. K., Burke, R. W. & Stolzenbach, K. D. 1984. Surface Infiltration in Salt Marshes: Theory, Measurement, and Biogeochemical Implications. *Water Resources Research,* 20**,** 591-600.

Hidding, B., Sarneel, J. M. & Bakker, E. S. 2014. Flooding tolerance and horizontal expansion of wetland plants: Facilitation by floating mats? *Aquatic Botany,* 113**,** 83-89.

Hilley, G. E., Burgmann, R., Ferretti, A., Novali, F. & Rocca, F. 2004. Dynamics of slow-moving landslides from permanent scatterer analysis. *Science,* 304**,** 1952-5.

Holden, J. 2005. Peatland hydrology and carbon release: why small-scale process matters. *Philos Trans A Math Phys Eng Sci,* 363**,** 2891-913.

Holden, J. 2009. Topographic controls upon soil macropore flow. *Earth Surface Processes and Landforms,* 34**,** 345-351.

Holden, J. & Burt, T. P. 2002. Infiltration, runoff and sediment production in blanket peat catchments: implications of field rainfall simulation experiments. *Hydrological Processes,* 16**,** 2537-2557.

Holden, J., Evans, M. G., Burt, T. P. & Horton, M. 2006. Impact of land drainage on peatland hydrology. *J Environ Qual,* 35**,** 1764-78.

Holden, J., Gascoign, M. & Bosanko, N. R. 2007. Erosion and natural revegetation associated with surface land drains in upland peatlands. *Earth Surface Processes and Landforms,* 32**,** 1547-1557.

Holden, J., Kirkby, M. J., Lane, S. N., Milledge, D. G., Brookes, C. J., Holden, V. & McDonald, A. T. 2008. Overland flow velocity and roughness properties in peatlands. *Water Resources Research,* 44.

Holden, J., Wallage, Z. E., Lane, S. N. & McDonald, A. T. 2011. Water table dynamics in undisturbed, drained and restored blanket peat. *Journal of Hydrology,* 402**,** 103-114.

Holzner, J. & Bamler, R. 2002. Burst-mode and ScanSAR interferometry. *IEEE Transactions on Geoscience and Remote Sensing,* 40**,** 1917-1934.

Hooijer, A., Page, S., Jauhiainen, J., Lee, W., Lu, X., Idris, A. & Anshari, G. 2012. Subsidence and carbon loss in drained tropical peatlands.

Hooper, A. 2008. A multi-temporal InSAR method incorporating both persistent scatterer and small baseline approaches. *Geophysical Research Letters,* 35.

Hooper, A., Zebker, H., Segall, P. & Kampes, B. 2004. A new method for measuring deformation on volcanoes and other natural terrains using InSAR persistent scatterers. *Geophysical Research Letters,* 31**,** n/a-n/a.

Howie, S. A. & Hebda, R. J. 2018. Bog surface oscillation (mire breathing): A useful measure in raised bog restoration. *Hydrological Processes,* 32**,** 1518-1530.

Joosten , H. 2009. The Global Peatland CO2 Picture. Peatland Status and Drainage Associated Emissions in All Countries of the World. *Wageningen, The Netherlands : Wetlands International* .

Joosten, H., Bonn, A., Allott, T., Evans, M., Joosten, H. & Stoneman, R. 2016a. Peatlands across the globe. In A. Bonn, T. Allott, M. Evans, H. Joosten, & R. Stoneman (Eds.), Peatland Restoration and Ecosystem Services: Science, Policy and Practice. Cambridge University Press.**,** 19-43.

Joosten , H. & Clarke , D. 2002. Wise Use of Mires and Peatlands: Background and Principles Including a Framework for Decision-making . *Saarijarvi: International Mire Conservation Group/International Peat Society* .

Joosten, H., Sirin, A., Couwenberg, J., Laine, J., Smith, P., Bonn, A., Allott, T., Evans, M., Joosten, H. & Stoneman, R. 2016b. The role of peatlands in climate regulation. In A. Bonn, T. Allott, M. Evans, H. Joosten, & R. Stoneman (Eds.), Peatland Restoration and Ecosystem Services: Science, Policy and Practice. Cambridge University Press.**,** 63-76.

Just, D. & Bamler, R. 1994. Phase statistics of interferograms with applications to synthetic aperture radar. *Applied Optics,* 33**,** 4361-4368.

Kaasalainen, S., Niittymaki, H., Krooks, A., Koch, K., Kaartinen, H., Vain, A. & Hyyppa, H. 2010. Effect of Target Moisture on Laser Scanner Intensity. *IEEE Transactions on Geoscience and Remote Sensing,* 48**,** 2128-2136.

Kaat, A. & Joosten, H. 2009. Fact book for UNFCCC policies on peat carbon emissions. *Wetlands International.*

Kampes, B. 2006. Radar Interferometry: Persistent Scatterer Technique. *Springer*.

Kampes, B. M. 2005. Displacement Parameter Estimation using Permanent Scatterer Interferometry. *PhD Thesis, Delft University of Technology*.

Kasischke, E. S. & BourgeauChavez, L. L. 1997. Monitoring South Florida wetlands using ERS-1 SAR imagery. *Photogrammetric Engineering and Remote Sensing,* 63**,** 281-291.

Kasischke, E. S., Smith, K. B., Bourgeau-Chavez, L. L., Romanowicz, E. A., Brunzell, S. & Richardson, C. J. 2003. Effects of seasonal hydrologic patterns in south Florida wetlands on radar backscatter measured from ERS-2 SAR imagery. *Remote Sensing of Environment,* 88**,** 423-441.

Kellner, E., Waddington, J. M. & Price, J. S. 2005. Dynamics of biogenic gas bubbles in peat: Potential effects on water storage and peat deformation. *Water Resources Research,* 41.

Kennedy, G. W. & Price, J. S. 2005. A conceptual model of volume-change controls on the hydrology of cutover peats. *Journal of Hydrology,* 302**,** 13-27.

Kettridge, N., Tilak, A. S., Devito, K. J., Petrone, R. M., Mendoza, C. A. & Waddington, J. M. 2016. Moss and peat hydraulic properties are optimized to maximize peatland water use efficiency. *Ecohydrology,* 9**,** 1039-1051.

Kim, J.-W., Lu, Z., Gutenberg, L. & Zhu, Z. 2017. Characterizing hydrologic changes of the Great Dismal Swamp using SAR/InSAR. *Remote Sensing of Environment,* 198**,** 187-202.

Kim, K. Y. & Wu, Q. G. 1999. A comparison study of EOF techniques: Analysis of nonstationary data with periodic statistics. *Journal of Climate,* 12**,** 185-199.

Kimmel, K. & Mander, Ü. 2010. Ecosystem services of peatlands: Implications for restoration. *Progress in Physical Geography,* 34**,** 491-514.

Kirschke, S., Bousquet, P., Ciais, P., Saunois, M., Canadell, J. G. & et al. 2013. Three decades of global methane sources and sinks. *Nature Geoscience,* 6**,** 813-823.

Klemas, V. 2011. Remote Sensing Techniques for Studying Coastal Ecosystems: An Overview. *Journal of Coastal Research,* 27**,** 2-17.

Klemas, V. 2013a. Remote Sensing of Coastal Wetland Biomass: An Overview. *Journal of Coastal Research,* 290**,** 1016-1028.

Klemas, V. 2013b. Remote sensing of emergent and submerged wetlands: an overview. *International Journal of Remote Sensing,* 34**,** 6286-6320.

Kondrashov, D. & Ghil, M. 2006. Spatio-temporal filling of missing points in geophysical data sets. *Nonlinear Processes in Geophysics,* 13**,** 151-159.

Kondrashov, D., Shprits, Y. & Ghil, M. 2010. Gap filling of solar wind data by singular spectrum analysis. *Geophysical Research Letters,* 37**,** n/a-n/a.

Kuenzer, C., Bluemel, A., Gebhardt, S., Quoc, T. V. & Dech, S. 2011. Remote Sensing of Mangrove Ecosystems: A Review. *Remote Sensing,* 3**,** 878-928.

Laine, A., Byrne, K. A., Kiely, G. & Tuittila, E. S. 2007. Patterns in vegetation and CO2 dynamics along a water level gradient in a lowland blanket bog. *Ecosystems,* 10**,** 890-905.

Lanari, R., Berardino, P., Bonano, M., Casu, F., De Luca, C., Elefante, S., Fusco, A., Manunta, M., Manzo, M., Ojha, C., Pepe, A., Sansosti, E. & Zinno, I. 2015. Sentinel-1 results: SBAS-DInSAR processing chain developments and land subsidence analysis. 2836-2839.

Lanari, R., Casu, F., Manzo, M., Zeni, G., Berardino, P., Manunta, M. & Pepe, A. 2007. An Overview of the Small BAseline Subset Algorithm: a DInSAR Technique for Surface Deformation Analysis. *Pure and Applied Geophysics,* 164**,** 637-661.

Lang, M. W. & Kasischke, E. S. 2008. Using C-Band Synthetic Aperture Radar Data to Monitor Forested Wetland Hydrology in Maryland's Coastal Plain, USA. *IEEE Transactions on Geoscience and Remote Sensing,* 46**,** 535-546.

Lapen, D. R., Price, J. S. & Gilbert, R. 2000. Soil water storage dynamics in peatlands with shallow water tables. *Canadian Journal of Soil Science,* 80**,** 43-52.

Lees, K. J., Quaife, T., Artz, R. R. E., Khomik, M. & Clark, J. M. 2018. Potential for using remote sensing to estimate carbon fluxes across northern peatlands - A review. *Sci Total Environ,* 615**,** 857-874.

Lillesand, T., Kiefer, R. & Chipman, J. 2004. *Remote sensing and image interpretation.*, John Wiley & Sons Ltd Chichester.UK.

Lindsay, R. 1987. The great flow-an international responsibility. New scientist expediting inc 200 mecham ave, Elmont, NY 11003.

Lindsay , R. 2010. Peatbogs and carbon: a critical synthesis to inform policy development in oceanic peat bog conservation and restoration in the context of climate change . *Technical Report. London: University of East London, RSPB, Natural England, SNH, CCW and the Forestry Commission*.

Lindsay, R., Birnie, R. & Clough, J. 2016. Peat Bog Ecosystems: Peatland Restoration. *Technical Report. International Union for the Conservation of Nature.*: University of East London.

Lindsay, R., Charman, D. J., Everingham, F., O'Reilly, R. M., Palmer, M. A., Rowell, T. A. & Stroud, D. A. 1988. The Flow Country: The peatlands of Caithness and Sutherland. *In:* Ratcliffe, D. A. & Oswald, P. H. (eds.). Peterborough: Joint Nature Conservation Committee.

Lyons, S. & Sandwell, D. 2003. Fault creep along the southern San Andreas from interferometric synthetic aperture radar, permanent scatterers, and stacking. *Journal of Geophysical Research: Solid Earth,* 108.

Massonnet, D. & Feigl, K. L. 1998. Radar interferometry and its application to changes in the Earth's surface. *Reviews of geophysics,* 36**,** 441-500.

Massonnet, D., Rossi, M., Carmona, C., Adragna, F., Peltzer, G., Feigl, K. & Rabaute, T. 1993. The Displacement Field of the Landers Earthquake Mapped by Radar Interferometry. *Nature,* 364**,** 138-142.

McCauley, J. F., Schaber, G. G., Breed, C. S., Grolier, M. J., Haynes, C. V., Issawi, B., Elachi, C. & Blom, R. 1982. Subsurface valleys and geoarcheology of the eastern sahara revealed by shuttle radar. *Science,* 218**,** 1004-20.

McKirdy, A. & Crofts, R. 1999. Scotland: The Creation of its Natural Landscape. *In:* McKirdy, A. (ed.).

Mezbahuddin, M., Grant, R. F. & Flanagan, L. B. 2017. Coupled eco-hydrology and biogeochemistry algorithms enable the simulation of water table depth effects on boreal peatland net CO2 exchange. *Biogeosciences,* 14**,** 5507-5531.

Milillo, P., Perissin, D., Lundgren, P. & Serio, C. 2015. Cosmo-skymed very short repeat-pass SAR interferometry over rural areas: The VAL D'agri and potenza test cases in Basilicata, Italy. 98-101.

Milton, E. J., Hughes, P. D., Anderson, K., Schulz, J., Lindsay, R., Kelday, S. & Hill, C. T. 2005. Remote sensing of bog surfaces.

Miranda, N. 2015. Definition of the TOPS SLC deramping function for products generated by the S-1 IPF.

Mitsch, W. J. & Gosselink, J. G. 1993. *Wetlands*, New York, NY, USA,, Van Nostrand Reinhold.

Moore, T. R., Roulet, N. T. & Waddington, J. M. 1998. Uncertainty in predicting the effect of climatic change on the carbon cycling of Canadian peatlands. *Climatic Change,* 40**,** 229-245.

Morel, A. C., Saatchi, S. S., Malhi, Y., Berry, N. J., Banin, L., Burslem, D., Nilus, R. & Ong, R. C. 2011. Estimating aboveground biomass in forest and oil palm plantation in Sabah, Malaysian Borneo using ALOS PALSAR data. *Forest Ecology and Management,* 262**,** 1786-1798.

Morrison, K., Bennett, J. C. & Nolan, M. 2013. Using DInSAR to Separate Surface and Subsurface Features. *IEEE Transactions on Geoscience and Remote Sensing,* 51**,** 3424-3430.

Mount, J. & Twiss, R. 2005. Subsidence, sea level rise, and seismicity in the Sacramento–San Joaquin Delta. *San Francisco Estuary and Watershed Science,* 3.

Nicoletti, V., Silvestri, S., Rizzetto, F., Tosi, L., Putti, M. & Teatini, P. Use of remote sensing for the delineation of surface peat deposits south of the Venice Lagoon (Italy). Geoscience and Remote Sensing Symposium, 2003. IGARSS'03. Proceedings. 2003 IEEE International, 2003. IEEE, 2881-2883.

Novellino, A., Cigna, F., Sowter, A., Ramondini, M. & Calcaterra, D. 2017. Exploitation of the Intermittent SBAS (ISBAS) algorithm with COSMO-SkyMed data for landslide inventory mapping in north-western Sicily, Italy. *Geomorphology,* 280**,** 153-166.

Nykanen, H., Alm, J., Lang, K., Silvola, J. & Martikainen, P. J. 1995. Emissions of CH4, N2O and CO2 from a virgin fen and a fen drained for grassland in Finland. *Journal of Biogeography,* 22**,** 351-357.

Ollinger, S. V. 2011. Sources of variability in canopy reflectance and the convergent properties of plants. *New Phytol,* 189**,** 375-94.

Onn, F. & Zebker, H. A. 2006. Correction for interferometric synthetic aperture radar atmospheric phase artifacts using time series of zenith wet delay observations from a GPS network. *Journal of Geophysical Research,* 111.

Osmanoglu, B., Dixon, T. H., Wdowinski, S., Cabral-Cano, E. & Jiang, Y. 2011. Mexico City subsidence observed with persistent scatterer InSAR. *International Journal of Applied Earth Observation and Geoinformation,* 13**,** 1-12.

Osmanoğlu, B., Sunar, F., Wdowinski, S. & Cabral-Cano, E. 2016. Time series analysis of InSAR data: Methods and trends. *ISPRS Journal of Photogrammetry and Remote Sensing,* 115**,** 90-102.

Ozesmi, S. L. & Bauer, M. E. 2002. Satellite remote sensing of wetlands. *Wetlands Ecology and Management,* 10**,** 381-402.

Parry, L. E., Holden, J. & Chapman, P. J. 2014. Restoration of blanket peatlands. *J Environ Manage,* 133**,** 193-205.

Poore, M. E. D. 1955. The Use of Phytosociological Methods in Ecological Investigations .1. The Braun-Blanquet System. *Journal of Ecology,* 43**,** 226-&.

Price, J., Evans, C., Evans, M., Allott, T., Shuttleworth, E., Bonn, A., Allott, T., Evans, M., Joosten, H. & Stoneman, R. 2016. Peatland restoration and hydrology. 77-94.

Price, J. S. & Schlotzhauer, S. M. 1999. Importance of shrinkage and compression in determining water storage changes in peat: the case of a mined peatland. *Hydrological Processes,* 13**,** 2591-2601.

Ramchunder, S. J., Brown, L. E. & Holden, J. 2009. Environmental effects of drainage, drain-blocking and prescribed vegetation burning in UK upland peatlands. *Progress in Physical Geography,* 33**,** 49-79.

Rangelova, E., Sideris, M. G. & Kim, J. W. 2012. On the capabilities of the multi-channel singular spectrum method for extracting the main periodic and non-periodic variability from weekly GRACE data. *Journal of Geodynamics,* 54**,** 64-78.

Rawat, J. S. & Kumar, M. 2015. Monitoring land use/cover change using remote sensing and GIS techniques: A case study of Hawalbagh block, district Almora, Uttarakhand, India. *The Egyptian Journal of Remote Sensing and Space Science,* 18**,** 77-84.

Reeve, A. S., Glaser, P. H. & Rosenberry, D. O. 2013. Seasonal changes in peatland surface elevation recorded at GPS stations in the Red Lake Peatlands, northern Minnesota, USA. *Journal of Geophysical Research: Biogeosciences,* 118**,** 1616-1626.

Refice, A., Capolongo, D., Pasquariello, G., DaAddabbo, A., Bovenga, F., Nutricato, R., Lovergine, F. P. & Pietranera, L. 2014. SAR and InSAR for Flood Monitoring: Examples With COSMO-SkyMed Data. *IEEE Journal of Selected Topics in Applied Earth Observations and Remote Sensing,* 7**,** 2711-2722.

Ribbes, F., Le Toan, T., Bruniquel, J., Floury, N., Stussi, N., Liew, S. C. & Wasrin, U. R. Deforestation monitoring in tropical regions using multitemporal ERS/JERS SAR and INSAR data. Geoscience and Remote Sensing, 1997. IGARSS'97. Remote Sensing-A Scientific Vision for Sustainable Development., 1997 IEEE International, 1997. IEEE, 1560-1562.

Rizzetto, F., Tosi, L., Carbognin, L., Bonardi, M. & Teatini, P. 2003. Geomorphic setting and related hydrogeological implications of the coastal plain south of the Venice Lagoon, Italy. *Hydrology of Mediterranean and Semiarid Regions,* 278**,** 463-470.

Robinson, E. L., Blyth, E. M., Clark, D. B., Finch, J. & Rudd, A. C. 2017. Trends in atmospheric evaporative demand in Great Britain using high-resolution meteorological data. *Hydrology and Earth System Sciences,* 21**,** 1189-1224.

Robroek, B. J. M., Limpens, J., Breeuwer, A. & Schouten, M. G. C. 2007. Effects of water level and temperature on performance of four Sphagnum mosses. *Plant Ecology,* 190**,** 97-107.

Rodriguez, E. & Martin, J. M. 1992. Theory and design of interferometric synthetic aperture radars. *IEE Proceedings F Radar and Signal Processing,* 139**,** 147.

Romshoo, S. A. 2004. Radar remote sensing for monitoring of dynamic ecosystem processes related to biogeochemical exchanges in tropical peatlands. *Visual Geosciences,* 9**,** 9-28.

Rosen, P. A., Hensley, S., Joughin, I. R., Li, F. K., Madsen, S. N., Rodriguez, E. & Goldstein, R. M. 2000. Synthetic aperture radar interferometry. *Proceedings of the IEEE,* 88**,** 333-382.

Rosenberry, D. O., Glaser, P. H., Siegel, D. I. & Weeks, E. P. 2003. Use of hydraulic head to estimate volumetric gas content and ebullition flux in northern peatlands. *Water Resources Research,* 39.

Rothwell, R. L., Silins, U. & Hillman, G. R. 1996. The effects of drainage on substrate water content at several forested Alberta peatlands. *Canadian Journal of Forest Research,* 26**,** 53-62.

Roulet, N., Moore, T. I. M., Bubier, J. & Lafleur, P. 1992. Northern fens: methane flux and climatic change. *Tellus B,* 44**,** 100-105.

Rover, J., Wylie, B. K. & Ji, L. 2010. A self-trained classification technique for producing 30 m percent-water maps from Landsat data. *International Journal of Remote Sensing,* 31**,** 2197-2203.

Salvi, S., Atzori, S., Tolomei, C., Allievi, J., Ferretti, A., Rocca, F., Prati, C., Stramondo, S. & Feuillet, N. 2004. Inflation rate of the Colli Albani volcanic complex retrieved by the permanent scatterers SAR interferometry technique. *Geophysical Research Letters,* 31.

Santos, J., Neeff, T., Dutra, L., Araujo, L., Gama, F. & Elmiro, M. 2004. Tropical forest biomass mapping from dual frequency SAR interferometry (X and P-Bands). *International Archives of Photogrammetry and Remote Sensing,* 35.

Scheiber, R. & Moreira, A. 2000. Coregistration of interferometric SAR images using spectral diversity. *IEEE Transactions on Geoscience and Remote Sensing,* 38**,** 2179-2191.

Schlogel, R., Doubre, C., Malet, J. P. & Masson, F. 2015. Landslide deformation monitoring with ALOS/PALSAR imagery: A D-InSAR geomorphological interpretation method. *Geomorphology,* 231**,** 314-330.

Schlotzhauer, S. M. & Price, J. S. 1999. Soil water flow dynamics in a managed cutover peat field, Quebec: Field and laboratory investigations. *Water Resources Research,* 35**,** 3675-3683.

Schothorst, C. J. 1977. Subsidence of low moor peat soils in the western Netherlands. *Geoderma,* 17**,** 265-291.

Shimada, M., Watanabe, M. & Motooka, T. Subsidence estimation of the peatland forest in the central Kalimantan using the PALSAR time series differential interferometry. IEEE International Geoscience and Remote Sensing Symposium - IGARSS, 2013. 1846-1849.

Shotbolt, L., Anderson, A. & Townend, J. 1998. Changes to blanket bog adjoining forest plots at Bad a′ Cheo, Rumster Forest, Caithness. *Forestry,* 71**,** 311-324.

Skolnik, M. 1990. Radar handbook. *McGraw-Hill Professional.*

Skolnik., M. 2002. Role of Radar in Microwaves. *IEEE Transactions on Microwave Theory and Techniques,* 50.

Smith, L. C., MacDonald, G. M., Velichko, A. A., Beilman, D. W., Borisova, O. K., Frey, K. E., Kremenetski, K. V. & Sheng, Y. 2004. Siberian peatlands a net carbon sink and global methane source since the early Holocene. *Science,* 303**,** 353-6.

Sowter, A., Amat, M. B., Cigna, F., Marsh, S., Athab, A. & Alshammari, L. 2016. Mexico City land subsidence in 2014-2015 with Sentinel-1 IW TOPS: Results using the Intermittent SBAS (ISBAS) technique. *International Journal of Applied Earth Observation and Geoinformation,* 52**,** 230-242.

Sowter, A., Bateson, L., Strange, P., Ambrose, K. & Syafiudin, M. F. 2013. DInSAR estimation of land motion using intermittent coherence with application to the South Derbyshire and Leicestershire coalfields. *Remote Sensing Letters,* 4**,** 979-987.

Stephens, J. C., Allen, L. H. & Chen, E. 1984. Organic soil subsidence. *Reviews in Engineering Geology,* 6**,** 107-122.

Stewart, A. J. A. & Lance, A. N. 1991. Effects of Moor-Draining on the Hydrology and Vegetation of Northern Pennine Blanket Bog. *The Journal of Applied Ecology,* 28**,** 1105-1117.

Stoneman, R. & Brooks, S. 1997. *Conserving Bogs - The Management Handbook,* Edinburgh, The Stationery Office.

Strack, M., Kellner, E. & Waddington, J. M. 2006a. Effect of entrapped gas on peatland surface level fluctuations. *Hydrological Processes,* 20**,** 3611-3622.

Strack, M. & Waddington, J. M. 2007. Response of peatland carbon dioxide and methane fluxes to a water table drawdown experiment. *Global Biogeochemical Cycles,* 21**,** n/a-n/a.

Strack, M., Waller, M. F. & Waddington, J. M. 2006b. Sedge succession and peatland methane dynamics: A potential feedback to climate change. *Ecosystems,* 9**,** 278-287.

Stramondo, S., Bozzano, F., Marra, F., Wegmuller, U., Cinti, F. R., Moro, M. & Saroli, M. 2008. Subsidence induced by urbanisation in the city of Rome detected by advanced InSAR technique and geotechnical investigations. *Remote Sensing of Environment,* 112**,** 3160-3172.

Suga, Y. & Takeuchi, S. 2000. Application of JERS-1 InSAR for monitoring deforestation of tropical rain forest. 1**,** 432-434.

Sun, Q., Zhang, L., Ding, X., Hu, J., Li, Z. W. & Zhu, J. J. 2015. Slope deformation prior to Zhouqu, China landslide from InSAR time series analysis. *Remote Sensing of Environment,* 156**,** 45-57.

Tallis, J. H. 1998. Growth and Degradation of British and Irish Blanket Mires. *Environment Reviews,* 6**,** 81-122.

Tang, P. P., Chen, F. L., Zhu, X. K. & Zhou, W. 2016. Monitoring Cultural Heritage Sites with Advanced Multi-Temporal InSAR Technique: The Case Study of the Summer Palace. *Remote Sensing,* 8.

Teatini, P., Strozzi, T., Tosi, L., Wegmüller, U., Werner, C. & Carbognin, L. 2007. Assessing short-and long-time displacements in the Venice coastland by synthetic aperture radar interferometric point target analysis. *Journal of Geophysical Research: Earth Surface,* 112.

Teatini, P., Tosi, L., Strozzi, T., Carbognin, L., Cecconi, G., Rosselli, R. & Libardo, S. 2012. Resolving land subsidence within the Venice Lagoon by persistent scatterer SAR interferometry. *Physics and Chemistry of the Earth,* 40-41**,** 72-79.

Teatini, P., Tosi, L., Strozzi, T., Carbognin, L., Wegmuller, U. & Rizzetto, F. 2005. Mapping regional land displacements in the Venice coastland by an integrated monitoring system. *Remote Sensing of Environment,* 98**,** 403-413.

Ticehurst, C., Guerschman, J. & Chen, Y. 2014. The Strengths and Limitations in Using the Daily MODIS Open Water Likelihood Algorithm for Identifying Flood Events. *Remote Sensing,* 6**,** 11791-11809.

Tizzani, P., Berardino, P., Casu, F., Euillades, P., Manzo, M., Ricciardi, G. P., Zeni, G. & Lanari, R. 2007. Surface deformation of Long Valley Caldera and Mono Basin,

California, investigated with the SBAS-InSAR approach. *Remote Sensing of Environment,* 108**,** 277-289.

Tofani, V., Del Ventisette, C., Moretti, S. & Casagli, N. 2014. Integration of Remote Sensing Techniques for Intensity Zonation within a Landslide Area: A Case Study in the Northern Apennines, Italy. *Remote Sensing,* 6**,** 907.

Torres, R., Snoeij, P., Geudtner, D., Bibby, D., Davidson, M., Attema, E., Potin, P., Rommen, B., Floury, N., Brown, M., Traver, I. N., Deghaye, P., Duesmann, B., Rosich, B., Miranda, N., Bruno, C., L'Abbate, M., Croci, R., Pietropaolo, A., Huchler, M. & Rostan, F. 2012. GMES Sentinel-1 mission. *Remote Sensing of Environment,* 120**,** 9-24.

Tosi, L., Carbognin, L., Teatini, P., Rosselli, R. & Gasparetto Stori, G. 2000. The ISES Project subsidence monitoring of the catchment basin south of the Venice Lagoon (Italy).

Trebitz, A. S., Brazner, J. C., Tanner, D. K. & Meyer, R. 2011. Interacting watershed size and landcover influences on habitat and biota of Lake Superior coastal wetlands. *Aquatic Ecosystem Health & Management,* 14**,** 443-455.

Ulaby, F., Moore, R. & Fung, A. 1982. Microwave remote sensing: Active and passive. 1-Microwave Remote Sensing Fundamentals and Radiometry.

Ulaby, F. T., Moore, R. K. & Fung, A. K. 1986. *Microwave Remote Sensing: Active and Passive*.

Valk, A. G. v. d. 2005. Water-level fluctuations in North American prairie wetlands. *Hydrobiologia,* 539**,** 171-188.

Vautard, R. & Ghil, M. 1989. Singular spectrum analysis in nonlinear dynamics, with applications to paleoclimatic time series. *Physica D: Nonlinear Phenomena,* 35**,** 395-424.

Vautard, R., Yiou, P. & Ghil, M. 1992. Singular-Spectrum Analysis - a Toolkit for Short, Noisy Chaotic Signals. *Physica D,* 58**,** 95-126.

Vitt, D. H., Wieder, K., Halsey, L. A. & Turetsky, M. 2003. Response of Sphagnum fuscum to Nitrogen Deposition: A Case Study of Ombrogenous Peatlands in Alberta, Canada. *The Bryologist,* 106**,** 235-245.

Waddington, J. M. & McNeil, P. 2002. Peat oxidation in an abandoned cutover peatland. *Canadian Journal of Soil Science,* 82**,** 279-286.

Warren, M. A. 2007. The development of a 3-Pass Persistent Scatterer algorithm using the Integer Ambiguity Search method. *PhD thesis, University of*

Nottingham.

Wegnüller, U., Werner, C., Strozzi, T., Wiesmann, A., Frey, O. & Santoro, M. 2016. Sentinel-1 Support in the GAMMA Software. *Procedia Computer Science,* 100**,** 1305-1312.

Werner, C., Wegmuller, U., Strozzi, T. & Wiesmann, A. 2003. Interferometric point target analysis for deformation mapping. 7**,** 4362-4364.

White, L., Brisco, B., Pregitzer, M., Tedford, B. & Boychuk, L. 2014. RADARSAT-2 Beam Mode Selection for Surface Water and Flooded Vegetation Mapping. *Canadian Journal of Remote Sensing,* 40**,** 135-151.

Whittington, P. N. & Price, J. S. 2006. The effects of water table draw-down (as a surrogate for climate change) on the hydrology of a fen peatland, Canada. *Hydrological Processes,* 20**,** 3589-3600.

Wickham, J. D., Stehman, S. V., Fry, J. A., Smith, J. H. & Homer, C. G. 2010. Thematic accuracy of the NLCD 2001 land cover for the conterminous United States. *Remote Sensing of Environment,* 114**,** 1286-1296.

Wickham, J. D., Stehman, S. V., Gass, L., Dewitz, J., Fry, J. A. & Wade, T. G. 2013. Accuracy assessment of NLCD 2006 land cover and impervious surface. *Remote Sensing of Environment,* 130**,** 294-304.

Wieder , R. K. & Vitt , D. H. 2006. Boreal Peatland Ecosystems. *Berlin: Springer.*

Wilson, B. A. & Rashid, H. 2005. Monitoring the 1997 flood in the Red River Valley using hydrologic regimes and RADARSAT imagery. *The Canadian Geographer/Le G?ographe canadien,* 49**,** 100-109.

Woodhouse, I. H. 2006. Introduction to Microwave Remote Sensing. *Taylor & Francis,*

Boca Raton, FL.

Wosten, J. H. M., Ismail, A. B. & vanWijk, A. L. M. 1997. Peat subsidence and its practical implications: A case study in Malaysia. *Geoderma,* 78**,** 25-36.

Wright, C. & Gallant, A. 2007. Improved wetland remote sensing in Yellowstone National Park using classification trees to combine TM imagery and ancillary environmental data. *Remote Sensing of Environment,* 107**,** 582-605.

Yague-Martinez, N., Prats-Iraola, P., Rodriguez Gonzalez, F., Brcic, R., Shau, R., Geudtner, D., Eineder, M. & Bamler, R. 2016. Interferometric Processing of Sentinel-1 TOPS Data. *IEEE Transactions on Geoscience and Remote Sensing,* 54**,** 2220-2234.

Yan, Y. J., Doin, M. P., Lopez-Quiroz, P., Tupin, F., Fruneau, B., Pinel, V. & Trouve, E. 2012. Mexico city subsidence measured by InSAR time series: joint analysis using PS and SBAS approaches. *Ieee Journal of Selected Topics in Applied Earth Observations and Remote Sensing,* 5**,** 1312-1326.

Yang, C. S., Zhang, Q., Xu, Q., Zhao, C. Y., Peng, J. B. & Ji, L. Y. 2016. Complex Deformation Monitoring over the Linfen-Yuncheng Basin (China) with Time Series InSAR Technology. *Remote Sensing,* 8.

Yang, X. J. 2005. Remote sensing and GIS applications for estuarine ecosystem analysis: an overview. *International Journal of Remote Sensing,* 26**,** 5347-5356.

Yu, Z., Loisel, J., Brosseau, D. P., Beilman, D. W. & Hunt, S. J. 2010. Global peatland dynamics since the Last Glacial Maximum. *Geophysical Research Letters,* 37**,** n/a-n/a.

Zanello, F. 2011. *Contributions to modeling of Venice coastal peatlands and wetlands.* PhD, University of Padova, Padova, Italy.

Zanello, F., Teatini, P., Putti, M. & Gambolati, G. 2011. Long term peatland subsidence: experimental study and modeling scenarios in the Venice coastland. *Journal of Geophysical Research-Earth Surface,* 116.

Zebker, H. A., Rosen, P. A., Goldstein, R. M., Gabriel, A. & Werner, C. L. 1994. On the derivation of coseismic displacement fields using differential radar interferometry: The Landers earthquake. *Journal of Geophysical Research: Solid Earth,* 99**,** 19617-19634.

Zebker, H. A., Rosen, P. A. & Hensley, S. 1997. Atmospheric effects in interferometric synthetic aperture radar surface deformation and topographic maps. *Journal of Geophysical Research-Solid Earth,* 102**,** 7547-7563.

Zebker, H. A. & Villasenor, J. 1992. Decorrelation in Interferometric Radar Echoes. *Ieee Transactions on Geoscience and Remote Sensing,* 30**,** 950-959.

Zhang, J., Hassani, H., Xie, H. & Zhang, X. 2014. Estimating multi-country prosperity index: A two-dimensional singular spectrum analysis approach. *Journal of Systems Science and Complexity,* 27**,** 56-74.

Zhou, X., Chang, N. B. & Li, S. 2009. Applications of SAR Interferometry in Earth and Environmental Science Research. *Sensors (Basel),* 9**,** 1876-912.

Zhou, Z., Li, Z., Waldron, S. & Tanaka, A. 2016. Monitoring peat subsidence and carbon emission in Indonesia peatlands using InSAR time series. 6797-6798.

Zhou, Z., Waldron, S. & Li, Z. 2010. Integration of PS-InSAR and GPS for monitoring seasonal and long-term peatland surface fluctuations. *Proceedings of the Remote Sensing and Photogrammetry Socity Confrence Remote Sensing and the Carbon Cycle.* Burlington House, London.

Appendix A



Figure A1: Blanket bog (the Flow country, Caithness and Sutherland). Adapted from Bruneau and Johnson (2014).



(a)



(b)



(c)

Figure A2: Examples of degraded peatland due to (a) moor-grips, (b) erosion and (c) peatslide. Adapted from Bruneau and Johnson (2014)

Appendix B

Methodology of the field survey that has been applied to assess the vegetation coverage for selected sites to be used for the calibration of the remote sensing images.

1. Walk to the GPS location and make a visual assessment of the general area
2. Mark a 10 x 10 square representative of the general area
3. Note the GPS coordinate of each corner on the designated space on the recording sheet and take a picture of the square
4. Fill in the details about the site and picture ID
5. Place yourself in the middle of the square and draw the outline of vegetation types in the square on the recording sheet
6. Note all Plant Functional Type in the square and give an overall cover class based on the Braun-Blanquet scale for each Plant Functional Type - you may need to walk in/around the plot to get a good estimate of smaller/non-dominant species.
7. Add any other relevant notes in the space provided
8. Remove the corner markers and move on to the next square

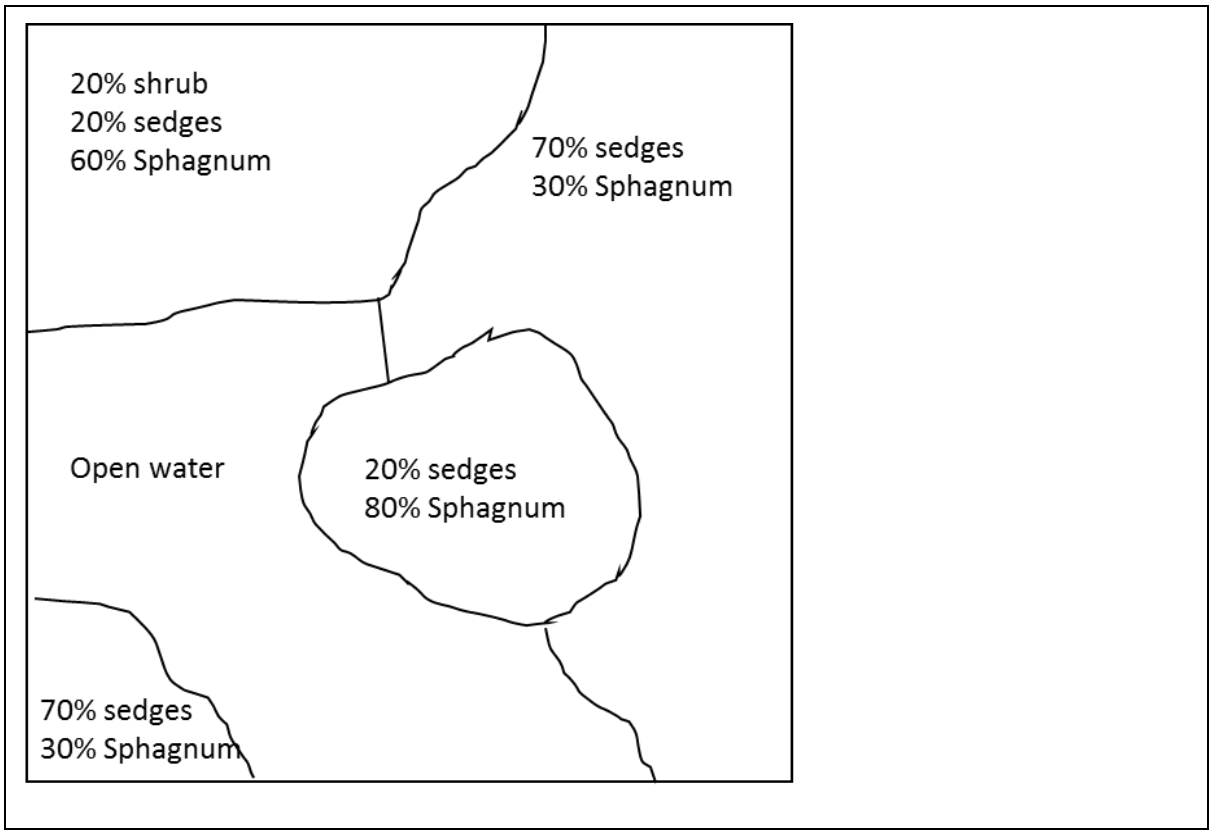
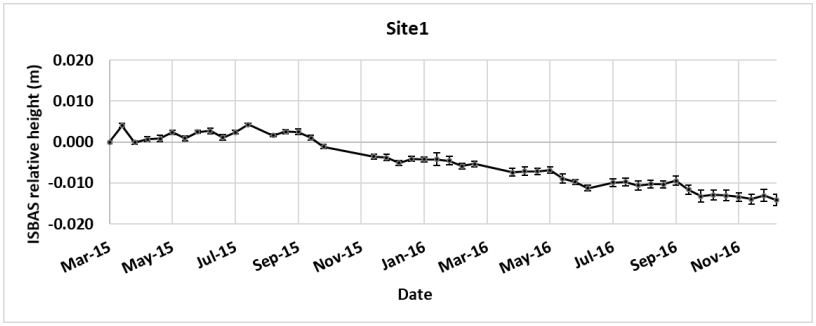
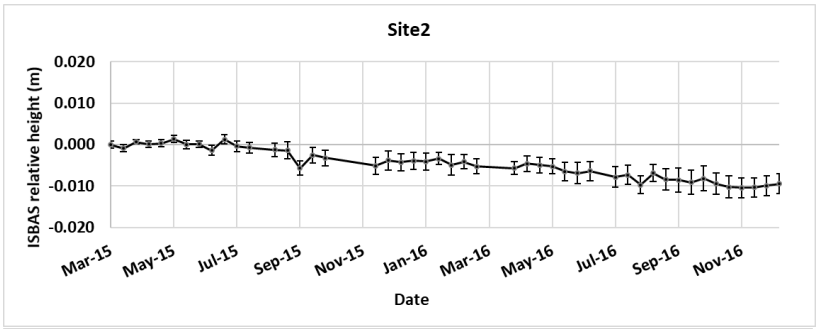
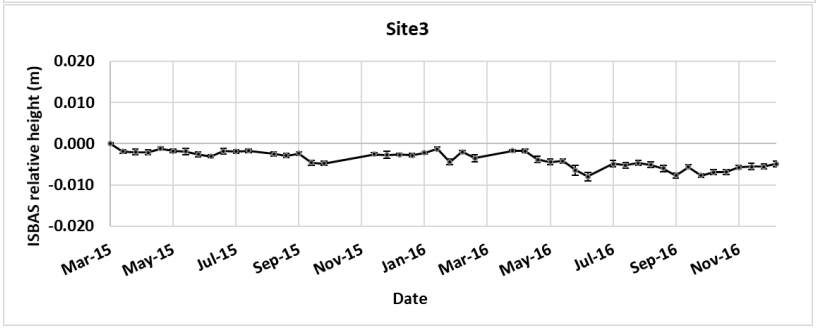


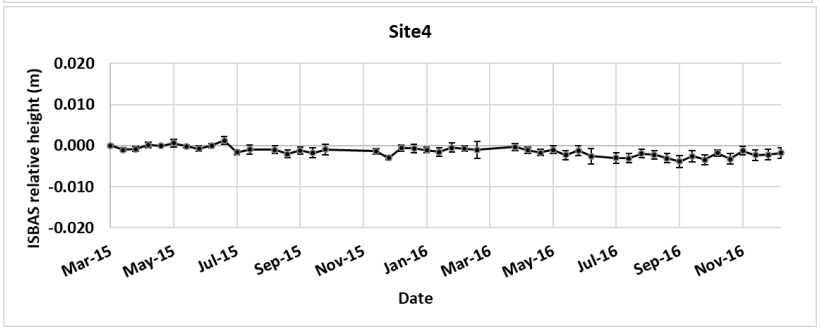
Figure B1: Example of drawing with the dominant Plant Functional Type vegetation outlined

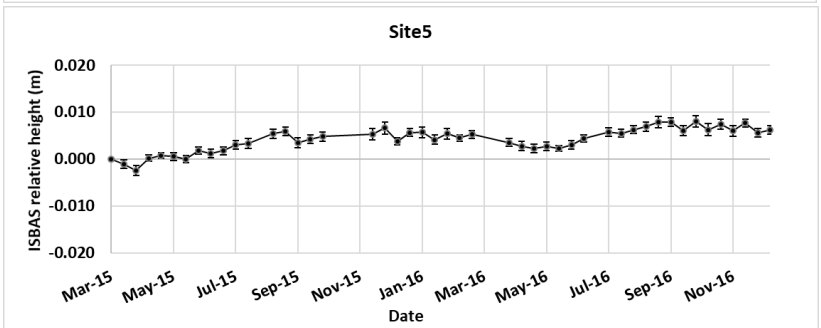
Appendix C

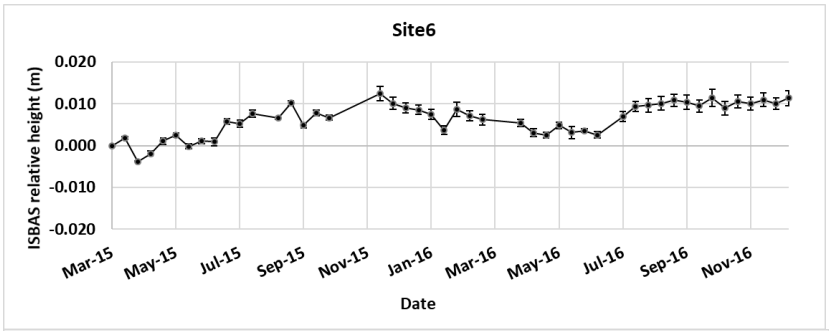

Site1
ISBAS relative height (m)
0.020
0.010
0.000
-0.010
-0.020
Mar-15
May-15
Jul-15
Sep-15
Nov-15
Jan-16
Mar-16
May-16
Jul-16
Sep-16
Nov-16
Date

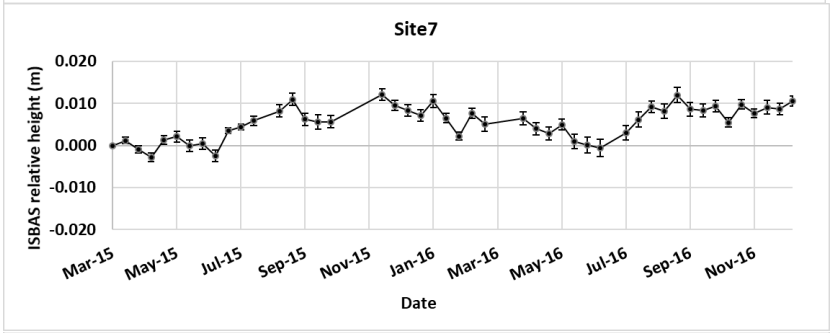

Site2
ISBAS relative height (m)
0.020
0.010
0.000
-0.010
-0.020
Mar-15
May-15
Jul-15
Sep-15
Nov-15
Jan-16
Mar-16
May-16
Jul-16
Sep-16
Nov-16
Date

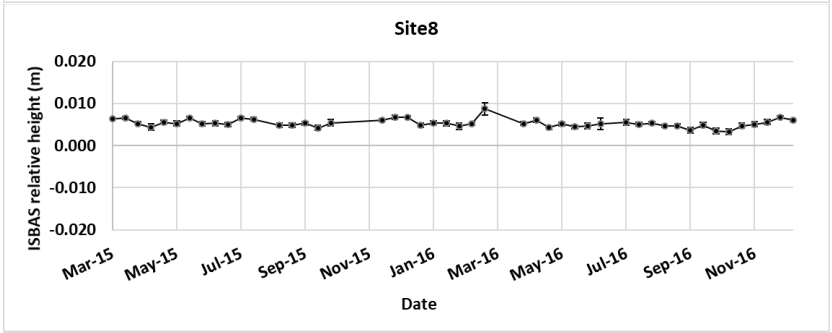

Site3
ISBAS relative height (m)
0.020
0.010
0.000
-0.010
-0.020
Mar-15
May-15
Jul-15
Sep-15
Nov-15
Jan-16
Mar-16
May-16
Jul-16
Sep-16
Nov-16
Date

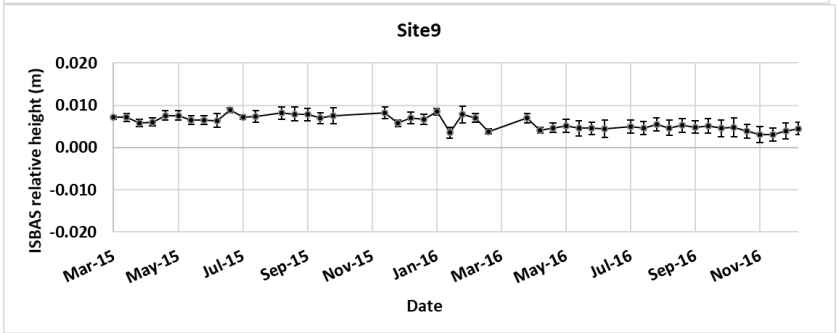

Site4
ISBAS relative height (m)
0.020
0.010
0.000
-0.010
-0.020
Mar-15
May-15
Jul-15
Sep-15
Nov-15
Jan-16
Mar-16
May-16
Jul-16
Sep-16
Nov-16
Date

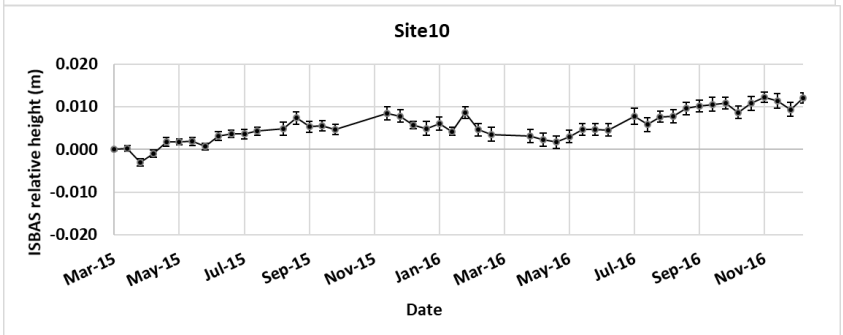

Site5
ISBAS relative height (m)
0.020
0.010
0.000
-0.010
-0.020
Mar-15
May-15
Jul-15
Sep-15
Nov-15
Jan-16
Mar-16
May-16
Jul-16
Sep-16
Nov-16
Date

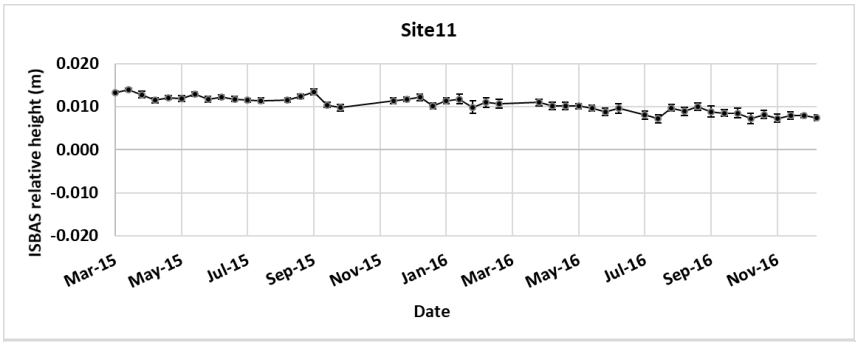

Site6
ISBAS relative height (m)
0.020
0.010
0.000
-0.010
-0.020
Mar-15
May-15
Jul-15
Sep-15
Nov-15
Jan-16
Mar-16
May-16
Jul-16
Sep-16
Nov-16
Date

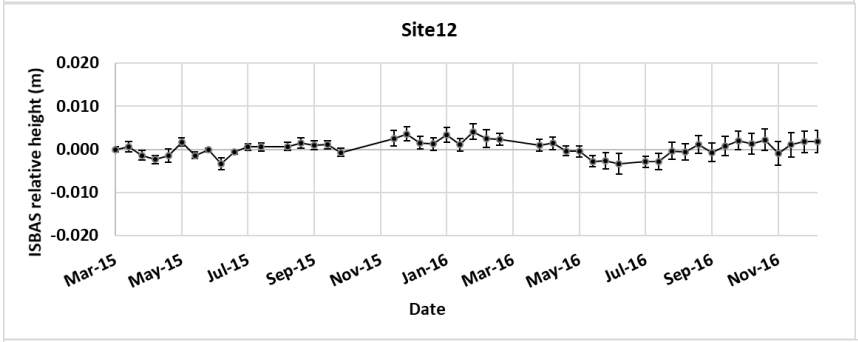

Site7
ISBAS relative height (m)
0.020
0.010
0.000
-0.010
-0.020
Mar-15
May-15
Jul-15
Sep-15
Nov-15
Jan-16
Mar-16
May-16
Jul-16
Sep-16
Nov-16
Date

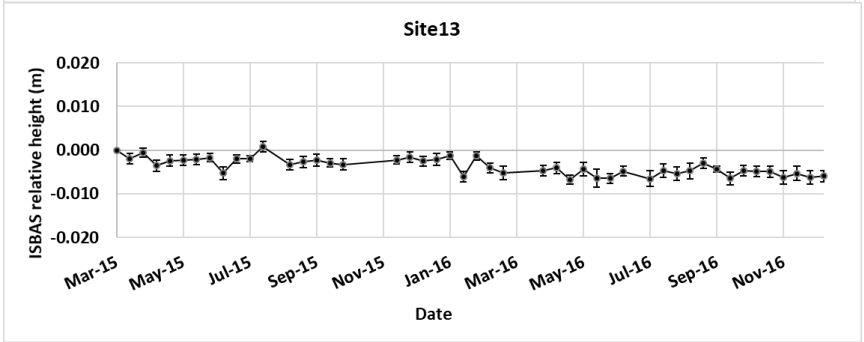

Site8
ISBAS relative height (m)
0.020
0.010
0.000
-0.010
-0.020
Mar-15
May-15
Jul-15
Sep-15
Nov-15
Jan-16
Mar-16
May-16
Jul-16
Sep-16
Nov-16
Date

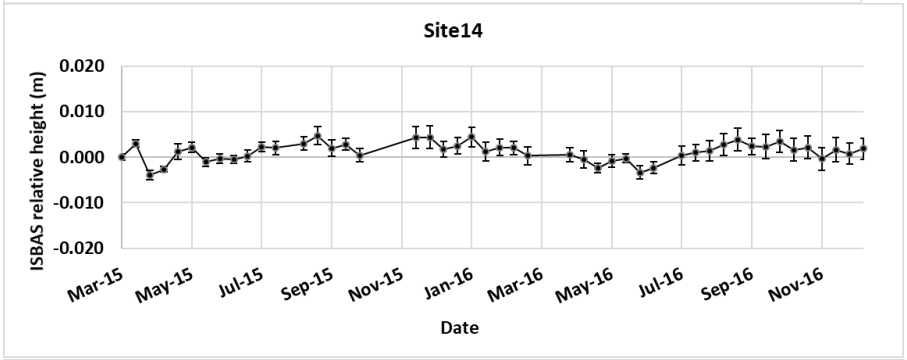

Site9
ISBAS relative height (m)
0.020
0.010
0.000
-0.010
-0.020
Mar-15
May-15
Jul-15
Sep-15
Nov-15
Jan-16
Mar-16
May-16
Jul-16
Sep-16
Nov-16
Date

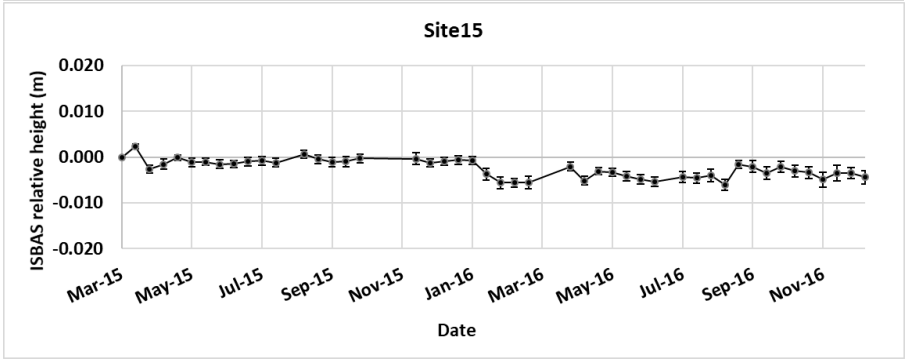

Site10
ISBAS relative height (m)
0.020
0.010
0.000
-0.010
-0.020
Mar-15
May-15
Jul-15
Sep-15
Nov-15
Jan-16
Mar-16
May-16
Jul-16
Sep-16
Nov-16
Date

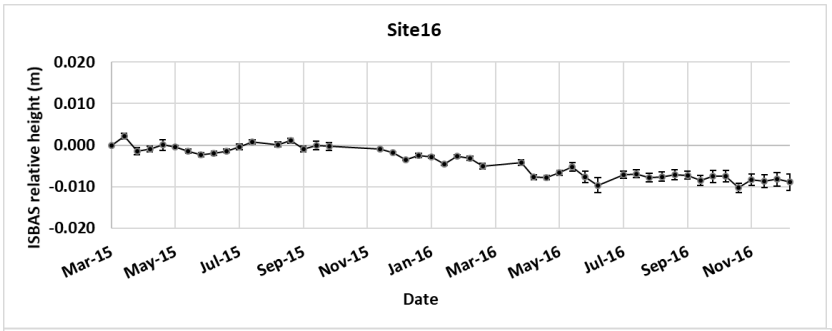

Site11
ISBAS relative height (m)
0.020
0.010
0.000
-0.010
-0.020
Mar-15
May-15
Jul-15
Sep-15
Nov-15
Jan-16
Mar-16
May-16
Jul-16
Sep-16
Nov-16
Date

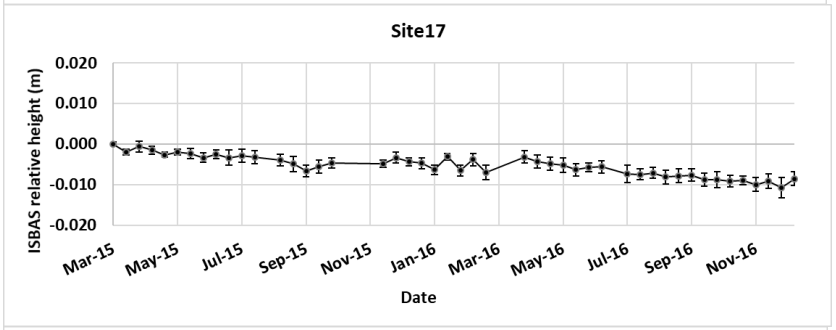

Site12
ISBAS relative height (m)
0.020
0.010
0.000
-0.010
-0.020
Mar-15
May-15
Jul-15
Sep-15
Nov-15
Jan-16
Mar-16
May-16
Jul-16
Sep-16
Nov-16
Date

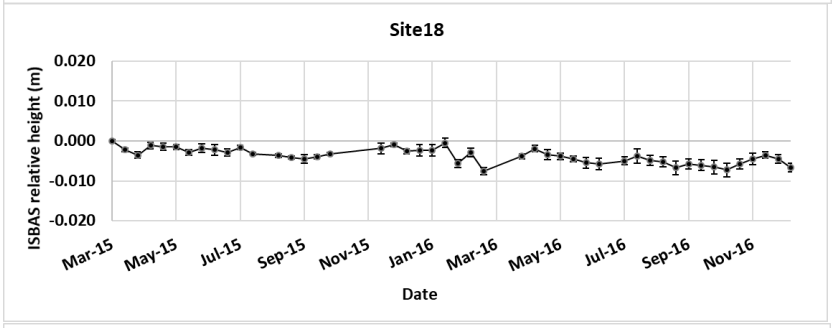

Site13
ISBAS relative height (m)
0.020
0.010
0.000
-0.010
-0.020
Mar-15
May-15
Jul-15
Sep-15
Nov-15
Jan-16
Mar-16
May-16
Jul-16
Sep-16
Nov-16
Date

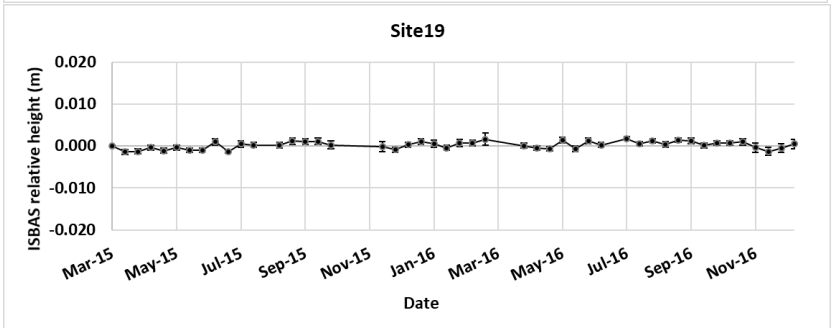

Site14
ISBAS relative height (m)
0.020
0.010
0.000
-0.010
-0.020
Mar-15
May-15
Jul-15
Sep-15
Nov-15
Jan-16
Mar-16
May-16
Jul-16
Sep-16
Nov-16
Date

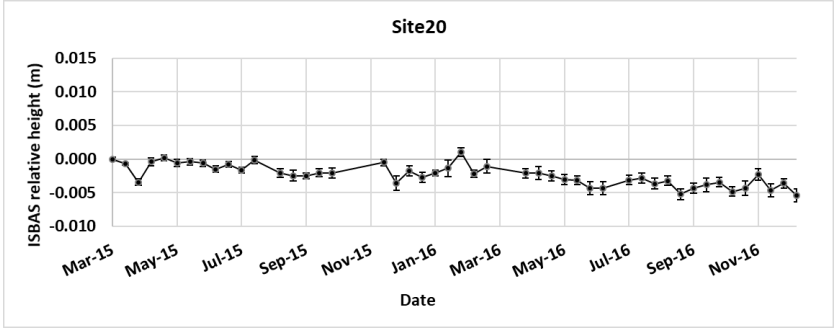

Site15
ISBAS relative height (m)
0.020
0.010
0.000
-0.010
-0.020
Mar-15
May-15
Jul-15
Sep-15
Nov-15
Jan-16
Mar-16
May-16
Jul-16
Sep-16
Nov-16
Date


Site16
ISBAS relative height (m)
0.020
0.010
0.000
-0.010
-0.020
Mar-15
May-15
Jul-15
Sep-15
Nov-15
Jan-16
Mar-16
May-16
Jul-16
Sep-16
Nov-16
Date


Site17
ISBAS relative height (m)
0.020
0.010
0.000
-0.010
-0.020
Mar-15
May-15
Jul-15
Sep-15
Nov-15
Jan-16
Mar-16
May-16
Jul-16
Sep-16
Nov-16
Date


Site18
ISBAS relative height (m)
0.020
0.010
0.000
-0.010
-0.020
Mar-15
May-15
Jul-15
Sep-15
Nov-15
Jan-16
Mar-16
May-16
Jul-16
Sep-16
Nov-16
Date


Site19
ISBAS relative height (m)
0.020
0.010
0.000
-0.010
-0.020
Mar-15
May-15
Jul-15
Sep-15
Nov-15
Jan-16
Mar-16
May-16
Jul-16
Sep-16
Nov-16
Date


Site20
ISBAS relative height (m)
0.015
0.010
0.005
0.000
-0.005
-0.010
Mar-15
May-15
Jul-15
Sep-15
Nov-15
Jan-16
Mar-16
May-16
Jul-16
Sep-16
Nov-16
Date

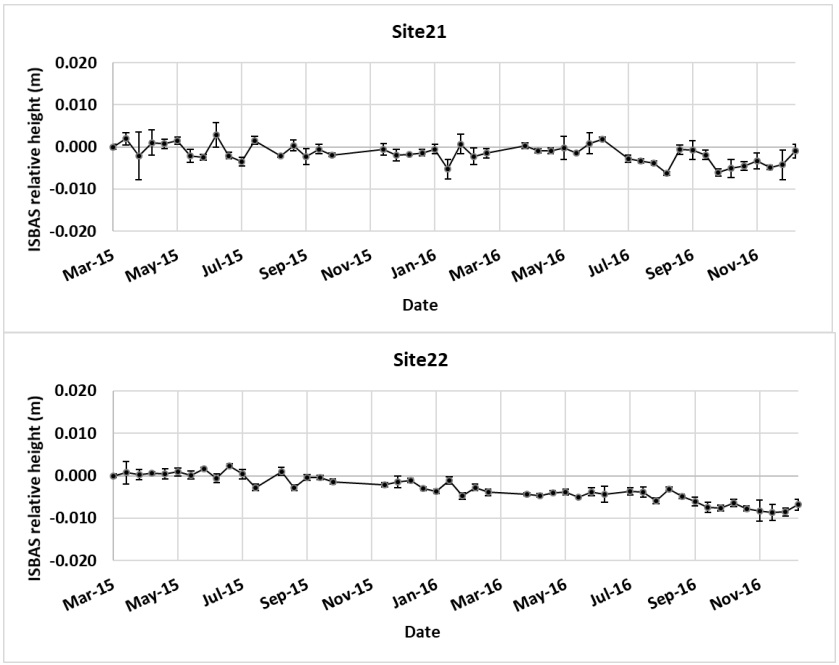


Figure C1: ISBAS DInSAR time-series from an average 5 adjoining pixels for the 22 sites

Table C1: Peat condition at each ISBAS point distributed in 22 sites. this was done using optical satellite data (Sentinel-2 and Google Earth provided VHR data) and field observations of plant functional type.

Point No.	Site_No	Decision	Point No.	Site_No	Decision
1	**1**	(3) Shrubs/Sedges/*Sphagnum*	**53**	**11**	(4) Bare peat/Shrubs/Sedges
2	**1**	(3) Shrubs/Sedges/*Sphagnum*	**54**	**12**	(1) *Sphagnum*/Sedges
3	**1**	(3) Shrubs/Sedges/*Sphagnum*	**55**	**12**	(1) *Sphagnum*/Sedges
4	**1**	(2) Sedges/*Sphagnum*/Shrubs	**56**	**12**	(1) *Sphagnum*/Sedges
5	**1**	(2) Sedges/*Sphagnum*/Shrubs	**57**	**12**	(1) *Sphagnum*/Sedges
6	**2**	(1) *Sphagnum*/Sedges	**58**	**13**	(3) Shrubs/Sedges/*Sphagnum*
7	**2**	(3) Shrubs/Sedges/*Sphagnum*	**59**	**13**	(3) Shrubs/Sedges/*Sphagnum*
8	**2**	(3) Shrubs/Sedges/*Sphagnum*	**60**	**13**	(2) Sedges/*Sphagnum*/Shrubs
9	**2**	(2) Sedges/*Sphagnum*/Shrubs	**61**	**13**	(2) Sedges/*Sphagnum*/Shrubs
10	**2**	(3) Shrubs/Sedges/*Sphagnum*	**62**	**14**	(1) *Sphagnum*/Sedges
11	**3**	(3) Shrubs/Sedges/*Sphagnum*	**63**	**14**	(2) Sedges/*Sphagnum*/Shrubs
12	**3**	(3) Shrubs/Sedges/*Sphagnum*	**64**	**14**	(1) *Sphagnum*/Sedges
13	**3**	(3) Shrubs/Sedges/*Sphagnum*	**65**	**14**	(2) Sedges/*Sphagnum*/Shrubs
14	**3**	(3) Shrubs/Sedges/*Sphagnum*	**66**	**15**	(3) Shrubs/Sedges/*Sphagnum*
15	**4**	(3) Shrubs/Sedges/*Sphagnum*	**67**	**15**	(3) Shrubs/Sedges/*Sphagnum*
16	**4**	(3) Shrubs/Sedges/*Sphagnum*	**68**	**15**	(3) Shrubs/Sedges/*Sphagnum*
17	**4**	(3) Shrubs/Sedges/*Sphagnum*	**69**	**15**	(3) Shrubs/Sedges/*Sphagnum*
18	**4**	(3) Shrubs/Sedges/*Sphagnum*	**70**	**15**	(3) Shrubs/Sedges/*Sphagnum*
19	**5**	(2) Sedges/*Sphagnum*/Shrubs	**71**	**15**	(3) Shrubs/Sedges/*Sphagnum*
20	**5**	(3) Shrubs/Sedges/*Sphagnum*	**72**	**16**	Demolished Wood land
21	**5**	(3) Shrubs/Sedges/*Sphagnum*	**73**	**16**	Demolished Wood land
22	**5**	(2) Sedges/*Sphagnum*/Shrubs	**74**	**16**	Demolished Wood land
23	**5**	(2) Sedges/*Sphagnum*/Shrubs	**75**	**16**	Demolished Wood land
24	**6**	(2) Sedges/*Sphagnum*/Shrubs	**76**	**17**	(1) *Sphagnum*/Sedges
25	**6**	(1) *Sphagnum*/Sedges	**77**	**17**	(3) Shrubs/Sedges/*Sphagnum*
26	**6**	(1) *Sphagnum*/Sedges	**78**	**17**	(3) Shrubs/Sedges/*Sphagnum*
27	**6**	(1) *Sphagnum*/Sedges	**79**	**17**	(3) Shrubs/Sedges/*Sphagnum*
28	**7**	(2) Sedges/*Sphagnum*/Shrubs	**80**	**17**	(3) Shrubs/Sedges/*Sphagnum*
29	**7**	(2) Sedges/*Sphagnum*/Shrubs	**81**	**17**	(3) Shrubs/Sedges/*Sphagnum*
30	**7**	(2) Sedges/*Sphagnum*/Shrubs	**82**	**18**	(1) *Sphagnum*/Sedges
31	**7**	(1) *Sphagnum*/Sedges	**83**	**18**	(2) Sedges/*Sphagnum*/Shrubs
32	**8**	(1) *Sphagnum*/Sedges	**84**	**18**	(3) Shrubs/Sedges/*Sphagnum*
33	**8**	(1) *Sphagnum*/Sedges	**85**	**18**	(1) *Sphagnum*/Sedges
34	**8**	(3) Shrubs/Sedges/*Sphagnum*	**86**	**19**	(1) *Sphagnum*/Sedges
35	**8**	(3) Shrubs/Sedges/*Sphagnum*	**87**	**19**	(1) *Sphagnum*/Sedges
36	**8**	(3) Shrubs/Sedges/*Sphagnum*	**88**	**19**	(2) Sedges/*Sphagnum*/Shrubs
37	**8**	(3) Shrubs/Sedges/*Sphagnum*	**89**	**19**	(1) *Sphagnum*/Sedges
38	**9**	(4) Bare peat/Shrubs/Sedges	**90**	**19**	(1) *Sphagnum*/Sedges
39	**9**	(4) Bare peat/Shrubs/Sedges	**91**	**19**	(5) Water
40	**9**	(4) Bare peat/Shrubs/Sedges	**92**	**20**	(4) Bare peat/Shrubs/Sedges
41	**9**	(3) Shrubs/Sedges/*Sphagnum*	**93**	**20**	(1) *Sphagnum*/Sedges
42	**10**	(3) Shrubs/Sedges/*Sphagnum*	**94**	**20**	(2) Sedges/*Sphagnum*/Shrubs

43	**10**	(2) Sedges/*Sphagnum*/Shrubs	**95**	**20**	(4) Bare peat/Shrubs/Sedges
44	**10**	(2) Sedges/*Sphagnum*/Shrubs	**96**	**20**	(3) Shrubs/Sedges/*Sphagnum*
45	**10**	(3) Shrubs/Sedges/*Sphagnum*	**97**	**20**	(3) Shrubs/Sedges/*Sphagnum*
46	**10**	(1) *Sphagnum*/Sedges	**98**	**21**	Wood land
47	**10**	(2) Sedges/*Sphagnum*/Shrubs	**99**	**21**	Wood land
48	**11**	(4) Bare peat/Shrubs/Sedges	**100**	**22**	(3) Shrubs/Sedges/*Sphagnum*
49	**11**	(4) Bare peat/Shrubs/Sedges	**101**	**22**	(3) Shrubs/Sedges/*Sphagnum*
50	**11**	(4) Bare peat/Shrubs/Sedges	**102**	**22**	(3) Shrubs/Sedges/*Sphagnum*
51	**11**	(4) Bare peat/Shrubs/Sedges	**103**	**22**	(3) Shrubs/Sedges/*Sphagnum*
52	**11**	(4) Bare peat/Shrubs/Sedges			